DEVELOPMENT AND EVALUATION OF TERAHERTZ TIME-DOMAIN SPECTROSCOPY FOR ELECTRIC PROPULSION PLASMA DIAGNOSTICS

A Dissertation
Presented to
The Academic Faculty

by

Nathan Parnell Brown

In Partial Fulfillment
of the Requirements for the Degree
Doctor of Philosophy in the
Daniel Guggenheim School of Aerospace Engineering

Georgia Institute of Technology
December 2020

COPYRIGHT © 2020 BY NATHAN PARNELL BROWN

DEVELOPMENT AND EVALUATION OF TERAHERTZ TIME-DOMAIN SPECTROSCOPY FOR ELECTRIC PROPULSION PLASMA DIAGNOSTICS

Approved by:

Dr. Mitchell Walker, Advisor
School of Aerospace Engineering
Georgia Institute of Technology

Dr. Lukas Graber
School of Electrical and
Computer Engineering
Georgia Institute of Technology

Dr. Adam Steinberg, Advisor
School of Aerospace Engineering
Georgia Institute of Technology

Dr. Wenting Sun
School of Aerospace Engineering
Georgia Institute of Technology

Dr. Jason Deibel
School of Physics
Wright State University

Date Approved: 11/12/2020

“What should we do but seek adventure after adventure?”

- C. S. Lewis in *The Voyage of the Dawn Treader*

ACKNOWLEDGEMENTS

This dissertation would not have been possible without help from many people and organizations. Thank you to the National Science Foundation Graduate Research Fellowship Program, ARCS Foundation, Georgia Tech President's Fellowship Program, and Georgia Tech Institute for Materials Graduate Student Fellowship Program for providing personal funding. Thank you to the Air Force Office of Scientific Research for purchasing many of the necessary optics and optomechanical components.

Thank you to my committee for reading the dissertation and providing helpful feedback. I appreciate the time each of you took out of your busy schedules to review the document and attend the defense. Thank you to Professor Jason Deibel for showing me around his laboratory at Wright State University and for taking the time to train me on his THz-TDS system. Your initial training and later THz-TDS advice were crucial to the completion of this dissertation. Thank you to Professors Adam Steinberg and Mitchell Walker for your advisement. Professor Steinberg, thank you for taking me on in my third year of graduate school and your first year as a Georgia Tech professor. Your expertise in optics and uncertainty quantification was needed and greatly appreciated. Professor Walker, thank you for giving me a place in your laboratory as an undergraduate student and for serving as my advisor throughout graduate school. You always pushed me to expand my boundaries, and I am exceedingly grateful for your mentorship.

Thank you to Professor Eric Feron and Drs. Dan Goebel, Kuei-Ru Chen, Tom Liu, Jason Frieman, Sam Langendorf, and Aaron Schinder for providing mentorship and encouraging me to pursue graduate school in EP. Thank you to Professors Julian Rimoli

and Jud Ready for the guidance and assistance you provided on EP projects not related to this dissertation. Thank you, Dr. Samuel Grauer, for the help you gave me with the Bayesian analysis framework. You will make an excellent professor, and I cannot wait to see what else you accomplish. Thank you, Dr. Logan Williams, for your help with RF circuit design. Jeremy Mitchell, thank you for showing me how to use the tools in the machine shop and for making sure I didn't lose any fingers.

Thank you to the current and recently graduated members of HPEPL, who helped ensure I will leave Georgia Tech with fond memories. Dr. Connie, thank you for helping me scrub vacuum chambers clean of sputtered graphite foil and for exploring electrical facility effects with me. David, thank you for sticking it through IHI Hall thruster test campaigns and first-year classes with me. Nick, thank you for challenging my understanding of vacuum and plasma theory and doing everything you could to ease P-card pain. Jean Luis, thank you for providing a sounding board for plasma and optical physics challenges. Thank you to Cameron, Wyatt, Collin, Muhannad, Adrian, Janice, and Will for helping me around the lab; I'm sure you will all have successful graduate careers. Naia, Chris, Ethan, Chhavi, and Mikal, though we never worked together, I appreciate our stimulating EP discussions and wish you the best as you work toward your degrees.

Michael, Omar, DiSalles, Miltners, Coats, Fees, and Hawkins, thank you for providing much-needed fun and hangouts during my time as a graduate student. Thank you to the Loverns, Ryans, Robinsons, Smiths, Ellingtons, and many other wonderful people I've met at Renovation Church. Ryans and Robinsons, thank you for providing much-needed community during an unprecedented pandemic. I thoroughly enjoyed our quarantine church.

Thank you to all my grandparents, cousins, aunts, and uncles for your support over the years. Davis, Samuel, Garrett, and Kelsi, thank you for being great siblings and siblings-in-law. Valerie and Craig, thank you for welcoming me into your family and rooting for me from across the country. Mom and Dad, thank you for raising me and encouraging me to pursue higher education.

Alissa, thank you for the tremendous support you have provided as my wife and best friend. Most people will never know how hard it is to persevere through a Ph.D. program; qualifying exams, chronically broken equipment, and bureaucratic roadblocks gave me plenty of opportunities to second-guess my career path. But you never wavered in your support. Thank you for always encouraging me and pushing me to pursue my dreams. I cannot wait to start the next phase of our lives together in New Mexico.

Finally, thank you, God, for creating a universe worth exploring and enabling me to play a small role in that exploration. Particles spawned in a Big Bang came together to form atoms and molecules that, after billions of years of evolution, combined to give rise to the consciousness writing this dissertation. Isn't that amazing?

TABLE OF CONTENTS

LIST OF TABLES

LIST OF FIGURES

NOMENCLATURE

A	Magnitude of spectral ratio
a	Fit coefficient
B	Magnetic field strength
B_c	Critical magnetic field strength for assumption validity
$\mathbf{b}$	Vector of measurements
$\mathbf{b}_{\mathrm{mod}}$	Vector of ideal measurements
c	Speed of light in vacuum
D	Transmission coefficient
d_b	Beam diameter
d_c	Collimation distance
E	Electric field amplitude
$\hat{E}$	Fourier transform of electric field amplitude
e	Electron charge
FP	Fabry-Pérot reflection term
G	Propagation and transmission terms shared by sample and reference
g_0	Gravitational acceleration at Earth's surface
I_{sp}	Specific impulse
i	Imaginary unit
$\tilde{J}$	Complex current density
$\tilde{J}_p$	Complex plasma current density
k	Discrete spectrum index
k_B	Boltzmann's constant

L	Propagation distance through medium
M	Number of discrete electric field indices
N	Number of entries in vector of measurements
m	Discrete field index
m_e	Electron mass
m_p	Propellant mass
m_v	Vehicle mass
n	Real refractive index
n_e	Electron number density
$n_{e,c}$	Critical electron number density for assumption validity
$n_{e,cr}$	Critical electron number density at plasma cut-off
n_p	Real plasma refractive index
$\tilde{n}$	Complex refractive index
$\tilde{n}_p$	Complex plasma refractive index
$\tilde{n}_{p_{l,r}}$	Complex plasma refractive index for parallel pulse propagation
$\tilde{n}_{p_\perp}$	Complex plasma refractive index for perpendicular pulse propagation
$p()$	Probability distribution function
R	Total demodulator signal magnitude
r	Magnitude correction factor
s	Standard deviation
T_e	Electron temperature
$T_{e,c}$	Critical electron temperature for assumption validity
T_{scan}	Total temporal duration of discrete field
t	Time
v_e	Propellant exhaust velocity

Δv	Total velocity increment
$\mathbf{x}$	Vector of extracted plasma parameters
X	Demodulator output
Y	Demodulator output
W	Number of discontinuities
z	Position
α	Absorption or extinction coefficient
β	Faraday rotation angle
$\mathbf{\Gamma}$	Error covariance matrix
$\tilde{\varepsilon}_p$	Complex plasma dielectric constant
ϵ_0	Permittivity of free space
$\boldsymbol{\theta}$	Vector of nuisance parameters
Λ	Amplitude
λ	Wavelength
μ	Average value
ν	Electron collision frequency
ν_c	Critical electron collision frequency for assumption validity
ξ	Electron displacement
$\tilde{\sigma}$	Complex conductivity
$\tilde{\sigma}_p$	Complex plasma conductivity
Φ	Phase of spectral ratio
φ_2	Phase correction factor
τ	Polarization ellipticity
ω	Frequency
ω_b	Electron cyclotron frequency

ω_p	Plasma frequency

SUMMARY

Terahertz time-domain spectroscopy (THz-TDS) is a novel plasma diagnostic that has the potential to fill present gaps in electric propulsion (EP) plasma diagnostic capabilities. However, there remain unanswered questions and challenges regarding THz-TDS capability and data interpretation that must be addressed before the diagnostic is readily applied to EP devices. The purpose of this dissertation is to develop and evaluate THz-TDS for EP plasma diagnostics. To that end, this dissertation provides three major contributions: 1) Analysis of the THz-TDS domain of applicability; 2) Development of a novel Bayesian THz-TDS plasma diagnostic analysis framework and subsequent evaluation of THz-TDS uncertainty; and 3) Development and application of THz-TDS to noninvasively probe plasma bounded and optically shielded by Hall thruster wall material.

CHAPTER 1. INTRODUCTION

This chapter introduces electric propulsion (EP), motivates the development of terahertz time-domain spectroscopy (THz-TDS) for EP plasma diagnostics, and concludes with a road map of the dissertation. The EP overview is provided in Section 1.1, the motivation is presented in Section 1.2, and the road map is given in Section 1.3.

1.1 EP Overview

1.1.1 Advantage of EP

Spacecraft propulsion operates on the principle of conservation of momentum; ejection of propellant mass in one direction imparts thrust in the opposite direction. Change in momentum can be expressed in terms of the resulting total vehicle velocity increment (Δv) and is related to the propellant exhaust velocity (v_e), vehicle mass (m_v), and propellant mass (m_p) by the ideal rocket equation [1-3]:

$$\Delta v = v_e \ln\left(\frac{m_v + m_p}{m_v}\right). \tag{1}$$

Achievable velocity increment is directly related to propellant exhaust velocity and only logarithmically related to propellant mass. In many cases, large savings in propellant mass can therefore be realized by comparably smaller increases in propellant exhaust velocity. As an example, Figure 1 shows the propellant mass required to achieve the 11 km/s total in-space velocity increment imparted to the approximately 750 kg NASA Dawn vehicle on its mission to Vesta and Ceres [4]. Increasing the propellant exhaust

velocity from 5 km/s to 6 km/s represents a 20% increase in exhaust velocity but results in an approximately 35% decrease in required propellant mass.

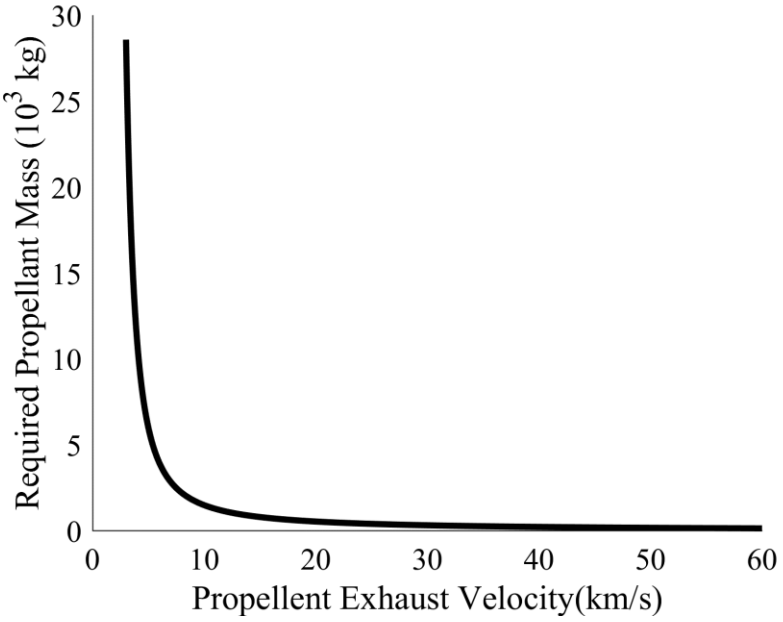

Figure 1 – Required propellant mass as a function of propellant exhaust velocity for the NASA Dawn mission (according to ideal rocket equation)

Chemical rockets accelerate propellant by releasing the energy stored in chemical bonds and are therefore limited to exhaust velocities of approximately 5 km/s [3]. EP devices, by contrast, harness electrical energy provided by an external source to accelerate propellant. Consequently, EP rockets have achieved exhaust velocities greater than 100 km/s [2, 3]. Dawn's NSTAR gridded ion thrusters were capable of exhaust velocities larger than 30 km/s, so the mission's 11 km/s velocity increment was achieved with less than 500 kg of propellant [4]. The use of chemical rockets to complete the same mission would have required Dawn to carry more than 6000 kg of propellant.

The tremendous propellant mass savings offered by EP makes it an ideal candidate for both deep-space exploration and satellite station-keeping and orbit-raising. In addition to NASA Dawn, EP devices have prominently featured on the ESA SMART-1 and ESA-JAXA BepiColombo missions and have planned roles in the upcoming NASA Psyche and Artemis missions [2, 5-8]. More than 600 satellites have utilized EP thrusters, and this number is rapidly growing as SpaceX is presently launching as many as 60 EP satellites at a time for its Starlink constellation program [8, 9].

1.1.2 EP Thrusters

EP technologies can be broadly categorized as electrothermal, electrostatic, or electromagnetic [1-3]. Electrothermal devices, such as the arcjet and resistojet, heat propellant with electricity and then accelerate it through a nozzle. Electrostatic and electromagnetic devices utilize electricity to ionize propellant and produce thrust by accelerating the resulting plasma with applied fields. Differentiation between these two categories is determined by the acceleration mechanism; electrostatic devices accelerate plasma by direct application of an electric field, whereas electromagnetic devices provide accelerating forces with a combination of electric and magnetic fields. The gridded ion thruster is an electrostatic device, the magnetoplasmadynamic (MPD) thruster is an electromagnetic device, and the categorization of the Hall thruster as either an electrostatic or electromagnetic device is debated [2, 3]. Figure 2 shows a Hall thruster operating at the Georgia Tech High-Power Electric Propulsion Laboratory (HPEPL).

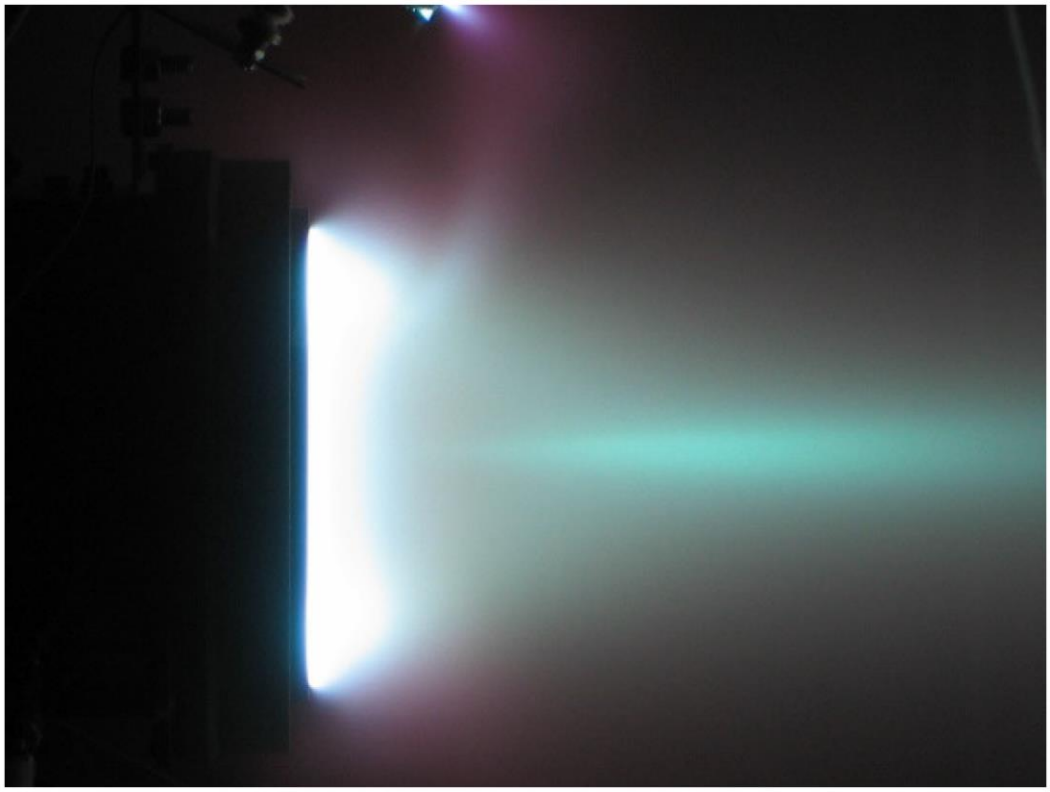

Figure 2 – Aerojet Rocketdyne T-140 Hall thruster

Standard metrics for EP thruster performance are specific impulse and thrust [3]. Specific impulse (I_{sp}) is the total momentum imparted per unit weight of propellant and, in the case of constant thrust, is related to propellant exhaust velocity and gravity's acceleration at Earth's surface (g_0) by

$$I_{sp} = \frac{v_e}{g_0}. \tag{2}$$

Typical values of specific impulse and thrust for some well-studied EP devices are shown in Table 1, which is directly reproduced from [3].

Table 1 – Typical specific impulse and thrust of EP devices (data from [3])

Device	Specific Impulse (s)	Thrust (N)
Resistojet	100 – 300	0.2
Arcjet	500	0.1
Gridded Ion Thruster	3000	0.001 – 0.1
Hall Thruster	1500	0.01 – 1
MPD Thruster	1000 – 10000	0.5 – 50

Other EP technologies include pulsed plasma thrusters, electrospray thrusters, radio frequency (RF) ion thrusters, and helicon thrusters.

1.1.3 EP Plasma

Nearly all established EP devices, with the notable exception of resistojets, generate plasma [3]. Plasma is a state of matter that consists of ions and free electrons and, therefore, exhibits a collective response to external electromagnetic fields.

Charge concentrations in plasmas are screened (or "shielded out") by the freely moving charge carriers. The scale across which charge screening occurs is called the Debye length (or radius of the Debye sphere). Three conditions must typically be met for a substance to be considered plasma [10]:

1. The Debye length is much smaller than the plasma extent
2. The number of particles in a Debye sphere is much greater than unity
3. The product of the frequency of typical plasma oscillations and the mean time between collisions of charged and neutral species is greater than unity

The tendency of plasmas to screen out charge concentrations causes most plasmas to be quasineutral, meaning the number of electrons in a volume much greater than the Debye sphere is approximately equal to the number of ions in that same volume. Notable exceptions to plasma quasineutrality occur in magnetically confined free-electron plasmas and in the sheath region of plasma-wall interfaces [10]. As neither of these exceptions is discussed in this document, the terms "plasma density" and "electron density" are used interchangeably.

Most EP plasmas feature moderate plasma densities, low electron temperatures, low collision frequencies, and weak applied magnetic fields [1-3]. The bulk plasma density inside gridded ion and Hall thrusters is on the order of $10^{17} – 10^{19}$ m^{-3}, whereas densities as large as 10^{21} m^{-3} are not uncommon in MPD and helicon thrusters and in ion and Hall thruster hollow cathodes. Electron temperatures typically remain below 100 eV (1.16×10^6 K), collision frequencies are generally much lower than characteristic plasma oscillation frequencies, and applied magnetic fields are usually weaker than 1 T.

Plasmas in EP devices are most commonly generated by direct current (DC) breakdown of gaseous propellant between a cathode and anode [1-3, 11]. Electrons are emitted by the cathode and energized by the potential difference between the cathode and anode. Emitted electrons collide with neutral particles and impart sufficient energy to free bound electrons, thereby forming ions. The newly freed electrons collide with other neutral particles and thereby free more electrons and form more ions in an ionization cascade that results in a sustained plasma. Ionization is often aided by the application of magnetic fields that serve to confine ionizing electrons to a desired ionization region.

RF discharges are also used to generate EP plasmas. In the case of RF ion thrusters and helicon thrusters, plasma is ignited and sustained by energy delivered to propellant in the form of electromagnetic radiation emitted from an antenna either wrapped around or submersed in the thruster discharge [12-14]. At low powers, plasma is generated by capacitive coupling; ionizing electrons are primarily accelerated into neutral particles by the oscillating potential difference between the ends of the antenna. Increasing power brings about the onset of the inductive coupling mode observed in RF ion thrusters. The denser plasma becomes more effective at shielding the potential between the antenna ends, and the antenna's induced electromagnetic field becomes the primary electron acceleration mechanism. Finally, if power is increased further and appropriate magnetic confinement and antenna design are employed, the discharge can enter the high-density helicon mode. Electrons are then primarily accelerated by helicon waves propagating through the plasma.

1.1.3.1 Hall Thruster Plasma

Due to the rising popularity of Hall thrusters for both satellite and space exploration vehicles, many recent EP research efforts have focused on understanding Hall thruster plasma [2, 15, 16]. As shown in Figure 3, Hall thruster plasma is generated when electrons emitted from a hollow cathode collide with neutral propellant atoms fed into the thruster interior through an anode. The propellant species is typically xenon, but other gases, such as krypton and argon, are also used. An electric field is established between the cathode and anode, and a magnetic field is established perpendicular to the electric field by solenoids. The solenoids are typically shielded from the discharge plasma by boron nitride-silica ($BN\text{-}SiO_2$) composite walls. The region between the composite walls is the Hall thruster discharge channel. The crossed electric and magnetic fields serve to trap electrons

emitted by the cathode in a Hall drift inside the thruster channel, thereby enhancing both ionization efficiency and maintenance of the electric field. Thrust is produced via the acceleration of ions by the electric field.

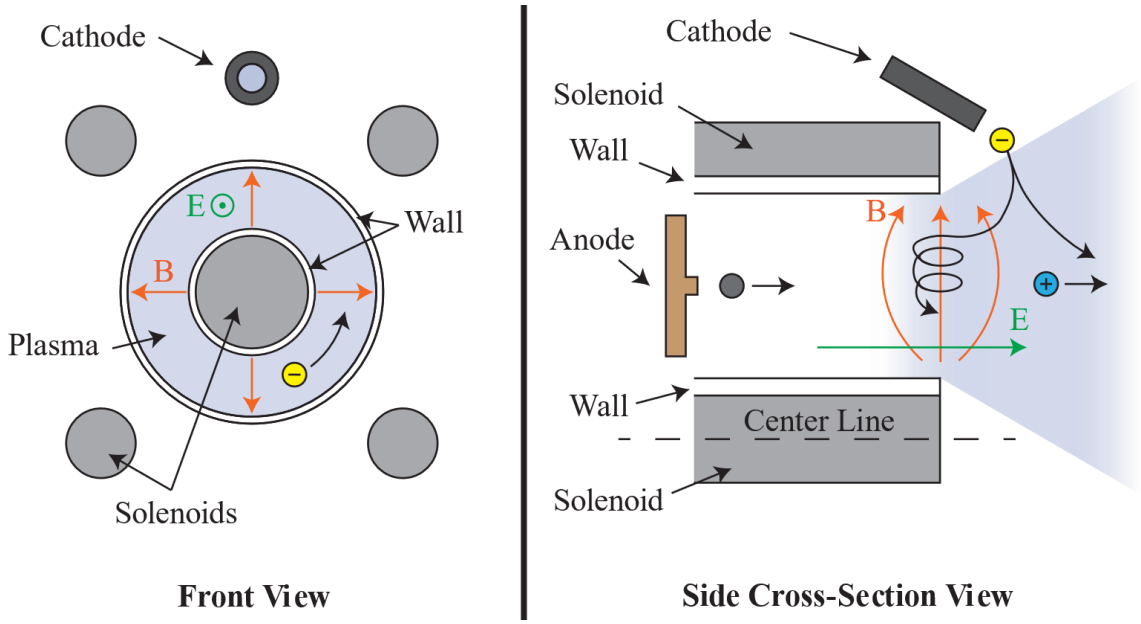

Figure 3 – Hall thruster schematic

1.2 Motivation

1.2.1 Outstanding EP Plasma Questions

The EP community endeavours to enhance EP capabilities by improving well-established EP devices (such as the Hall thruster) and developing promising technologies (such as the MPD and helicon thrusters) to sufficient technological maturity for widespread use on spacecraft. Progress in these areas, however, requires an improved understanding of the plasma physics that drive EP devices. Outstanding EP plasma questions must be

answered to maximize the performance of established devices and further develop promising technologies.

Two prominent examples of poorly understood phenomena in established devices are “anomalous” electron mobility inside the Hall thruster discharge channel [17, 18] and the formation of “anomalous” erosion ridges on Hall thruster walls [16]. Anomalous electron mobility is the enhanced transport of electrons across confining magnetic field lines. Electrons escape the magnetic field and are collected at the anode at a rate that is 10-1000 times greater than what is predicted by classical electromagnetism. Failure to confine the electrons represents a loss in electrical efficiency, as power is wasted on the emission of electrons that do not ionize neutral propellant. Proposed sources for anomalous electron mobility include small-scale plasma fluctuations, rotating plasma spokes, secondary electron emission (SEE), and even photoelectrons emitted from the discharge walls. However, no theory incorporating these possible sources has enabled self-consistent modelling of the electron transport [18].

Anomalous erosion ridges are mm-scale features that form during sputtering of the Hall thruster channel walls by the discharge plasma [16]. The resulting sawtooth pattern in the initially smooth walls is discernible within the first 100 hours of thruster operation and is clearly visible in thrusters that have been operated for thousands of hours. Classic plasma sputtering theory predicts the plasma should evenly erode the walls in a fashion that maintains their macroscopically smooth nature. Proposed mechanisms for ridge formation exist, but no work has successfully identified the cause; the failure of contemporary sputtering models to recover erosion ridges prevents the development of self-consistent

Hall thruster erosion models. Figure 4 shows erosion ridges on the inner and outer walls of the Aerojet Rocketdyne BPT-4000 and Snecma PPS®-1350 Hall thrusters.

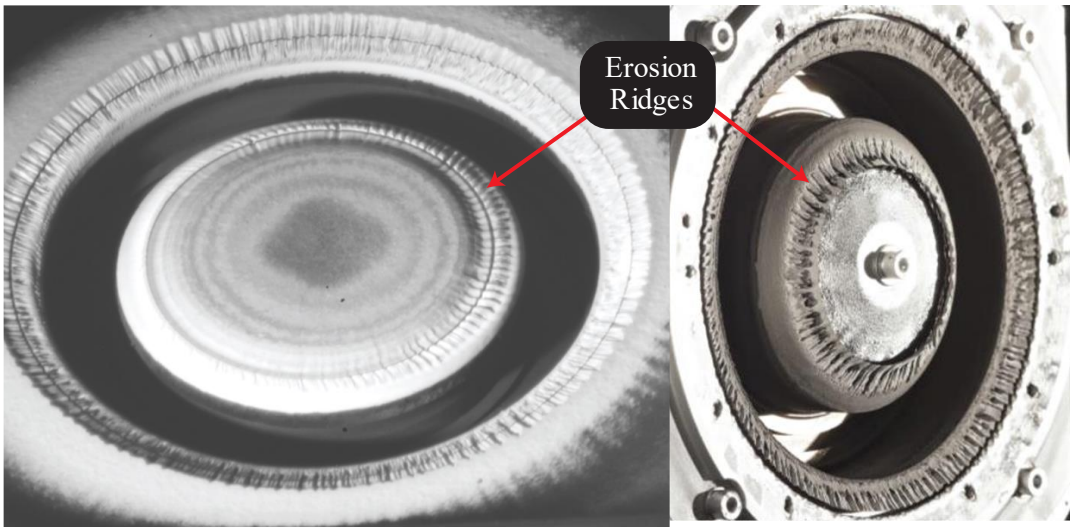

Figure 4 – Hall thruster erosion ridges (BPT-4000 and PPS®-1350 images reprinted from [19] and [20] with permission from Aerojet Rocketdyne and Snecma, respectively)

Examples of phenomena that must be better understood to enable further development of promising technologies include high-density plasma sputtering [21] and magnetic nozzle plasma detachment [22]. EP devices that use high-density plasmas (such as MPD thrusters, helicon thrusters, and the VASIMR rocket) can achieve larger thrust and specific impulse than established EP technologies. However, the higher plasma densities can enhance sputtering rates to presently intolerable levels. More work is required to understand the mechanisms of high-density plasma sputtering (including the possible role of electrons [23]) so that techniques and materials can be developed to limit sputtering.

Many promising technologies utilize magnetic nozzles to accelerate and exhaust plasma. However, magnetic nozzle operation requires the successful detachment of plasma from magnetic field lines. Though experimental and computational evidence has shown the feasibility of plasma detachment, more work is required to understand its mechanism so that nozzle design may be optimized [24, 25].

1.2.2 Contemporary EP Plasma Diagnostics

Answers to EP plasma questions require models that can self-consistently describe plasma phenomena. Model development, in turn, requires input plasma properties measured by plasma diagnostics. Limits to contemporary understanding of EP plasma physics are therefore strongly determined by contemporary plasma diagnostic capabilities.

Plasma diagnostics can be broadly categorized as electrostatic or optical. Common examples of electrostatic diagnostics are Langmuir, Faraday, emissive, E×B, and retarding potential analyzer (RPA) probes. Taken together, these tools can provide spatially resolved plasma density, electron and ion temperature, electron and ion energy distribution, plasma potential, and ion charge state. However, electrostatic probes are inherently invasive because their application requires the insertion of electrically biased components into the plasma. These probes can significantly alter the very plasma properties they attempt to measure and can be damaged by harsh plasma environments – especially inside or in the near-field plume of EP thrusters [26]. Furthermore, proper interpretation of probe data can be difficult and may depend on many assumptions; plasma density measurements gleaned from Langmuir probes in harsh EP environments, for example, have been reported with uncertainties as large as 50 – 200% [27, 28].

The EP community has attempted to overcome the limitations of physical probes by employing noninvasive optical diagnostics. This class of measurement techniques includes optical emission spectroscopy (OES), laser-induced fluorescence (LIF), laser Thomson scattering (LTS), and microwave interferometry [29, 30]. OES can measure plasma density and electron temperature, LIF directly measures the ion velocity distribution function, LTS can provide plasma density and electron temperature, and microwave interferometry yields electron density and collision frequency. Though not invasive, each optical diagnostic comes with its own set of limitations. Large uncertainties can exist in data interpretation of OES, LIF, and Thomson scattering measurements, and the single-frequency nature of microwave interferometry equipment limits the applicability of a given setup to a narrow band of electron densities [29, 31-34]. Additionally, because optical diagnostic techniques require optical access to plasma regions of interest, measurements are often limited to the exterior of EP devices. Measurements of the Hall thruster discharge channel plasma, in particular, have thus far not been achieved with optical diagnostics.

Limitations inherent in both electrostatic and optical EP plasma diagnostics prevent accurate measurement of plasma properties in the full range of EP plasma conditions and preclude noninvasive investigation of the plasma inside the Hall thruster channel. The EP community therefore requires an accurate and widely applicable diagnostic capable of probing the Hall thruster interior

1.2.3 Plasma Diagnostics with THz-TDS

A novel plasma diagnostic with the potential to meet the above requirements is THz-TDS [35]. THz-TDS uses broadband pulsed electromagnetic radiation in the THz regime ($0.1 – 10 \times 10^{12}$ Hz) to noninvasively measure line-integrated electron density and line-

averaged electron collision frequency. The broad frequency composition should enable measurements in a large range of plasma conditions and could provide a means for minimizing measurement error. Further, because previous work [36] has shown that BN exhibits transparency to THz radiation, THz-TDS may be a candidate to provide the first-ever noninvasive measurements of the Hall thruster discharge channel plasma.

However, compared to the well-established techniques discussed above, THz-TDS is in its infancy as a plasma diagnostic. The domain of applicability, for instance, has not been previously studied: In what EP plasma environments can THz-TDS make measurements? What factors determine measurement capability?

Furthermore, due to deficiencies in the standard THz-TDS plasma diagnostic data analysis method, authors almost exclusively report electron density and do so without including any uncertainties. THz-TDS requires a robust analysis framework that can consistently provide electron density, electron collision frequency, and associated uncertainties. Only with such a framework will it become possible to determine typical uncertainty values and study how plasma and THz pulse parameters impact measurement uncertainty.

Finally, though THz radiation has been shown to propagate through BN, more development and study are required before THz-TDS can become a candidate for performing Hall thruster discharge channel plasma measurements. Can THz radiation also propagate through the BN-SiO_2 composite typically used as Hall thruster wall material? What are the implications of the wall composition and thickness on the detected THz pulse signal? The standard THz-TDS plasma theory does not account for plasma boundaries.

How would a new theory account for these boundaries and the THz pulse reflections they induce?

These knowledge and capability gaps must be addressed before THz-TDS can fill the EP plasma diagnostic need. The motivation for this dissertation is, therefore, provided by the necessity to develop and evaluate THz-TDS for the purpose of expanding the EP plasma diagnostic suite to confront unanswered EP plasma physics questions.

1.3 Research Contributions and Dissertation Roadmap

1.3.1 Research Contributions

This dissertation seeks to close the aforementioned THz-TDS knowledge and capability gaps. To that end, the following research contributions are made:

1. Analysis of the THz-TDS domain of applicability
2. Development of a novel THz-TDS Bayesian analysis framework and evaluation of THz-TDS uncertainty
3. Development and application of THz-TDS to probe plasma bounded and optically shielded by Hall thruster wall material

1.3.1.1 Contribution 1: Analysis of the THz-TDS Domain of Applicability

Contribution 1 is an analysis of the equations that govern pulsed THz radiation propagation through plasma. The THz-TDS domain of applicability is examined in the context of both standard assumptions and overall measurement capability, with specific emphasis on EP plasma diagnostic capabilities. The plasma and THz-TDS properties that

govern each region of the domain are identified, and simplified relationships that describe domain boundaries are extracted from the complex, nonlinear governing equations.

1.3.1.2 Contribution 2: Development of a Novel THz-TDS Bayesian Analysis Framework and Evaluation of THz-TDS Uncertainty

Contribution 2 is the development of an improved analysis framework that can consistently compute the electron density, electron collision frequency, and associated parameter uncertainties. A subsequent study of the framework reveals how THz pulse properties impact uncertainty. The novel framework is Bayesian because the Bayesian approach enables incorporation of data measured across all resolvable THz frequencies and propagation of uncertainty from time-domain measurements through complex, nonlinear equations into the frequency domain.

1.3.1.3 Contribution 3: Development and Application of THz-TDS to Probe Plasma Bounded and Optically Shielded by Hall Thruster Wall Material

Contribution 3 is the first-ever noninvasive measurement of plasma bounded and optically shielded by Hall thruster wall material. The contribution includes development of the necessary THz-TDS plasma theory, measurement of the impact of Hall thruster wall material on THz pulse properties, and demonstration of the efficacy of THz-TDS to measure plasma bounded by Hall thruster wall material in a range of plasma conditions. Contribution 3 firmly establishes THz-TDS as a candidate to perform the first-ever noninvasive measurement of the Hall thruster discharge channel plasma.

1.3.2 Dissertation Roadmap

The remainder of this dissertation may be broadly split into two parts. Part 1 provides necessary background and describes the THz-TDS system designed and constructed for this dissertation; Part 2 presents contributions and conclusions. Part 1 consists of Chapters 2, 3, and 4. Chapter 2 overviews THz-TDS and provides detailed derivations of the governing equations. Chapter 3 describes the THz-TDS system and discusses the physics that enable THz pulse emission and detection. Chapter 4 details the standard plasma THz-TDS data analysis technique and provides measurements made by the THz-TDS system. Chapters 5, 6, 7, and 8 together encompass part 2. Research contributions 1, 2, and 3, are presented in Chapters 5, 6, and 7, respectively. Chapter 8 concludes the dissertation and discusses possibilities for future work.

CHAPTER 2. THZ-TDS BACKGROUND

This chapter provides an overview of THz-TDS and presents the equations necessary to connect plasma electron density and collision frequency to the measured electric fields of THz pulses. Section 2.1 introduces THz-TDS and Section 2.2 provides all applicable equations.

2.1 Introduction

2.1.1 THz Radiation

Electromagnetic radiation consists of synchronized waves of oscillating electric and magnetic fields. According to Maxwell's equations, these fields oscillate perpendicular to each other and to the direction of wave propagation at identical frequency. THz radiation is typically defined as the subset of electromagnetic radiation that oscillates with frequencies between 0.1 and 10 THz. This range corresponds to wavelengths between approximately 0.03 and 3 mm in vacuum, so the THz band is often termed the "sub-millimeter" range [37, 38].

The historical dearth of sources and detectors capable of producing and sensing THz radiation has led to the terming of this portion of the electromagnetic spectrum as the "THz gap." However, recent technological advances have begun to fill that gap [37]. Broadband THz pulses can be generated when an ultrashort (< 100 femtosecond (fs)) laser pulse strikes a nonlinear crystal, photoconductive antenna, or electron bunch to produce picosecond (ps)-scale electric field oscillations. Continuous wave (CW) THz radiation is produced by free-electron lasers, backward wave oscillators, and photomixing of two CW optical beams. Coherent detection can be achieved by electro-optic sampling, photoconductive

switching, photomixing, and heterodyne detection. Incoherent detection is made possible by bolometers, Golay cells, and pyroelectric devices.

2.1.2 THz-TDS

THz-TDS is a spectroscopic technique that relies on the emission and time-domain detection of broadband pulsed THz radiation. The technique was developed in the late 1980's and early 1990's upon the achievement of pulsed THz radiation generation and detection with photoconductive antennas (PCA) by Auston et al. [39]. Shortly thereafter, THz-TDS spread to the domains of materials science and chemistry for the purpose of measuring material optical properties [38, 40].

Pulsed THz radiation is generated by an electric field that varies on a picosecond scale [37, 38, 40-42]. In a typical THz-TDS setup, this is achieved by optically pumping either a PCA or nonlinear crystal with an ultrashort laser pulse. In the case of PCA emision, incident photons with sufficient energy briefly excite electrons into the conduction band of a semiconductor and these electrons respond to an externally imposed voltage bias to produce a transient current that radiates as a THz pulse. A nonlinear crystal, on the other hand, generates THz radiation by optical rectification; due to the noncentrosymmetric structure of the crystal, incident ultrashort laser pulses briefly modify the medium polarization and thereby cause the crystal to emit THz radiation. THz pulses typically feature an average power below 10 μW, but specialized antennas can generate powers on the order of 100 μW. An example THz pulse generated with a BATOP PCA-60-05-10-800-h antenna is shown in Figure 5.

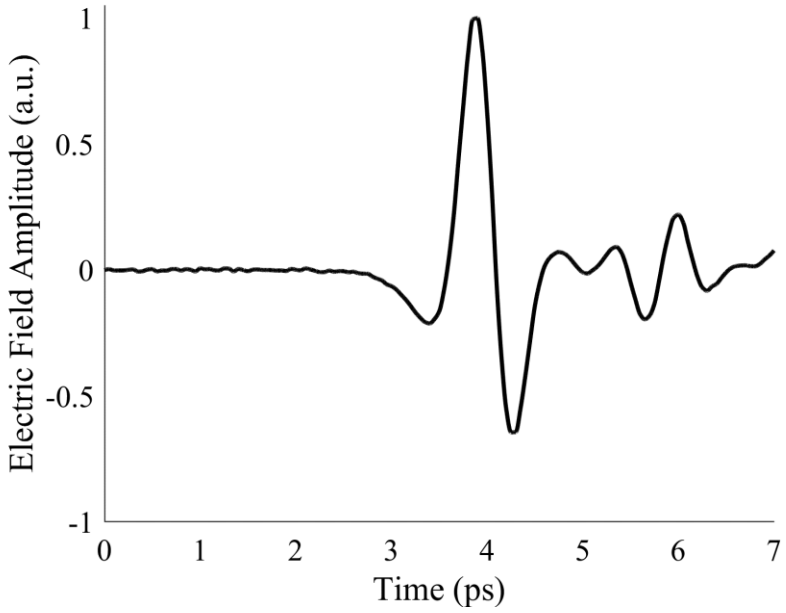

Figure 5 – THz pulse produced by a BATOP PCA-60-05-10-800-h

Detection of THz pulses requires measurement of the picosecond-scale electric field variations with a typical resolution of 10 – 100 fs [37, 38, 40, 41]. Again, this is usually achieved either with a PCA or nonlinear crystal. In PCA detection, a voltage bias is induced across the PCA by the electric field of the incident THz pulse. An ultrashort laser pulse arriving at the same instance as the THz radiation excites electrons into the semiconductor's conduction band, and the electrons respond to the voltage bias induced by the THz pulse. The resulting measured current is proportional to the electric field strength of the THz pulse averaged over the duration of the ultrashort laser pulse.

Detection with a nonlinear crystal is electro-optical and relies on the Pockels effect; the electric field of the incident THz pulse induces a birefringence in the crystal that changes the polarization of a copropagating ultrashort laser pulse [37, 38, 42]. Measurement of the induced change in polarization provides a relative measurement of the

THz pulse electric field strength. Whether a PCA or nonlinear crystal is used for detection, scanning of the entire THz pulse is typically achieved by incrementally delaying the arrival of the ultrashort laser pulse to either the detector or emitter with an optical delay line.

2.1.3 Plasma Diagnostics with THz-TDS

Jamison et al. [43] recognized the potential of THz-TDS to measure plasma electron density and collision frequency. In 2003, they reported line-averaged plasma densities in the range of 10^{17} to 10^{19} m^{-3} and electron collision frequencies on the order of 0.1 THz in a DC pulsed plasma discharge. Under the assumption that the pulsed plasma was repeatable, their work resolved plasma property evolution at a timescale of just 30 ps by employing electronic gating techniques. However, their work also noted that the values of the measured electron collision frequencies were “anomalously” large.

Later work by Kolner et al. [44], Ando et al. [45], and others [46-53] experimentally and theoretically demonstrated the efficacy of THz-TDS on a range of laboratory plasma discharges. Kolner et al. [44] notably utilized fluorescence imaging to determine plasma properties along the THz pulse path, and Ando et al. [45] demonstrated general agreement between electron density measurements taken with THz-TDS and Langmuir probes. Though Kolner et al. [44] presented electron collision frequency results without qualification, all other authors [45-50, 52, 53] only presented electron density – even though published images of THz pulses indicate non-negligible electron collision frequency. The probable reason for the reluctance to report electron collision frequency results is discussed in Section 4.1.3.

2.2 Governing Equations

Plasma parameter determination with THz-TDS requires measurement of how THz pulses are modified by propagation through plasma. Section 2.2.1 derives the standard THz-TDS relations, Section 2.2.2 shows how the standard THz-TDS relations can be applied to determine the properties of a Lorentz plasma, and Section 2.2.3 discusses the impact of relaxing the Lorentz plasma assumptions. All plasma THz-TDS references cited in Section 2.1.3 use some form of the equations presented in Sections 2.2.1 and 2.2.2 but do not include complete (or sometimes even correct) derivations or account for all assumptions. Full derivations of these relations are therefore provided here.

It is important to note that all frequencies discussed here (radiation, plasma, and collision) are *angular* frequencies. Though often expressed or plotted as frequencies in units of Hz or THz, these quantities must be inputted as angular frequencies (standard units of rad/s) in the equations derived below.

2.2.1 THz-TDS Relations

In the classical description of the interaction of electromagnetic radiation with a medium, the electric field of the incident light wave induces charged particle oscillations in the medium, which, in turn, generate an electric field that interferes with and alters the incident light wave. The effect of the magnetic field is discarded because, unless charged particles in the medium move at relativistic speeds, its impact is negligible. For monochromatic light, the effect of passage through a medium is to produce a resultant electric field of the same frequency but altered wavelength and amplitude [54]. Figure 6 illustrates this effect.

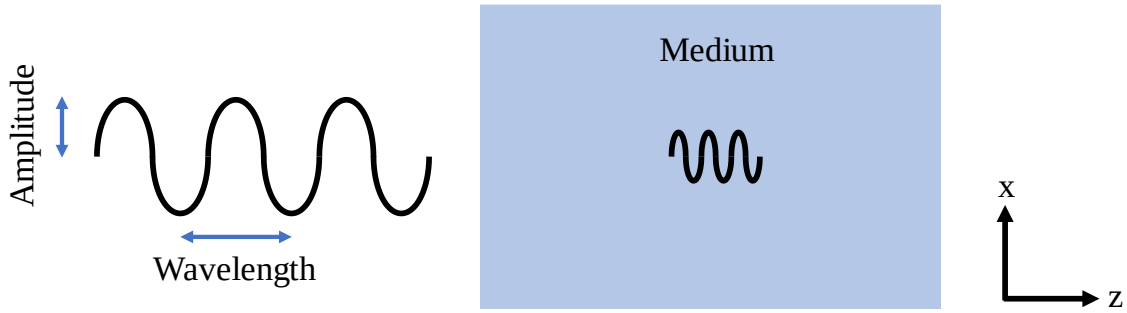

Figure 6 – Illustration of interaction between an electric field and a medium

Assuming inelastic interactions are negligible, changes to the wavelength and amplitude are quantified in terms of the medium refractive index (n) and absorption coefficient (α), respectively, after propagation through a distance (L) of a homogeneous medium by

$$\lambda_f = \frac{\lambda_0}{n}$$

and (3)

$$\Lambda_f = \Lambda_0 \exp\left(\frac{-\alpha}{2} L\right),$$

where λ_f and Λ_f are the resulting wavelength and amplitude, respectively, and λ_0 and Λ_0 are the incident wavelength and amplitude, respectively. If scattering is not negligible, it is more appropriate to label α as an "extinction" coefficient rather than as an absorption coefficient. It is convenient to combine n and α into a complex refractive index ($\tilde{n}$) given by

$$\tilde{n} = n + \frac{c}{\omega}\frac{i}{2}\alpha, \tag{4}$$

where c is the speed of light in vacuum and ω is the angular frequency of the light wave.

The electric field of the broadband THz pulse is modeled as the superposition of one-dimensional plane waves of various frequencies transmitting through linear dielectric media along the z-axis. Represented in the time (t) domain at a position (z) as $E(z,t)$, the electric field is cast to the angular frequency (ω) domain as $\hat{E}(z,\omega)$ through the Fourier transform by

$$\hat{E}(z,\omega) = \int_{-\infty}^{\infty} E(z,t)\exp[-i\omega t]\,\mathrm{d}t \tag{5}$$

under the assumption that each plane wave oscillates in time as $\exp[-i\omega t]$ and that spatial dispersion is negligible. Assuming forward-propagating waves, if the pulse enters a homogeneous medium at $z = 0$ and propagates a distance L, the resulting and original electric fields in the angular frequency domain are related by

$$\hat{E}(L,\omega) = \hat{E}(0,\omega)\exp\left[i\frac{\omega}{c}\tilde{n}(\omega)\,L\right]. \tag{6}$$

Relaxing the requirement for homogeneity across the length of the sample and instead assuming that the refractive index does not vary significantly on the scale of the radiation

wavelength in this dimension, the Wentzel-Kramers-Brillouin (WKB) approximation may be invoked to yield

$$\hat{E}(L,\omega) = \hat{E}(0,\omega)\exp\left[i\frac{\omega}{c}\int_0^L \tilde{n}(\omega,z)\mathrm{d}z\right]. \quad (7)$$

In THz-TDS, the electric field of the THz radiation is measured in the time domain with and without the sample in place to establish sample and reference electric fields, respectively [37, 38, 55, 56]. Assuming the sample is bounded by vacuum during measurement of the sample electric field and the sample is replaced by vacuum for measurement of the reference electric field, the sample and reference pulses propagate through the paths shown in Figure 7.

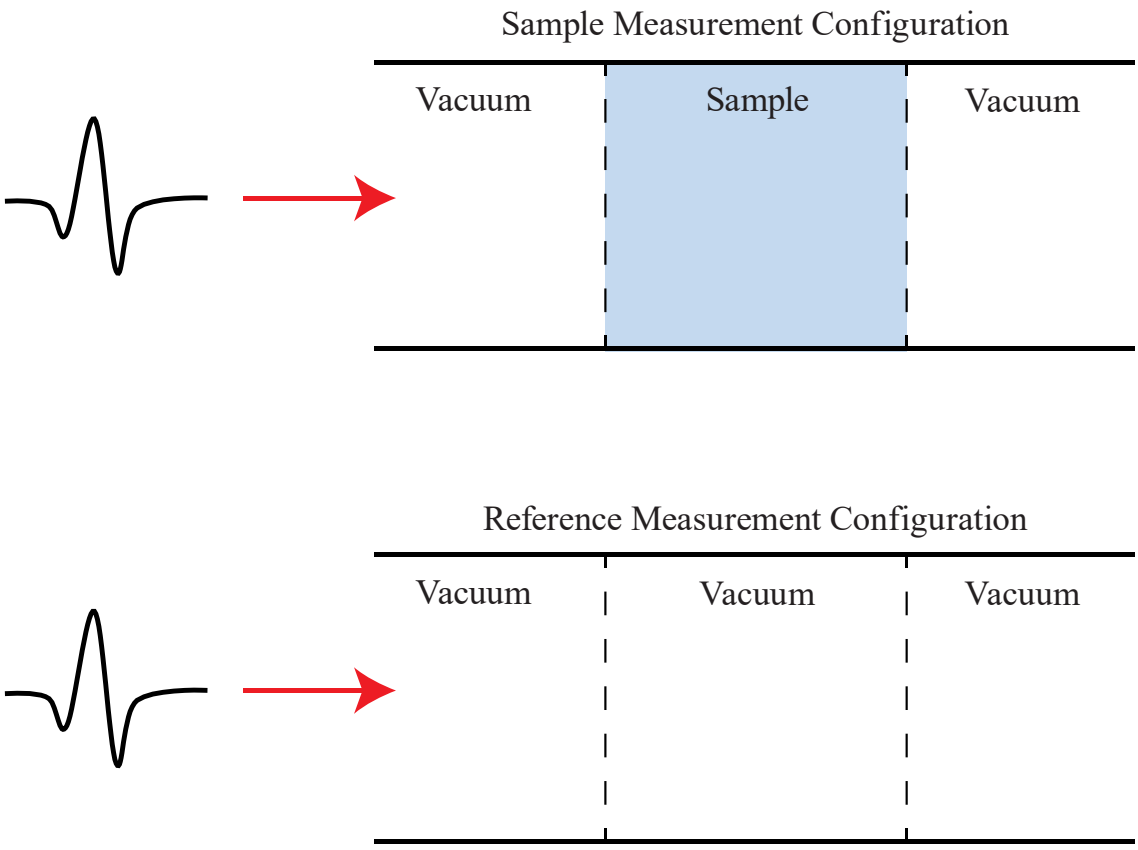

Figure 7 – Schematic of reference and sample THz-TDS measurements

Further assuming the sample does not refract the THz pulse away from the detector, the measured reference (E_{ref}) and sample (E_{sam}) electric field spectra are expressed as

$$\hat{E}_{ref}(\omega) = \hat{E}_{gen}(\omega)G(\omega)\exp\left[i\frac{\omega}{c}L\right]$$

and

(8)

$$\hat{E}_{sam}(\omega) = \hat{E}_{gen}(\omega)G(\omega)D_{vs}(\omega)D_{sv}(\omega)FP(\omega)\exp\left[i\frac{\omega}{c}\int_0^L \tilde{n}(\omega,z)\mathrm{d}z\right],$$

where E_{gen} is the THz pulse electric field spectrum generated by the THz-TDS system, G accounts for propagation and transmission terms shared by both fields, D_{vs} is the transmission coefficient for propagation from vacuum to the sample, D_{sv} is the transmission coefficient for propagation from the sample to vacuum, and FP encompasses the impact of Fabry-Pérot (FP) reflections in the sample.

Taking the ratio of the two complex spectra in Eq. (8) yields

$$\frac{\hat{E}_{sam}(\omega)}{\hat{E}_{ref}(\omega)} = D_{vs}(\omega)D_{sv}(\omega)FP(\omega)\exp\left[i\frac{\omega}{c}\int_0^L\{\tilde{n}(\omega,z)-1\}\mathrm{d}z\right] \tag{9}$$

and eliminates measurement dependence on E_{gen} and G. The spectral ratio is also referred to as the transfer function and can be written in terms of the frequency-dependent magnitude (A) and phase (Φ):

$$\frac{\hat{E}_{sam}(\omega)}{\hat{E}_{ref}(\omega)} = A(\omega)\exp[i\Phi(\omega)]. \tag{10}$$

If the sample under investigation is a plasma without sharp boundaries, boundary reflections can be ignored and the transmission coefficients may be set to unity. Furthermore, if the time required for a FP-reflected pulse to exit the sample is larger than the measured duration of the THz pulse, FP reflections may also be ignored and the FP term may also be set to unity. If these simplifying assumptions apply, Eq. (9) becomes

$$\frac{\hat{E}_{sam}(\omega)}{\hat{E}_{ref}(\omega)} = \exp\left[i\frac{\omega}{c}\int_0^L \{\tilde{n}(\omega,z)-1\}\mathrm{d}z\right] \tag{11}$$

and the magnitude and phase become

$$A(\omega) = \exp\left[-\frac{\omega}{c}\int_0^L \mathrm{Im}\{\tilde{n}(\omega,z)\}\mathrm{d}z\right]$$

and (12)

$$\Phi(\omega) = \frac{\omega}{c}\int_0^L [\mathrm{Re}\{\tilde{n}(\omega,z)\}-1]\mathrm{d}z,$$

where Re{ } and Im{ } denote real and imaginary components, respectively.

2.2.2 Interaction of THz Radiation with Lorentz Plasma

This section details the derivation of the complex refractive index in terms of the electron density and collision frequency of a Lorentz plasma [34, 35]. Inputting the complex refractive index into Eq. (12) relates these plasma parameters to the phase and amplitude of the THz-TDS transfer function. Further simplification enables determination of the electron density from phase information alone.

2.2.2.1 Complex Refractive Index

The complex refractive index is derived for a uniform region of Lorentz plasma. The plasma is unmagnetized and electrons are assumed to move through a stationary "fluid" of ions and neutrals and to interact with each other exclusively through collective space charge. It is further assumed that the interaction between electrons and the background fluid may be approximated as viscous damping, properties dependent upon electron temperature can be neglected, and the motion of a single electron is representative of the behavior of all electrons in the plasma. Under these assumptions, the spatial displacement of an electron (ξ), under forcing from an electric field (E) that is uniform across the scale of the electron displacement can be modeled as a damped harmonic oscillator by

$$m_e \frac{\partial^2 \xi(t)}{\partial t^2} + \nu m_e \frac{\partial \xi(t)}{\partial t} = -eE(t), \tag{13}$$

where electron mass and charge are m_e and e, respectively, and ν is the damping coefficient, which can be interpreted physically as the average plasma momentum transfer collision rate. Assuming all quantities oscillate in time as $\exp(-i\omega t)$, the Fourier transform allows for the steady-state solution to be determined in the spectral domain by letting $\partial/\partial t \rightarrow -i\omega$:

$$m_e(-i\omega)^2 \xi(\omega) + \nu m_e(-i\omega)\xi(\omega) = -eE(\omega). \tag{14}$$

Re-arranging produces

$$\xi(\omega) = \frac{eE(\omega)}{m_e\omega(\omega + i\nu)}. \tag{15}$$

The resulting complex current density ($\tilde{J}_p$) can be determined through multiplication of the charge density ($-n_e e$) and the electron velocity in the spectral domain ($-i\omega\xi$) and is given by

$$\tilde{J}_p(\omega) = -n_e e(-i\omega)\xi(\omega) = \frac{in_e e^2}{m_e(\omega + i\nu)}E(\omega), \tag{16}$$

where n_e is the electron number density. The complex dielectric constant ($\tilde{\varepsilon}_p$) is therefore given by

$$\tilde{\varepsilon}_p(\omega) = 1 + i\frac{\tilde{\sigma}_p(\omega)}{\omega\epsilon_0} = 1 + i\frac{\tilde{J}_p(\omega)}{\omega\epsilon_0 E(\omega)} = 1 - \frac{n_e e^2}{\omega\epsilon_0 m_e(\omega + i\nu)}, \tag{17}$$

where $\tilde{\sigma}_p$ is the complex conductivity and ϵ_0 is the permittivity of free space. The plasma frequency (ω_p) is

$$\omega_p^2 = \frac{n_e e^2}{\epsilon_0 m_e}, \tag{18}$$

so, in terms of the plasma frequency, Eq. (17) is

$$\tilde{\varepsilon}_p(\omega) = 1 - \frac{\omega_p^2}{\omega(\omega + i\nu)}. \tag{19}$$

The complex dielectric constant is related to the complex index of refraction by

$$\tilde{\varepsilon}(\omega) = \tilde{n}^2(\omega), \tag{20}$$

so the complex plasma refractive index is

$$\tilde{n}_p^2(\omega) = 1 - \frac{\omega_p^2}{\omega(\omega + i\nu)}. \tag{21}$$

2.2.2.2 Phase and Magnitude of the THz-TDS Transfer Function

Splitting the real and imaginary parts of the complex dielectric constant yields

$$\tilde{\varepsilon}_p(\omega) = 1 - \frac{\omega_p^2}{\omega^2 + \nu^2} + i\left(\frac{\omega_p^2 \nu}{\omega[\omega^2 + \nu^2]}\right). \tag{22}$$

Letting ε_R and ε_I be the real and imaginary parts of $\tilde{\varepsilon}_p$, respectively, and n_R and n_I be the real and imaginary parts of $\tilde{n}_p$, respectively, Eq. (20) becomes

$$(n_R + in_I)^2 = \varepsilon_R + i\varepsilon_I. \tag{23}$$

Equating the real and imaginary parts of Eq. (23) yields

$$n_R^2 - n_I^2 = \varepsilon_R$$

and (24)

$$2n_R n_I = \varepsilon_I.$$

The real and imaginary parts of the complex refractive index can therefore be expressed in terms of the real and imaginary parts of the complex dielectric constant by

$$n_R = \sqrt{\frac{\varepsilon_R + \sqrt{\varepsilon_R^2 + \varepsilon_I^2}}{2}}$$

and (25)

$$n_I = \sqrt{\frac{-\varepsilon_R + \sqrt{\varepsilon_R^2 + \varepsilon_I^2}}{2}}.$$

Substituting Eq. (22) into Eq. (25) yields

$$\tilde{n}_p(\omega) = \sqrt{\frac{1}{2}\left(1 - \frac{\omega_p^2}{\omega^2 + \nu^2}\right) + \frac{1}{2}\sqrt{\left(1 - \frac{\omega_p^2}{\omega^2 + \nu^2}\right)^2 + \left(\frac{\omega_p^2 \nu}{\omega[\omega^2 + \nu^2]}\right)^2}} + i\sqrt{-\frac{1}{2}\left(1 - \frac{\omega_p^2}{\omega^2 + \nu^2}\right) + \frac{1}{2}\sqrt{\left(1 - \frac{\omega_p^2}{\omega^2 + \nu^2}\right)^2 + \left(\frac{\omega_p^2 \nu}{\omega[\omega^2 + \nu^2]}\right)^2}}. \quad (26)$$

If the plasma under investigation is homogeneous across the beam waist of the THz radiation and does not vary significantly at the scale of the THz wavelength along the radiation propagation direction (WKB approximation), the complex refractive index may be considered a function of position and integrated across the length of the plasma. The relation for $\tilde{n}_p$ given by Eq. (26) may be substituted into Eq. (12) for $\tilde{n}$ to yield

$$A(\omega) = \exp\left[-\frac{\omega}{c}\int_0^L \sqrt{-\frac{1}{2}\left(1-\frac{\omega_p^2(z)}{\omega^2+\nu^2(z)}\right)+\frac{1}{2}\sqrt{\left(1-\frac{\omega_p^2(z)}{\omega^2+\nu^2(z)}\right)^2+\left(\frac{\omega_p^2(z)\nu(z)}{\omega[\omega^2+\nu^2(z)]}\right)^2}}\,dz\right]$$

and

$$\Phi(\omega) = \frac{\omega}{c}\int_0^L \left[\sqrt{\frac{1}{2}\left(1-\frac{\omega_p^2(z)}{\omega^2+\nu^2(z)}\right)+\frac{1}{2}\sqrt{\left(1-\frac{\omega_p^2(z)}{\omega^2+\nu^2(z)}\right)^2+\left(\frac{\omega_p^2(z)\nu(z)}{\omega[\omega^2+\nu^2(z)]}\right)^2}}-1\right]\mathrm{dz}, \tag{27}$$

Further assuming the plasma is approximately uniform along the direction of THz radiation propagation yields

$$A(\omega) = \exp\left[-\frac{\omega L}{c}\sqrt{-\frac{1}{2}\left(1-\frac{\omega_p^2}{\omega^2+\nu^2}\right)+\frac{1}{2}\sqrt{\left(1-\frac{\omega_p^2}{\omega^2+\nu^2}\right)^2+\left(\frac{\omega_p^2\nu}{\omega[\omega^2+\nu^2]}\right)^2}}\right]$$

and

$$\Phi(\omega) = \frac{\omega L}{c}\left[\sqrt{\frac{1}{2}\left(1-\frac{\omega_p^2}{\omega^2+\nu^2}\right)+\frac{1}{2}\sqrt{\left(1-\frac{\omega_p^2}{\omega^2+\nu^2}\right)^2+\left(\frac{\omega_p^2\nu}{\omega[\omega^2+\nu^2]}\right)^2}}-1\right]. \tag{28}$$

Eqs. (27) and (28) directly relate plasma properties to measured THz spectra.

2.2.2.3 Common Simplifications

Simplifying assumptions can be made to enable determination of the electron density from phase information alone and thereby avoid the need to invert Eq. (27) or Eq. (28) [34, 45]. Under the assumptions that $\nu \ll \omega_p$ and $\omega_p < \omega$, in which case the plasma acts as a low-loss dielectric with little absorption, the expression for the phase in Eq. (27) can be expanded to first order with the binomial theorem and assessed in the limit of $\nu^2 \ll \omega^2 - \omega_p^2$ and $\nu^2 \ll \omega^2\left(\omega^2 - \omega_p^2\right)^2/\omega_p^4$ to yield

$$\Phi(\omega) = \frac{\omega}{c}\int_0^L \left[\sqrt{1 - \frac{\omega_p^2(z)}{\omega^2}} - 1\right] dz. \tag{29}$$

Equation (29) can be further expanded to first order with the binomial theorem in the limit of $\omega_p^2 \ll \omega^2$ to yield

$$\Phi(\omega) = -\frac{1}{2\omega c}\int_0^L \omega_p^2\,(z)dz. \tag{30}$$

Further assumption that the plasma is uniform enables simple computation of the electron density with

$$n_e = -\Phi(\omega)\frac{2\epsilon_0 m_e c\omega}{e^2 L}. \tag{31}$$

The sign preceding Φ depends upon the chosen signs of the exponents in Eqs. (6) and (10) and is positive elsewhere in the literature.

2.2.3 Interaction of THz Radiation with Magnetized Thermal Plasma

Section 2.2.2 details the derivation of the equations required to relate the phase and magnitude of the measured transfer function to the electron density and collision frequency of a Lorentz plasma. Relaxation of the Lorentz plasma assumptions entails the inclusion of magnetic fields and thermal effects. A general treatment requires a kinetic (rather than fluid) description of the plasma and produces a three-dimensional spatially dispersive system of equations with many solution regimes [57].

However, under the assumption that the electron temperature is below 100 keV, two particular cases with relevancy to EP plasma diagnostics simplify to produce one-dimensional complex refractive indices [34, 58]. Case 1 is THz pulse propagation parallel to an applied magnetic field and Case 2 is pulse propagation perpendicular to an applied magnetic field such that pulse polarization is parallel to the magnetic field. The complex refractive index for Case 1 ($\tilde{n}_{p_{l,r}}$) is given by

$$\tilde{n}_{p_{l,r}}^2(\omega) = \left\{1 - \frac{\omega_p^2}{\omega[(\omega + i\nu) \pm \omega_b]}\right\} \Big/ \left\{1 + \frac{\omega\omega_p^2}{[(\omega + i\nu) \pm \omega_b]^3} \frac{k_B T_e}{m_e c^2}\right\} \tag{32}$$

and the complex refractive index for Case 2 ($\tilde{n}_{p_\perp}$) is given by

$$\tilde{n}_{p_\perp}^2(\omega) = \left\{1 - \frac{\omega_p^2}{\omega(\omega + i\nu)}\right\} \Big/ \left\{1 + \frac{\omega\omega_p^2}{(\omega + i\nu)[(\omega + i\nu)^2 - \omega_b]} \frac{k_B T_e}{m_e c^2}\right\}, \tag{33}$$

where the electron temperature is T_e, Boltzmann's constant is k_B, and ω_b is the electron cyclotron frequency given as a function of the magnetic field strength (B) by

$$\omega_b = \frac{|e|B}{m_e} \ . \tag{34}$$

Throughout this dissertation, as is typical in the plasma literature, the electron temperature is combined with Boltzmann's constant so that the quantity $k_B T_e$ is collectively reported as the electron temperature in standard units of electronvolts (eV). The l and r subscripts in Eq. (32) refer to the left- and right-handed circular polarization components of the THz pulse and correspond to the $+$ and $-$ signs in the $\pm$, respectively. In this work, right-handed circular polarization refers to an electric field in which the y-component lags the x-component by a phase of $\pi/2$ in a standard Cartesian coordinate system.

Contrary to the refractive index given by Eq. (21), the refractive indices given by Eqs. (32) and (33) do not yield simple analytical expressions for the transfer function phase and magnitude. Application of Eqs. (32) and (33) therefore require numerical computation of the phase and magnitude with Eq. (12).

CHAPTER 3. THZ-TDS SYSTEM

A THz-TDS system and tabletop plasma were designed and constructed around a previously purchased ultrafast laser. Section 3.1 provides an overview of the system, Section 3.2 details the system's THz radiation generation and detection, Section 3.3 discusses system measurement verification, and Section 3.4 describes the tabletop plasma discharge.

3.1 System Overview

The THz-TDS system is diagrammed in Figure 8. The system generates and detects THz radiation in a pump-probe configuration: one laser beam pumps a PCA to produce THz pulses while the other probes a zinc telluride (ZnTe) crystal to electro-optically detect THz pulses.

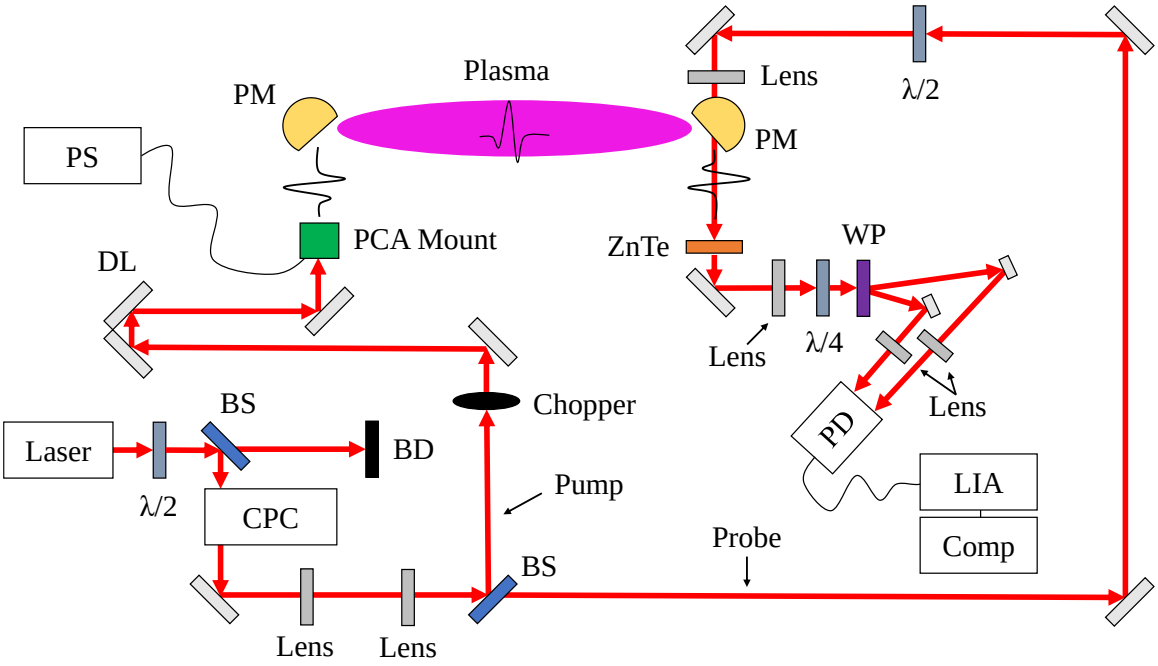

Figure 8 – Tabletop THz-TDS system diagram (BD: *beam dump*, BS: *beam splitter*, Comp: *computer*, CPC: *pulse compressor*, DL: *delay line*, LIA: *lock-in amplifier*, PCA: *photoconductive antenna*, PD: *photodetector*, PM: *parabolic mirror*, PS: *power supply*, WP: *Wollaston prism*, ZnTe: *zinc telluride crystal*, λ/2: *half-wave plate*, λ/4: *quarter-wave plate*)

The laser beam is generated by a mode-locked Ti:Sapphire laser (Coherent Vitara-T HP) that provides ultrashort pulses with 800 nm center wavelength at a repetition rate of 100 MHz and average power of 1.2 W. The beam then travels through a half-wave plate and polarization-dependent beam splitter to give adjustable control of power inputted into the setup. Next, the beam is guided through a pulse compressor (Coherent CPC-II) and then recollimated with a pair of lenses before it is split into pump and probe paths by a fixed-ratio beam splitter.

The pump beam passes through an optical chopper (Scitec Instruments 300 CD) and then reflects from a hollow corner cube retroreflector mounted on a delay line (Newport DL325) before reaching the PCA mount. THz radiation emitted from the PCA (BATOP

PCA-60-05-10-800-h) is collimated to a beam diameter of approximately 40 mm and steered into the plasma by a gold parabolic mirror. After passage through the plasma, the THz radiation is focused onto the ZnTe crystal (Eskma Optics ZnTe-1000H) by a second parabolic mirror.

The probe beam is routed through a second half-wave plate to control polarization orientation and then focused through a hole in the second parabolic mirror and onto the ZnTe crystal so that it propagates simultaneously and collinearly with the THz radiation at identical polarization. After passage through the crystal, the probe beam is recollimated and guided through a quarter-wave plate and Wollaston prism. The two beams exiting the Wollaston prism are focused onto the two photodiodes of a balanced photodetector (Thorlabs PDB415A-AC). The output of the photodetector is read by a dual-phase lock-in amplifier (Zurich Instruments MFLI) connected to a desktop computer running a custom LabVIEW virtual instrument. The optical table is electrically grounded and is actively vibration-isolated by isolators (Newport S-2000A) floating on nitrogen gas. All instruments are housed in the environmentally controlled enclosure shown in Figure 9.

Figure 9 – Tabletop THz-TDS system enclosure

3.1.1 Ultrashort Laser Pulse Considerations

The laser produces ultrashort pulses with a measured temporal full width at half maximum (FWHM) of approximately 30 fs at the laser output. The uncertainty principle dictates that such pulses are necessarily spectrally broad and not monochromatic. In this setup, for instance, the measured spectral FWHM is 60 nm. For such pulses, group velocity dispersion (GVD) can have a major impact on temporal pulse width and must be accounted for in the optics setup. GVD occurs because the refractive index of each optical component (and even air) varies as a function of frequency. As a laser pulse travels through a setup,

each of its spectral components experiences a different refractive index and therefore travels at a different wave speed. GVD, therefore, spectrally separates the pulse in time and thus increases the overall temporal pulse width [59].

GVD is mitigated in this setup by the use of commercially available specially coated low-GVD mirrors, lenses, beam splitters, and wave plates designed for ultrashort pulses centered at 800 nm. GVD pre-compensation is provided by the pulse compressor. Before the beam is split into pump and probe paths, it undergoes multiple reflections from negative GVD-coated mirrors and makes four passes through prism elements inside the pulse compressor. These events serve to lengthen each laser pulse in the opposite manner as the rest of the optical setup: the pulse compressor accelerates the shorter wavelength components ahead of the longer wavelength components to compensate for the tendency of the other optics to accelerate longer wavelength components ahead of shorter wavelength components. As illustrated in Figure 10, the pulse compressor therefore lengthens the pulse duration so that the other optical components provide recompression.

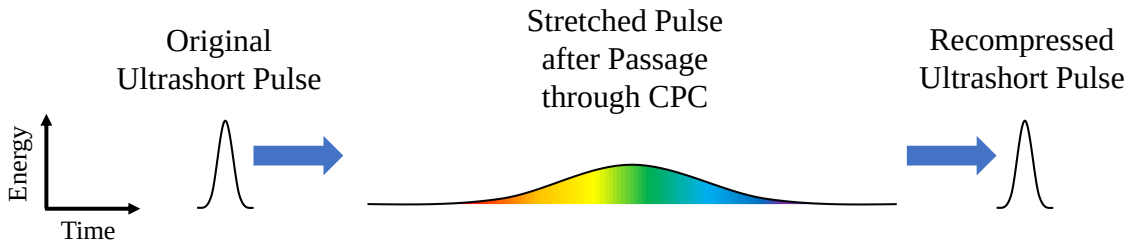

Figure 10 – Illustrated pulse compensation process (CPC*: pulse compressor*)

The GVD compensation schemes ensure the measured FWHM temporal pulse width remains less than 50 fs at both the PCA and ZnTe crystal. Temporal pulse width measurements were made with an autocorrelator (APE pulseCheck) loaned by Coherent.

3.2 THz Radiation Generation and Detection

3.2.1 Generation

The PCA used in this work is a low temperature-grown gallium arsenide (LT-GaAs) parallel-line antenna. The photoconductive substrate consists of a thin (~1 micron) LT-GaAs buffer layer grown atop a much thicker (~500 micron) semi-insulating gallium arsenide (SI-GaAs) region. Gold electrodes patterned onto the LT-GaAs form a 5-micron dipole gap, across which a DC bias of 15 V is applied. The pump beam is limited to an average power of 5 mW to avoid damaging the PCA and is focused onto the dipole gap with an aspheric lens positioned with micron precision by a custom mount assembled with commercially available optomechanical components. Figure 11 shows a front view schematic of the PCA.

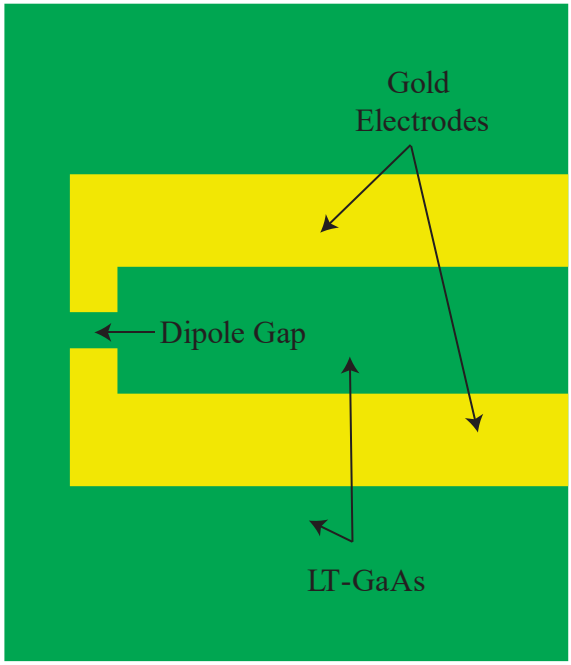

Figure 11 – BATOP PCA-60-05-10-800-h front view schematic (LT-GaAs*: low temperature-grown gallium arsenide*)

Each ultrashort laser pulse in the pump beam acts as a fast switch for the PCA's electrical circuit [37-39, 60]. Photons impinging on the surface of the antenna are absorbed by the LT-GaAs substrate and excite electrons from the semiconductor's valence band into its conduction band. These newly freed photoelectrons accelerate across the dipole gap in response to the applied voltage bias and thereby produce a transient current that, in turn, alters the local electric field and generates pulsed THz radiation. The process depends upon the temporally short nature of both the 50 fs incident laser pulses and the 0.2 – 0.3 ps average semiconductor photoelectron lifetime. Due to the highly divergent nature of the emitted THz radiation and severe refractive index mismatch at the GaAs-air interface, the radiation is coupled to air with a precisely positioned hyper-hemispherical high-resistivity

float-zone silicon lens fixed to the SI-GaAs [61]. Figure 12 illustrates the THz generation process from a side view of the PCA.

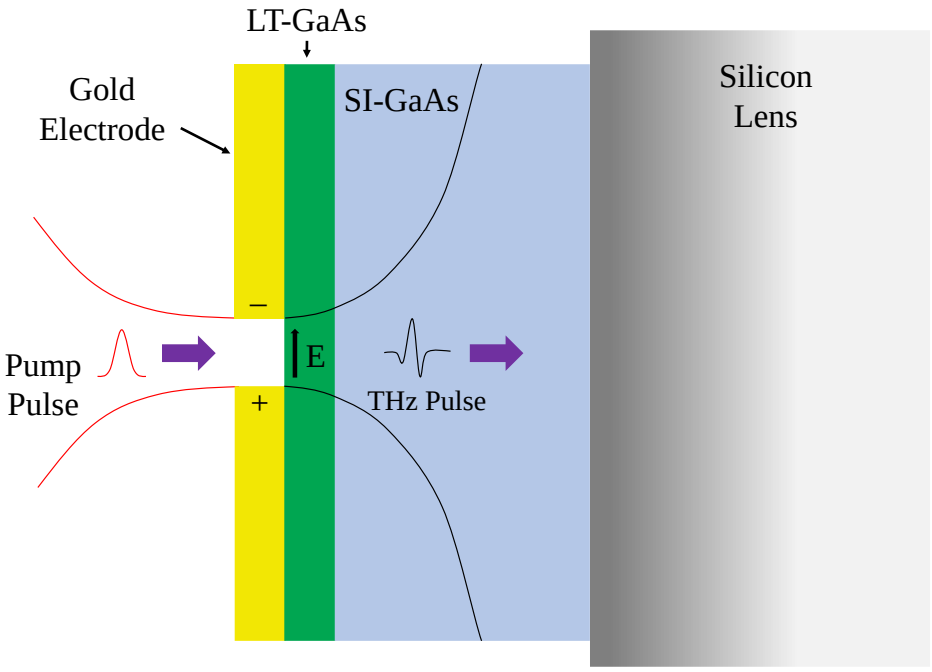

Figure 12 – Illustrated THz generation process (LT-GaAs: *low temperature-grown gallium arsenide*, SI-GaAs: *semi-insulating gallium arsenide*)

3.2.2 Detection

After passage through the plasma, the THz radiation is focused onto a 1 mm-thick <110> ZnTe crystal oriented such that propagation is along the [110] axis and polarization is along the $[1\bar{1}0]$ axis. The probe beam has the same polarization as the THz radiation and

is focused onto the ZnTe so that it propagates simultaneously and collinearly through the crystal with the THz beam [37, 62].

Because ZnTe possesses non-zero electro-optic coefficients, the electric field of the THz radiation induces birefringence in the crystal [37, 38, 42, 63, 64]. This induced birefringence causes a differential phase delay in the copropagating probe pulse polarization components, thereby causing the originally linearly polarized probe pulse to become slightly elliptically polarized to a degree that is linearly proportional to the strength of the THz field. The modified pulse is guided through a quarter-wave plate so that its polarization is shifted from nearly linear to nearly circular and then through a Wollaston prism so that it is split into its two orthogonal polarization components. The intensities of the two components are differenced by the balanced photodetector to determine the ellipticity of the probe pulse and, thus, the relative THz field strength. The evolution of the probe pulse polarization is illustrated in Figure 13.

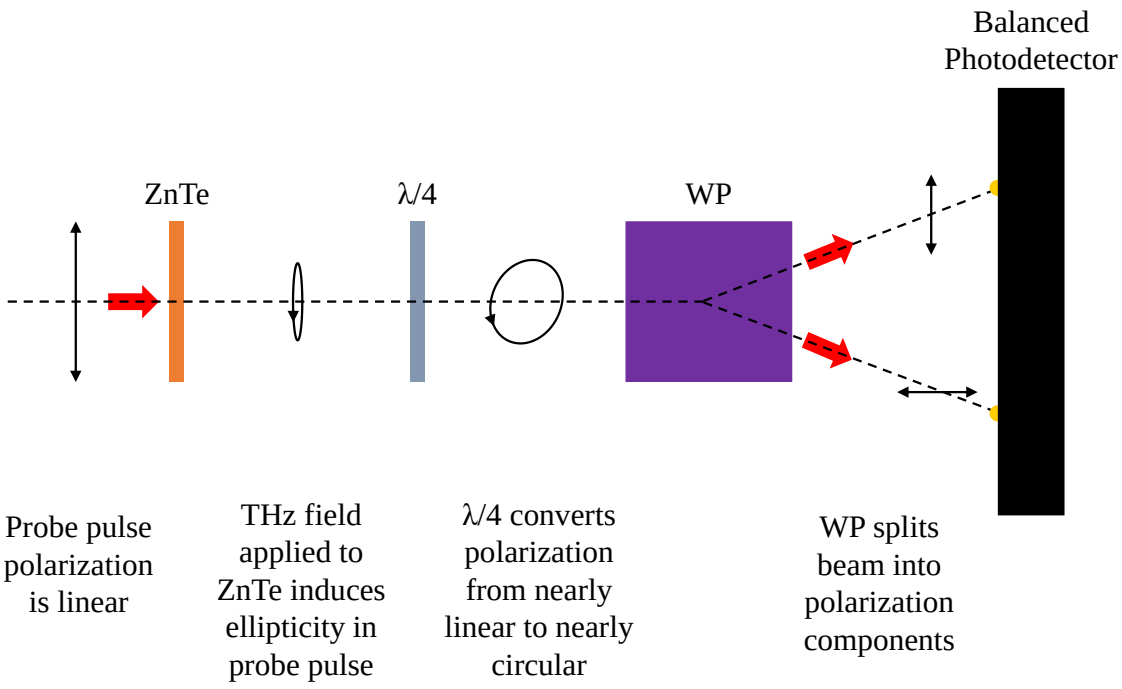

Figure 13 – Illustrated THz detection process (WP: *Wollaston prism*, ZnTe: *zinc telluride crystal*, λ/4: *quarter-wave plate*)

The pump beam is chopped at a rate of 1 kHz with the optical chopper so that the photodetector signal can be extracted from background noise by the lock-in amplifier (LIA). The LIA is operated with a typical filter order of 3 and a time constant of 61 ms. These values were chosen because larger selectable filter orders and time constants were observed to increase the required sampling time without significantly reducing noise. Smaller selectable filter orders and time constants significantly increased the noise floor without significantly decreasing the required sampling time.

Depending on the application, relevant information in the THz field is contained in a duration of 5 to 300 ps. Therefore, the ultrashort probe beam must be scanned across the duration of the THz pulse for acquisition of the entire field. Scanning is achieved with a delay line that delays the arrival of the pump beam to the PCA, thereby delaying the arrival

of each THz pulse to the ZnTe relative to each pulse in the probe beam. The FWHM of the laser pulses in the probe beam is 46 ± 4 fs at the ZnTe, so the delay line is moved in increments corresponding to time delays of 50 fs to resolve the THz electric field with approximately 50 fs resolution. The positional delay line increment (Δz) required to achieve a temporal delay (Δt) is given by

$$\Delta z = \frac{c}{2n_{air}}\Delta t, \tag{35}$$

where n_{air} is the refractive index of the surrounding air at the center wavelength of the laser pulse. The factor of 2 is included in the denominator because, as is evident in Figure 8, an increment of Δz in the delay line position generates an increment of $2\Delta z$ in the probe beam path.

Scanning proceeds as follows: the delay line is moved to the desired position; software waits for the LIA output to reach its 99% settling time; the signal is acquired as the average of a selectable number of samples over a selectable sampling time; the delay line moves to its next position. The starting position of the delay line is typically chosen such that the probe pulses arrive at the ZnTe a few ps before the THz pulses to establish a zero-signal reference. Figure 14 outlines the THz pulse data acquisition process.

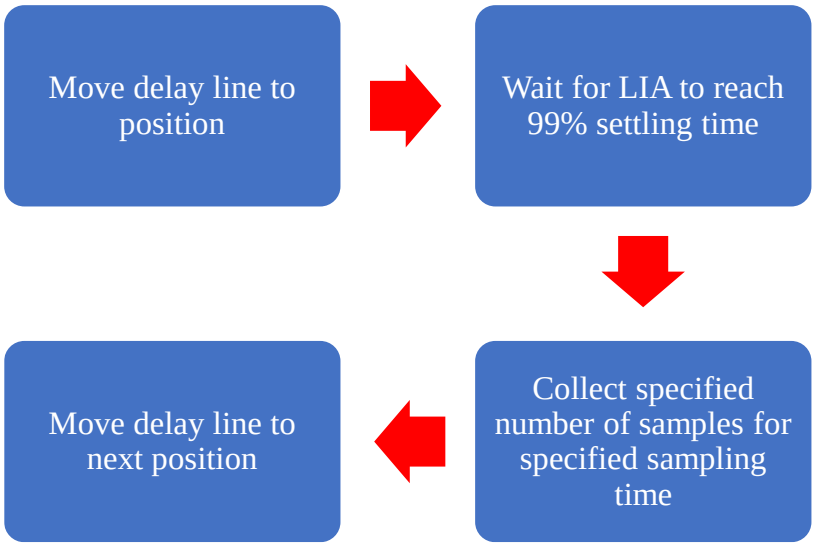

Figure 14 – Outline of THz pulse data acquisition process

Though each individual THz pulse has picosecond-scale duration, the use of an LIA and mechanical delay line requires acquisition of many individual pulses to construct a single composite pulse over the course of a typical measurement time of a few minutes. Measured plasma properties are therefore "time-resolved" on a minute, rather than picosecond scale. Previous authors [43, 44, 49] have achieved picosecond- and nanosecond-scale resolution of plasma property evolution by repeatedly pulsing the plasma and employing electronic gating techniques to collect sufficient data at each delay line position to enable LIA filtering and sample averaging. Such techniques are more accurately described as "phase-resolved" and have been employed in the EP field to perform phase-resolved LIF measurements of oscillating discharges [65]. However, as single-shot THz-TDS detection schemes improve, the possibility of resolving the entire THz electric field at a picosecond scale may one day become a reality [66].

Figure 15 shows an example pulse generated and detected by the THz-TDS system; Figure 16 and Figure 17 show the magnitude and phase, respectively, of its corresponding

spectrum. Readily resolvable frequencies range from approximately 0.2 to 2.5 THz. Deviations from an ideal THz pulse are caused by electron screening in the PCA, reflections in the ZnTe, and the presence of water vapor in the pulse path.

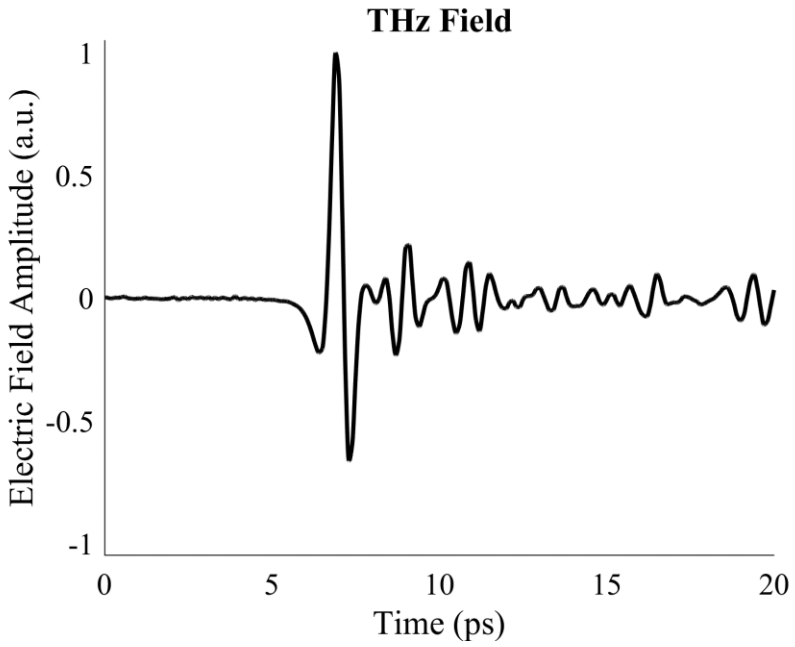

Figure 15 – THz pulse generated and detected by the THz-TDS system

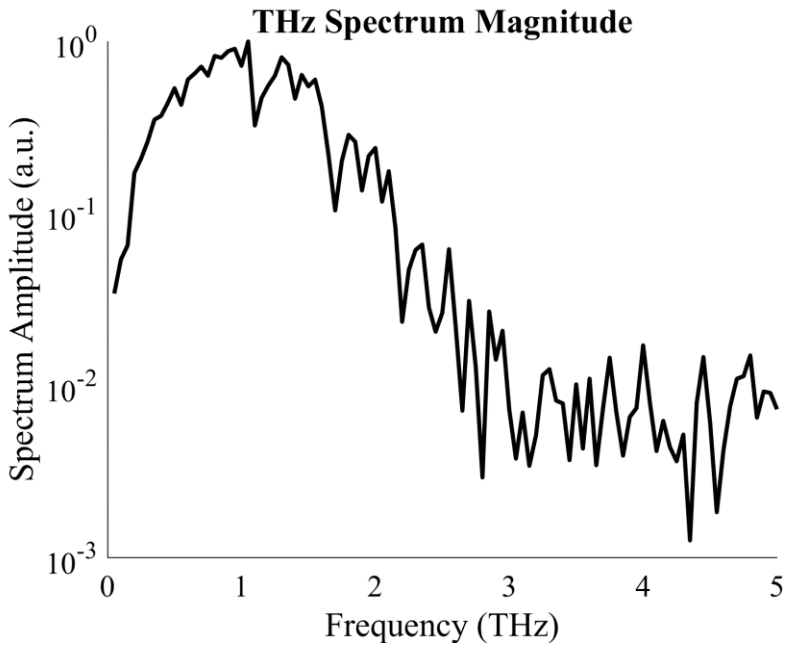

Figure 16 – Magnitude of THz spectrum measured by THz-TDS system

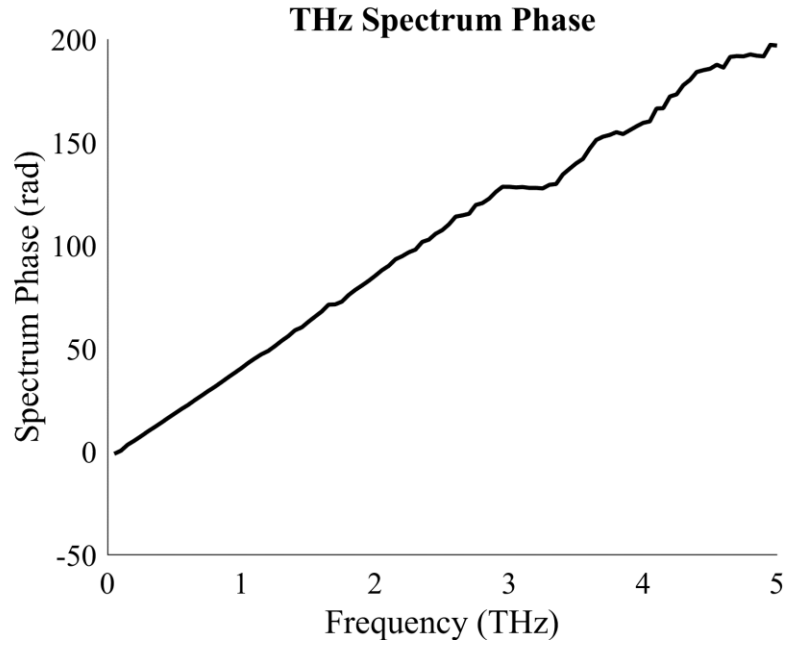

Figure 17 – Phase of THz spectrum measured by THz-TDS system

3.3 Measurement Verification

Verification of THz-TDS system operation for this dissertation was performed in two stages: 1) verification of the recovery of water absorption lines in humid air and 2) comparison of refractive index and extinction coefficients of a sample material with published data.

Figure 18 shows a 100 ps THz trace measured after propagation through 1 m of 60% relative humidity (RH) air. The scan duration of 100 ps enables a spectral resolution of 0.01 THz. The corresponding spectrum is shown in Figure 19.

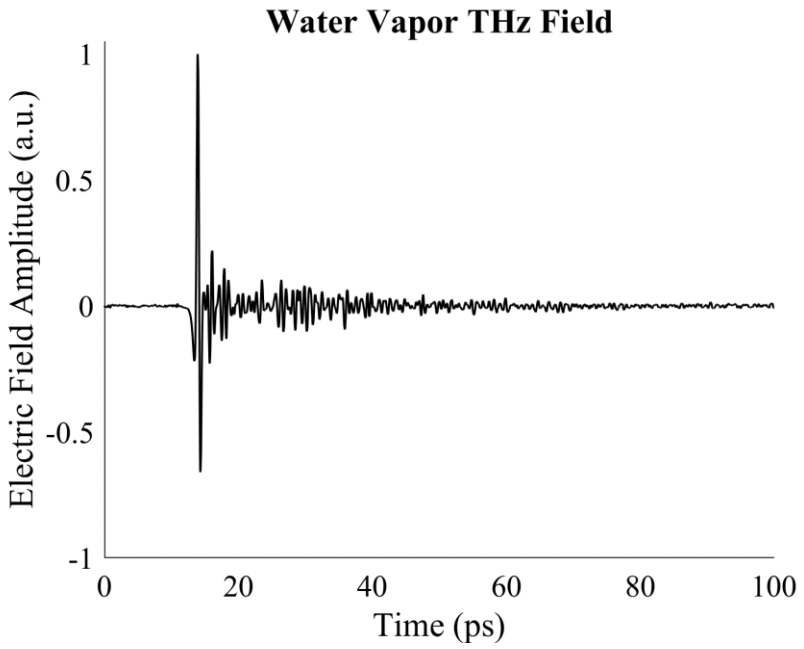

Figure 18 – Water vapor test THz pulse (1 m through 60% RH)

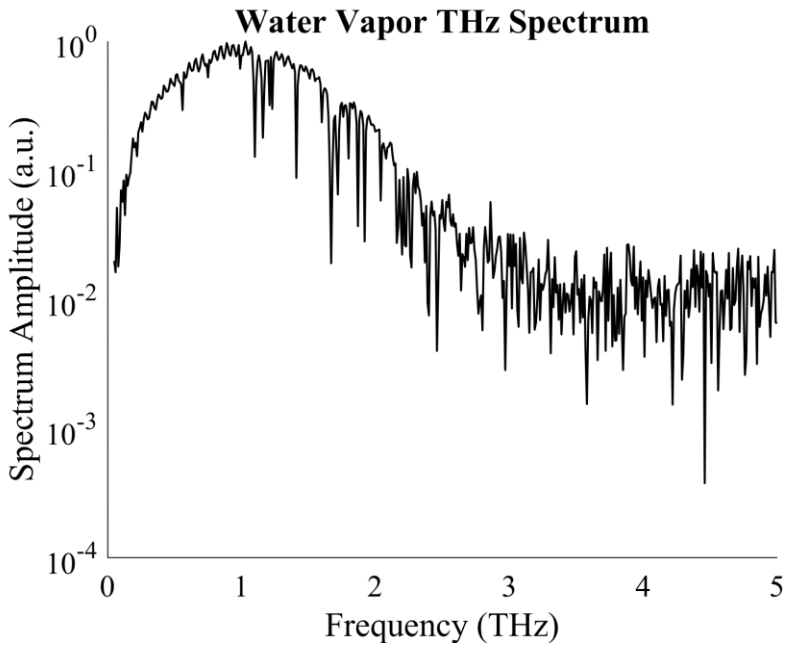

Figure 19 – Water vapor test THz spectrum (1 m through 60% RH)

Between 0.5 and 1.5 THz, where the THz spectrum signal strength is greatest, theory predicts strong water absorption lines exist at 0.56, 1.10, 1.16, and 1.41 THz [67]. Figure 20 shows the spectrum in Figure 19 from 0 to 1.5 THz and demonstrates that these water absorption lines are indeed recovered by the THz-TDS system, within the spectral resolution.

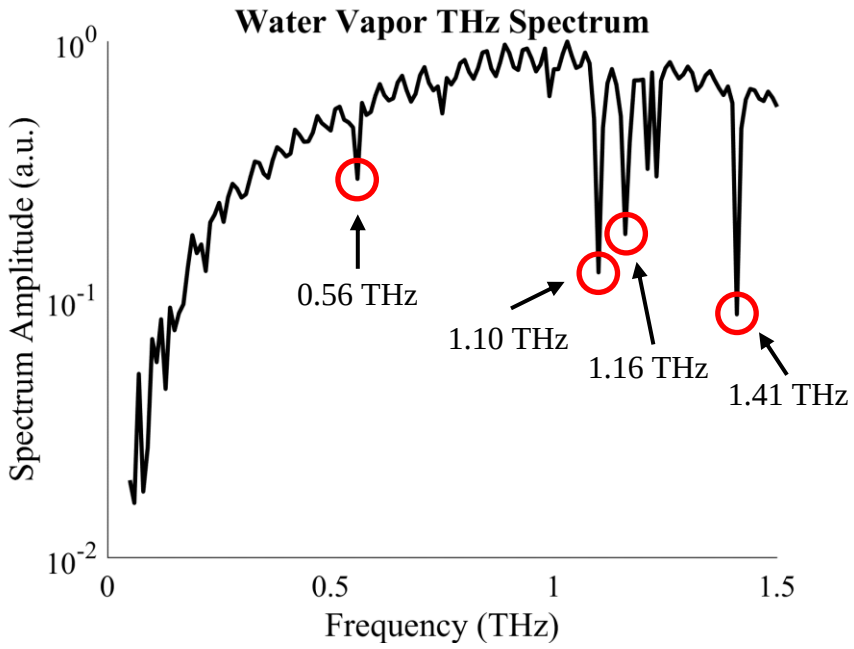

Figure 20 – Water vapor test THz spectrum highlighting water absorption lines (1 m through 60% RH)

Further confirmation of THz-TDS system operation is provided by the recovery of published refractive index and extinction coefficient data. Figure 21 shows sample and reference THz traces taken with a 0.1 in-thick sample of HP grade BN manufactured by Saint-Gobain Ceramic Materials. HP BN is hexagonal close-packed BN hot-pressed in a calcium borate ($Ca_3(BO_3)_2$) binder. THz pulse propagation was along the optic axis of the HP BN, so measured properties correspond to that of the ordinary ray. The sample was surrounded by vacuum for recording of the sample pulse and replaced by vacuum for recording of the reference pulse, per the measurement setup diagrammed in Figure 7.

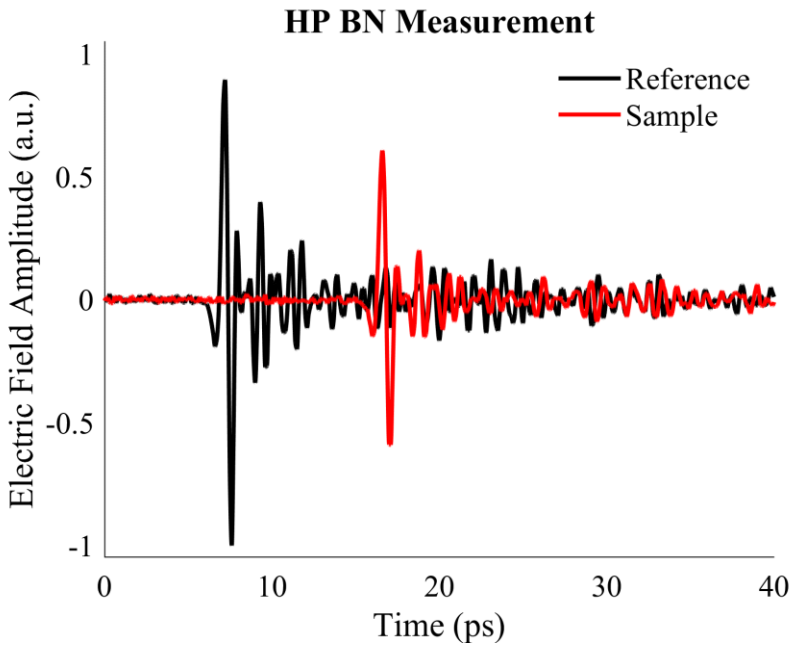

Figure 21 – Sample and reference THz pulses for HP BN measurement

The optical properties of the HP BN were calculated using the relationship between the measured THz spectra and refractive index and extinction coefficient given by Eqs. (4) and (12). The frequency-dependent results of these calculations are shown in Figure 22.

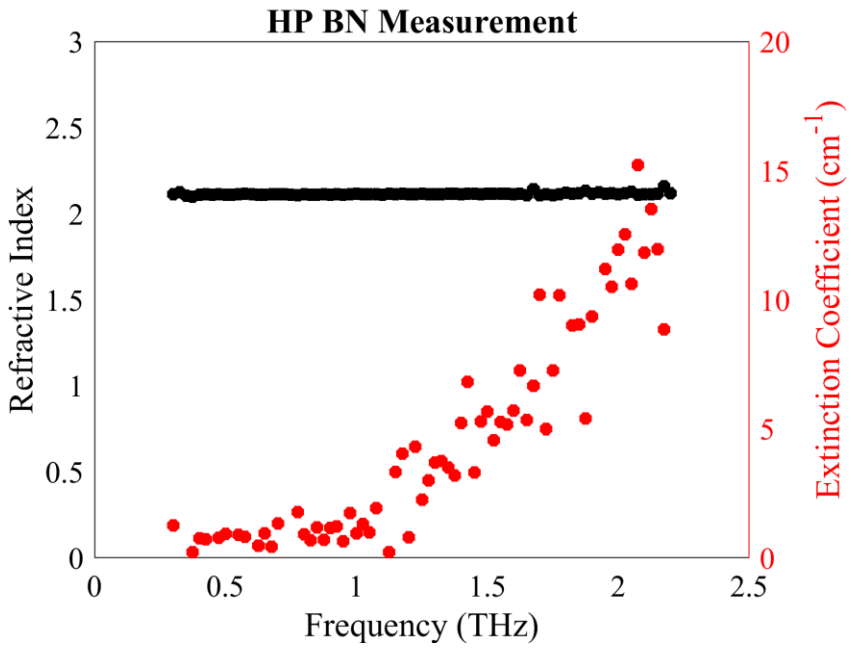

Figure 22 – HP BN refractive index and extinction coefficient (ordinary ray)

Naftaly et al. [36] published refractive index and extinction coefficient data for multiple grades of BN in the THz regime. One grade, HBR BN manufactured by Momentive Performance Materials, is of similar composition to HP BN because it also consists of hexagonal close-packed BN hot-pressed in a calcium borate binder. Their results, which are curve fits of raw measurement data, are shown in Figure 23.

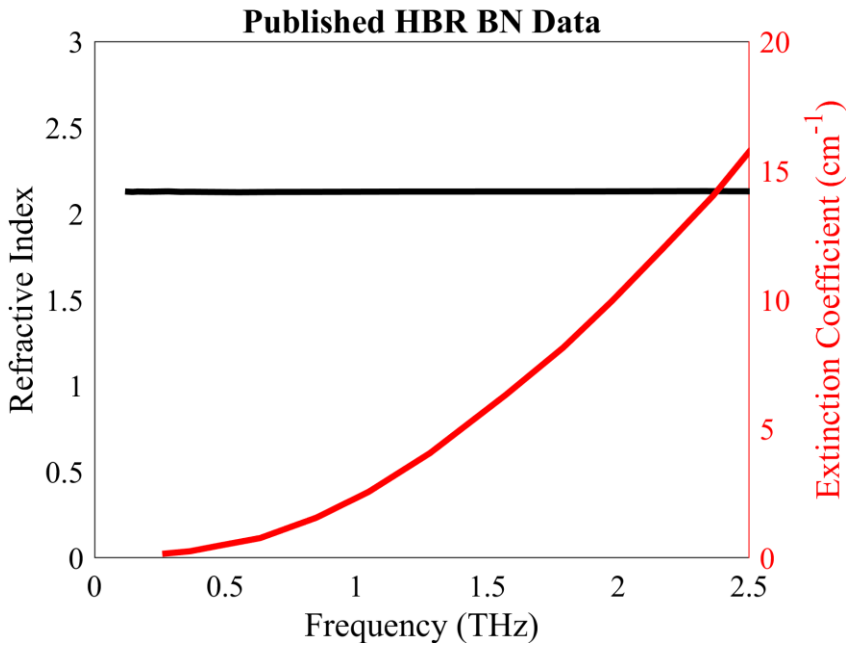

Figure 23 – Published HBR BN refractive index and extinction coefficient curve fits (ordinary ray)

Similarity between the datasets plotted in Figure 22 and Figure 23 is evident. Figure 24 directly plots the measured HP BN values with the HBR BN curve fits to facilitate comparison of the datasets.

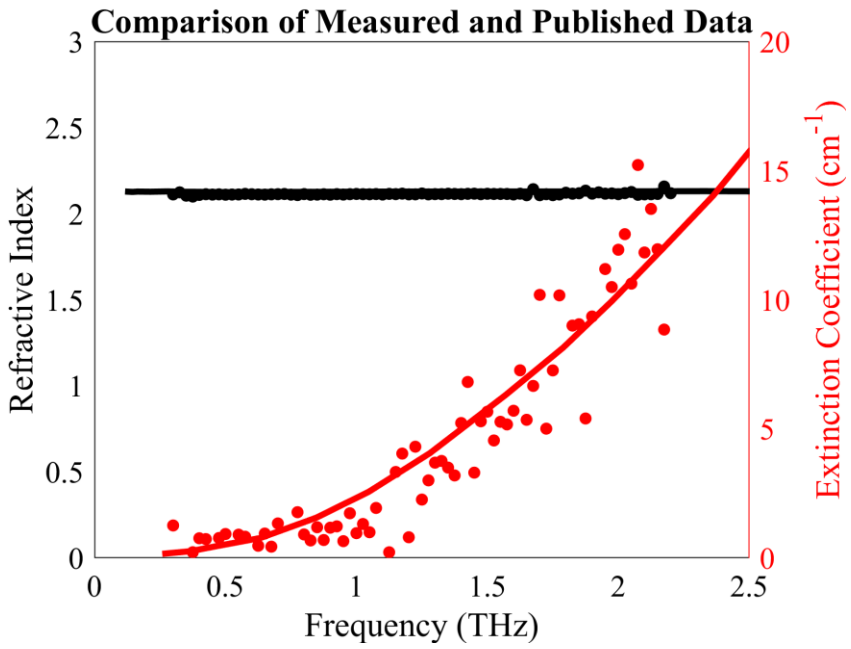

Figure 24 – Comparison of measured HP BN and published curve fit HBR BN refractive index and extinction coefficient (ordinary ray)

The trends in refractive index and extinction coefficient are approximately the same, and, though the BN samples were produced by different manufacturers, the measured values agree well with the published curve fits. At 1 THz, for instance, the HBR refractive index curve fit differs from the measured HP refractive index by just 0.5%. Additionally, as shown in Figure 24, the HBR extinction coefficient curve fit falls within the spread of measured HP extinction coefficients at all resolvable THz frequencies. The agreement between the two datasets provides strong evidence for the validity of measurements made by the THz-TDS system.

In conjunction with the well-established nature of the basic physics connecting optical properties to plasma parameters, the above results provide implicit verification of the THz-TDS system's plasma property measurement capability. As noted in Chapter 1, direct verification of plasma property measurements would require use of either

electrostatic probes or additional optical techniques. Electrostatic probes, though relatively easy to implement, suffer ablation, are invasive, and feature large uncertainties in the high-density plasma environments for which THz-TDS is well-suited. In fact, the standard approach for extracting data from electrostatic probes in the type of plasma discharge discussed in Section 3.4 is to calibrate the probe measurements against microwave interferometry data [68]. Though one previous THz-TDS effort found general agreement between Langmuir probe and THz-TDS results, the authors noted deviations between the datasets were likely driven by unsuitability of the probe for high-density plasma diagnostics [45].

Optical techniques capable of directly corroborating either electron density or both electron density and collision frequency include OES, LTS, and microwave interferometry. However, interpretation of OES data requires detailed knowledge of plasma collisional-radiative processes and can therefore be fraught with error; implementation of LTS would require significant financial investment and nontrivial system setup and calibration; and interpretation of microwave interferometry results relies on the same basic physics as THz-TDS – meaning that interferometric measurements would provide virtually no additional measurement confidence. In the absence of an available and suitable direct measurement verification technique, implicit verification of THz-TDS operation must suffice.

3.4 Radio Frequency Inductively Coupled Plasma Discharge

An argon radio frequency (RF) inductively coupled plasma (ICP) discharge serves as the plasma testbed for the THz-TDS system. The RF ICP discharge type was chosen for the plasma testbed because it is representative of a relevant EP plasma discharge (RF ion thruster) and generates a stable, uniform plasma with densities within the expected

detection range of THz-TDS [45, 68]. The RF circuit design was largely based on the practical considerations presented by Williams [69].

The discharge consists of a quartz tube cross (50 mm outer diameter, 3 mm wall thickness, 460 mm length, 250 mm width, custom-built by Technical Glass Products) connected to steel KF vacuum flanges by quick-connect couplings (Kurt J. Lesker QF50XVC200). A rotary-vane mechanical pump (Pfeiffer Adixen PASCAL 2021SD) evacuates the discharge chamber to a base pressure of 1 mTorr, as measured by a convection pressure gauge (Kurt J. Lesker KJL275807LL). Ultra-high purity (99.999%) argon is fed into the discharge by a regulator and precision flow meter. Pressure values outputted by the pressure gauge are corrected for argon according to fits made from argon calibration data provided by the manufacturer.

RF power is coupled to the plasma via a three-turn hollow copper antenna wrapped around the glass tube. The unbalanced 13.56 MHz RF signal is generated by an RF power supply (Materials Science, Inc. RF-3-XIII), tuned by an RF radio antenna tuner (Palstar HF-AUTO), and converted to a balanced signal by a custom 1000 Ω current balun connected to each end of the antenna. Power is carried between devices by 50 Ω RG400 coaxial patch cables with UHF connectors (Pasternack PE3743 series). The plasma discharge is always operated with a standing wave ratio of 1.05 or less, and forward power drift was observed to remain within ±1 W throughout the duration of all THz-TDS measurements. Figure 25 shows the simplified RF circuit schematic.

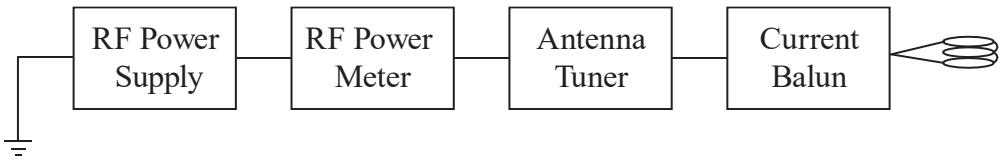

Figure 25 – Simplified RF circuit schematic

An electrically grounded Faraday cage surrounding the antenna prevents stray electromagnetic radiation or electrical arcs from interfering with THz-TDS measurement equipment. The discharge viewports (Torr Scientific BKVPZ50NQZ) feature Z-cut crystalline quartz windows that, compared to standard amorphous quartz windows, exhibit relatively low absorption in the THz regime [70]. THz radiation is sent through the longer dimension of the quartz tube. The discharge is pictured in Figure 26 operating at 1 Torr argon and 200 W input power.

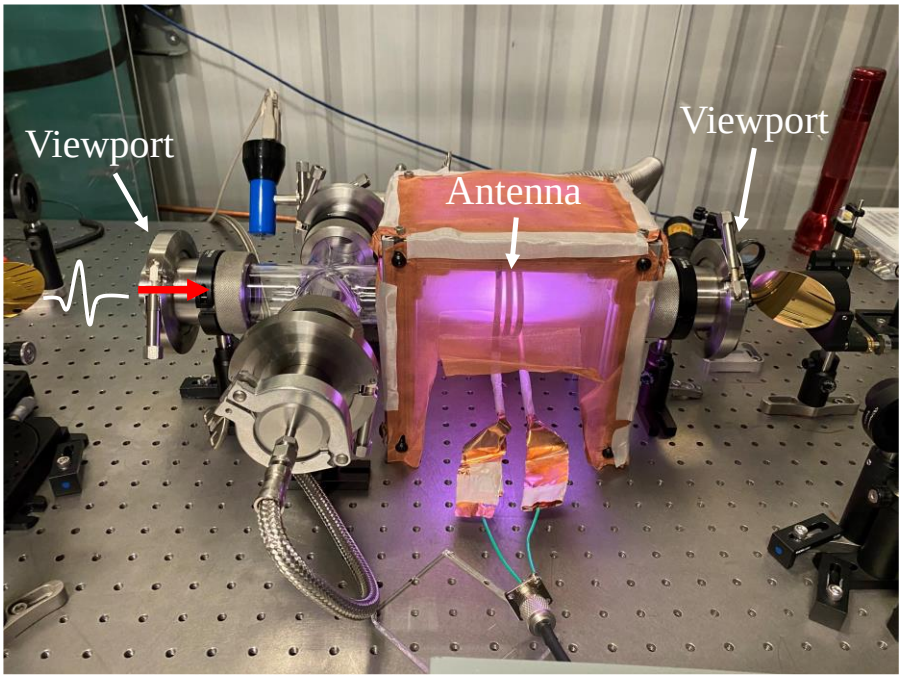

Figure 26 – RF ICP discharge (200 W, 1 Torr)

CHAPTER 4. STANDARD ANALYSIS METHOD

Chapter 4 details the standard analysis of THz-TDS data (Section 4.1) and presents electron densities measured with the THz-TDS system for a range of RF ICP operating powers and pressures (Section 4.2). The term “standard” refers to the analysis framework used by previous authors in the literature and is distinct from the Bayesian framework developed for this dissertation and discussed in Chapter 6. Electron collision frequency results are not presented in Section 4.2 due to deficiencies in the standard analysis framework explained in Section 4.1.3.

4.1 Analysis

Raw sample and reference electric field data outputted by the LIA are used to calculate the THz-TDS transfer function phase and magnitude at each resolvable THz frequency. The phase data are corrected for phase wrapping and delay line registration error. The standard analysis framework assumes the plasma is uniform and that the assumptions required to use Eq. (28) are valid. The validity of these assumptions is discussed in Section 5.1. After the phase data are corrected, Eq. (28) is inverted to determine the line-averaged electron density and collision frequency as a function of THz pulse frequency. Figure 27 outlines the data analysis procedure.

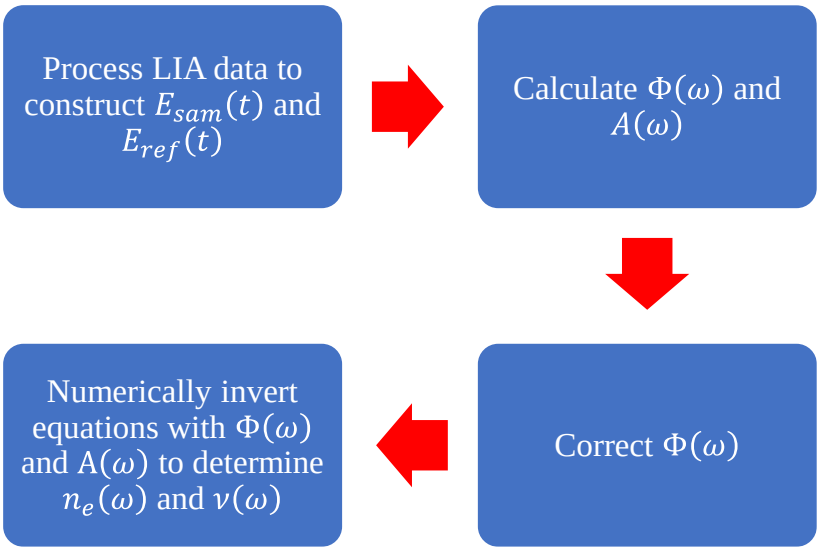

Figure 27 – Outline of standard data analysis procedure

4.1.1 Calculation of Phase and Magnitude

4.1.1.1 Electric Field Calculation from LIA Data

The LIA extracts the THz signal above noise by demodulating the signal with a reference input provided by the optical chopper. The LIA used in this dissertation is a dual-phase LIA that utilizes two demodulators to enable compensation for phase drifts in the THz and reference signals. The two demodulator outputs (X and Y) are quadrature components of the total signal magnitude (R) and are therefore related to the total signal magnitude by

$$R^2 = X^2 + Y^2. \tag{36}$$

Many (X,Y) sample pairs are recorded at each delay line position. Each delay line position corresponds to a temporal position on the THz pulse, according to Eq. (35). The

X and Y samples are averaged at each position to establish the averaged X and Y signals. Due to phase drift in the optical chopper reference signal, the averaged X and Y signals linearly drift in opposite directions and do not have baseline values of zero. These imperfections are quantified by linear fits of the average signal tips, where the THz electric field strength is equal to zero.

The raw, pre-averaged X and Y signal data are leveled and zeroed with the linear fits of the averaged signal tips. Each leveled (X,Y) datapoint is then used to calculate each R datapoint via Eq. (36). The sign of each R datapoint is determined by comparing its composite X and Y data points. If the absolute value of the zeroed and leveled X is greater than that of Y, the sign of R is assigned to be that of X. If the absolute value of the zeroed and leveled X is less than that of Y, the sign of R is assigned to be that of Y. The reported electric field is then calculated by averaging across all signed R samples at each delay line position. Averaging is performed in the time domain (rather than in the frequency domain after calculation of spectra) because time-domain averaging has been shown to significantly reduce variance in output spectra [55].

4.1.1.2 Phase and Magnitude Calculation

The sample and reference electric field spectra are calculated from the sample and reference electric fields, respectively, via the fast Fourier transform (FFT) implementation of the discrete Fourier transform (DFT). According to the convention of Eq. (5), the DFT is given by

$$\hat{E}_k = \sum_{m=0}^{M-1} E_m \exp\left(-\frac{i2\pi km}{M}\right), \tag{37}$$

where m is the index of the discrete electric field (beginning at zero), M is the number of entries in the discrete electric field, and k is the index of the discrete spectrum (also beginning at zero). Because indexing begins at zero, E_m denotes the $(m+1)^{\text{th}}$ element of the discrete electric field and $\hat{E}_k$ denotes the $(k+1)^{\text{th}}$ element of the discrete spectrum. Due to the redundancy of the information above the Nyquist frequency, the values of k are limited to integers that satisfy $0 \leq k \leq M/2$. The corresponding discrete angular frequencies (ω_k) are given by

$$\omega_k = \frac{2\pi k}{\mathrm{T}_{scan}}, \tag{38}$$

where T_{scan} is the total temporal duration of the discrete electric field [71].

The spectral ratio is computed by dividing the sample spectrum by the reference spectrum, and the phase and magnitude of the transfer function are extracted according to Eq. (10). Implementation of the FFT and subsequent determination of the phase and magnitude of the transfer function can be performed with software packages available in most programming languages.

Figure 28 shows sample and reference electric fields measured for RF ICP discharge conditions of 1 Torr and 200 W. The extracted phase and magnitude computed at each resolvable THz frequency are shown in Figure 29 and Figure 30, respectively. Because the

phase extracted from the transfer function can only exist from -π to π, phase wrapping generates 2π discontinuities in the phase data [55].

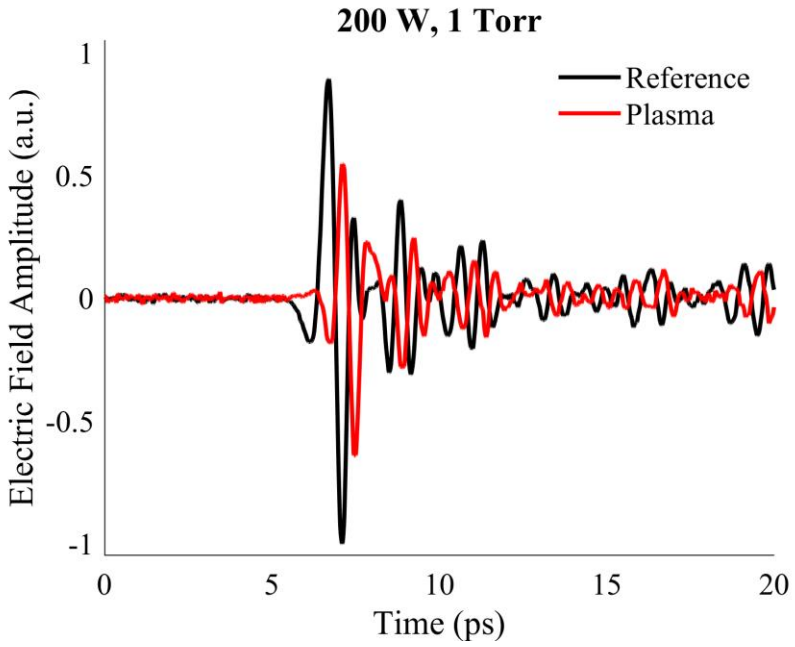

Figure 28 – Sample and reference THz pulses (200 W, 1 Torr)

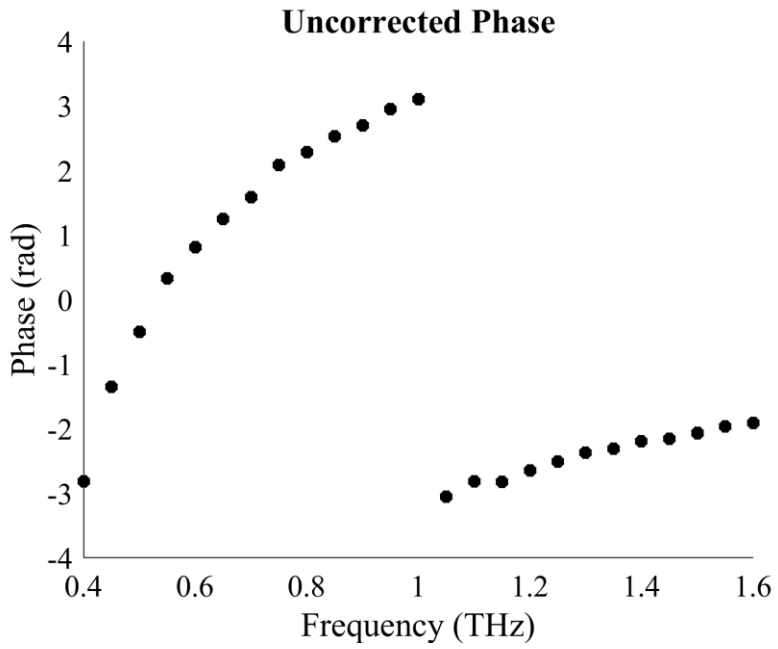

Figure 29 – Uncorrected phase (200 W, 1 Torr)

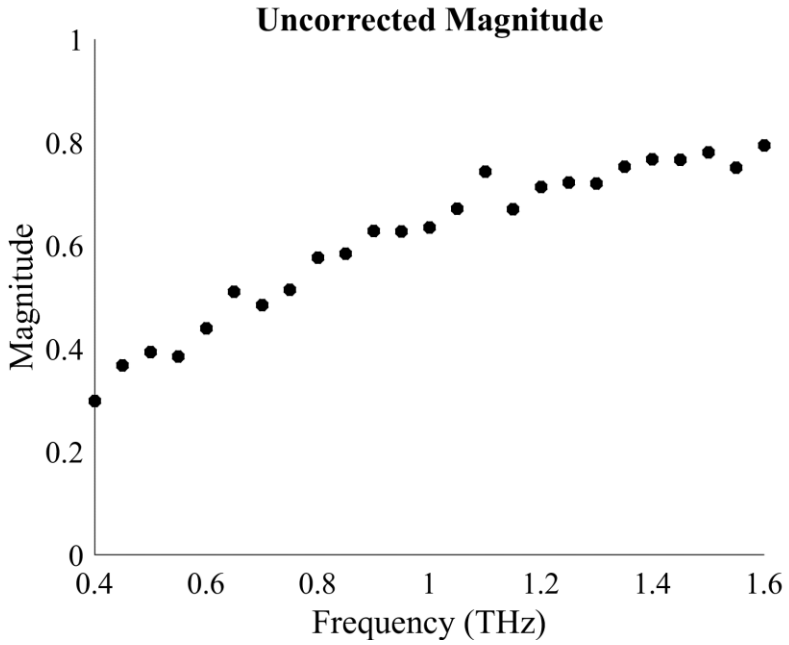

Figure 30 – Uncorrected magnitude (200 W, 1 Torr)

4.1.2 Phase Corrections

Two phase corrections are necessary. The first is phase unwrapping, whereby the 2π discontinuities in the phase data are eliminated by subtracting integer multiples of 2π from the phases at frequencies impacted by the discontinuity. The unwrapped phase (Φ) is related to the measured phase (Φ_m) by

$$\Phi(\omega) = \Phi_m(\omega) - 2\pi W(\omega), \tag{39}$$

where W is the number of discontinuities impacting ω. The phase unwrapping process is straightforward for data with high SNR but can be challenging for data with low SNR, as noise may mask the location of the phase discontinuities. A thorough discussion of phase unwrapping strategies for a variety of conditions is provided by Jepsen [72]. Figure 31 shows the phase data from Figure 29 after phase unwrapping.

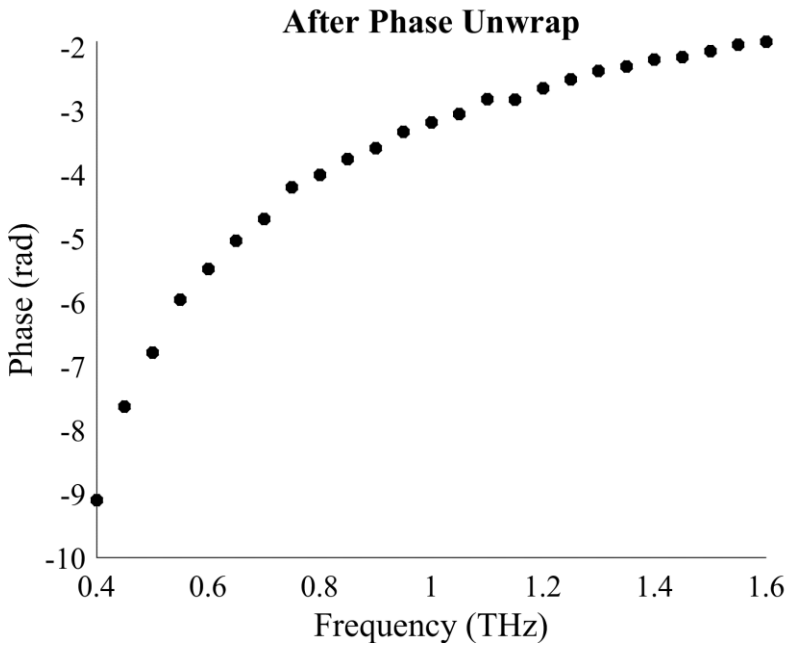

Figure 31 – Phase after unwrap (200 W, 1 Torr)

The second phase correction accounts for delay line registration error. Delay line registration error occurs when the delay line fails to return to exactly the same starting position after scanning a THz pulse. The resulting offset in starting position introduces an artificial phase shift in the next scan. First reported by Meier et al. [49], delay line registration error between the reference and sample THz pulses introduces an artificial linear dependence of phase with THz frequency and therefore results in a linear trend in calculated electron density with THz frequency. Figure 32 shows the electron density calculated for the 200 W, 1 Torr operating conditions prior to implementation of the delay line registration error phase correction.

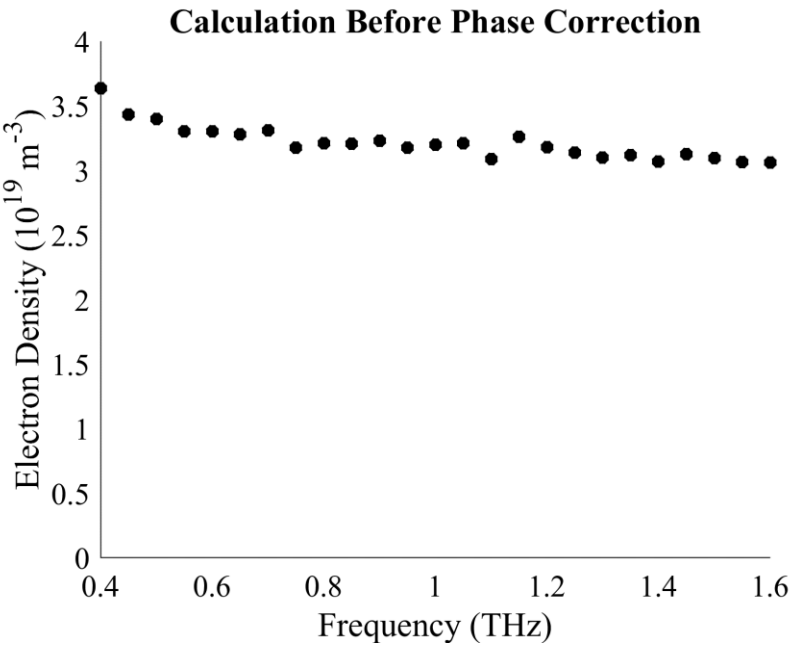

Figure 32 – Electron density calculated before phase correction (200 W, 1 Torr)

Delay line registration error follows a normal distribution and has been quantified in solid material THz-TDS uncertainty analysis as a standard deviation measured from multiple delay line scans [73]. However, when measuring plasma properties with THz-TDS, it is typically desirable to scan the delay line just once for each sample and reference pulse. Using Eq. (31) as a guide, Meier et al. [49] therefore fit their phase data to

$$\Phi(\omega) = \frac{\varphi_1}{\omega} + \varphi_2\omega + \varphi_3 \tag{40}$$

and corrected for delay line registration error by subtracting away the linear ($\varphi_2\omega$) component of the fit.

Meier et al. [49] also reported the need to subtract away the intercept (φ_3) to accurately process the data. However, there is no clear physical justification for the

presence of the intercept. The phase data collected for this dissertation feature negligibly small values of φ_3, so the data are instead fit to

$$\Phi(\omega) = \frac{\varphi_1}{\omega} + \varphi_2\omega \tag{41}$$

and only the linear portion of the fit is removed from the phase data. Figure 33 shows the 200 W, 1 Torr electron density calculated with the corrected phase data.

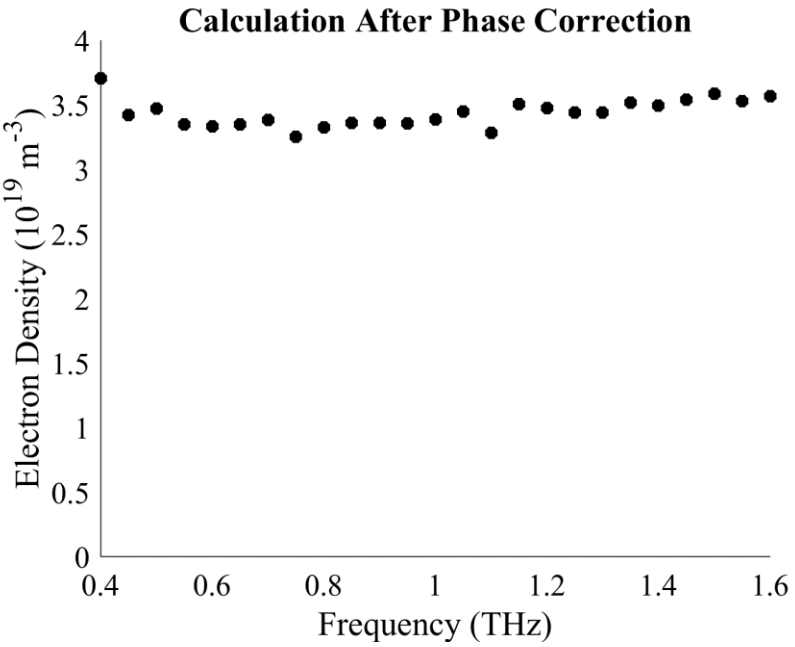

Figure 33 – Electron density calculated after phase correction (200 W, 1 Torr)

It is important to note that the phase correction provided by Eq. (41) is strictly valid only if the assumptions inherent in the derivation of Eq. (31) are met. Otherwise, if the influence of the electron collision frequency on the phase is not negligible, correcting the phase according to Eq. (41) will introduce error into the calculation. A more robust

correction scheme with less restrictive assumptions is discussed as part of the Bayesian framework in Section 6.1. The standard units for φ_2 are s/rad, but the value can be converted to units of s through multiplication by 2π rad.

4.1.3 Calculation of Plasma Properties

After corrections are applied to the phase data, an initial guess for the electron density is computed with Eq. (31) at each resolvable THz frequency. The initial electron density guess and a guess for the electron collision frequency are used to seed an iterative computational inverter to solve for the electron density and collision frequency with Eq. (28) at each resolvable THz frequency. The reported electron density and collision frequency are averaged over the values calculated at each THz frequency. Such averaging assumes the properties calculated at each frequency should be equally weighted, an assumption that is not necessary in the Bayesian analysis framework provided in Section 6.1.

Data collected for this dissertation at every tested plasma condition resulted in the calculation of electron collision frequencies that exhibit a severe positive linear trend with THz pulse frequency. Figure 34 shows the electron collision frequency calculated for the 200 W, 1 Torr condition. The nonphysical trend in the data suggests the need for a correction to the magnitude, but, because most THz-TDS plasma diagnostics publications do not report electron collision frequency, no information on magnitude corrections exists in the literature. This problem is overcome by the implementation of a magnitude correction in Section 6.1.1 as part of the Bayesian analysis framework.

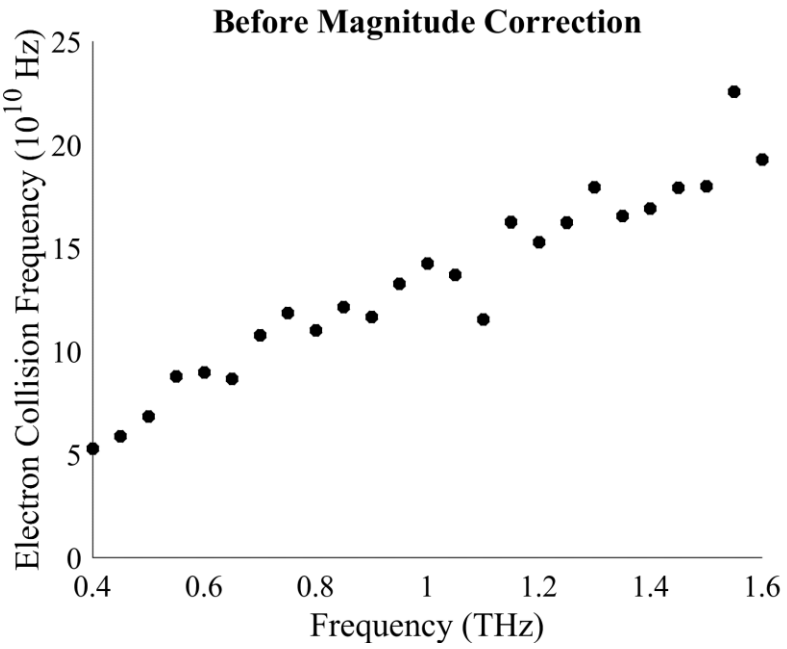

Figure 34 – Calculated electron collision frequency before magnitude correction (200 W, 1 Torr)

4.2 Plasma Property Results

Figure 35 shows the measured electron densities (as calculated through the standard analysis framework) for various input powers and discharge operating pressures. No electron collision frequency results are presented due to the apparent need for a measurement correction. Observed plasma lengths ranged from 0.11 to 0.13 m, depending on the condition, so a uniform plasma length of 0.12 m was used to normalize the line-integrated electron density for all cases. The implications of the use of a uniform assumed plasma length are discussed in Section 5.1.2.

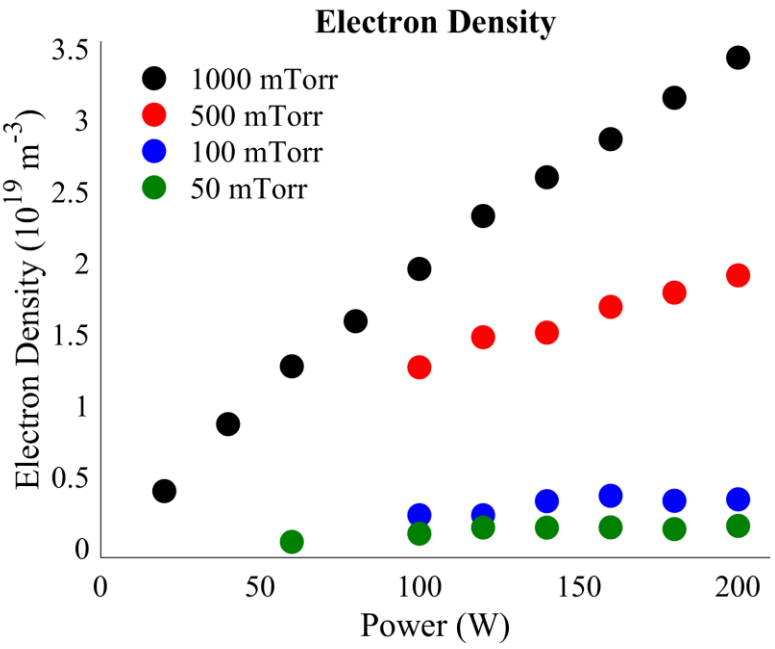

Figure 35 – Electron density calculated with standard analysis procedure (no error bars shown)

The electron density increases linearly with power at all pressure conditions. The 1 Torr and 500 mTorr electron density values are of the same order of magnitude as those measured in a similar ICP at similar conditions [45]. No error bars are included in the plot because the standard analysis framework does not include a method for accurate uncertainty quantification.

CHAPTER 5. DOMAIN OF APPLICABILITY

This chapter investigates the THz-TDS plasma diagnostic domain of applicability. Section 5.1 discusses the validity of standard assumptions and provides simple rules for evaluating assumption validity as a function of plasma conditions. Section 5.2 maps out the feasible THz-TDS measurement space and discusses the physics and THz-TDS system parameters that define the boundaries of the measurement space. Section 5.3 evaluates the feasibility of THz-TDS measurements in a variety of EP plasma conditions. Section 5.4 summarizes the findings of this chapter.

5.1 Validity of Standard Assumptions

This section investigates the applicability of standard assumptions used to process THz-TDS plasma diagnostic data. Section 5.1.1 quantifies the error associated with calculating electron density with Eq. (31), Section 5.1.2 discusses the validity of reporting line-averaged electron density and electron collision frequency, and Section 5.1.3 quantifies the error associated with using Eq. (28) in magnetized thermal plasmas.

5.1.1 Calculation of Electron Density from Phase Information Alone

Parameter extraction is greatly simplified if Eq. (31) can be used to directly determine the electron density from phase information alone. Use of Eq. (31) bypasses the need to numerically invert Eq. (28) and eliminates uncertainties in the magnitude measurement. As a result, the bulk of publications in the THz-TDS plasma literature use Eq. (31) in place of Eq. (28). The assumptions used to derive Eq. (31) suggest that it is

applicable if the THz pulse radiation frequency is larger than the plasma frequency and if the electron collision frequency is much less than the plasma frequency.

The applicability of Eq. (31) is tested here through quantification of the absolute value of the electron density error caused by its use in place of Eq. (28) for various measurement conditions. Equation (28) is a function of the electron density, electron collision frequency, THz pulse frequency, and plasma length, so the error is quantified here as a function of these parameters. Figure 36 and Figure 37 compare the electron density error as a function of electron density and collision frequency for a uniform plasma length of 0.1 m and THz pulse frequencies of 0.1 and 1 THz, respectively. Figure 38 and Figure 39 show the same computation for a THz pulse frequency of 1 THz and uniform plasma lengths of 0.01 and 1 m, respectively. In all plots, the error was calculated by inputting a range of electron density and collision frequency values into Eq. (28) to determine the measured magnitude and phase of the THz-TDS transfer function, computing the electron density from the phase alone with Eq. (31), and comparing the input and output electron densities.

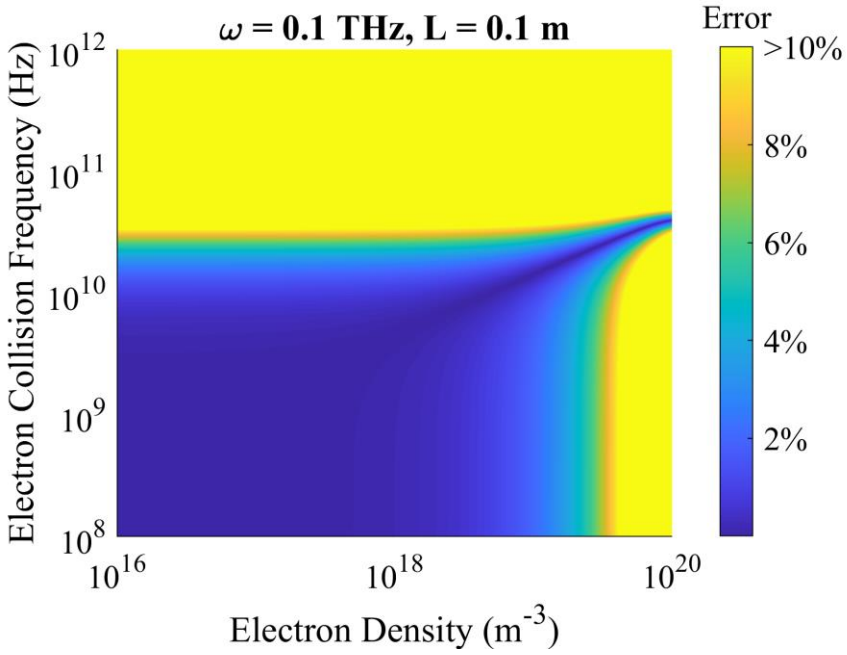

Figure 36 – Electron density calculation error from the use of Eq. (31) for a pulse frequency of 0.1 THz and uniform plasma length of 0.1 m

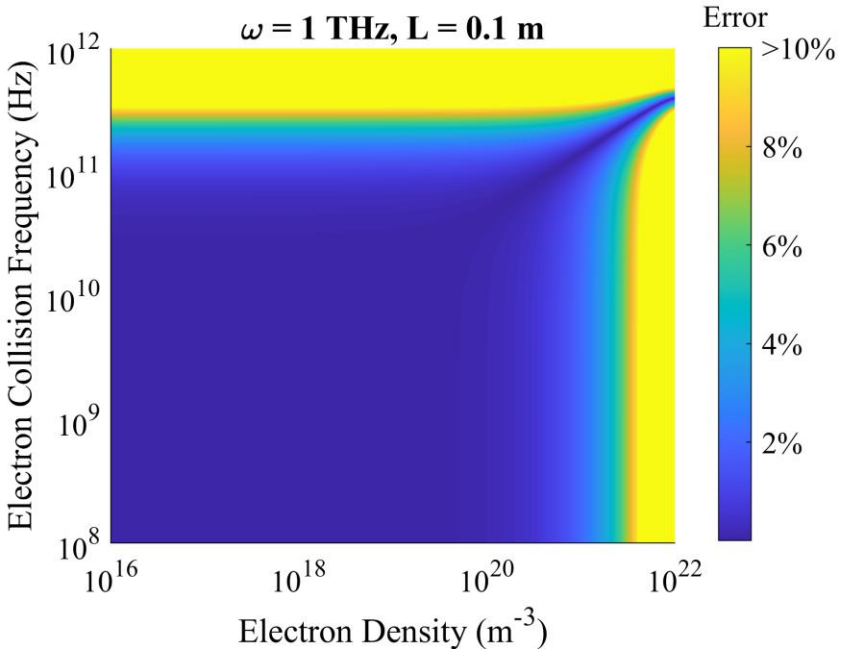

Figure 37 – Electron density calculation error from the use of Eq. (31) for a pulse frequency of 1 THz and uniform plasma length of 0.1 m

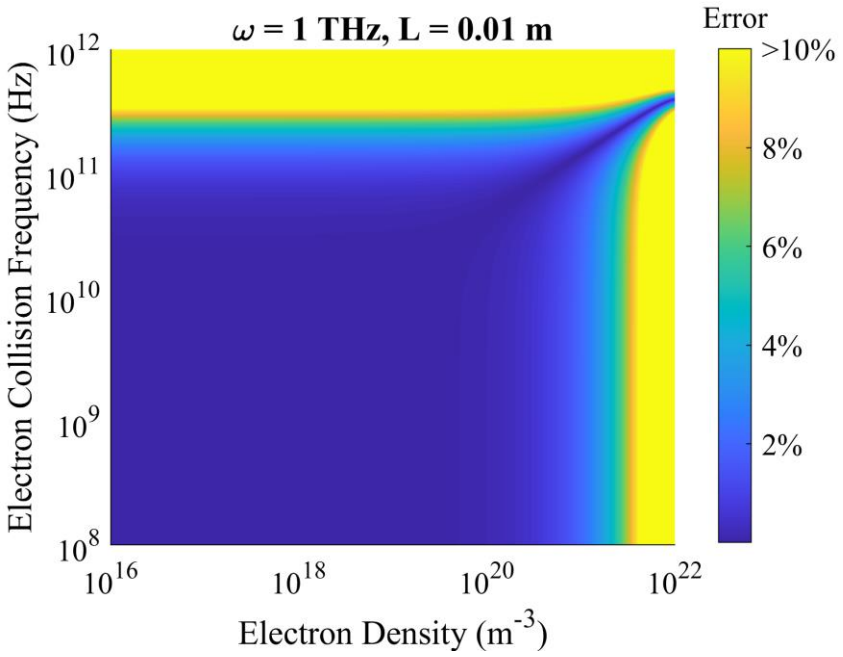

Figure 38 – Electron density calculation error from the use of Eq. (31) for a pulse frequency of 1 THz and uniform plasma length of 0.01 m

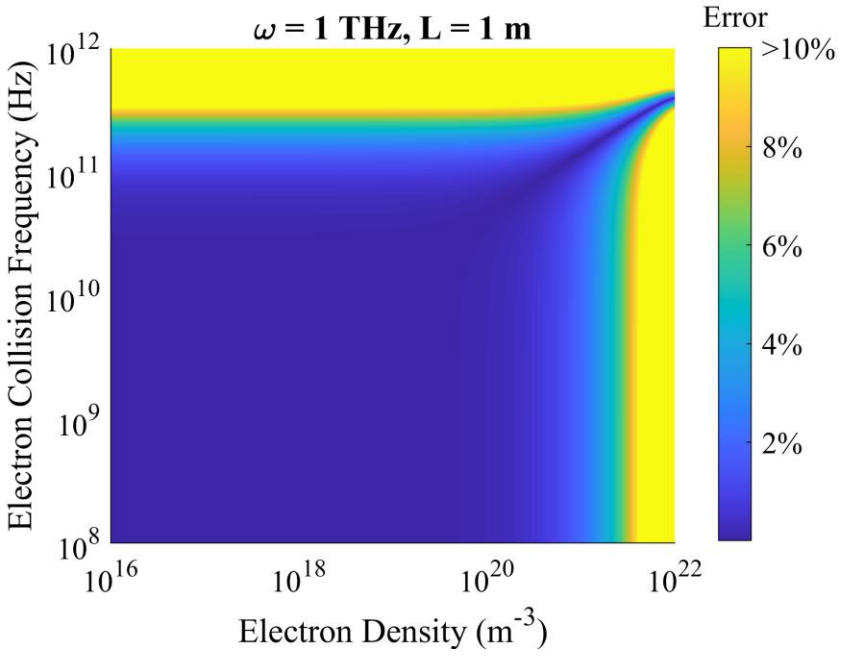

Figure 39 – Electron density calculation error from the use of Eq. (31) for a pulse frequency of 1 THz and uniform plasma length of 1 m

The plots indicate that error is low (< 4%) for values of the electron collision frequency at least an order of magnitude smaller than the THz radiation frequency and values of the electron density for which the corresponding plasma frequency is at least an order of magnitude smaller than the THz radiation frequency. The error rises sharply and rapidly exceeds 10% as either the electron collision frequency or plasma frequency approaches the value of the THz radiation frequency.

This result is independent of the plasma length, which does not appear to impact the calculation error. Though the data presented here are for specific conditions and, therefore, are not strictly general, the results suggest that critical values of the electron density ($n_{e,c}$) and electron collision frequency (ν_c) for which error from the use of Eq. (31) becomes significant are given by

$$n_{e,c} \sim \frac{\omega^2 \epsilon_0 m_e}{10 e^2}$$

and (42)

$$\nu_c \sim \frac{\omega}{10}.$$

Though derivation of Eq. (31) assumes the electron collision frequency is much smaller than the plasma frequency, the results do not indicate that violation of this assumption causes significant error. An electron density of 10^{18} m^{-3}, for instance, corresponds to a plasma frequency of approximately 9×10^9 Hz; however, the error incurred through the use of Eq. (31) is less than 2% in all plots at an electron density of 10^{18} m^{-3} and electron collision frequency of 9×10^9 Hz.

5.1.2 Impact of Distribution on Line-Integrated and Line-Averaged Assumptions

If the electron density and collision frequency distributions are unknown, it is convenient to report an average electron density and collision frequency. Regardless of distribution and plasma extent, the measured phase and magnitude are assumed to correspond to line-integrated electron density and line-averaged electron collision frequency. The line-integrated electron density can then be converted into an average value through normalization by an estimated plasma length. Even if the plasma length measurement is not accurate, the reported average electron density is understood to be a line-integrated quantity that has been normalized by a quasi-arbitrary value. The calculated electron collision frequency, on the other hand, is assumed to be independent of the plasma extent (both distribution and length) so that its value is a true averaged quantity. These assumptions are evaluated here through the calculation of the electron collision frequency error caused by inputting the incorrect plasma length into Eq. (28) and the electron density error caused by using Eq. (28) in place of the integrated Eq. (27) for various electron density distributions with the same integrated electron density.

Figure 40 shows the impact of plasma length on the average electron collision frequency error for various incorrect plasma lengths for an electron density of 10^{19} m^{-3}, electron collision frequency of 10^{11} Hz, and plasma length of 0.1 m. The plasma condition values are representative of the RF ICP discharge. The electron collision frequency error was calculated as follows: An electron density, electron collision frequency, and plasma length were inputted into Eq. (28) to calculate the resulting magnitude and phase for a range of THz pulse frequencies. Equation (28) was then inverted to calculate the electron density and collision frequency at each THz pulse frequency for an incorrect plasma length

value with the magnitude and phase calculated from the input plasma length value. The input electron collision frequency was compared to the output electron collision frequency to determine the error caused by assuming the incorrect plasma length.

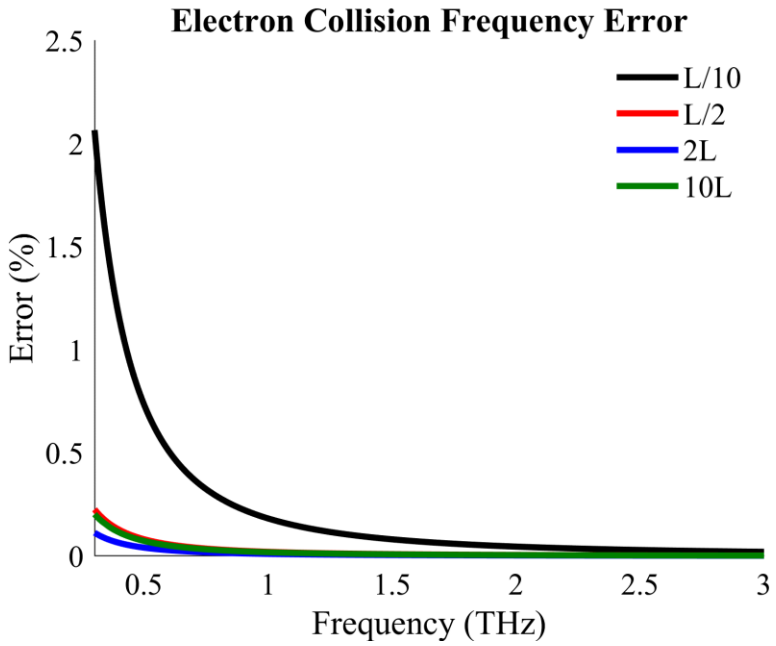

Figure 40 – Average electron collision frequency calculation error caused by the input of incorrect plasma length ($n_e = 10^{19}$ m^{-3}, $\nu = 10^{11}$ Hz, $L = 0.1$ m)

At the input conditions, even for plasma lengths incorrect by an order of magnitude, the error in calculated average electron collision frequency remains below 2% for almost all THz pulse frequencies. Plasma lengths incorrect by 50% produce negligibly small calculation errors of less than 0.1% for most THz pulse frequencies. Error increases with decreasing THz pulse frequency and becomes nonnegligible near plasma cut-off (discussed in Section 5.2.3). The results suggest that if the THz pulse frequency is not near its cut-off value (at which point detection above noise becomes infeasible anyway), the assumed

plasma distribution and length produce negligible errors in the average electron collision frequency calculation.

Strictly, these results only apply to the input plasma conditions and are not necessarily general. However, the large degree of insensitivity of computed electron collision frequency to order of magnitude changes to the input plasma length suggest that more realistic errors in input plasma length (~10%) will produce negligible electron collision frequency calculation error in laboratory plasma measurements.

The impact of the electron density distribution on the error of the calculated line-averaged electron density was computed for parabolic and linear distributions across a range of plasma conditions. The error is a function of the electron density, electron collision frequency, THz pulse frequency, plasma distribution, and plasma length. These parameters were therefore varied from a set of standard conditions to determine the impact of each on the error. Unless otherwise specified, the standard plasma conditions consist of a uniform electron density of 10^{19} m^{-3}, uniform electron collision frequency of 10^{11} Hz, and uniform plasma length of 0.1 m.

The impact of electron density distribution on the error of the calculated line-averaged electron density was calculated as follows: An input uniform electron density and plasma length were used to form parabolic and linear electron density distributions that span across the input plasma length and feature the same integrated electron density as the uniform distribution. The parabolic and linear electron density distributions were inputted into Eq. (27) (along with a uniform electron collision frequency) to determine the magnitude and phase corresponding to each distribution as a function of THz pulse frequency. Equation (28) was then inverted with these magnitude and phase values to

determine the line-averaged electron density and collision frequency calculated at each THz pulse frequency, under the incorrect assumption of a uniform plasma distribution. The error caused by assuming a uniform electron density distribution was calculated by comparing the input and output electron density values.

Figure 41 shows the three distributions for a uniform plasma density of 10^{19} m^{-3} spanning across a plasma length of 0.1 m (line-integrated density of 10^{18} m^{-2}).

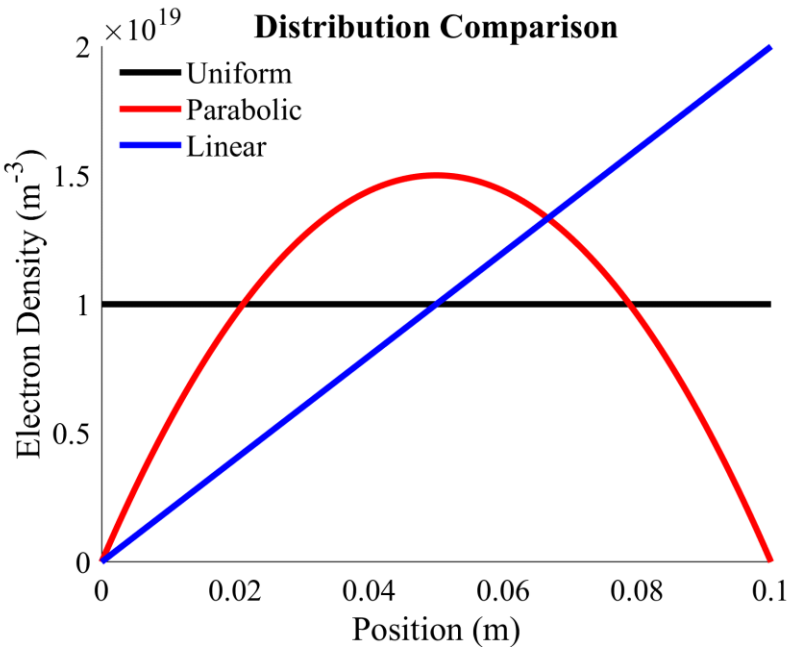

Figure 41 – Sample input electron density distributions ($n_e = 10^{19}$ m^{-3}, $L = 0.1$ m)

Figure 42, Figure 43, and Figure 44 show the parabolic electron density calculation error for various input uniform plasma densities, electron collision frequencies, and lengths, respectively. Figure 45, Figure 46, and Figure 47 show the same results for the linear distribution.

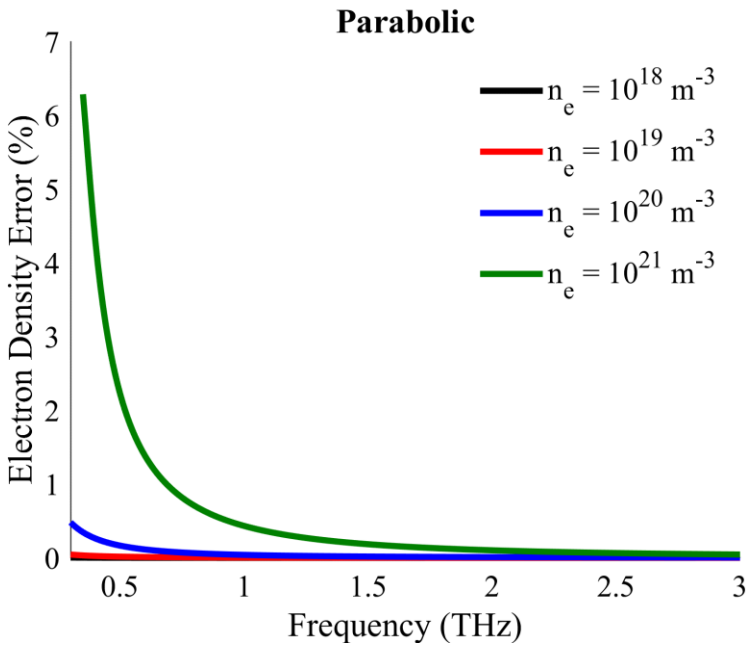

Figure 42 – Impact of electron density on electron density calculation error caused by parabolic density distribution ($\nu = 10^{11}$ Hz, $L = 0.1$ m)

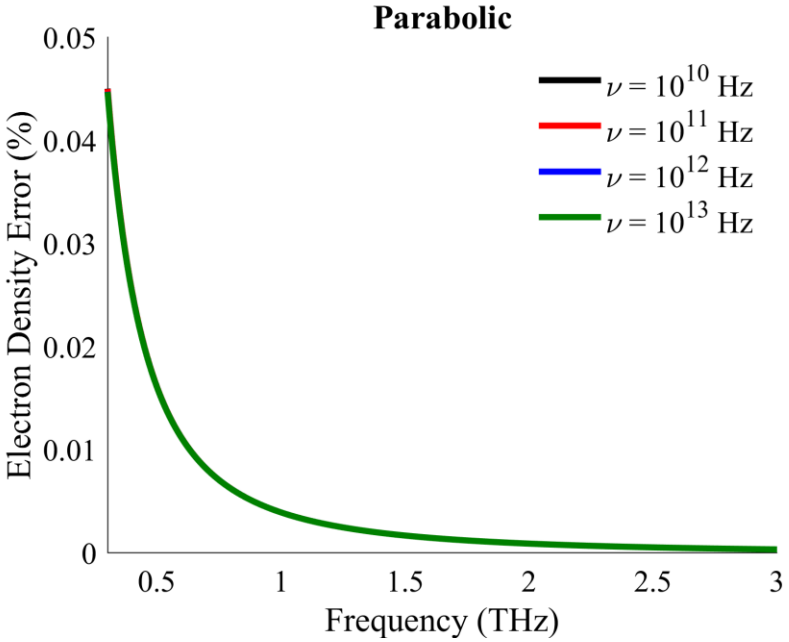

Figure 43 – Impact of electron collision frequency on electron density calculation error caused by parabolic density distribution ($n_e = 10^{19}$ m^{-3}, $L = 0.1$ m)

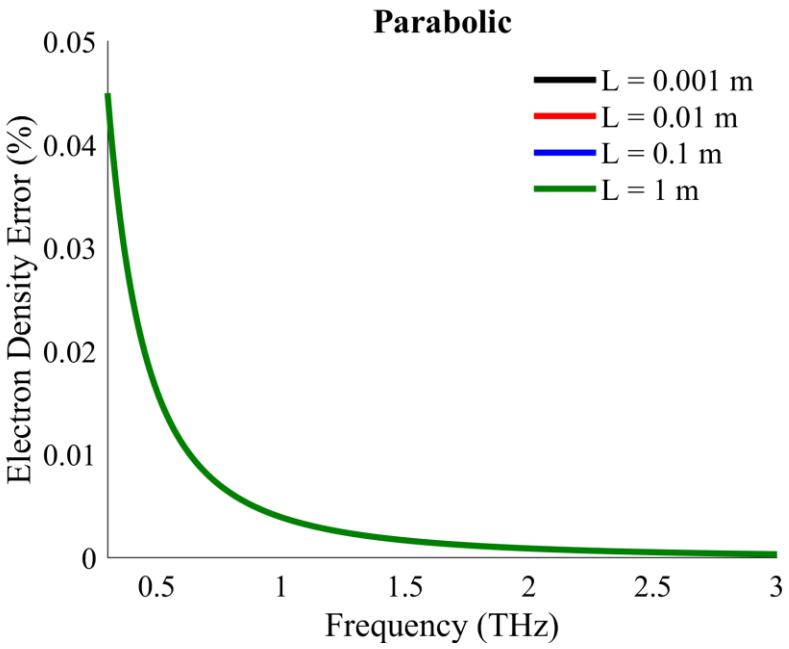

Figure 44 – Impact of plasma length on electron density calculation error caused by parabolic density distribution ($n_e = 10^{19}$ m^{-3} , $\nu = 10^{11}$ Hz)

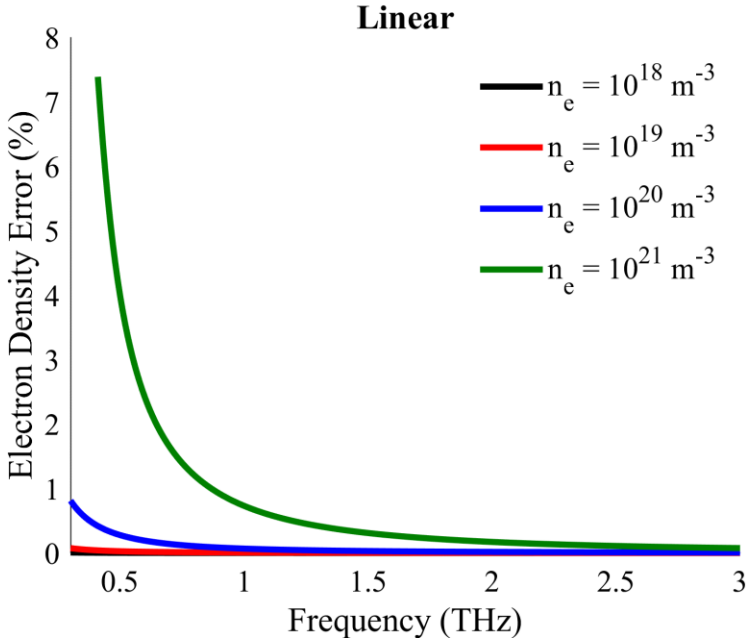

Figure 45 – Impact of electron density on electron density calculation error caused by linear density distribution ($\nu = 10^{11}$ Hz, $L = 0.1$ m)

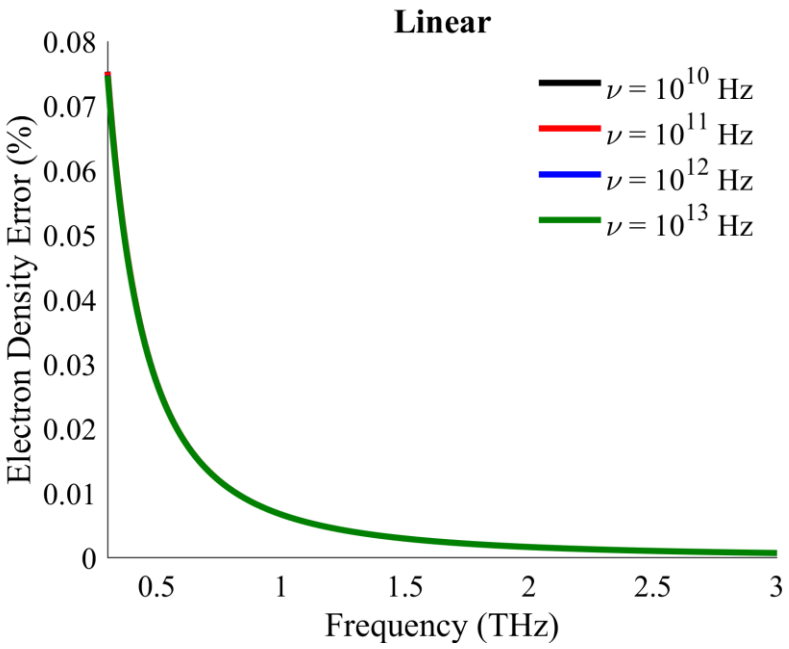

Figure 46 – Impact of electron collision frequency on electron density calculation error caused by linear density distribution ($n_e = 10^{19}$ m^{-3}, $L = 0.1$ m)

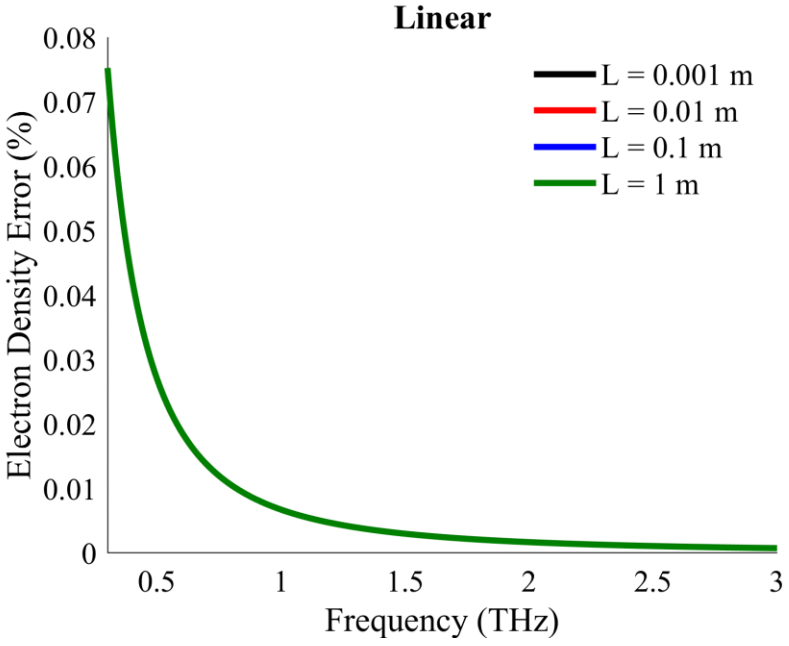

Figure 47 – Impact of plasma length on electron density calculation error caused by linear density distribution ($n_e = 10^{19}$ m^{-3} , $\nu = 10^{11}$ Hz)

For the cases plotted here, error in the line-averaged electron density calculation caused by the assumption of uniform electron density is typically below 0.1% and does not vary with length or average electron collision frequency. However, increasing the average electron density to 10^{21} m^{-3} produces a significant error (> 5%) at the lower THz pulse frequencies. This is because the validity of the line-averaged (and equivalently line-integrated) assumption requires that the electron density be primarily determined by the phase and that the phase vary linearly with the electron density. Because Eq. (31) describes this exact scenario, the line-averaged assumption is valid if the electron density is below the critical value given by Eq. (42).

As only two non-uniform distributions were analyzed for a finite set of measurement conditions, the results presented here are not strictly general. However, given the large differences in distribution shapes, the findings presented here are expected to be applicable to a broad range of possible laboratory plasma conditions. It should also be noted that distributions with more rapid changes in electron density (such as the exponential distribution) were analyzed but are not presented here. Distributions that feature large changes on scales of a few mm or smaller violate the WKB approximation and invalidate the governing equations presented in Section 2.2.

5.1.3 Impact of Electron Temperature and Applied Magnetic Field

The impacts of electron temperature and applied magnetic field are quantified here for the two specific cases discussed in Section 2.2.3. Case 1 is pulse propagation parallel to the applied magnetic field and Case 2 is pulse propagation perpendicular to the applied magnetic field, such that pulse polarization is parallel to the applied magnetic field. Propagation is a function of electron density, electron collision frequency, THz pulse

frequency, plasma length, electron temperature, and applied magnetic field. These parameters are therefore varied from a set of standard parameters to determine the impact of each on the propagating THz pulse. Each plot in this section shows the impact of varying two parameters in the presence of nonzero electron temperature and applied magnetic field. Though parameters are varied independently, it should be noted that, because nonvarying parameters are taken from a standard set, the results are not strictly general. However, the general trends and findings are expected to hold for a broad range of measurement conditions.

Nonvarying parameters are taken from the following standard set: electron temperature of 100 eV, applied magnetic field of 1 T, electron density of 10^{20} m^{-3}, electron collision frequency of 10^{11} Hz, plasma length of 1 m, and THz pulse frequency of 1 THz. The standard set was chosen to represent or exceed expected upper boundary values in EP plasma diagnostic scenarios, as well as clearly show the impact of the electron temperature and applied magnetic field.

5.1.3.1 Case 1: Pulse Propagation Parallel to Applied Magnetic Field

Case 1 is most easily analyzed by decomposing the linearly polarized THz electric field into left- and right-handed circularly polarized components to enable direct use of the complex plasma refractive index given in Eq. (32). If the pulse attenuation is small enough that the THz electric field does not become significantly elliptically polarized, the impact of the magnetic field is to rotate the linearly polarized electric field by a Faraday rotation angle (β) according to

$$\beta(\omega) = \frac{1}{2}|\Phi_l(\omega) - \Phi_r(\omega)|. \tag{43}$$

However, if one circularly polarized component is attenuated significantly more than another, the pulse becomes elliptically polarized. The ellipticity (τ) of the polarization is quantified here as

$$\tau(\omega) = 100 \times \left(1 - \frac{\min[A_l(\omega), A_r(\omega)]}{\max[A_l(\omega), A_r(\omega)]}\right) \tag{44}$$

so that $\tau = 0$ corresponds to linear polarization and $\tau = 100$ corresponds to circular polarization. Faraday rotation and pulse ellipticity produce errors in standard THz-TDS systems because such systems can only measure linear polarization in one axis. Faraday rotation produces a cosine loss error, whereas pulse ellipticity nonlinearly impacts error in a situation-specific manner.

The impact of plasma properties on Faraday rotation and pulse ellipticity is shown in the figures below. Figure 48 and Figure 49 show the impact of electron temperature and applied magnetic field; Figure 50 and Figure 51 show the impact of plasma length and applied magnetic field; Figure 52 and Figure 53 show the impact of electron density and applied magnetic field; Figure 54 and Figure 55 show the impact of electron collision frequency and applied magnetic field; and Figure 56 and Figure 57 show the impact of THz pulse frequency and applied magnetic field.

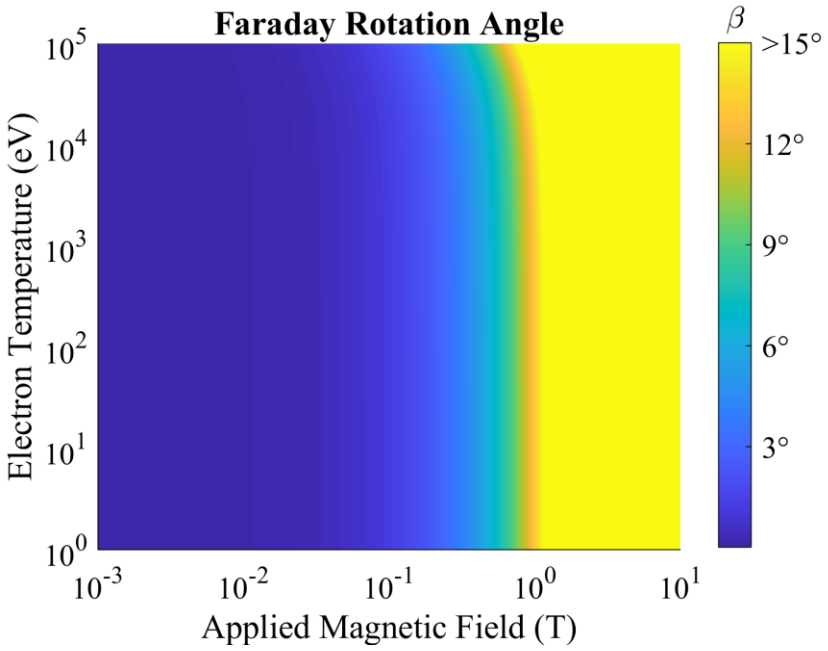

Figure 48 – Impact of electron temperature and applied magnetic field on Faraday rotation angle ($n_e = 10^{20}$ m^{-3}, $\nu = 10^{11}$ Hz, $\omega = 1$ THz, $L = 0.1$ m)

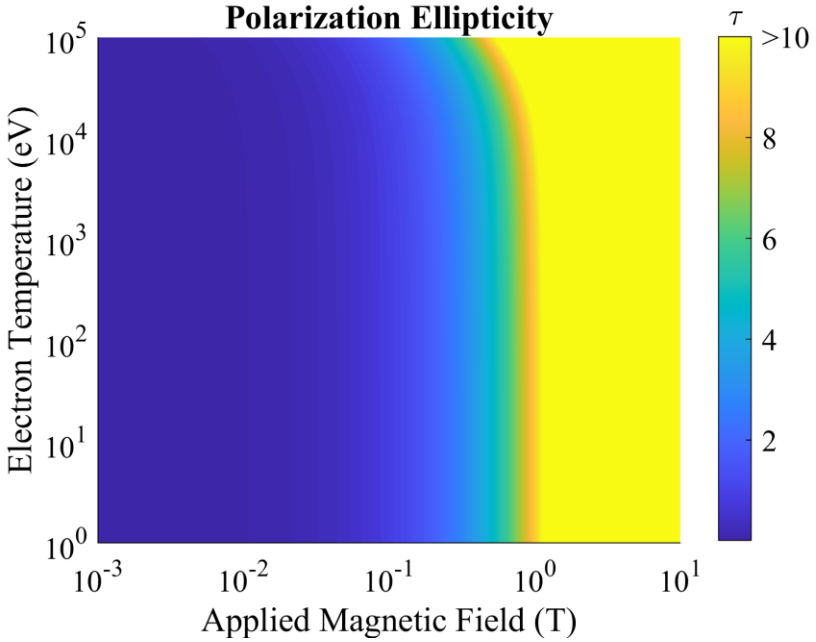

Figure 49 – Impact of electron temperature and applied magnetic field on polarization ellipticity ($n_e = 10^{20}$ m^{-3}, $\nu = 10^{11}$ Hz, $\omega = 1$ THz, $L = 0.1$ m)

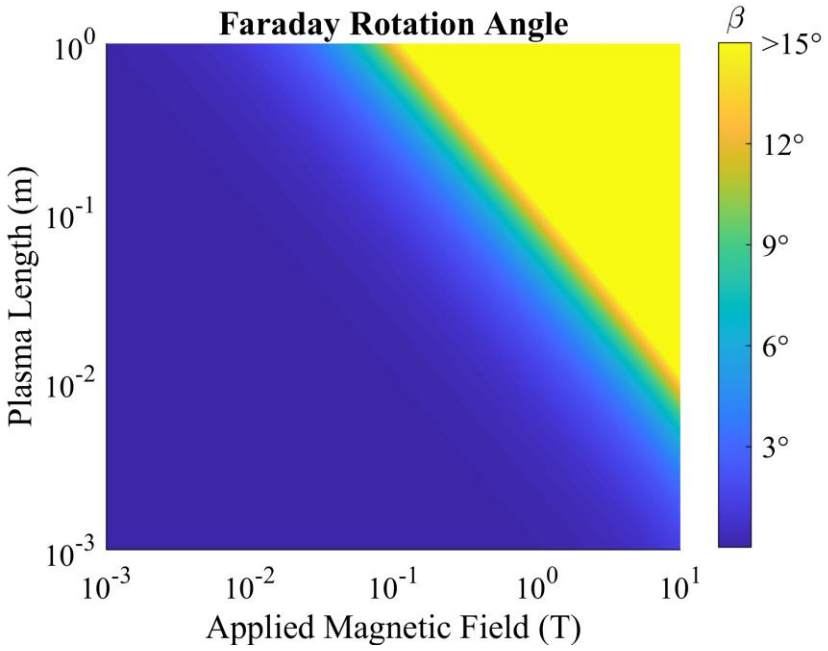

Figure 50 – Impact of plasma length and applied magnetic field on Faraday rotation angle ($T_e = 100$ eV, $n_e = 10^{20}$ m^{-3}, $\nu = 10^{11}$ Hz, $\omega = 1$ THz)

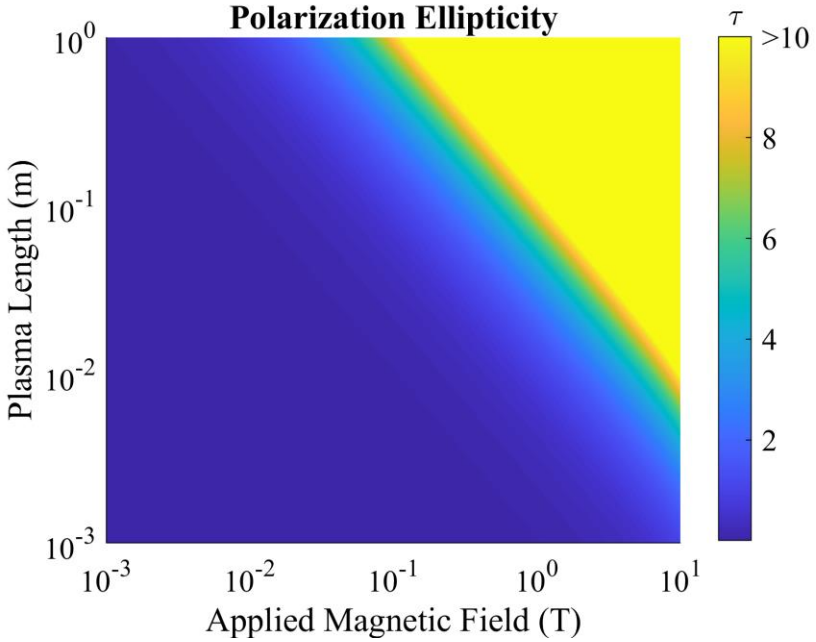

Figure 51 – Impact of plasma length and applied magnetic field on polarization ellipticity ($T_e = 100$ eV, $n_e = 10^{20}$ m^{-3}, $\nu = 10^{11}$ Hz, $\omega = 1$ THz)

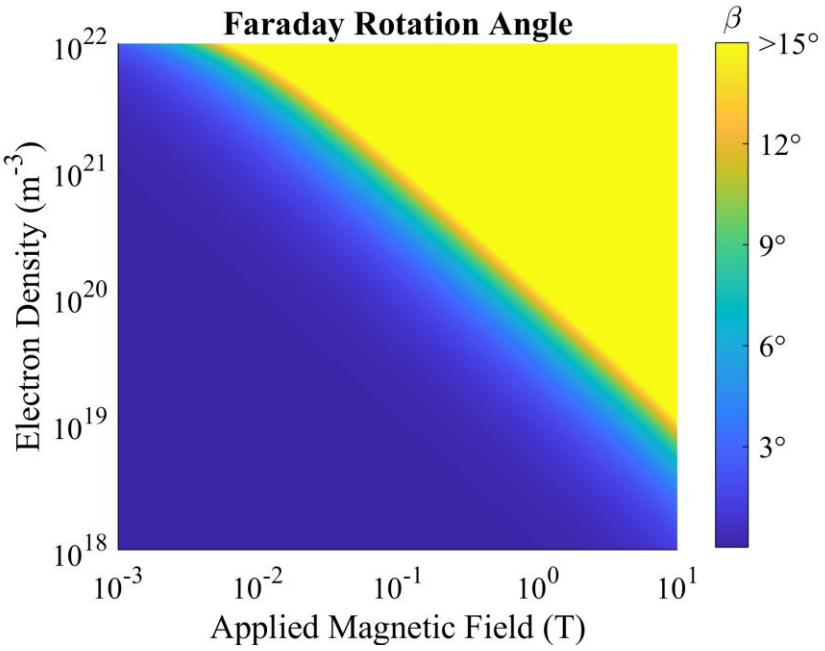

Figure 52 – Impact of electron density and applied magnetic field on Faraday rotation angle ($T_e = 100$ eV, $\nu = 10^{11}$ Hz, $\omega = 1$ THz, $L = 0.1$ m)

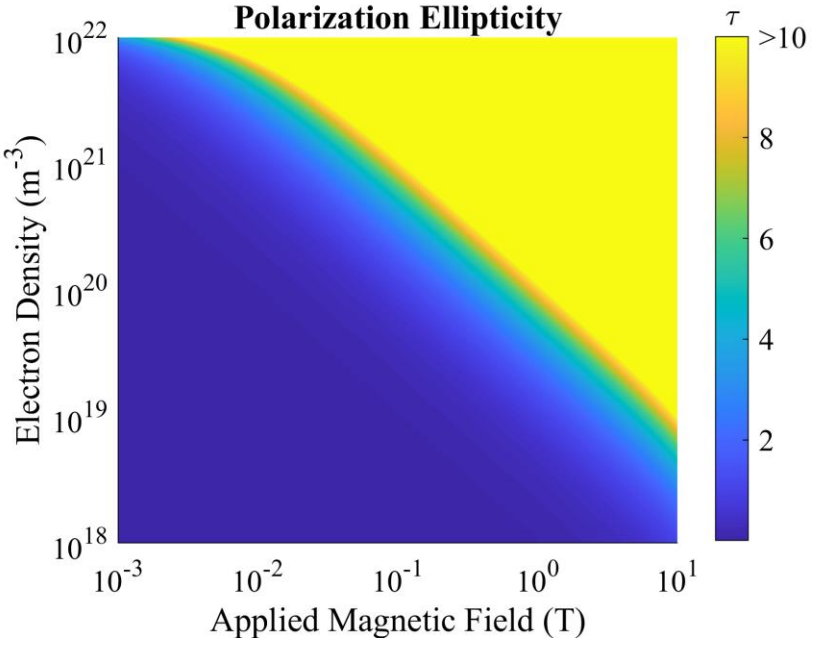

Figure 53 – Impact of electron density and applied magnetic field on polarization ellipticity ($T_e = 100$ eV, $\nu = 10^{11}$ Hz, $\omega = 1$ THz, $L = 0.1$ m)

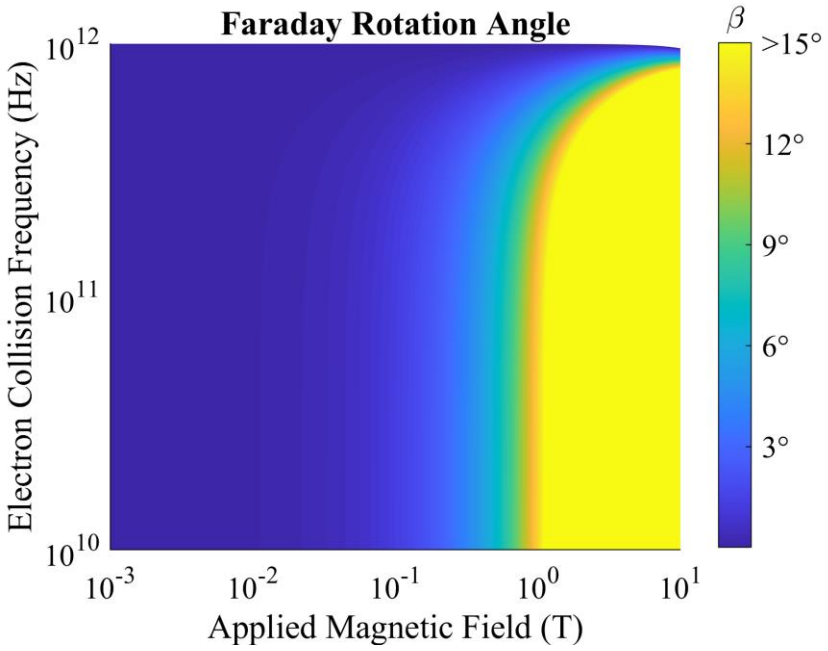

Figure 54 – Impact of electron collision frequency and applied magnetic field on Faraday rotation angle ($T_e = 100$ eV, $n_e = 10^{20}$ m^{-3}, $\omega = 1$ THz, $L = 0.1$ m)

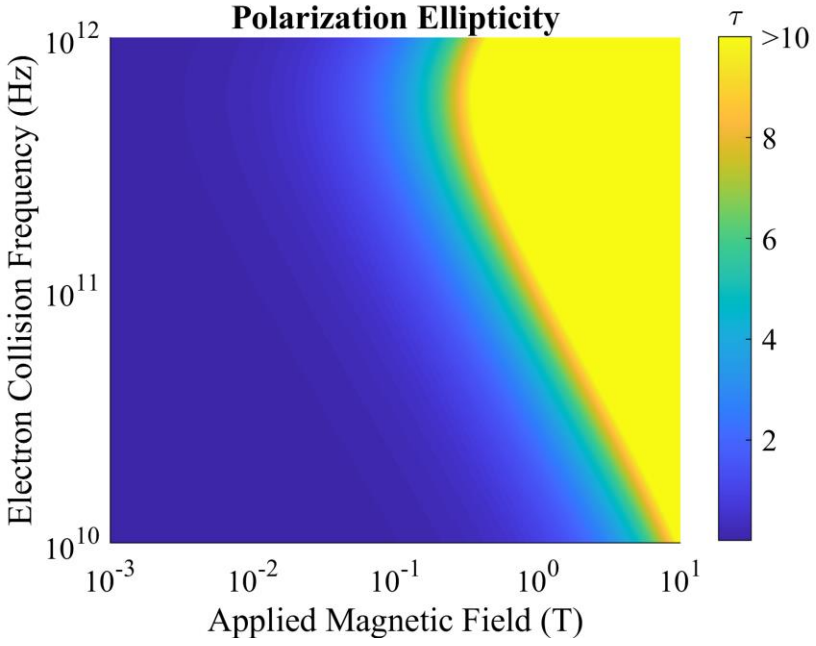

Figure 55 – Impact of electron collision frequency and applied magnetic field on polarization ellipticity ($T_e = 100$ eV, $n_e = 10^{20}$ m^{-3}, $\omega = 1$ THz, $L = 0.1$ m)

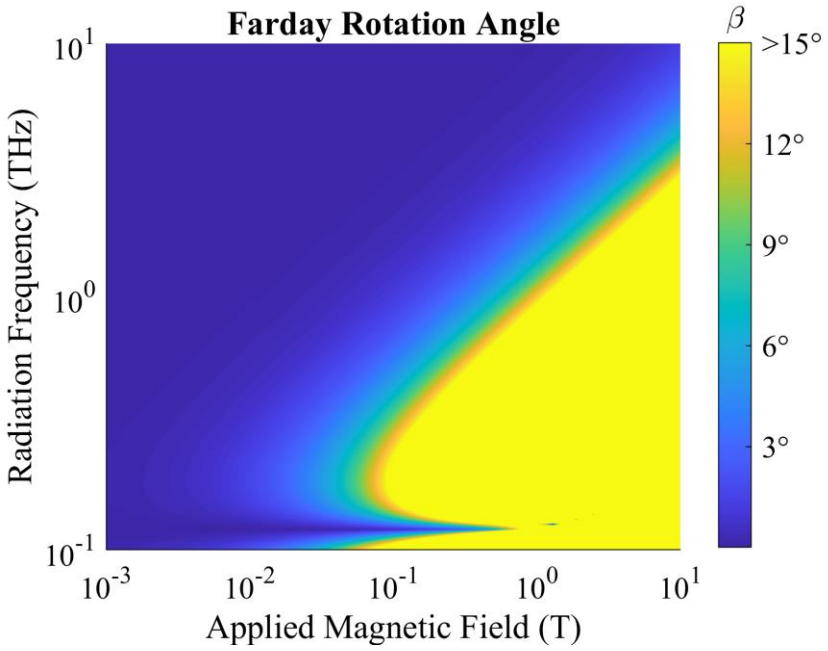

Figure 56 – Impact of THz pulse frequency and applied magnetic field on Faraday rotation angle ($T_e = 100$ eV, $n_e = 10^{20}$ m^{-3}, $\nu = 10^{11}$ Hz, $L = 0.1$ m)

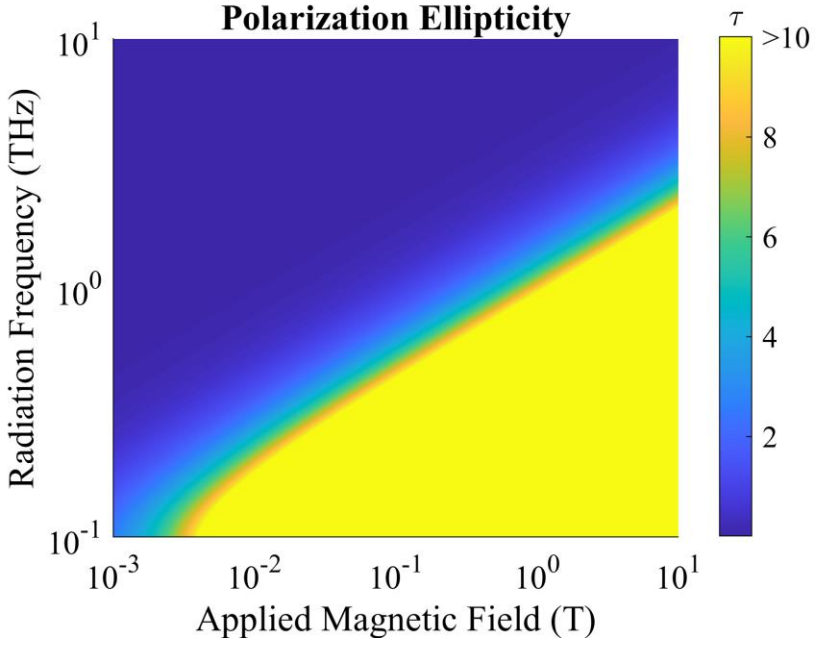

Figure 57 – Impact of THz pulse frequency and applied magnetic field on polarization ellipticity ($T_e = 100$ eV, $n_e = 10^{20}$ m^{-3}, $\nu = 10^{11}$ Hz, $L = 0.1$ m)

In each case, there exists a critical magnetic field (B_c) for which the Faraday rotation angle and/or polarization ellipticity rise relatively sharply with changes in the magnetic field. According to the results plotted above, this value is essentially independent of the electron temperature and electron collision frequency but varies with plasma length, electron density, and THz pulse frequency. These dependencies are expressed as

$$\begin{gathered} B_c(T_e) \sim a_1(L, n_e, \omega), \\ B_c(\nu) \sim a_1(L, n_e, \omega), \\ \log_{10}[B_c(L)] \sim -a_2(n_e, \omega)\log_{10}[L], \\ \log_{10}[B_c(n_e)] \sim -a_3(L, \omega)\log_{10}[n_e], \\ \text{and} \\ \log_{10}[B_c(\omega)] \sim a_4(L, n_e)\log_{10}[\omega], \end{gathered} \tag{45}$$

where each a is a positive constant that depends on the variables inside the parentheses.

The negative dependence of the critical magnetic field strength on plasma length and electron temperature is caused by the increase in pulse reshaping that occurs with increases in these values. The trend is similar to that for the simplified Eq. (31), where the phase is proportional to the plasma length and electron density. In this case, increasing the plasma length and electron density exacerbates the differences in the phases of the left- and right-circularly polarized components of the THz pulse and leads to greater changes in polarization. Similarly, as the THz pulse frequency is inversely related to the phase in

Eq. (31), increases in the THz pulse frequency minimize differences in the left- and right-circularly polarized components of the THz pulse and lead to smaller changes in polarization.

5.1.3.2 Case 2: Pulse Propagation Perpendicular to Applied Magnetic Field with Polarization Parallel to Applied Magnetic Field

THz pulse propagation in Case 2 changes the transfer function magnitude and phase but does not impact the pulse polarization. Therefore, Case 2 results are presented as errors in the calculated electron density and collision frequency incurred from failure to account for electron temperature and magnetic field effects. Error analysis was performed as follows: the magnitude and phase of the THz-TDS transfer function were determined with the complex plasma refractive index given in Eq. (33) for input electron density and collision frequency. Equation (28), which does not account for electron temperature or magnetic field effects, was then numerically inverted with the calculated magnitude and phase to determine the electron density and collision frequency. The error incurred for failure to account for the electron temperature and magnetic field was quantified by comparing the input electron density and collision frequency to the output electron density and collision frequency.

The impact of plasma properties on the electron density and collision frequency error is shown in the figures below. Figure 58 and Figure 59 show the impact of electron temperature and applied magnetic field; Figure 60 and Figure 61 show the impact of electron temperature and plasma length; Figure 62 and Figure 63 show the impact of electron temperature and electron density; Figure 64 and Figure 65 show the impact of

electron temperature and electron collision frequency; and Figure 66 and Figure 67 show the impact of electron temperature and THz pulse frequency.

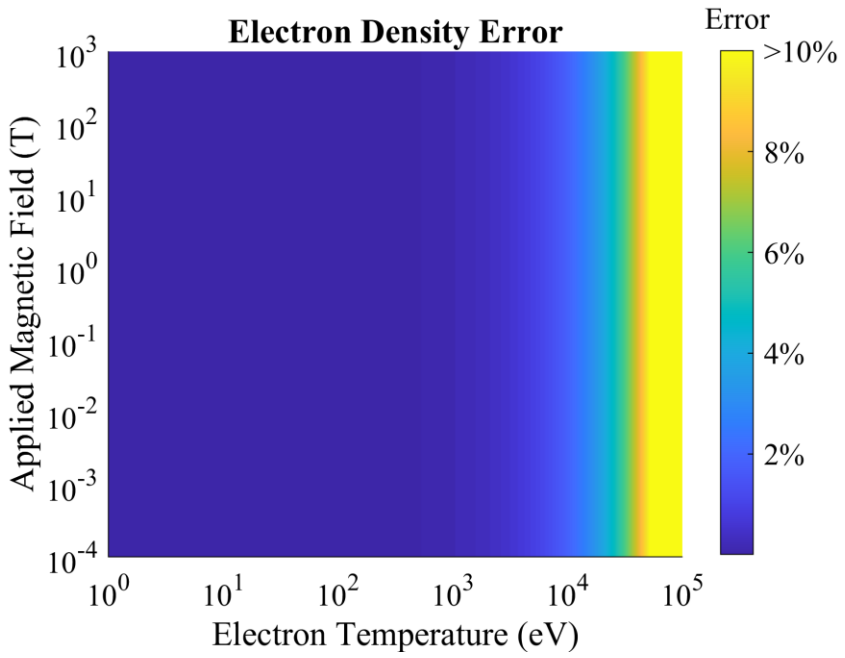

Figure 58 – Impact of electron temperature and applied magnetic field on electron density error ($n_e = 10^{20}$ m^{-3}, $\nu = 10^{11}$ Hz, $\omega = 1$ THz, $L = 0.1$ m)

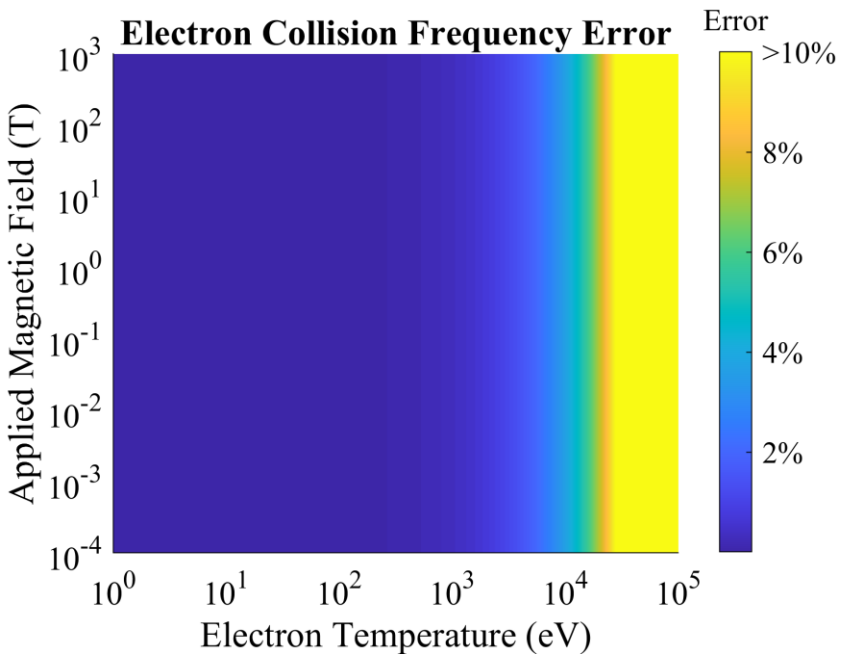

Figure 59 – Impact of electron temperature and applied magnetic field on electron collision frequency error ($n_e = 10^{20}$ m^{-3}, $\nu = 10^{11}$ Hz, $\omega = 1$ THz, $L = 0.1$ m)

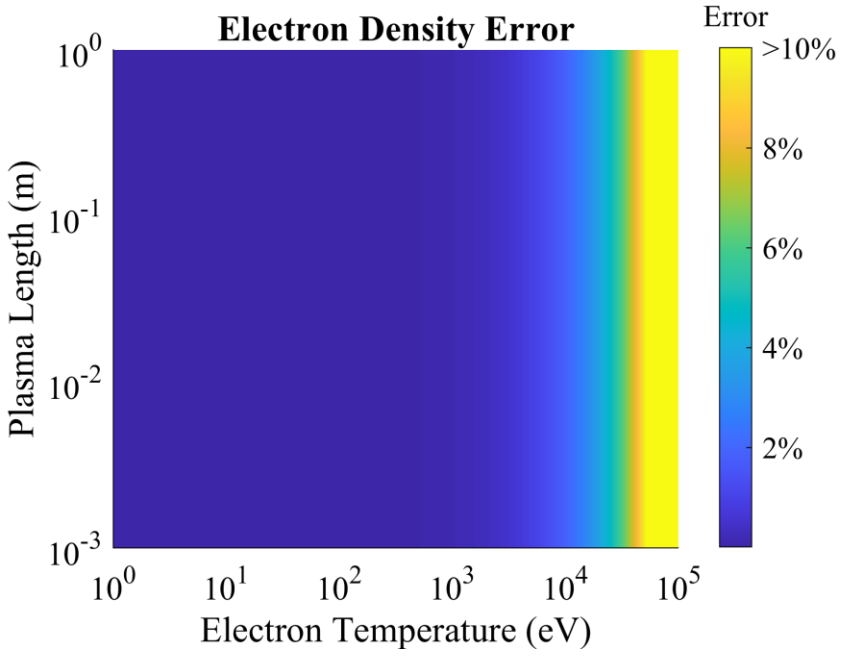

Figure 60 – Impact of electron temperature and plasma length on electron density error ($B = 1$ T, $n_e = 10^{20}$ m^{-3}, $\nu = 10^{11}$ Hz, $\omega = 1$ THz)

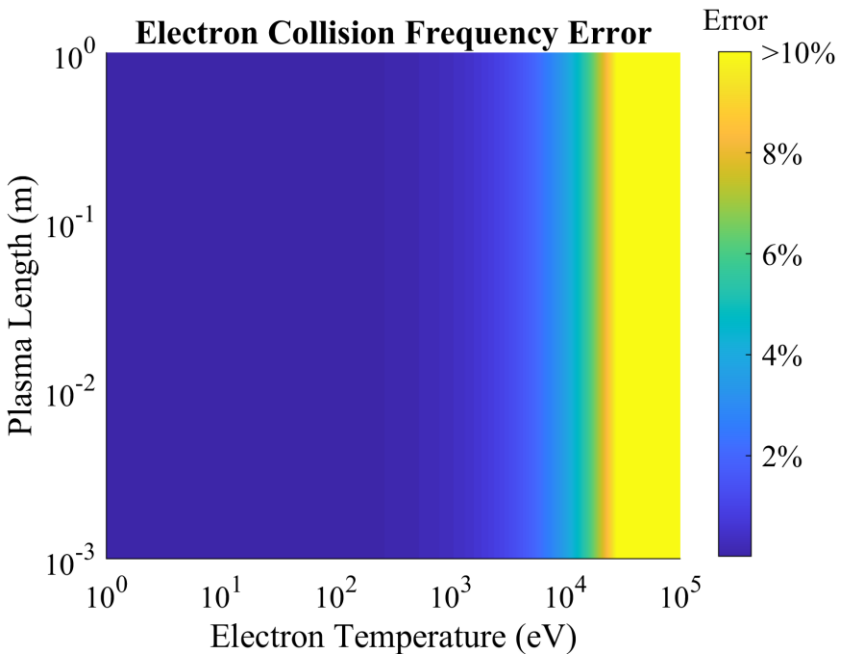

Figure 61 – Impact of electron temperature and plasma length on electron collision frequency error ($B = 1$ T, $n_e = 10^{20}$ m^{-3}, $\nu = 10^{11}$ Hz, $\omega = 1$ THz)

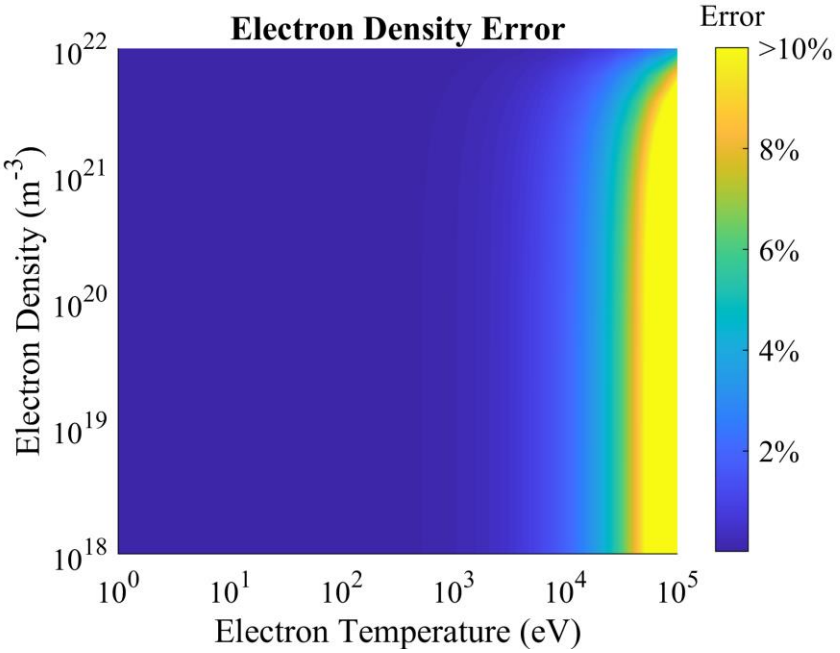

Figure 62 – Impact of electron temperature and electron density on electron density error ($B = 1$ T, $\nu = 10^{11}$ Hz, $\omega = 1$ THz, $L = 0.1$ m)

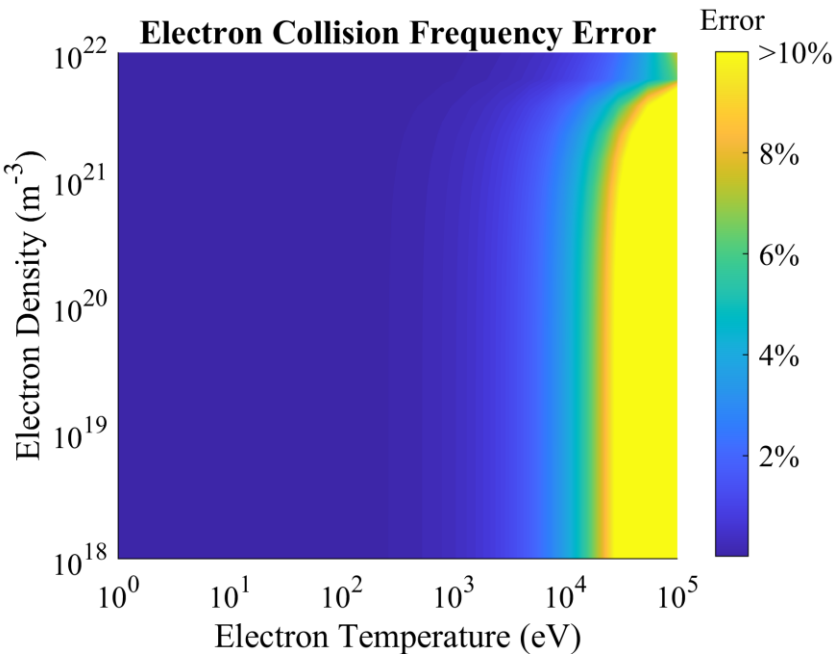

Figure 63 – Impact of electron temperature and electron density on electron collision frequency error ($B = 1$ T, $\nu = 10^{11}$ Hz, $\omega = 1$ THz, $L = 0.1$ m)

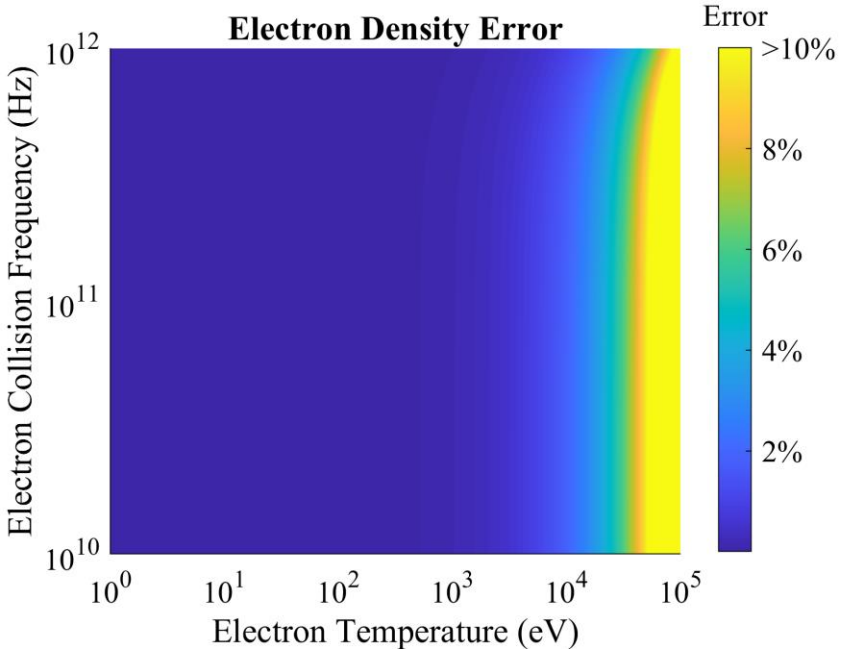

Figure 64 – Impact of electron temperature and electron collision frequency on electron density error ($B = 1$ T, $n_e = 10^{20}$ m^{-3}, $\omega = 1$ THz, $L = 0.1$ m)

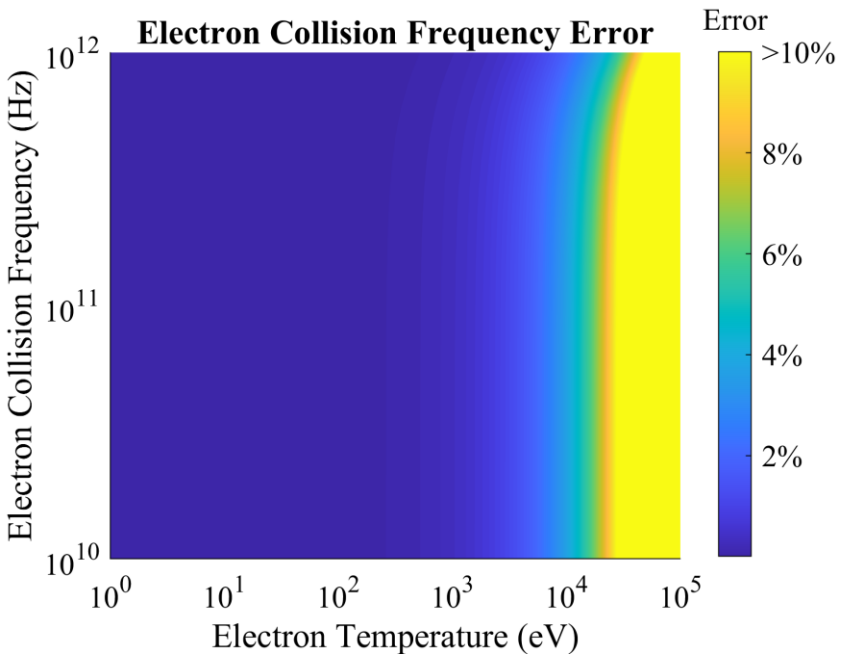

Figure 65 – Impact of electron temperature and electron collision frequency on electron collision frequency error ($B = 1$ T, $n_e = 10^{20}$ m^{-3}, $\omega = 1$ THz, $L = 0.1$ m)

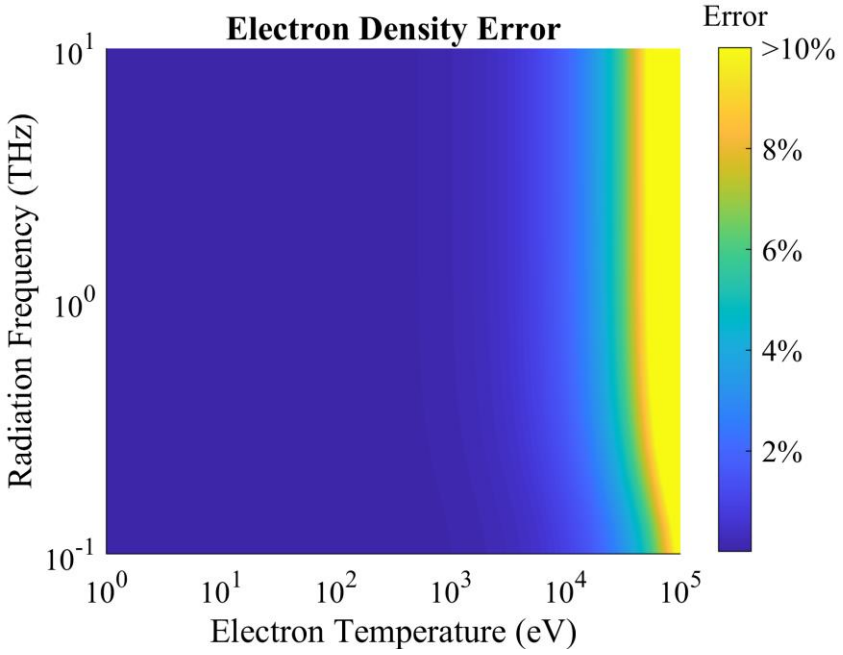

Figure 66 – Impact of electron temperature and THz pulse frequency on electron density error ($B = 1$ T, $n_e = 10^{20}$ m^{-3}, $\nu = 10^{11}$ Hz, $L = 0.1$ m)

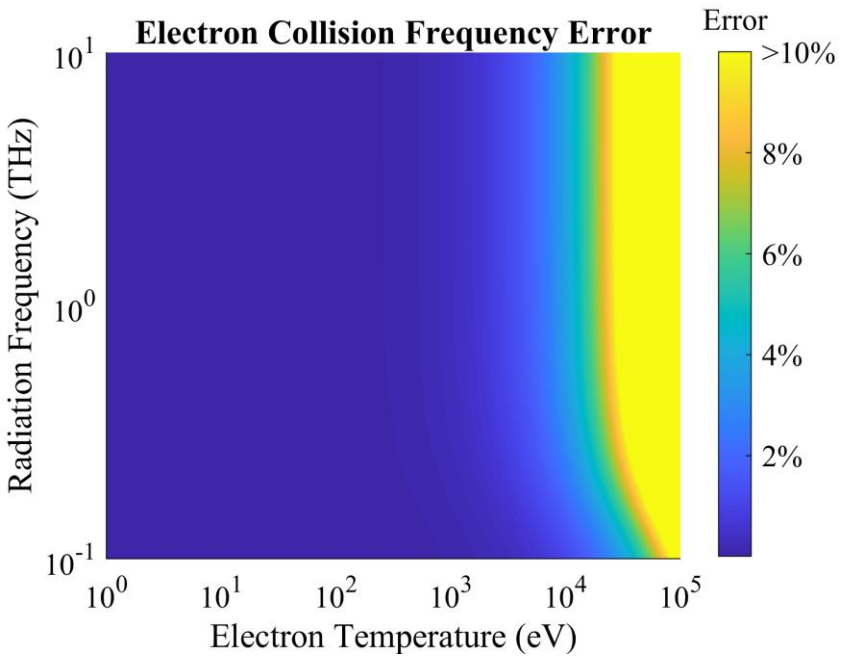

Figure 67 – Impact of electron temperature and THz pulse frequency on electron collision frequency error ($B = 1$ T, $n_e = 10^{20}$ m^{-3}, $\nu = 10^{11}$ Hz, $L = 0.1$ m)

For the cases plotted above, error in the calculated electron density and collision frequency depends strongly on the electron temperature but is virtually independent of all other factors. This is the case because setting the electron temperature to zero in Eq. (33) recovers the electron temperature- and magnetic field-independent complex refractive index given by Eq. (21). Therefore, the electron temperature is the factor that seeds differences between Eq. (21) and Eq. (33). The critical electron temperature at which error begins to grow beyond 2% and becomes nonnegligible is given by

$$T_{e,c} \sim 10^4 \text{ eV}. \tag{46}$$

5.2 Measurable Electron Density and Collision Frequency

This section quantifies measurable plasma property limits and investigates the relationship between these limits and THz-TDS system properties. Maximum limits exist where the electron density and collision frequency are large enough to attenuate the THz pulse sufficiently that the transmitted signal strength is equal to the noise floor at all THz frequencies. Minimum limits are equal to the minimum resolvable electron density and collision frequency.

5.2.1 Definitions of "Resolvable" and "Measurable"

In the absence of large electron temperatures and applied magnetic fields (the impact of which are evaluated in Section 5.1.3), Eq. (28) relates the phase and magnitude of the THz-TDS transfer function to the average plasma electron density and collision frequency. The minimum resolvable electron density and collision frequency vary with THz frequency and are functions of the frequency-dependent minimum resolvable phase and magnitude change.

The term "resolvable" lacks a precise definition because uncertainty varies continuously and can be defined above and below arbitrary "resolution" limits. Therefore, it is necessary to impose definitions for the resolvable phase and magnitude change (Φ_{min} and ΔA_{min}). So that the resolution limits correspond to approximately 100% uncertainty, they are defined as

$$|\Phi_{min}(\omega)| = \omega\delta t \ni \mathrm{SNR}_{\mathrm{sam}}(\omega) \geq 2$$

and (47)

$$\Delta A_{min}(\omega) = [\mathrm{SNR}_{\mathrm{ref}}(\omega)]^{-1},$$

where δt is the temporal resolution of the THz pulse, $\mathrm{SNR}_{\mathrm{sam}}(\omega)$ is the spectrum magnitude SNR of the sample pulse, $\mathrm{SNR}_{\mathrm{ref}}(\omega)$ is the spectrum magnitude SNR of the reference pulse, and ω is the THz pulse angular frequency. The spectrum magnitude SNR is equal to the spectrum magnitude divided by the maximum value of the noise floor. The noise floor is defined as the peak measured signal at frequencies well outside the range of resolvable THz pulse frequencies (> 6 THz).

The relationships for the minimum resolvable phase and magnitude change are derived from the definitions of the phase and magnitude. A phase of 2π corresponds to the period of a wave, so the minimum resolvable phase is equal to the resolvable fraction of the period multiplied by 2π. Because the THz radiation frequency is equal to the inverse of its period, the minimum resolvable phase may also be expressed as the THz pulse temporal resolution multiplied by the THz pulse angular frequency. As noted in Eq. (47), the SNR of the sample spectrum is assumed to have a value of at least 2; experience has shown that, otherwise, the THz frequency is unresolvable and necessary phase corrections are unreliable.

The magnitude is equal to the real portion of the ratio of the sample and reference spectra. Therefore, changes in the magnitude induced by the plasma are only resolvable if they are larger than the reference spectrum noise floor. This definition assumes the noise

floor of the sample spectrum is approximately equal to that of the reference spectrum. Experience has shown this to be a valid approximation.

An electron density and collision frequency pair is considered "measurable" here if the input of these values into Eq. (28) produces phase and magnitude values that satisfy

$$|\Phi(\omega)| > |\Phi_{min}(\omega)|$$

and (48)

$$1 - \Delta A_{min}(\omega) > \Delta A(\omega) > \Delta A_{min}(\omega)$$

for at least one THz pulse frequency with $\mathrm{SNR}_{\mathrm{sam}}(\omega) \geq 2$. These definitions ensure the plasma alters the THz pulse to a resolvable degree without attenuating it beyond detectability.

Measurement of the collision frequency requires that both the phase and magnitude be measurable; however, for a collision frequency too small to be resolved, the electron density may be determined from phase information alone via Eq. (31). It is therefore possible for a set of plasma conditions to produce one of three measurability outcomes: 1) the electron density and collision frequency are both measurable, 2) the electron density is measurable and the electron collision frequency is not measurable, and 3) neither the electron density nor collision frequency is measurable.

5.2.2 Measurement Capability Maps

Two types of measurement capability maps are presented here: one for an ideal system (Section 5.2.2.1) and one for the real system discussed in Chapter 3

(Section 5.2.2.2). The ideal system is assumed to have simultaneous access to all commercially available PCAs, the commercially available delay line with the highest position precision, and the commercially available ultrafast laser with the shortest laser pulses. These attributes give the ideal system the ability to continuously resolve reference pulse frequencies ranging from 0.01 to 5 THz with SNR better than 20:1 and to resolve the THz pulse with 10 fs resolution [74]. The real system has a THz pulse resolution of approximately 50 fs and experimentally quantified SNR at the discrete frequencies measured in a real THz pulse. Maps were generated by calculating the magnitude and phase of the THz-TDS transfer function with Eq. (28) and comparing these values to the definitions given by Eq. (48).

5.2.2.1 Ideal System

Figure 68, Figure 69, Figure 70, and Figure 71 show the measurement capability map for uniform plasma lengths of 1 m, 0.1 m, 0.01 m, and 0.001 m, respectively. In each map, the yellow region indicates that both electron density and collision frequency are resolvable, the teal region indicates that only the electron density is measurable, and the purple region indicates that neither the electron density nor collision frequency is measurable.

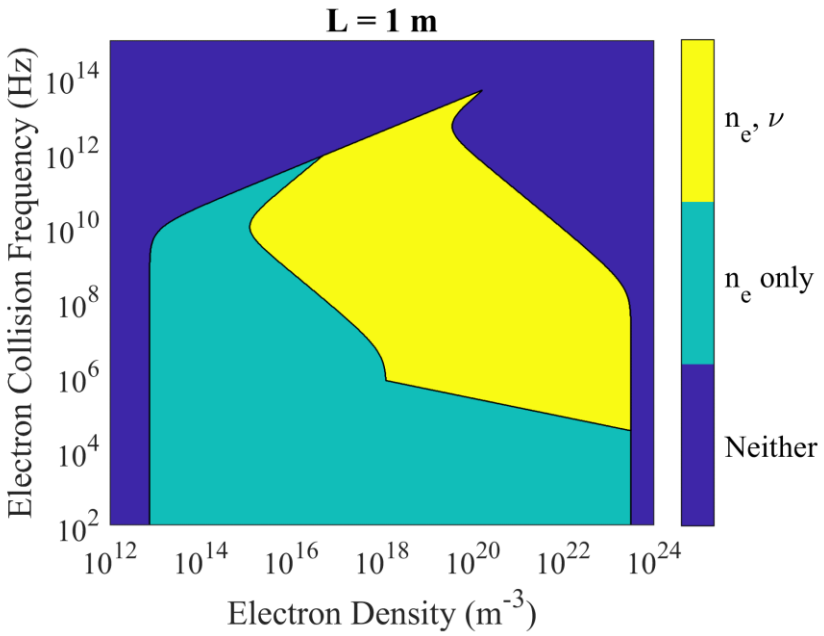

Figure 68 – Measurement capability map of an ideal system for a plasma length of 1 m

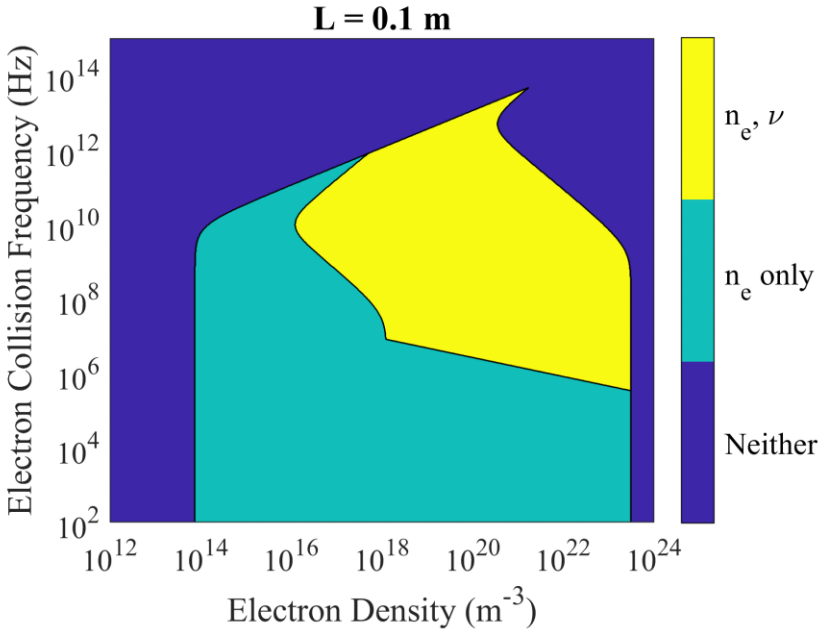

Figure 69 – Measurement capability map of an ideal system for a plasma length of 0.1 m

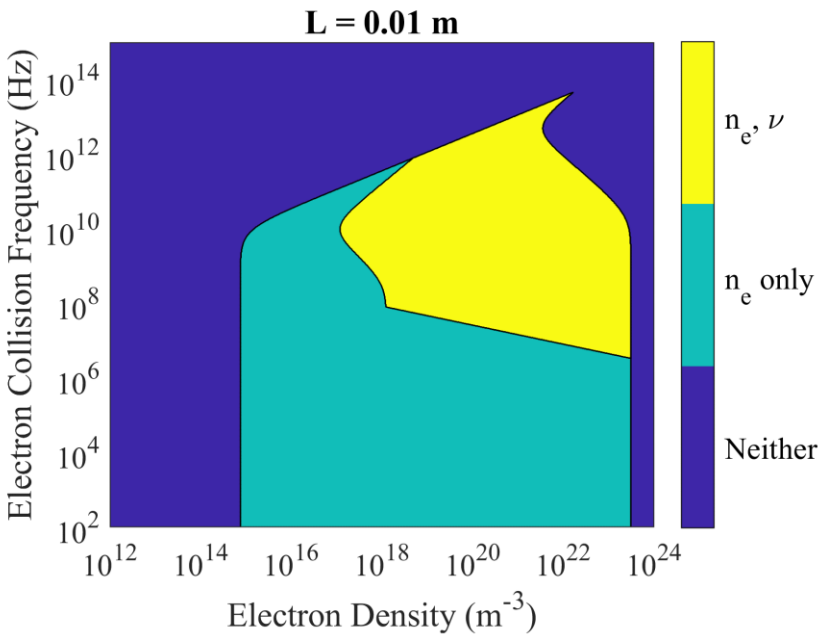

Figure 70 – Measurement capability map of an ideal system for a plasma length of 0.01 m

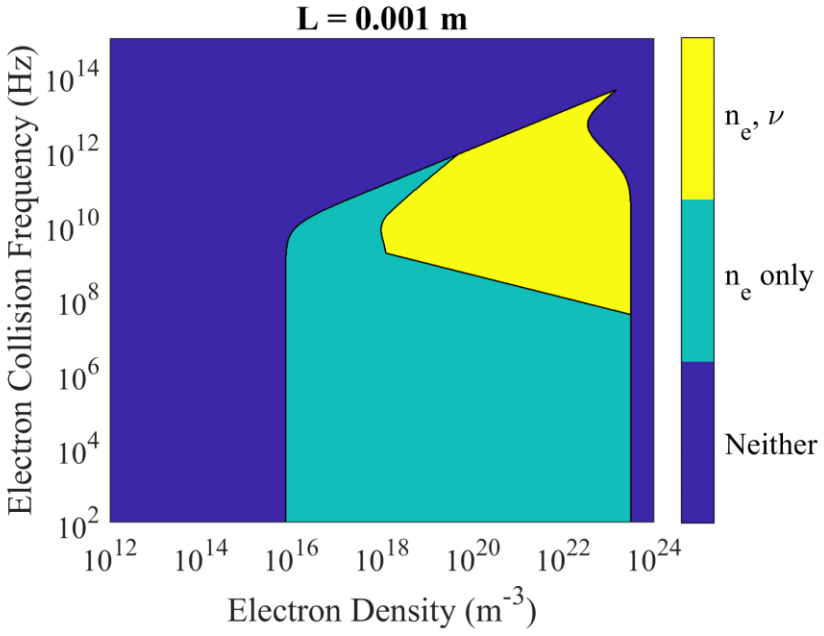

Figure 71 – Measurement capability map of an ideal system for a plasma length of 0.001 m

Resolvable electron density limits vary as a function of plasma length. Increasing the plasma length enables the resolution of lower electron densities and impacts the upper measurable limit at larger electron collision frequencies. Resolvable electron densities range from approximately 10^{13} to 10^{23} m^{-3} for a plasma length of 1 m and from 10^{16} to 10^{23} m^{-3} for a plasma length of 0.001 m.

The resolvable electron collision frequency varies with both length and electron density. At the electron density with the largest spread of resolvable collision frequencies, these values range from 10^{5} to 10^{13} Hz for a plasma length of 1 m and 10^{8} to 10^{13} Hz for a plasma length of 0.001 m. Section 5.2.3 further investigates the impact of THz-TDS system parameters on the measurable parameter limits.

5.2.2.2 Real System

Figure 72 shows the real THz-TDS system measurement capability map for a uniform plasma length of 0.1 m (approximately equal to the length of the RF ICP). The yellow region indicates that both electron density and collision frequency are resolvable, the teal region indicates that only the electron density is measurable, and the purple region indicates that neither the electron density nor collision frequency is measurable.

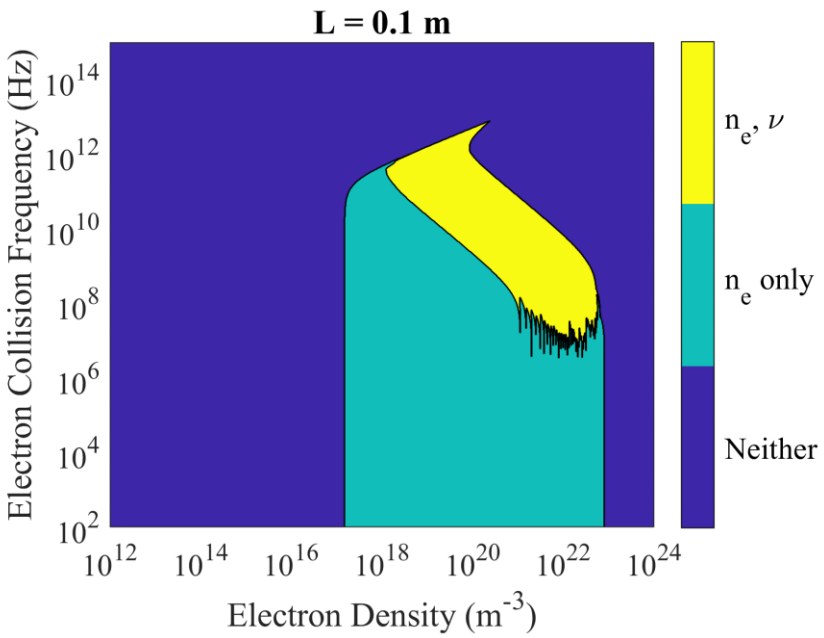

Figure 72 – Measurable line-averaged electron densities and frequencies with the real THz-TDS system for a plasma length of 0.1 m

The resolvable electron density ranges from 10^{17} to 10^{22} m^{-3} and, depending on the electron density value, the resolvable electron collision frequency ranges from 10^{7} to 10^{13} Hz. Compared to the ideal system operating with the same plasma length, the minimum resolvable electron density is increased by three orders of magnitude and the maximum resolvable electron density is decreased by an order of magnitude. These performance differences are caused by the real system's smaller range of resolvable reference THz pulse frequencies (approximately 0.2 to 2.6 THz) and lower pulse temporal resolution (50 fs). The jagged features visible on the teal and yellow boundary in Figure 72 are caused by the discrete nature of the resolvable THz frequencies. All boundaries are smooth for the ideal system maps because the ideal system is assumed to have access to a continuous range of frequencies.

5.2.3 Map Boundaries

5.2.3.1 Left Boundary

The left boundary is the leftmost demarcation of the purple and either teal or yellow regions and therefore serves as a boundary between resolvable plasma parameters and irresolvably small plasma parameters. The boundary can be divided into two regions: one for which the impact of the electron collision frequency can be neglected and one for which the boundary varies as a function of the electron collision frequency. As discussed in Section 5.1.1, Eq. (31) is a good approximation of the relationship between the phase and electron density if the electron collision frequency is at least an order of magnitude smaller than the THz radiation frequency and if the THz radiation frequency is an order of magnitude smaller than the plasma frequency. Consequently, the figures in Section 5.2.2 show that the minimum resolvable electron density does not vary with collision frequency if the minimum resolvable THz frequency is approximately an order of magnitude or greater than the collision frequency.

Inserting the minimum resolvable phase relation from Eq. (47) into Eq. (31) yields

$$n_{e,min} = \frac{2\omega^2 \delta t \epsilon_0 m_e c}{e^2 L}, \tag{49}$$

where $n_{e,min}$ is the minimum resolvable electron density. Figure 73 plots the minimum resolvable electron density as a function of frequency with Eq. (49) at several THz pulse temporal resolution values in a uniform plasma length of 0.1 m. Figure 74 plots the

minimum resolvable electron density as a function of frequency with Eq. (49) at several uniform plasma lengths for a THz pulse temporal resolution of 50 fs.

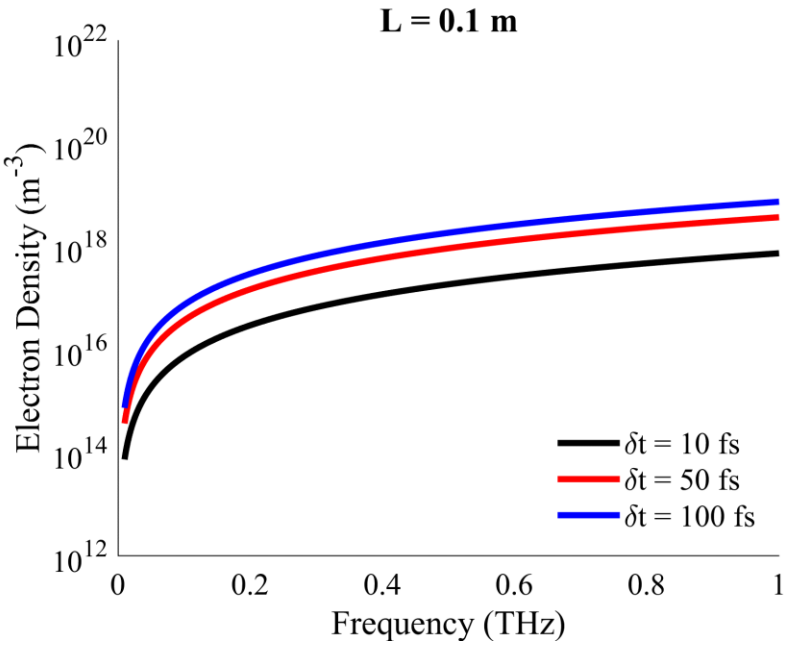

Figure 73 – Minimum resolvable electron density for a plasma length of 0.1 m

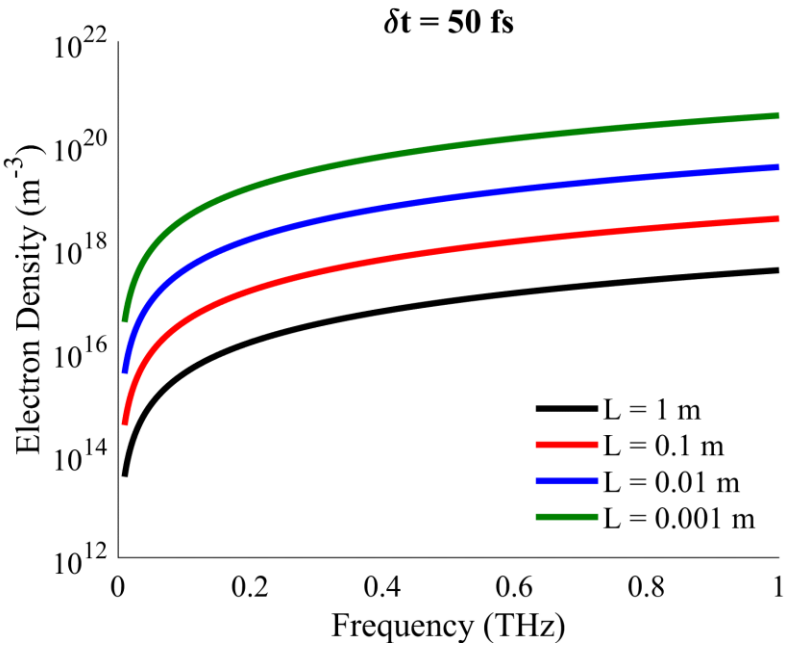

Figure 74 – Minimum resolvable electron density for a THz pulse resolution of 50 fs

The minimum resolvable electron density is inversely proportional to the plasma length and directly proportional to the THz pulse temporal resolution and the square of the THz pulse frequency. Minimizing the lowest resolvable THz pulse frequency provides the most efficient mechanism for increasing the electron density resolution.

In the other region, for which the electron collision frequency is of the same order of magnitude or greater than the THz pulse frequency, the left boundary varies as a function of the electron collision frequency and Eq. (49) does not apply. The phase in this region is inversely related to the electron collision frequency according to Eq. (28), so increases in the electron collision frequency decrease the phase. The result, as demonstrated in the figures of Section 5.2.2, is that the minimum resolvable electron density decreases with electron collision frequency. The maps indicate a linear relationship between the logarithm of the electron collision frequency and the logarithm of the minimum electron density for

most of the region. Trade studies demonstrated that the slope of the relationship is insensitive to changes in minimum resolvable THz frequency, plasma length, and THz pulse temporal resolution. The minimum resolvable electron density in this region is therefore approximately given by

$$\log_{10} n_{e,min} \approx 2 \log_{10} \nu + a, \tag{50}$$

where a is the intercept determined by the start of the linear region.

An inner left boundary separates the yellow and teal regions and therefore serves as the boundary between measurement of both electron density and collision frequency and electron density alone. This boundary shape varies nonlinearly with many factors, so no simple relationship describes it.

5.2.3.2 Right Boundary

The right boundary is the rightmost demarcation of the purple and either teal or yellow regions and therefore serves as the boundary between measurable plasma parameters and immeasurably large plasma parameters. As is the case for the left boundary, two regions exist for the right boundary: one region that is independent of the electron collision frequency and one region that varies with the electron collision frequency. In the independent region, the maximum measurable electron density is governed by the "cut-off" condition for which the square of the plasma frequency approaches the value of the maximum resolvable THz pulse frequency. In this case, the electron collision frequency is small enough that the real part of the plasma dielectric constant given in Eq. (19) approaches zero and the plasma no longer behaves like a dielectric. Figure 75 plots the

magnitude of the THz-TDS transfer function for 5 THz near plasma cut-off for an electron collision frequency of 10^6 Hz and plasma length of 1 m. As shown in the figure, the sample pulse magnitude decreases sharply within a small range of electron density values. The electron density value for which the transfer function magnitude forms a vertical line is called the "critical density."

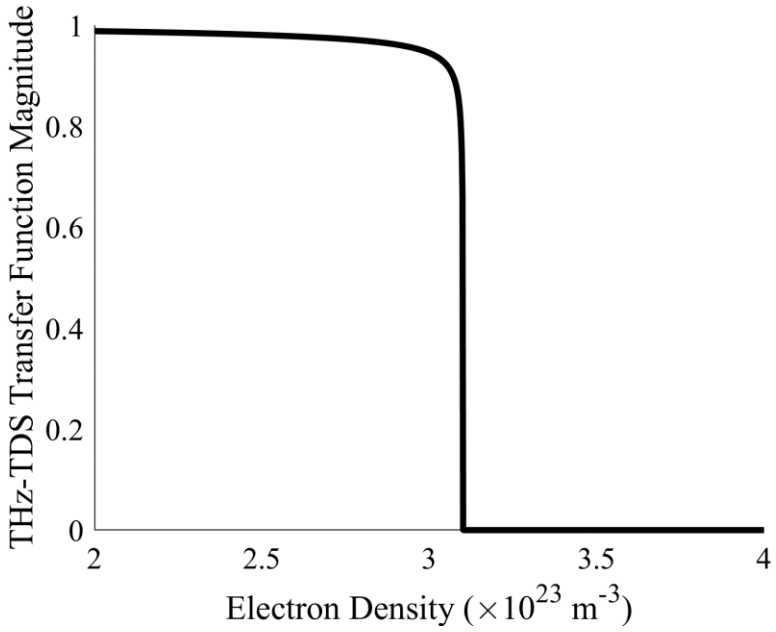

Figure 75 – THz-TDS transfer function magnitude plotted as a function of electron density for a pulse frequency of 5 THz, electron collision frequency of 10^6 Hz, and plasma length of 1 m

Setting the plasma frequency equal to the THz pulse frequency and re-arranging yields the critical density ($n_{e,cr}$) at which plasma cut-off occurs:

$$n_{e,cr} = \frac{\omega^2 \epsilon_0 m_e}{e^2}. \tag{51}$$

Unlike the minimum resolvable electron density, the critical density is not a function of the plasma length. Figure 76 plots the cut-off frequency as a function of the critical density and thereby provides the approximate maximum THz pulse frequency required to measure input electron densities.

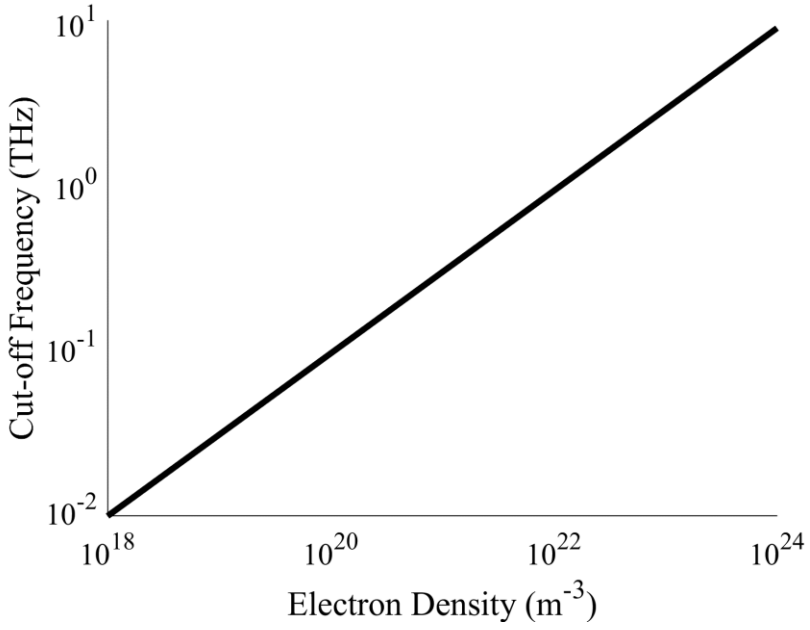

Figure 76 – Cut-off frequency plotted as a function of electron density

Because the critical density is directly proportional to the square of the THz pulse frequency, large gains in maximum measurable electron density can be realized with comparably smaller increases in resolvable THz pulse frequency. The maximum measurable electron density for the ideal THz-TDS system, for instance, can be increased from $3 \times 10^{23}\ m^{-3}$ to $1 \times 10^{24}\ m^{-3}$ by increasing the maximum resolvable radiation frequency from 5 THz to 10 THz.

At non-negligible electron collision frequencies, the THz pulse is attenuated beyond detectible limits at electron density values lower than the critical density. The impact of larger electron collision frequencies for the conditions used in Figure 75 is shown in Figure 77.

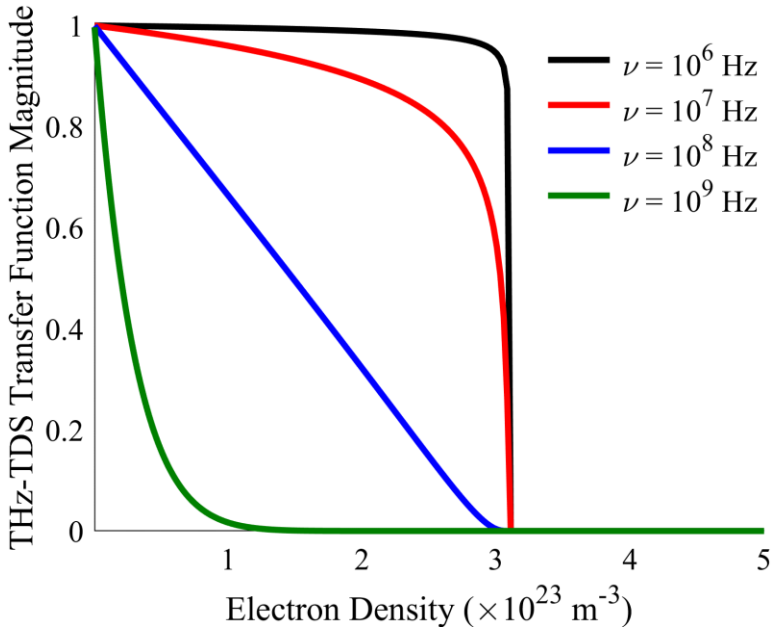

Figure 77 – Impact of electron collision frequency on THz-TDS transfer function magnitude near plasma cut-off for a pulse frequency of 5 THz and plasma length of 1 m

At larger electron collision frequencies, the maximum detectable electron density becomes a nonlinear function of the electron collision frequency, plasma length, and signal SNR, thereby precluding the development of a simple relationship for the effective critical density. However, trade studies suggested the effective critical density diverges from the collisionless critical density as the electron collision frequency approaches $(10^8 \text{Hz} \cdot \text{m})/L$.

This result is insensitive to changes in maximum resolvable THz pulse frequencies ranging from 0.5 to 5 THz.

5.2.3.3 Top and Bottom Boundaries

The top boundary forms where the collision frequency-dependent left and right boundaries meet. Because the collision frequency-dependent right boundary lacks a simple relationship, no simple relationship exists for the top boundary. Comparison of the Section 5.2.2 maps reveals that the shape of the top boundary varies as a function of resolvable frequencies, plasma length, and signal SNR.

No bottom boundary exists because electron densities are resolvable in the limit of a vanishingly small electron collision frequency. However, a bottom interior boundary demarcates resolvable and irresolvable electron collision frequencies. Like the top boundary, the bottom boundary shape varies as a function of many factors and precludes the development of a simple relationship.

5.3 Feasibility of EP Diagnostic Scenarios

This section investigates the feasibility of using THz-TDS to make electron density and collision frequency measurements in four EP environments: 1) Hall thruster channel, 2) cathode plume, 3) MPD thruster plume, and 4) ion thruster plume. Feasibility is quantified here in terms of required spatial resolution, resolvable THz pulse frequencies, THz pulse temporal resolution, and reference signal SNR. THz-TDS spatial resolution is discussed in Section 5.3.1 and required THz pulse temporal resolution and reference signal SNR are related to measured THz-TDS values by Eqs. (47) and (48) in Section 5.2.1.

Sections 5.3.2 – 5.3.5 present evaluations of measurement feasibility for the four sample EP environments. Nominal electron density and collision frequency distributions were estimated from publications cited in the appropriate sections. Because these values may vary by orders of magnitude due to differences in equipment design and operating conditions, the measurement feasibilities of hypothetical "high" and "low" density and collision frequency distributions are also considered.

5.3.1 Spatial Resolution

Spatial resolution must be considered in two dimensions: along the THz beam path and across the THz beam diameter. If a secondary measurement technique is used to estimate the plasma parameter distributions along the THz beam path, resolution in this dimension is ultimately limited by the WKB approximation and is therefore approximately equal to the radiation wavelength. Radiation frequencies of 0.01 THz and 5 THz correspond to wavelengths of 30 mm and 0.06 mm, respectively.

The smallest achievable focused beam diameter is approximately equal to one half of the radiation wavelength, so the spatial resolution in this dimension is on the order of the ultimate resolution along the beam path. However, it is often desirable to collimate the THz beam across the plasma length. The smallest achievable collimated Gaussian beam diameter (d_b) is given as a function of the collimation distance (d_c) and radiation wavelength (λ) by

$$d_b = \frac{1}{2}\max\left(\sqrt{\frac{d_c\lambda}{2\pi}}, \lambda\right). \tag{52}$$

Figure 78 shows the minimum focused beam diameter and minimum collimated beam diameters for various collimation distances as a function of THz radiation frequency.

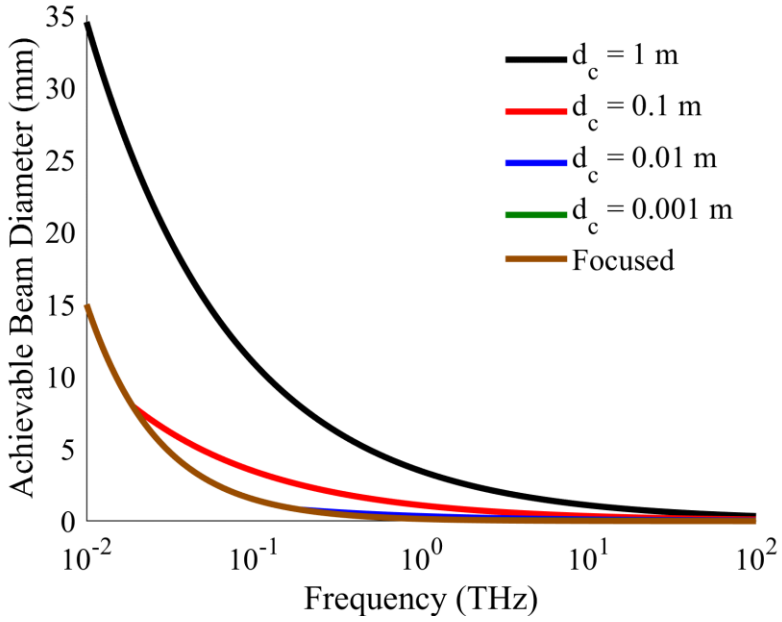

Figure 78 – Minimum attainable focused and collimated THz beam diameters

5.3.2 Hall Thruster Channel

Because published Hall thruster channel measurement data is sparse (and of dubious reliability due to the use of electrostatic probes), the nominal Hall thruster electron density distribution is taken from the simulation work of Gamero-Castaño and Katz [75]. The electron collision frequency distribution is unknown, and estimates of its peak value vary by many orders of magnitude [18]. The distribution is assumed here to have the same shape as the electron density. Peak values of the nominal, high, and low electron density and collision frequency distributions are shown in Table 2. The nominal electron density and electron collision frequency distributions are plotted in Figure 79.

Table 2 – Hall thruster channel peak distribution values

	Nominal	High	Low
Peak Electron Density (m^{-3})	1.2×10^{18}	1.2×10^{19}	1.2×10^{17}
Peak Electron Collision Frequency (Hz)	1.0×10^{7}	1.0×10^{9}	1.0×10^{5}

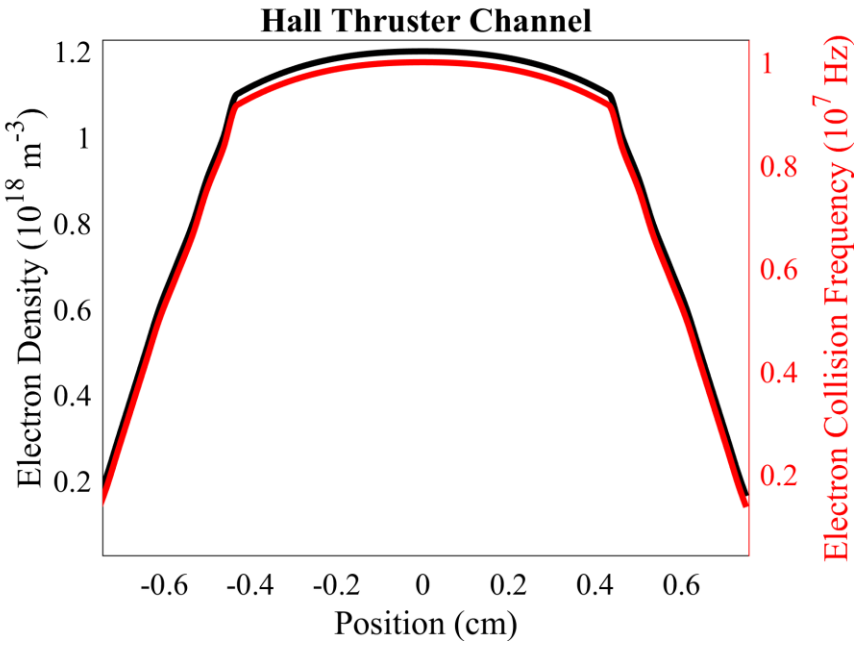

Figure 79 – Hall thruster channel nominal electron density and collision frequency distributions

A channel measurement with THz-TDS could require radiation propagation both along and perpendicular to magnetic field lines. However, the low applied magnetic field (~ 0.02 T) and low electron temperature (~ 200 eV) render thermal and magnetic field effects negligible [15]. Equation (27) is therefore used to model THz pulse propagation through the plasma. Figure 80 shows the THz pulse temporal resolution required to

measure the electron density as a function of THz frequency. Figure 81 shows the sample pulse SNR required to measure both the electron density and electron collision frequency as a function of THz frequency. Distributions are nominal unless otherwise specified on the plot. The nominal case overlaps with the high and low electron collision frequency cases in Figure 80. Frequencies below cut-off are not plotted.

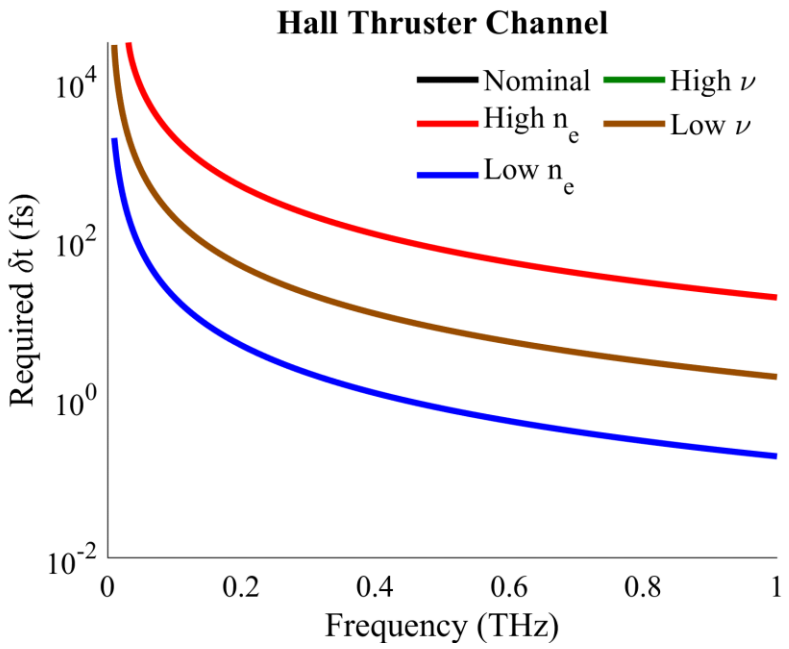

Figure 80 – Required THz pulse temporal resolution for Hall thruster channel electron density measurement

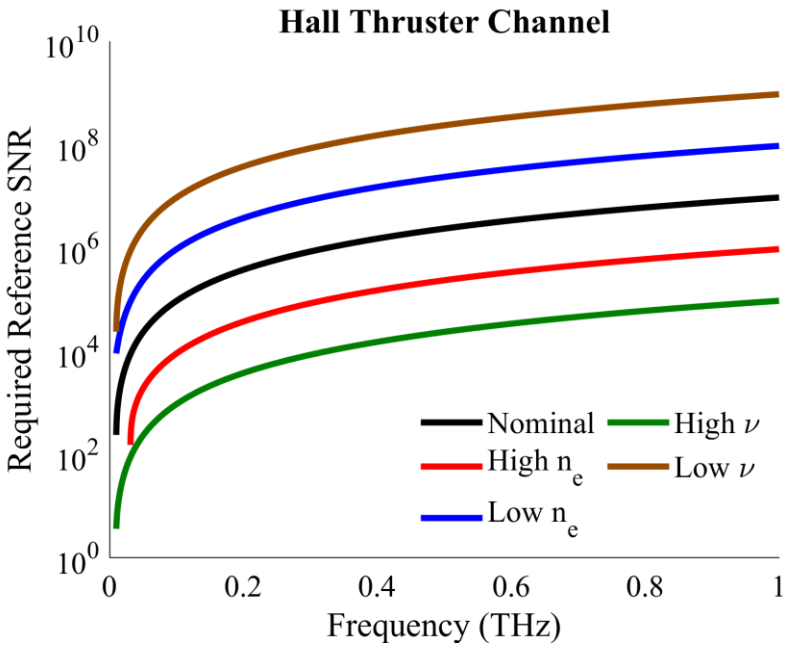

Figure 81 – Required THz pulse reference SNR for Hall thruster channel electron density and collision frequency measurement

Resolution of the electron density is achievable with 100 fs temporal pulse resolution for frequencies under 1 THz for the high-density case. The nominal density case is resolvable with frequencies under 0.5 THz with 10 fs pulse resolution, and the low-density case is resolvable with frequencies under 0.1 THz with 10 fs temporal pulse resolution. The required sample signal SNR is below 1000:1 only for very low THz pulse frequencies (~0.01 THz) for the nominal case. This range is extended to approximately 0.2 THz for the high collision frequency case.

As the required THz frequencies can be collimated to beam diameters below the cm-scale Hall thruster channel dimensions, the Hall thruster channel electron density is resolvable with commercially available equipment. However, the SNR required to resolve the electron collision frequency may be too high for commercially available equipment –

especially considering the probing THz pulse will lose SNR during transmission through the Hall thruster channel walls.

5.3.3 Cathode Plume

The nominal hollow cathode plume electron density distribution is taken from the experimental measurements made by Goebel et al. [76] of a hollow cathode with an axial confining magnetic field. The electron collision frequency distribution is unknown, and, as is the case for the Hall thruster channel, estimates of its peak value vary by many orders of magnitude [77]. The distribution is assumed to have the same shape as the electron density. Peak values of the nominal, high, and low electron density and collision frequency distributions are shown in Table 3. The nominal electron density and electron collision frequency distributions are plotted in Figure 82.

Table 3 – Cathode plume channel peak distribution values

	Nominal	High	Low
Peak Electron Density (m^{-3})	4.2×10^{19}	4.2×10^{20}	1.2×10^{18}
Peak Electron Collision Frequency (Hz)	1.0×10^{9}	1.0×10^{11}	1.0×10^{6}

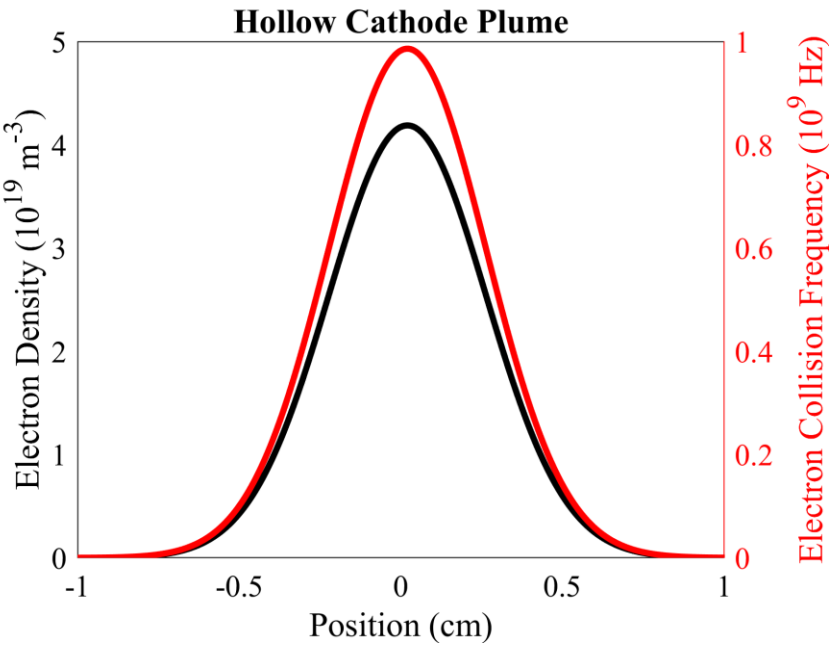

Figure 82 – Cathode plume nominal electron density and collision frequency distributions

A hollow cathode plume measurement with THz-TDS could require radiation propagation perpendicular to magnetic field lines. However, the low electron temperature (~5 eV) renders thermal and magnetic field effects negligible for this type of propagation. Equation (27) is therefore used to model THz pulse propagation through the plasma. Figure 83 shows the THz pulse temporal resolution required to measure the electron density as a function of THz frequency. Figure 84 shows the sample pulse SNR required to measure both the electron density and electron collision frequency as a function of THz frequency. Distributions are nominal unless otherwise specified on the plot. The nominal case overlaps with the low electron collision frequency case in Figure 83. Frequencies below cut-off are not plotted.

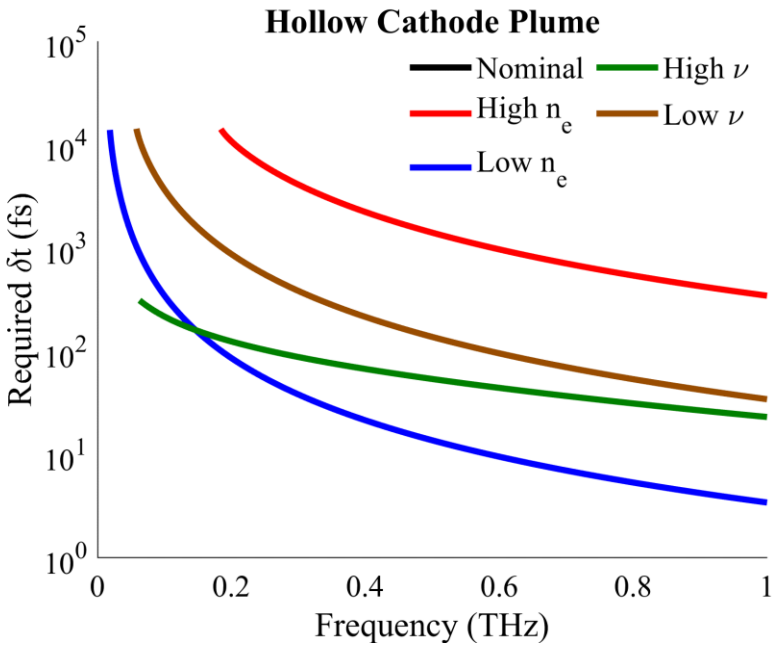

Figure 83 – Required THz pulse temporal resolution for cathode plume electron density measurement

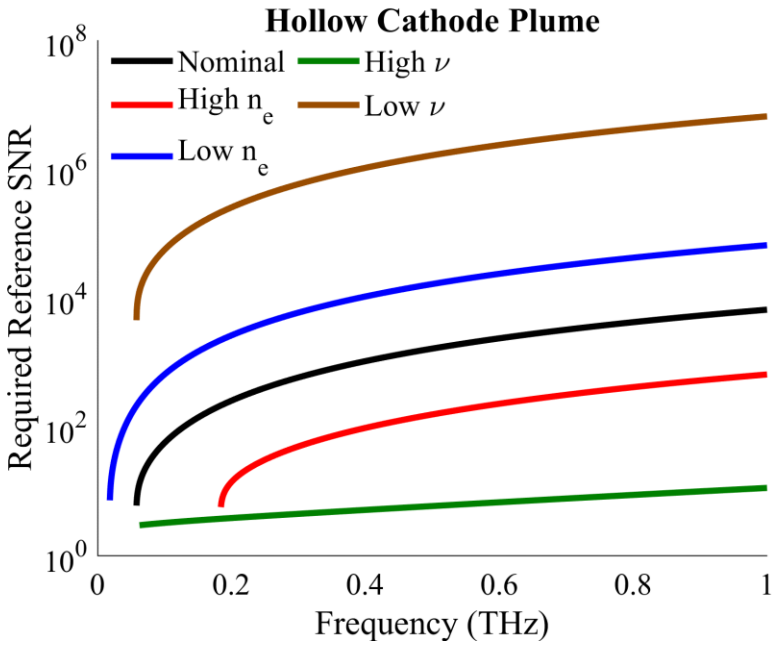

Figure 84 – Required THz pulse reference SNR for cathode plume electron density and collision frequency measurement

Resolution of the electron density is achievable with 100 fs temporal pulse resolution for frequencies under 1 THz for both the nominal and high-density cases. The low-density case is resolvable with frequencies under 0.8 THz with 10 fs temporal pulse resolution. The required sample signal SNR is readily achievable (< 100:1) for multiple frequencies across all cases.

The electron density is large enough that higher THz frequencies that can be collimated to mm-scale beam widths can be used to resolve the mm-scale cathode beam width. However, the lower THz frequencies required to resolve the electron collision frequency from some cases cannot be collimated to the scale of the cathode plume width. The electron density of the cathode plume is measurable by THz-TDS, but the electron collision frequency is only measurable if the electron density or electron collision frequency values are on the order of the high cases examined here.

5.3.4 MPD Thruster Plume

The MPD thruster plume electron density distribution is taken from the experimental measurements made by Gardner et al. [78]. The electron collision frequency distribution is unknown, so it is assumed here to have the same shape as the electron density. Peak values of the nominal, high, and low electron density and collision frequency distributions are shown in Table 4. The nominal electron density and electron collision frequency distributions are plotted in Figure 85.

Table 4 – MPD thruster plume channel peak distribution values

	Nominal	High	Low
Peak Electron Density (m^{-3})	6.6×10^{19}	6.6×10^{20}	6.6×10^{18}
Peak Electron Collision Frequency (Hz)	1.0×10^{4}	1.0×10^{6}	1.0×10^{2}

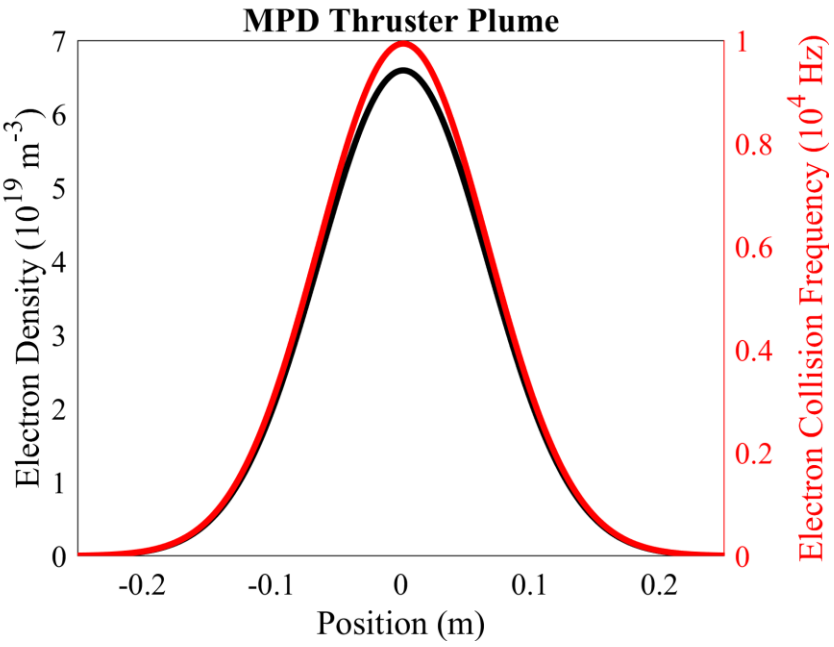

Figure 85 – MPD thruster plume nominal electron density and collision frequency distributions

An MPD thruster plume measurement with THz-TDS could require radiation propagation perpendicular to magnetic field lines. However, the low electron temperature (~1 eV) renders thermal and magnetic field effects negligible for this type of propagation. Equation (27) is therefore used to model THz pulse propagation through the plasma. Figure 86 shows the THz pulse temporal resolution required to measure the electron

density as a function of THz frequency. Figure 87 shows the sample pulse SNR required to measure both the electron density and electron collision frequency as a function of THz frequency. Distributions are nominal unless otherwise specified on the plot. The nominal case overlaps with the low and high electron collision frequency cases in Figure 86. Frequencies below cut-off are not plotted.

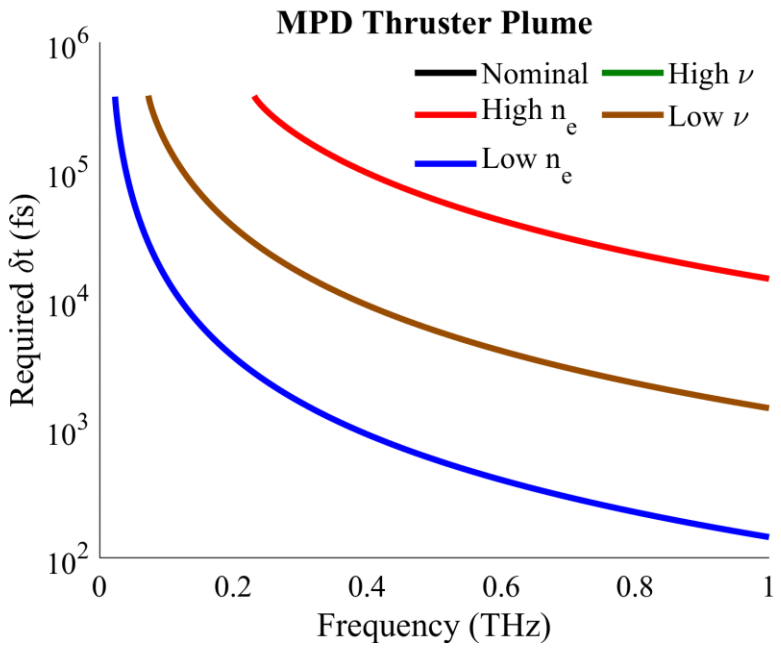

Figure 86 – Required THz pulse temporal resolution for MPD thruster plume electron density measurement

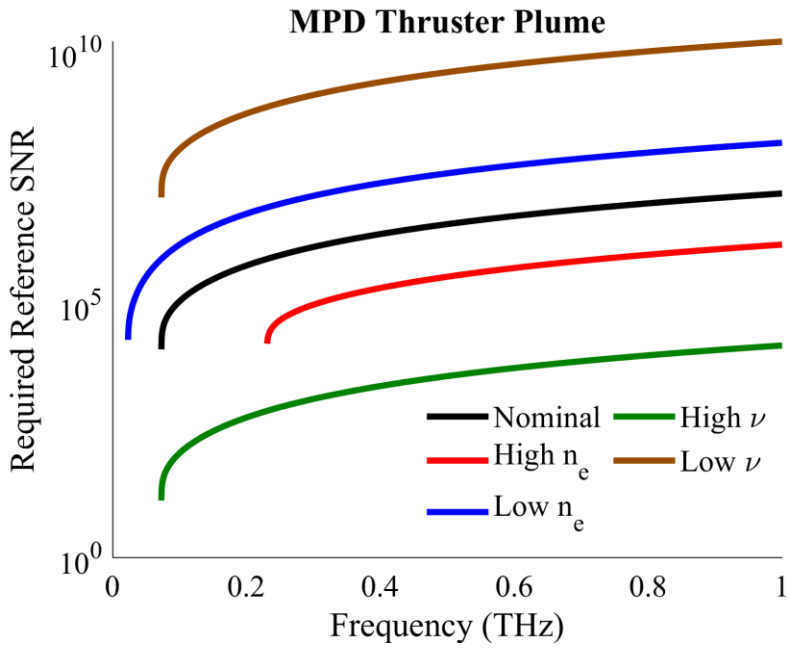

Figure 87 – Required THz pulse reference SNR for MPD thruster plume electron density and collision frequency measurement

Resolution of the electron density is achievable with 100 fs temporal pulse resolution for frequencies under 1 THz for all cases. The required sample signal SNR, however, is likely infeasible for all cases. The electron density is therefore readily resolvable with THz-TDS, but the electron collision frequency is not resolvable.

5.3.5 Gridded Ion Thruster Plume

The gridded ion thruster plume electron density distribution is taken from the experimental measurements made by de Boer [79]. The electron collision frequency distribution is unknown, so it is assumed here to have the same shape as the electron density. Peak values of the nominal, high, and low electron density and collision frequency distributions are shown in Table 5. The nominal electron density and electron collision frequency distributions are plotted in Figure 88.

Table 5 – Gridded ion thruster plume channel peak distribution values

	Nominal	High	Low
Peak Electron Density (m^{-3})	2.2×10^{15}	2.2×10^{16}	2.2×10^{14}
Peak Electron Collision Frequency (Hz)	1.0×10^{4}	1.0×10^{7}	1.0×10^{2}

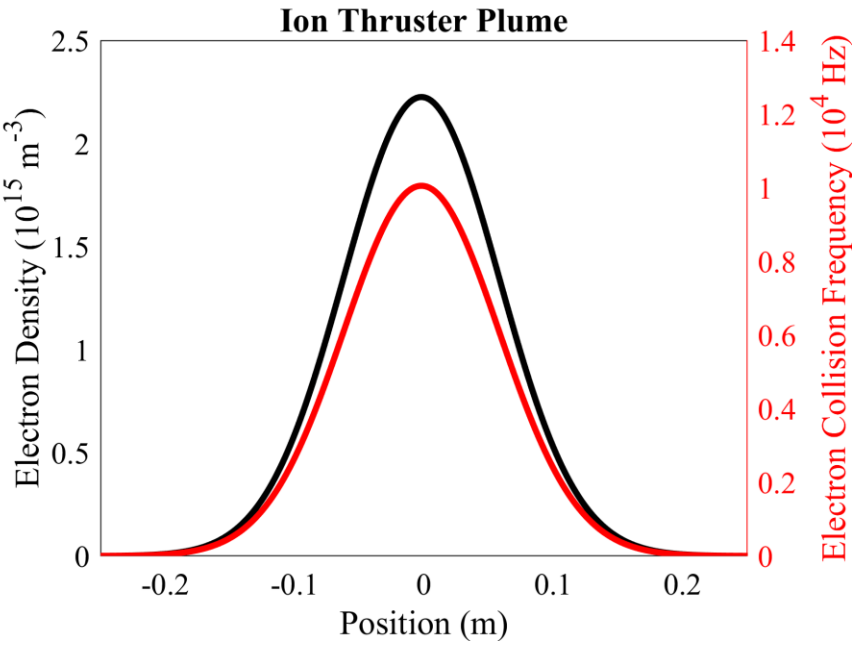

Figure 88 – Gridded ion thruster plume nominal electron density and collision frequency distributions

As the magnetic field in the ion thruster plume is negligibly small, Eq. (27) is used to model THz pulse propagation through the plasma. Figure 89 shows the THz pulse temporal resolution required to measure the electron density as a function of THz frequency. Figure 90 shows the sample pulse SNR required to measure both the electron density and electron collision frequency as a function of THz frequency. Distributions are

nominal unless otherwise specified on the plot. The nominal case overlaps with the low and high electron collision frequency cases in Figure 89. Frequencies below plasma cut-off are not plotted.

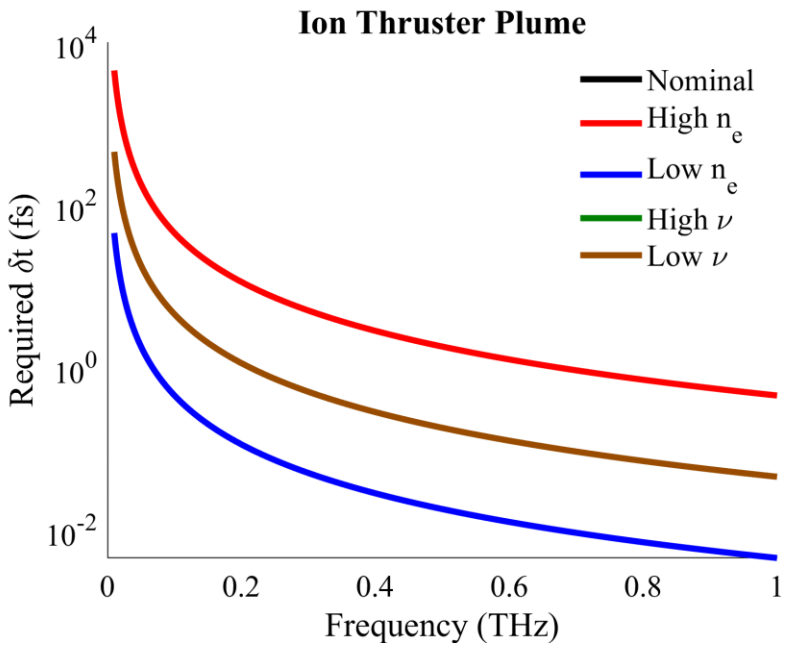

Figure 89 – Required THz pulse temporal resolution for gridded ion thruster plume electron density measurement

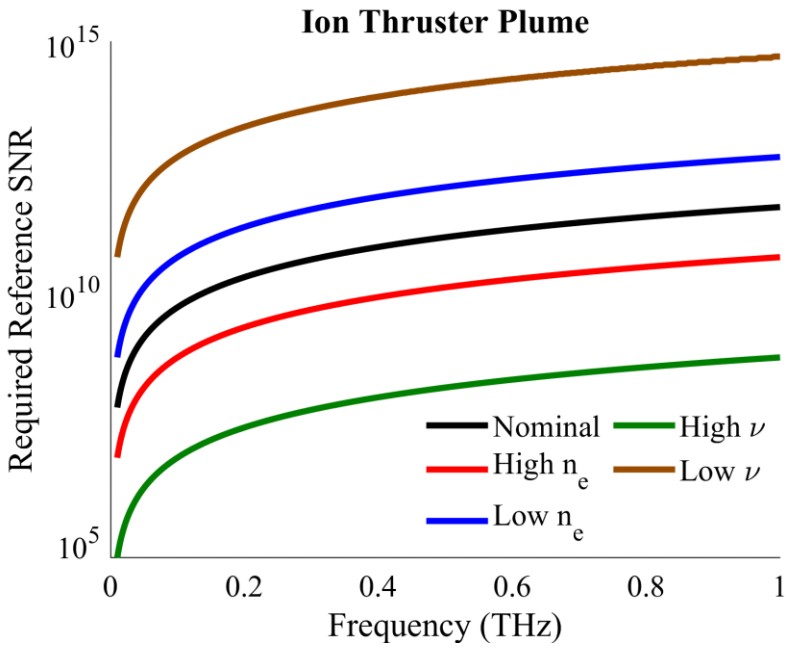

Figure 90 – Required THz pulse reference SNR for gridded ion thruster plume electron density and collision frequency measurement

Resolution of the electron density is achievable with 10 fs temporal pulse resolution for frequencies under 0.2 THz for the high-density case, under 0.07 THz for the nominal case, and near 0.01 THz for the low-density case. The required sample signal SNR, however, is infeasible for all cases. The electron density is resolvable with commercially available THz-TDS equipment, but the THz-TDS system described in Chapter 3 would not be able to resolve the density. The electron collision frequency is not resolvable.

5.4 Summary

Section 5.1 examines the validity of standard assumptions. The use of Eq. (31) in place of Eq. (28) to enable calculation of the electron density from phase information alone was found to be a valid assumption below the critical values of the electron density and collision frequency defined by Eq. (42). The calculated average electron collision

frequency was found to be virtually invariant with assumed plasma length and distribution. In contrast, invariance of the calculated integrated electron density was found to be a good assumption if the electron density is below the critical value defined by Eq. (42).

Use of Eq. (28) in a thermal magnetized plasma was found to be valid for pulse propagation parallel to the magnetic field as long as the magnetic field strength is below the critical values defined by Eq. (45). If THz pulse propagation is perpendicular to the magnetic field and pulse polarization is parallel to the magnetic field, use of Eq. (28) produces negligible error as long as the electron temperature remains below the critical value defined by Eq. (46). In the THz-TDS system described in Chapter 3, the THz pulse propagates parallel to the induced magnetic field of the ICP discharge. The use of Eq. (28) to analyze data is justified because the magnetic field reverses direction at a rate of 13.56 MHz. Hence, the average magnetic field is approximately zero and therefore lower than the critical magnetic field.

Section 5.2 presents maps of measurable electron density and collision frequency for various plasma lengths and discusses the physics associated with the map boundaries. Assuming access to the full breadth of commercially available equipment, resolvable electron densities were found to range from approximately 10^{13} to 10^{23} m^{-3} for a uniform plasma length of 1 m and from 10^{16} to 10^{23} m^{-3} for a uniform plasma length of 0.001 m. The resolvable electron collision frequency varies with both length and electron density. At the electron density with the largest spread of resolvable collision frequencies, these values were found to range from 10^{5} to 10^{13} Hz for a uniform plasma length of 1 m and 10^{8} to 10^{13} Hz for a uniform plasma length of 0.001 m.

If the electron collision frequency is below the critical value defined by Eq. (42), the minimum resolvable density was found to be a function of the lowest resolvable THz frequency and THz pulse duration according to Eq. (49). The maximum measurable density is given by the critical density at which collisionless plasma cut-off occurs, given by Eq. (51).

For electron frequencies above the critical value, the minimum resolvable electron density was found to be approximately given by Eq. (50). No simple relationship for collisional cut-off frequency was developed, but results suggest that this value diverges from the collisionless value as the electron collision frequency approaches $(10^8 \text{Hz} \cdot \text{m})/L$.

Section 5.3 investigates the feasibility of various EP diagnostic scenarios. THz-TDS was found to be a viable diagnostic for measuring electron density in the Hall thruster channel and in the plumes of cathodes, MPD thrusters, and ion thrusters. THz-TDS was not found to be a viable diagnostic for measuring electron collision frequency in the plumes of MPD thrusters or ion thrusters. The ability of THz-TDS to measure electron collision frequency in the Hall thruster channel and cathode plume was found to depend on the electron collision frequency values of those environments, estimates of which vary widely.

CHAPTER 6. BAYESIAN ANALYSIS FRAMEWORK

This chapter presents a novel Bayesian THz-TDS plasma diagnostic analysis framework and uses it to quantify the impact of THz pulse parameters on uncertainty. The Bayesian analysis framework offers significant advantages over the standard framework of Chapter 4 because it appropriately weights measurements taken at each THz pulse frequency, can reliably calculate the electron collision frequency, and can compute plasma parameter uncertainties. Section 6.1 details the analysis framework, Section 6.2 provides electron density and collision frequency results calculated with the Bayesian analysis framework, Section 6.3 investigates the impact of THz pulse properties on parameter uncertainty, and Section 6.4 summarizes the findings of this chapter.

6.1 Framework

This section details the Bayesian analysis framework. The first analysis steps in the Bayesian framework are the same as those for the standard framework: the LIA data are processed to compute the magnitude and phase of the transfer function, and phase unwrapping is performed. Then, Bayes' equation is numerically sampled with the input magnitude and unwrapped phase data to find the posterior probability density function (PDF) that describes the plasma properties. The posterior PDF is evaluated to find the most probable estimates and credibility intervals of the desired plasma parameters. Figure 91 provides an outline of the Bayesian analysis procedure.

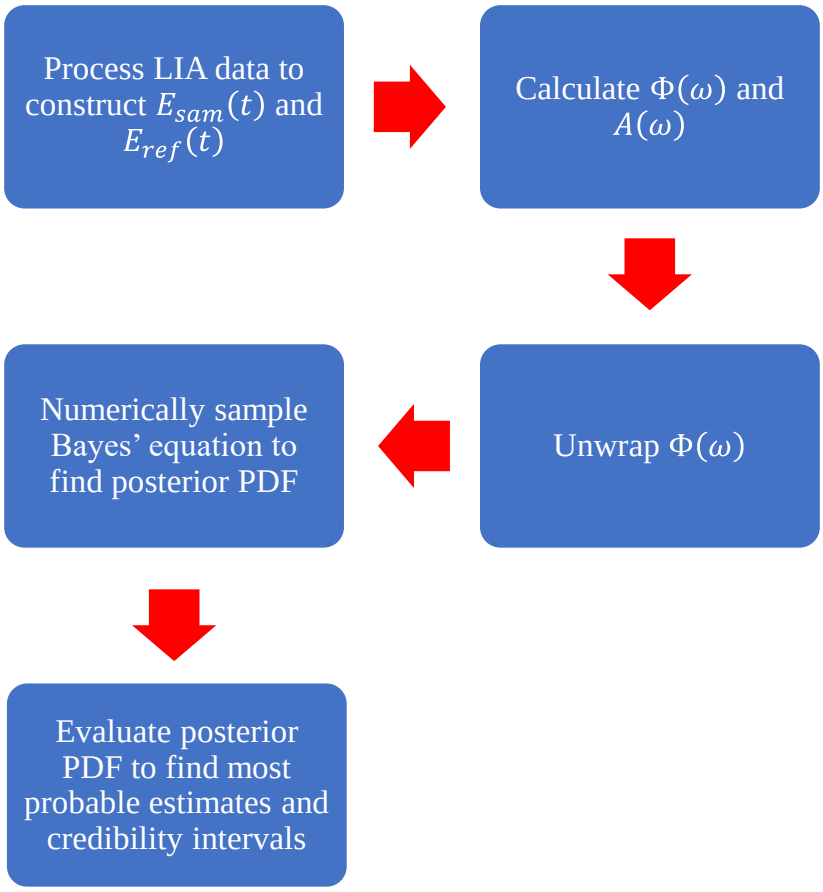

Figure 91 – Outline of Bayesian analysis procedure

The following sections detail the Bayesian analysis procedure. Section 6.1.1 introduces a magnitude correction not present in the standard analysis framework, Section 6.1.2 overviews Bayes' equation, Section 6.1.3 explicitly defines the terms in Bayes' equation, Section 6.1.4 describes the computational scheme used to numerically sample Bayes' equation, Section 6.1.5 compares output Bayesian analysis results to ideal plasma parameter inputs, and Section 6.1.6 discusses the impact of the assumed plasma length and associated uncertainty on the resulting average electron density and collision frequency.

6.1.1 Magnitude Correction

The skew in electron collision frequency data reported in Figure 34 in Section 4.1.3 must be addressed if the Bayesian analysis framework is to provide accurate electron collision frequency results. A clue that points to the source of the measurement aberration is provided by Jamison et al. [43], who note that their reported electron collision frequency values are “anomalously” large. A possible cause for such a measurement artifact was identified by the microwave interferometry community many decades ago: the plasma can refract the probing radiation away from the signal and thereby result in erroneously high absorption measurements that artificially inflate the output electron collision frequency [34].

Even for the largest electron density and collision frequency plasma condition measured for this dissertation, the refractive index across all resolvable THz frequencies varies by less than 2%. Refraction of the THz beam at a given plasma condition is therefore approximately independent of frequency and uniformly decreases the measured transfer function magnitude across all frequencies by the same percentage. Figure 92 shows the impact of uniform refraction on the magnitude for a measurement in a plasma with electron density of 4×10^{19} m^{-3}, electron collision frequency of 6×10^{10} Hz, and uniform plasma length of 0.1 m. Figure 93 shows the resulting impact on the calculated electron collision frequency.

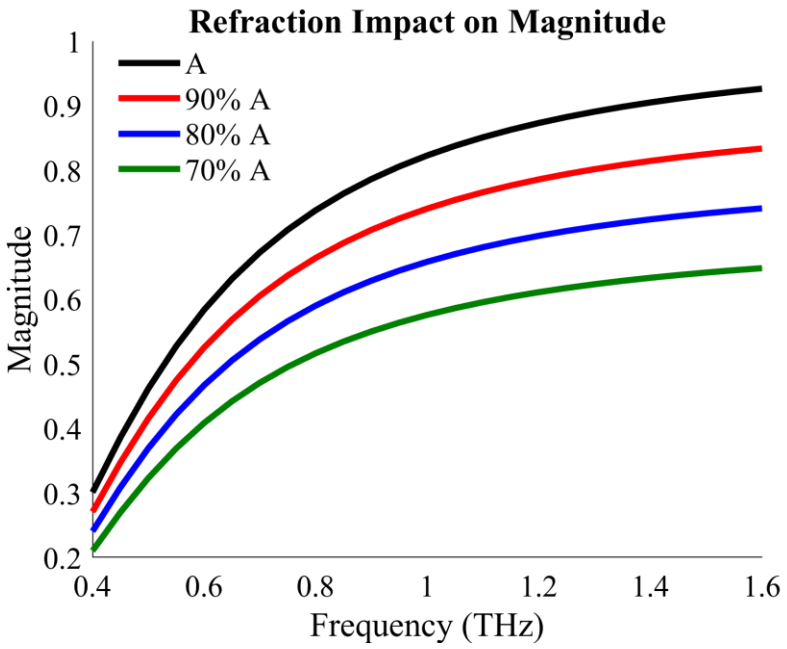

Figure 92 – Impact of refraction on measured transfer function magnitude (*A*)

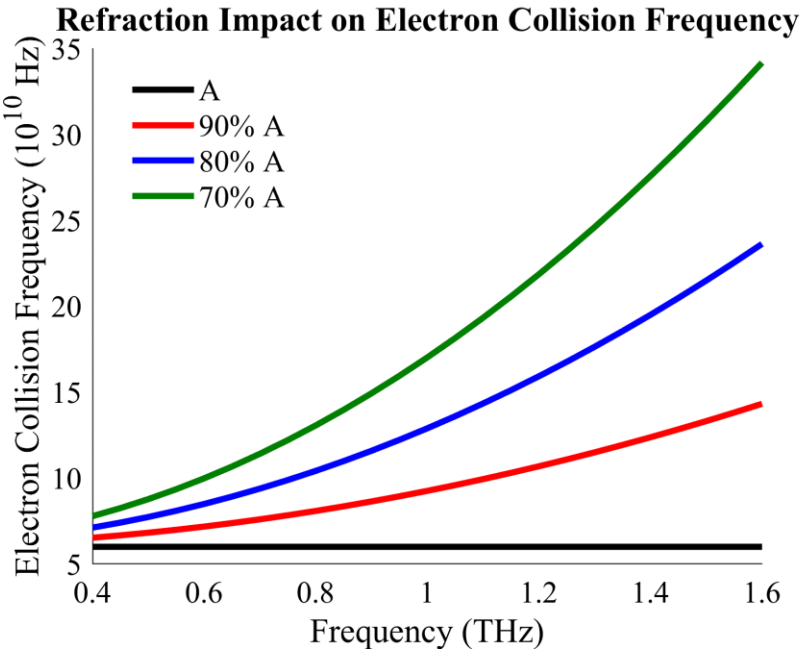

Figure 93 – Impact of refraction on calculated electron collision frequency

Similarity in the simulated data trends shown in Figure 93 and the measured data trend shown in Figure 34 suggests that refraction may be influencing the calculated electron collision frequency. To test this hypothesis, the RF ICP discharge was misaligned by approximately 5 degrees from the THz pulse path to exacerbate the influence of refraction on the transfer function. Sample and reference electric fields were recorded in this misaligned configuration and used to calculate the electron collision frequency. The discharge was operated at 200 W and 1 Torr. Figure 94 shows the electron collision frequency calculated with the standard analysis method.

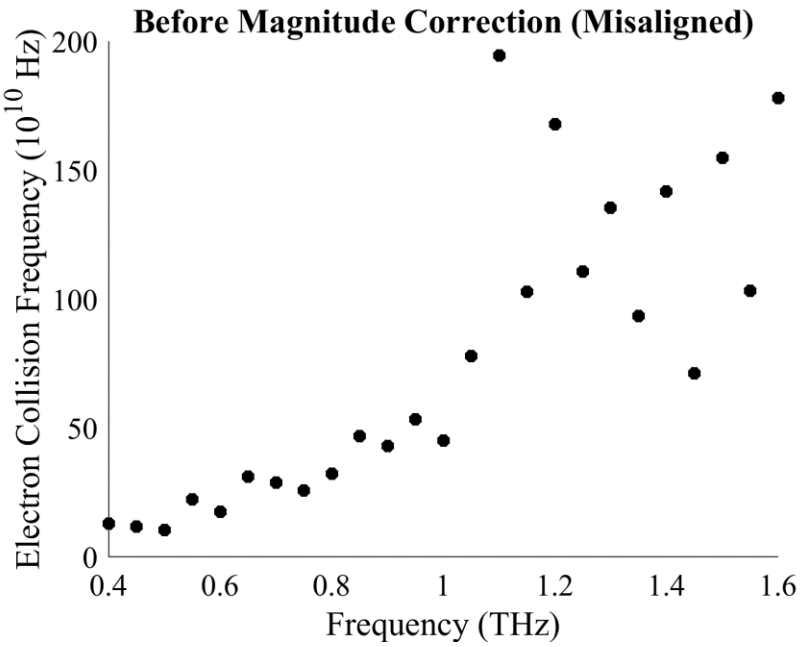

Figure 94 – Calculated electron collision frequency in misaligned configuration prior to magnitude correction (200 W, 1 Torr)

The slope of the trend and resulting difference in maximum and minimum calculated electron collision frequency are an order of magnitude larger for the misaligned dataset, indicating that refraction indeed plays an important role in the calculated electron collision

frequency. To correct for refraction, a THz frequency-independent correction factor (r) is multiplied to the measured transfer function magnitude (A_m) to determine the corrected magnitude (A_c) according to

$$A_c(\omega) = rA(\omega). \tag{53}$$

Within the standard analysis framework, the value of the correction factor is iterated until the linear slope in the calculated electron collision frequency is minimized. Figure 95 shows the electron collision frequencies calculated with corrected magnitude data for the aligned case originally presented in Figure 34.

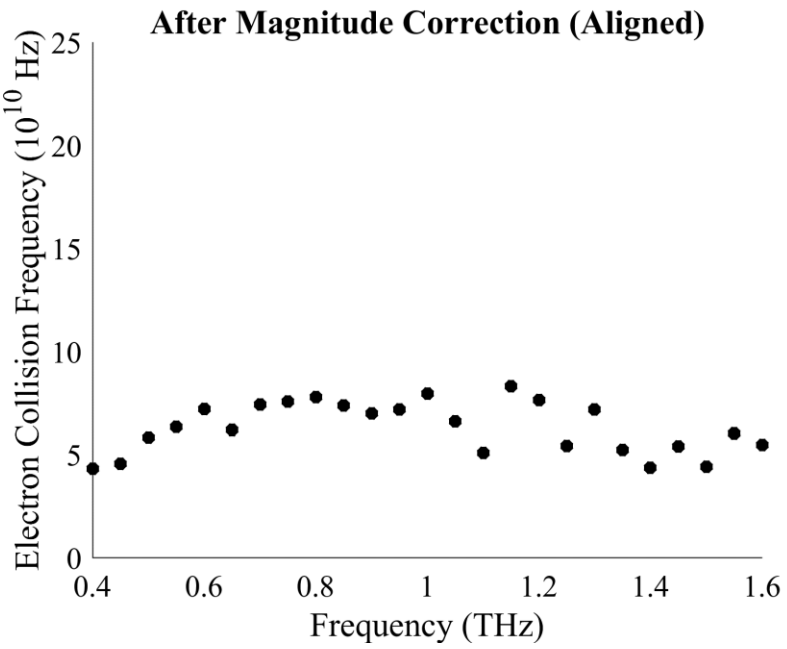

Figure 95 – Electron collision frequency calculated with corrected magnitude (200 W, 1 Torr)

The electron collision frequencies calculated with the corrected magnitude span 4×10^{10} Hz for the aligned case and do not exhibit a linear trend. This is a significant improvement over the uncorrected aligned case, in which the span is approximately 20×10^{10} Hz in Figure 34.

6.1.2 Bayesian Framework Overview

Development of the magnitude correction enables construction of a Bayesian THz-TDS plasma diagnostic analysis framework that can robustly calculate both the electron density and collision frequency from measured THz-TDS data. Treating all quantities as random variables, Bayesian inference combines prior knowledge with measured data to generate a posterior joint probability distribution function (PDF) of inferred parameters [80]. The most probable estimate and associated credible interval are extracted from the posterior PDF for each inferred parameter and correspond to the measured value and associated uncertainty, respectively, in a classical uncertainty quantification framework. In the context of THz-TDS plasma diagnostics, the inferred parameters are the electron density and collision frequency, the measured data are the sample and reference THz pulse spectra, and the prior knowledge consists of inferred parameter distributions or permissible parameter intervals known prior to the measurement.

Bayesian inference is performed by analytically or computationally solving Bayes' equation:

$$p(\mathbf{x}, \boldsymbol{\theta}|\mathbf{b}) = \frac{p(\mathbf{x}, \boldsymbol{\theta})p(\mathbf{b}|\mathbf{x}, \boldsymbol{\theta})}{p(\mathbf{b})}. \tag{54}$$

The variables in Bayes' equation are the inferred parameter vector (**x**), nuisance parameter vector (**θ**), and measured data vector (**b**). The PDFs in Bayes' equation are the posterior of **x** and **θ** conditional on **b** ($p(\mathbf{x},\boldsymbol{\theta}|\mathbf{b})$); prior of **x** and **θ** ($p(\mathbf{x},\boldsymbol{\theta})$); likelihood of **b** conditional on **x** and **θ** ($p(\mathbf{b}|\mathbf{x},\boldsymbol{\theta})$); and evidence ($p(\mathbf{b})$). Typically, Eq. (54) is solved for the posterior with input prior, likelihood, and evidence.

The posterior describes parameter knowledge after the measurement, the prior encodes information known prior to the measurement, and the likelihood incorporates an uncertainty model to describe the probability that a set of inferred parameters matches the measured data. The evidence is a normalization factor that ensures the integral of the posterior is equal to unity. It is simply the marginalization of the numerator over **x** and **θ**:

$$p(\mathbf{b}) = \iint p(\mathbf{x},\boldsymbol{\theta})p(\mathbf{b}|\mathbf{x},\boldsymbol{\theta})\mathrm{d}\mathbf{x}\mathrm{d}\boldsymbol{\theta}. \tag{55}$$

In the context of this dissertation, the goal of the analysis is to compute the PDF of **x** conditional on **b** ($p(\mathbf{x}|\mathbf{b})$), which is equal to the posterior marginalized over the nuisance parameters:

$$p(\mathbf{x}|\mathbf{b}) = \int p(\mathbf{x},\boldsymbol{\theta}|\mathbf{b})\mathrm{d}\boldsymbol{\theta}. \tag{56}$$

The resulting $p(\mathbf{x}|\mathbf{b})$ may be further marginalized over subsets of **x** to compute multivariate or univariate distributions of select inferred parameters.

The most probable estimate of a specific inferred parameter (x_{prob}) is computed here as the mean of its univariate PDF:

$$x_{prob} = \int p(x|\mathbf{b}) x \mathrm{d}x. \tag{57}$$

The credible interval is equal to the range of values about the mean for which the integral of the PDF is equal to the chosen credible interval percentage (P_{CI}). The upper and lower values of the credibility interval (x_{low} and x_{high}) therefore satisfy

$$\int_{-\infty}^{x_{low}} p(x|\mathbf{b}) \mathrm{d}x = \int_{x_{high}}^{\infty} p(x|\mathbf{b}) \mathrm{d}x = \frac{1 - P_{CI}}{2}. \tag{58}$$

6.1.3 Variable and PDF Definitions

6.1.3.1 Variables

The vector of inferred parameters contains the line-averaged electron density and collision frequency; the vector of nuisance parameters contains the plasma length, linear phase fit parameter, and refractive index correction factor; and the measured parameter vector contains the frequency-dependent magnitudes and unwrapped phases of the THz-TDS transfer function. It is important to emphasize that the phases in **b** must be unwrapped per Eq. (39) but are otherwise uncorrected. The variables are therefore defined as

$$\mathbf{x} = [n_e, \nu]^{\mathrm{T}},$$

$$\boldsymbol{\theta} = [L, \varphi_2, r]^{\mathrm{T}},$$

(59)

and

$$\mathbf{b} = \left[A\left(\omega_{k_s}\right), A\left(\omega_{k_s+1}\right), \ldots A\left(\omega_{k_{max}}\right), \Phi\left(\omega_{k_s}\right), \Phi\left(\omega_{k_s+1}\right), \ldots \Phi\left(\omega_{k_{max}}\right)\right]^{\mathrm{T}}.$$

The indexing convention used for the frequencies in **b** is identical to the indexing convention used to define the DFT in Eqs. (37) and (38). However, the first index is $k = k_s$ rather than $k = 0$ because frequencies near zero exhibit DC biasing that artificially inflates their magnitude. The index k_s corresponds to the first frequency that does not exhibit artificial inflation of magnitude due to DC bias.

The range of frequencies in **b** may be further windowed to the loosely defined "resolvable" frequencies used in the standard analysis of Chapter 4. Such windowing only removes the contribution of frequencies with low SNR and therefore has no discernable impact on the results.

6.1.3.2 Prior PDF

The prior PDF incorporates information known about the plasma prior to measurement with THz-TDS. Examples of known information include known distributions or permittable ranges of plasma parameters and correction factors. The prior PDF developed for this work is given by

$$p(\mathbf{x}, \boldsymbol{\theta}) = p(n_e)p(\nu)p(L)p(\varphi_2)p(r), \tag{60}$$

and its constituent parameter PDFs are given by

$$p(n_e) = \left[n_e \ln\left(\frac{n_{e,max}}{n_{e,min}}\right)\right]^{-1},$$

$$p(\nu) = \left[\nu \ln\left(\frac{\nu_{max}}{\nu_{min}}\right)\right]^{-1},$$

$$p(L) = \frac{\exp\left(-\frac{1}{2}\left(\frac{L-\mu_L}{s_L}\right)^2\right)}{s_L\sqrt{2\pi}} \quad or \quad \frac{1}{L_{max} - L_{min}}, \tag{61}$$

$$p(\varphi_2) = \frac{1}{\varphi_{2,max} - \varphi_{2,min}},$$

and

$$p(r) = \frac{1}{r_{max} - r_{min}},$$

where the min and max subscripts denote the minimum and maximum permissible values, respectively, and μ and s denote the average and standard deviation, respectively. The prior PDFs for electron density and collision frequency are scale-invariant forms of the uniform PDF, the prior PDF for the plasma length is either a normal or uniform PDF, and the prior PDFs for the correction factors are uniform PDFs.

The scale-invariant PDF is an appropriate prior for electron density and collision frequency because possible values of these parameters typically span many orders of magnitude. The scale-invariant PDF permits values across the entire span of possible values and gives equal weight to each included order of magnitude. The use of a uniform PDF in place of a scale-invariant PDF would disproportionally weight larger orders of magnitude and potentially skew results.

The plasma length is typically given a normal distribution because its value is measured independently and can be assigned a mean and standard deviation related to the measurement technique. However, as discussed in more detail in Section 6.1.6, it is sometimes convenient to separately evaluate the uncertainty of the normalized electron density and the average electron density. In the normalized electron density case, the uniform length prior is employed with a small difference between L_{max} and L_{min} so that the influence of the length uncertainty is virtually eliminated.

The correction factors are conservatively given uniform prior PDFs to eliminate the necessity of correlating these values to plasma conditions. Table 6 shows the values of all prior PDF inputs used for measurements made in the RF ICP discharge.

Table 6 – Prior PDF input values

Parameter	Value
$n_{e,max}$	10^{21} m^{-3}
$n_{e,min}$	10^{17} m^{-3}
ν_{max}	10^{13} Hz
ν_{min}	10^{7} Hz
μ_L	0.12 m
s_L	0.01 m
L_{max}	0.12 m + 10^{-6} m
L_{min}	0.12 m - 10^{-6} m
$\varphi_{2,max}$	1 ps
$\varphi_{2,min}$	-1 ps
r_{max}	2
r_{min}	1

It is important to note that the use of Eq. (60) with scale-invariant prior PDFs for the inferred parameters and uniform prior PDFs for the correction factors does not assume that these parameters are independent of each other. Instead, this formulation conservatively refrains from inadvertently providing undue weight to certain variable combinations by not imposing assumed correlations. If correlations were known, the form of the prior PDF could be altered to enable the incorporation of correlation data and could use more targeted constituent PDF types. Such changes would decrease the resultant uncertainty and may be appropriate for some plasma diagnostic scenarios.

6.1.3.3 Likelihood PDF

The likelihood PDF describes the likelihood of obtaining a measurement, given known plasma conditions. The likelihood PDF developed for this work is a multivariate normal distribution, with each dimension corresponding to an element of $\mathbf{b}$. The use of a multivariate normal distribution here is justified by the observed normal distribution of measured THz electric field values for this dissertation and THz-TDS magnitude and phase values by other works [49, 73]. The likelihood PDF is given by

$$p(\mathbf{b}|\mathbf{x},\boldsymbol{\theta}) = \frac{\exp\left(-\frac{1}{2}(\mathbf{b}-\mathbf{b}_{\mathrm{mod}})^{\mathrm{T}}\boldsymbol{\Gamma}^{-1}(\mathbf{b}-\mathbf{b}_{\mathrm{mod}})\right)}{\sqrt{(2\pi)^{N}\det(\boldsymbol{\Gamma})}}, \tag{62}$$

where $\mathbf{b}_{\mathrm{mod}}$ is the vector of expected measurements for an input plasma condition, $\boldsymbol{\Gamma}$ is the error covariance matrix, and N is the length of $\mathbf{b}$.

The vector of expected measurements is computed with a modified form of Eq. (28) that accounts for the correction factors. Compared to their use in the direct computation of plasma parameters within the standard analysis framework, the correction factors are inversely applied to Eq. (28) so that the expected measurements computed for a set of plasma conditions and necessary correction factors can be directly compared to actual measurements. The modified equations are therefore

$$A_{mod}(\omega) = \left(\frac{1}{r}\right)\exp\left[-\frac{\omega L}{c}\sqrt{-\frac{1}{2}\left(1-\frac{\omega_p^2}{\omega^2+\nu^2}\right)+\frac{1}{2}\sqrt{\left(1-\frac{\omega_p^2}{\omega^2+\nu^2}\right)^2+\left(\frac{\omega_p^2\nu}{\omega[\omega^2+\nu^2]}\right)^2}}\right]$$

and

$$\Phi_{mod}(\omega) = \varphi_2\omega + \frac{\omega L}{c}\left[\sqrt{\frac{1}{2}\left(1-\frac{\omega_p^2}{\omega^2+\nu^2}\right)+\frac{1}{2}\sqrt{\left(1-\frac{\omega_p^2}{\omega^2+\nu^2}\right)^2+\left(\frac{\omega_p^2\nu}{\omega[\omega^2+\nu^2]}\right)^2}}-1\right]. \quad (63)$$

It is important to note that the phase correction factor in Eq. (63) only assumes the contribution of the delay line registration error is linear with pulse frequency. This is in contrast to Eq. (41) of Section 4.1.2, which assumes that Eq. (31) is a good approximation of the phase.

The diagonal of the error covariance matrix contains the variance (s^2) of each element of **b**, and the off-diagonal components contain the covariances between the different elements of **b**. However, analysis of pre-averaged *R* data (defined in Eq. (36)) found that covariances between different elements in both the time and frequency domains were 100-1000 times smaller than the variances of each element. The distributions of the elements in **b** are therefore assumed to be uncorrelated, and the off-diagonal components of the error covariance matrix are set to zero. The error covariance matrix is given by

$$\mathbf{\Gamma} = \begin{bmatrix} s_{\mathrm{b}_1}^2 & \cdots & 0 \\ \vdots & \ddots & \vdots \\ 0 & \cdots & s_{\mathrm{b}_\mathrm{N}}^2 \end{bmatrix}. \quad (64)$$

As discussed in Section 4.1.1.1, THz-TDS datasets are averaged in the time domain because, compared to frequency-domain averaging, time-domain averaging has been

shown to reduce the variance in calculated spectra [55]. Variances measured in the time domain must therefore be propagated to the frequency domain. Withayachumnankul et al. [73] provide a convenient means for propagating the error across domains in the context of THz-TDS optical parameter extraction for solid samples. However, their work accounts for drift and uncertainties in the time axis by incorporating data taken from many delay line scans. As discussed in Section 3.2.2, when THz-TDS is applied to plasma diagnostics, the delay line is scanned just once for each sample and reference electric field (though multiple samples are acquired at each delay line position). Scanning the delay line many times is not preferred because it significantly increases the time required to make a single measurement.

Introduced here is an adaptation of the method presented in [73] for calculation of frequency-domain variance in the context of "single-scan" THz-TDS. The time-domain variance of the discrete electric field (s_E^2) is assumed equal to the sum of the random ($s_{E,r}^2$) and drift ($s_{E,d}^2$) error contributions:

$$s_E^2(t_m) = s_{E,r}^2(t_m) + s_{E,d}^2(t_m), \tag{65}$$

where the m index is identical to that defined for Eq. (37). The random error varies rapidly according to a normal distribution and is therefore naturally captured by the computed variance of the discrete electric field. Drift error, on the other hand, varies slowly and may either proceed in only one direction or change direction once or twice throughout the duration of a measurement. Drift error can be assigned a variance through the conservative

assumption that the total signal amplitude drift (ΔE) is equal to twice the standard deviation of a representative drift normal distribution. The drift error variance is then given by

$$s_{\tilde{E},d}^2(t_m) = \frac{1}{4}[\Delta E(t_m)]^2. \tag{66}$$

The signal drift may be measured independently and assumed equal for all future measurements or it can be estimated through the comparison of reference electric fields measured before and after sample electric fields. If reference electric fields are used as baselines for computing drift, the variance due to drift is only added to the sample electric field variance.

Adapted from [73] and converted to the DFT convention of this dissertation, the following equation propagates the time-domain variances of the sample and reference electric fields ($s_{E_{sam}}^2$ and $s_{E_{ref}}^2$) to the frequency-domain amplitude and phase ($s_{A,\widehat{E}}^2$ and $s_{\Phi,\widehat{E}}^2$):

$$s_{A,\hat{E}}^2(\omega_k) = \frac{1}{\left|\hat{E}_{ref}(\omega_k)\hat{E}_{sam}(\omega_k)\right|^2}\sum_{m=0}^{M-1}\mathrm{Re}^2\left[\hat{E}_{sam}(\omega_k)\exp\left(\frac{i2\pi km}{M}\right)\right]s_{E_{sam}}^2(t_m) +$$

$$\frac{\left|\hat{E}_{sam}(\omega_k)\right|^2}{\left|\hat{E}_{ref}(\omega_k)\right|^6}\sum_{m=0}^{M-1}\mathrm{Re}^2\left[\hat{E}_{ref}(\omega_k)\exp\left(\frac{i2\pi km}{M}\right)\right]s_{E_{ref}}^2(t_m)$$

and (67)

$$s_{\Phi,\hat{E}}^2(\omega_k) = \frac{1}{\left|\hat{E}_{sam}(\omega_k)\right|^4}\sum_{m=0}^{M-1}\mathrm{Im}^2\left[\hat{E}_{sam}(\omega_k)\exp\left(\frac{i2\pi km}{M}\right)\right]s_{E_{sam}}^2(t_m) +$$

$$\frac{1}{\left|\hat{E}_{ref}(\omega_k)\right|^4}\sum_{m=0}^{M-1}\mathrm{Im}^2\left[\hat{E}_{ref}(\omega_k)\exp\left(\frac{i2\pi km}{M}\right)\right]s_{E_{ref}}^2(t_m).$$

All indices conform to the definitions given in Eq. (37). Variables in Eq. (67) could be expressed in the form of $\hat{E}_{sam,k}$ to match the convention of Eq. (37) but are instead expressed as $\hat{E}_{sam}(\omega_k)$ for the sake of clarity. Only the subset of k used to form **b** are included in the calculation. Equation (67) changes as a function of DFT convention; a complete derivation that can be adapted for other DFT conventions is presented in the appendix of [73].

The contribution of uncertainty in the time axis to the phase variance ($s_{\Phi,\delta t}^2$) is directly added to the post-propagated phase variance in the frequency domain so that the total phase variance (s_Φ^2) is given by

$$s_\Phi^2(\omega_k) = s_{\Phi,\hat{E}}^2(\omega_k) + s_{\Phi,\delta t}^2(\omega_k). \quad (68)$$

Assuming the laser pulse is approximately Gaussian in the time domain with known pulse width FWHM (δt_{FWHM}), the temporal pulse shape approximately represents the normal distribution of the variance contribution from temporal axis uncertainty. In this case, the FWHM is equal to $2\sqrt{2\ln(2)}$ times the standard deviation of the temporal axis uncertainty distribution. Inserting this into the relation for the phase resolvability given in Eq. (47), the associated contribution to the phase variance becomes

$$s_{\Phi,\delta t}^2(\omega_k) = \frac{\delta t_{FWHM}^2 \omega_k^2}{8\ln(2)}. \tag{69}$$

The contribution of the temporal axis uncertainty on the magnitude variance depends nonlinearly on the frequency and has been found to be negligibly small compared to the other uncertainty contributions. The total amplitude variance (s_A^2) is therefore given by

$$s_A^2(\omega_k) = s_{A,\hat{E}}^2(\omega_k). \tag{70}$$

The above methods and equations for calculating the frequency-dependent variances of the magnitude and phase for single-scan THz-TDS should be viewed as a general framework rather than a specific recipe. More sophisticated methods may be used to improve estimates of the variance contributions of drift and time axis uncertainty in different measurement scenarios.

6.1.4 Computational Scheme

The posterior PDF is computed by directly sampling the right-hand side of a modified Bayes' equation. The directly sampled equation is the logarithm of Eq. (54), with explicit inclusion of the evidence removed:

$$\ln[p(\mathbf{x},\boldsymbol{\theta}|\mathbf{b})] \propto \ln[p(\mathbf{x},\boldsymbol{\theta})] + \ln[p(\mathbf{b}|\mathbf{x},\boldsymbol{\theta})]. \tag{71}$$

The corresponding logarithm of the prior PDF is given by

$$\ln[p(\mathbf{x},\boldsymbol{\theta})] = \ln[p(n_e)] + \ln[p(v)] + \ln[p(L)] + \ln[p(\varphi_2)] + \ln[p(r)], \tag{72}$$

the logarithms of the constituent prior PDFs are given by

$$\begin{gathered}
\ln[p(n_e)] = -\{\ln(n_e) + \ln[ln(n_{e,max}) - ln(n_{e,min})]\}, \\
\ln[p(v)] = -\{\ln(v) + \ln[ln(v_{max}) - ln(v_{min})]\}, \\
\ln[p(L)] = -\left\{\ln(s_L) + \frac{1}{2}\left[\ln(2\pi) + \left(\frac{L-\mu_L}{s_L}\right)^2\right]\right\}, \\
\ln[p(\varphi_2)] = \ln(1) - \ln(\varphi_{2,max} - \varphi_{2,min}),
\end{gathered} \tag{73}$$

and

$$\ln[p(r)] = \ln(1) - \ln(r_{max} - r_{min}),$$

and the logarithm of the likelihood PDF is given by

$$\ln[p(\mathbf{b}|\mathbf{x},\boldsymbol{\theta})] = -\frac{1}{2}\{N\ln(2\pi) + \ln(\det(\boldsymbol{\Gamma})) + (\mathbf{b}-\mathbf{b_{mod}})^{\mathrm{T}}\boldsymbol{\Gamma}^{-1}(\mathbf{b}-\mathbf{b_{mod}})\}, \tag{74}$$

where the logarithm of the determinant of the covariance matrix is given by

$$\ln(\det(\boldsymbol{\Gamma})) = 2\sum \mathrm{diag}\big(\mathrm{chol}(\boldsymbol{\Gamma})\big) \tag{75}$$

and $\mathrm{diag}\big(\mathrm{chol}(\boldsymbol{\Gamma})\big)$ denotes the diagonal of the Cholesky factorization of $\boldsymbol{\Gamma}$.

The use of logarithms makes the sampling scheme more computationally stable. Multivariate PDFs typically output very small probabilities that may be zero-rounded by a computer during numerical sampling. If, however, the logarithm of the PDF is directly computed, the output probabilities become finite negative numbers that are much easier for a computer to store in memory.

The purpose of not explicitly including the evidence PDF is to simplify computation. The evidence PDF does not change the shape of the output posterior PDF – it serves to normalize the posterior PDF so that its integral is unity. Normalization of the posterior PDF and, equivalently, computation of the evidence is easily achieved after sampling.

The right-hand side of Eq. (71) is sampled with an algorithm that produces a so-called Markov chain of $\mathbf{x}$ and $\boldsymbol{\theta}$ that forms a representative sampling of the posterior PDF. The sampling algorithm used here is the multivariate slice sampling method described by Neil [81]. The basic sampling steps for a univariate PDF ($p(x)$) slice sampling algorithm are as follows [80]:

1. With a random uniform draw, choose an initial value of x_i within the domain of $p(x)$
2. With a random uniform draw, choose a "slice" height value of y_{slice} from 0 to $p(x_i)$
3. Iteratively determine the slice interval by identifying the values of x that satisfy $y_{slice} \leq p(x)$
4. Randomly choose a sample value (x_{sample}) from the slice interval and add this to the Markov chain
5. Set $x_i = x_{sample}$ and repeat steps 2-4.

The basic algorithm is similar for the multivariate case, except that "slices" become multidimensional regions of the parameter space. Slice sampling was chosen for this work because the slice sampling algorithm does not require input of a proposal distribution. Slice sampling is therefore easily applied to a wide range of distributions of unknown shape. Robust implementations of the slice sampling algorithm are available in many software packages.

The algorithm is executed and samples are added to the Markov chain until a sampling termination criterion is met. Good results (evaluated in Section 6.1.5) were achieved in this work by doubling the Markov chain length until doubling of the length changed the mean distribution value of both the electron density and collision frequency by less than 0.5%. The initial chain length is 10,000 samples, so the first evaluation occurs at 20,000 samples. The sampling termination criterion was achieved after 80,000 or 160,000 samples for most cases but required as many as 1,280,000 samples in some cases. More computing power would enable the use of a stricter criterion, but it was found that

requiring 0.1% or 0.01% change after length doubling significantly increased computational time without appreciably impacting the results.

Because the Markov chain constitutes a representative sampling of the multivariate posterior PDF, the relevant univariate or multivariate posterior PDF samplings are formed by simply discarding unneeded parameter dimensions from the Markov chain. The most probable estimate of each parameter is therefore computed as the mean of the Markov chain computed along that parameter's dimension, according to Eq. (57). Credibility intervals are formed by computing the empirical cumulative probability distribution along each relevant parameter dimension and numerically approximating the boundaries that satisfy Eq. (58).

6.1.5 Ideal Data Verification

The basic efficacy of the Bayesian inference scheme was tested by comparing the output results to ideal input data. Ideal values of A and Φ corresponding to input electron density, collision frequency, and plasma length were manufactured with Eq. (28) to produce ideal $\mathbf{b}$ vectors for various input conditions. The Bayesian inference scheme was run with these ideal input vectors, small variances ($s_A^2 = s_\Phi^2 = 1 \times 10^{-16}$), and the input prior PDF parameters given by Table 6. The uniform plasma length prior PDF with small width was used to virtually eliminate dependence of the output electron density on uncertainty in the plasma length. The ideal input plasma conditions are shown in Table 7, and the resulting differences between the input conditions and means of the Bayesian inference output posterior PDFs are shown in Figure 96 and Figure 97.

Table 7 – Ideal data verification conditions

Electron Density (m^{-3})	Electron Collision Frequency (Hz)
1.00×10^{18}	1.00×10^{9}
1.67×10^{18}	2.15×10^{9}
2.78×10^{18}	4.64×10^{9}
4.64×10^{18}	1.00×10^{10}
7.74×10^{18}	2.15×10^{10}
1.29×10^{19}	4.64×10^{10}
2.15×10^{19}	1.00×10^{11}
3.59×10^{19}	2.15×10^{11}
6.00×10^{19}	4.64×10^{11}
1.00×10^{20}	1.00×10^{12}

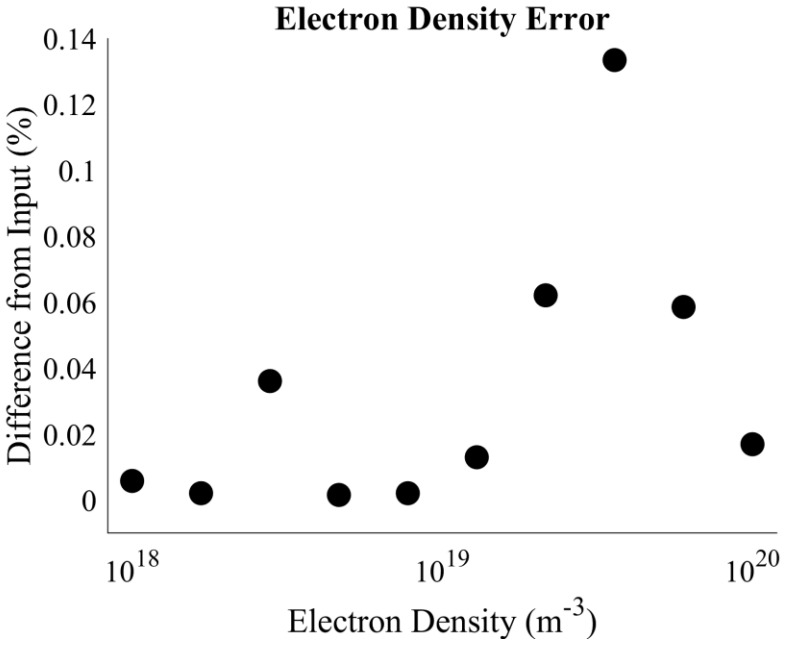

Figure 96 – Difference between input ideal electron density and mean of output posterior PDF

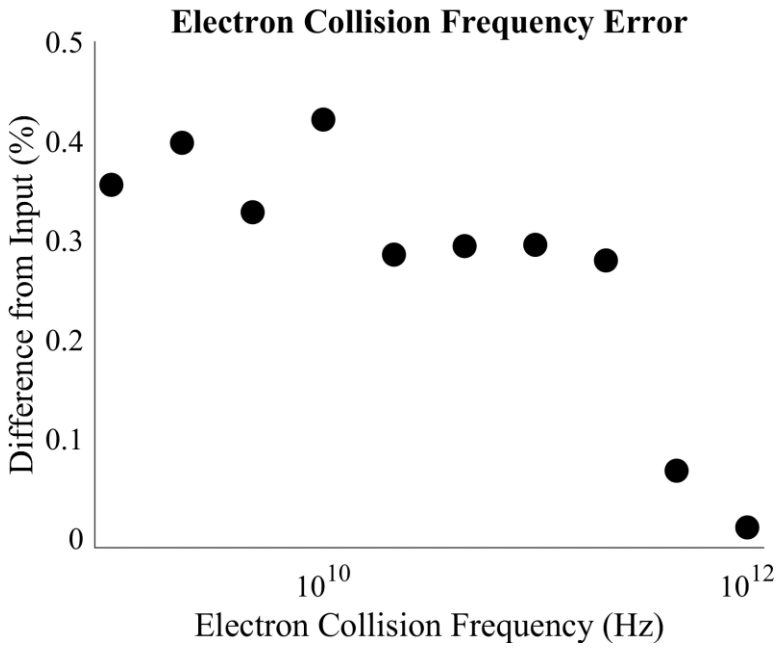

Figure 97 – Difference between input ideal electron collision frequency and mean of output posterior PDF

Differences between the input and output values are less than 1% in each case. No data corrections are necessary for the ideal input data, and the Bayesian inference scheme correctly settled on mean values of 0 and 1 (within 0.01%) for the phase and magnitude correction factors, respectively, for each case. These results demonstrate that the Bayesian inference scheme outlined in this chapter is able to correctly calculate the electron density and collision frequency. Importantly, these results also show that, across the orders of magnitude relevant to this work, the means of the posterior PDFs are independent of the input prior PDFs. All error is caused by numerical rounding and can be reduced through the use of a stricter termination criterion.

6.1.6 Impact of Plasma Length Prior PDF

As discussed in Section 5.1.2 in the context of this work, the line-integrated electron density and average electron collision frequency are virtually independent of the assumed plasma length and distribution. Standard practice in THz-TDS plasma diagnostic data analysis is to assume a uniform plasma length. The reported electron density is then a value that has been normalized by an assumed plasma length, whereas the electron collision frequency is a true average value. The data presented in Section 4.2 follows this convention.

By definition, if reporting a normalized electron density, uncertainties in the assumed plasma length should not be included in the normalized electron density uncertainty evaluation. In this case, the uniform plasma length prior PDF with small width should be used to eliminate uncertainty in the plasma length from the normalized electron density uncertainty.

The RF ICP discharge, however, produces an approximately uniform plasma along the THz pulse path [45, 68]. The reported electron density could therefore correspond to either a normalized or average value. If reporting an average electron density value, uncertainties in the assumed plasma length should indeed be included in the reported density uncertainty. In this case, the normal plasma length prior PDF should be employed.

Figure 98 shows the impact of changing the mean of the normal plasma length prior PDF on the output average electron density PDF for the 200 W, 1 Torr case. Increasing the mean of the prior PDF decreases the mean of the output electron density PDF and widens the distribution. Figure 99 shows the impact of changing the width of the prior PDF on the resulting electron density PDF. Increasing the standard deviation increases the width of the

electron density PDF and decreases its mean value. The calculated electron density and uncertainty are highly sensitive to the input plasma length prior PDF.

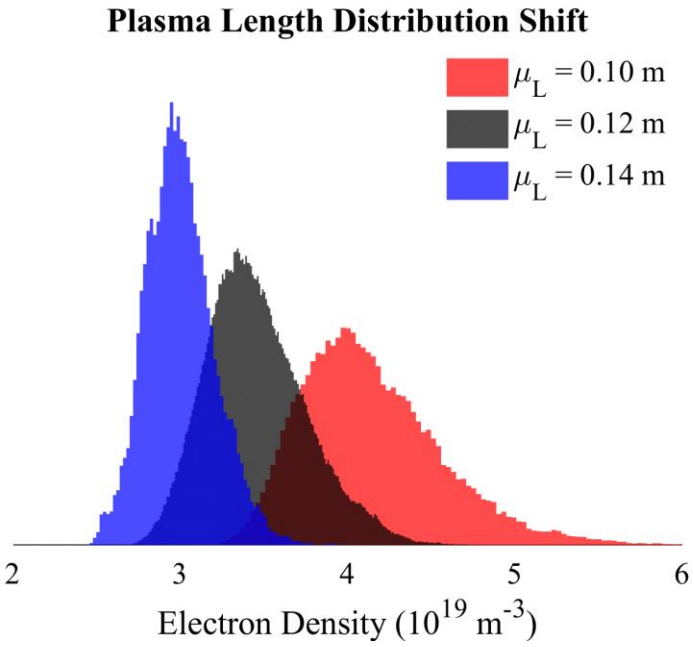

Figure 98 – Impact of shifting plasma length prior PDF mean on average electron density PDF (200 W, 1 Torr)

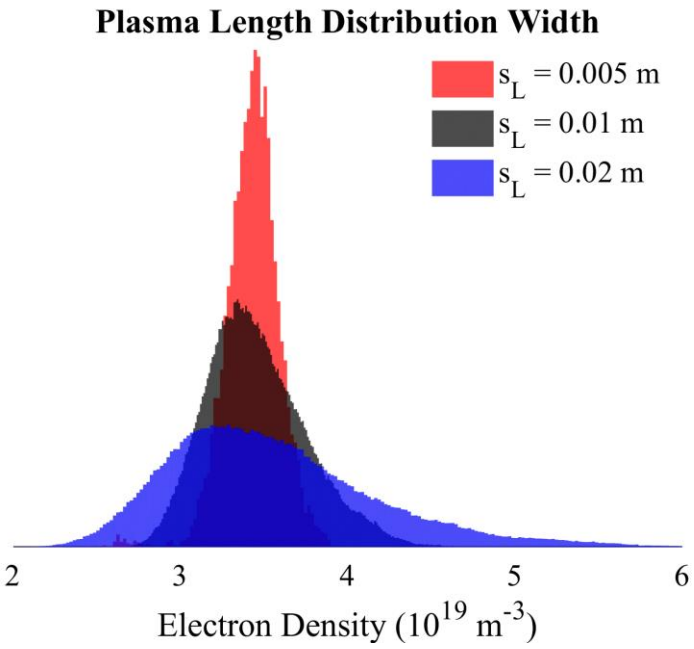

Figure 99 – Impact of plasma length prior PDF width on average electron density PDF (200 W, 1 Torr)

Figure 100 and Figure 101 show the impact of changing the mean and standard deviation of the normal plasma length prior PDF on the output average electron collision frequency PDF for the 200 W, 1 Torr case. As expected, differences in the resulting PDFs are negligible compared to the variance expected among different sampling iterations. It is notable, however, that increasing the standard deviation increases the Markov chain length. This is evident in Figure 101, where the histogram resolution increases with increased standard deviation.

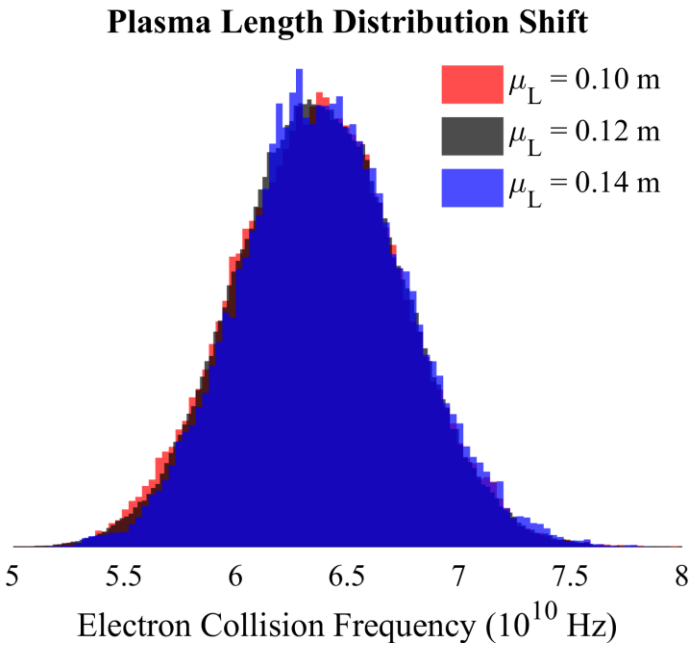

Figure 100 – Impact of shifting plasma length prior PDF mean on average electron collision frequency PDF (200 W, 1 Torr)

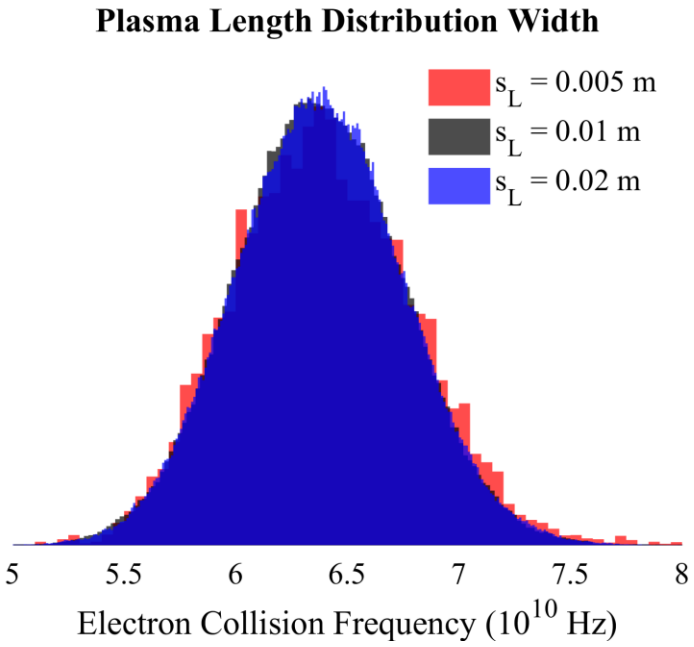

Figure 101 – Impact of plasma length prior PDF width on average electron collision frequency PDF (200 W, 1 Torr)

6.2 Plasma Property Results with Uncertainty Quantification

This section presents the Bayesian analysis results of the plasma measurements provided in Section 4.2. The results presented in this section differ from those in Section 4.2 in two important ways: electron collision frequency is computed and uncertainty is quantified. Section 6.2.1 presents Bayesian inference results computed with the uniform plasma length prior PDF and Section 6.2.2 presents the Bayesian inference results computed with the normal plasma length prior PDF. The results in Section 6.2.1 are directly comparable to those of Section 4.2 because, in both cases, the reported electron density is a line-integrated value that has been normalized by a quasi-arbitrary plasma length. Section 6.2.2 differs from Section 6.2.1 by reporting a true average electron density that incorporates nonzero uncertainty in the measured plasma length.

6.2.1 Plasma Property Results (Normalized Line-Integrated Density)

6.2.1.1 Electron Density and Collision Frequency

Figure 102 shows the normalized electron density for all plasma conditions, and Figure 103 shows the normalized electron density for the low-pressure conditions. Figure 104, Figure 105, Figure 106, and Figure 107 show the average electron collision frequency for all conditions, high-pressure conditions, 100 mTorr conditions, and 50 mTorr conditions, respectively. In all plots, error bars encompass a 2-sigma credibility interval (68.27…%). The error bars in Figure 102 are smaller than the data points.

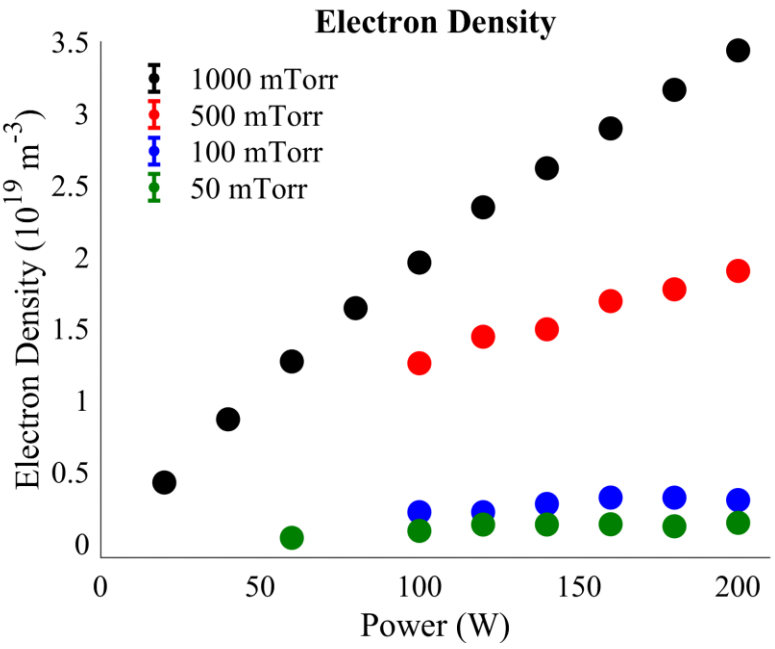

Figure 102 – Normalized electron density

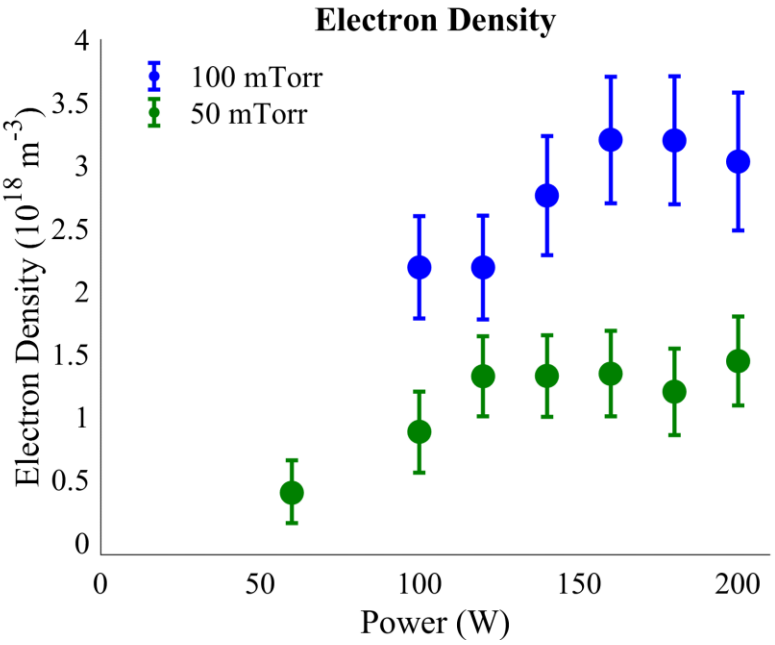

Figure 103 – Normalized electron density (low-pressure conditions)

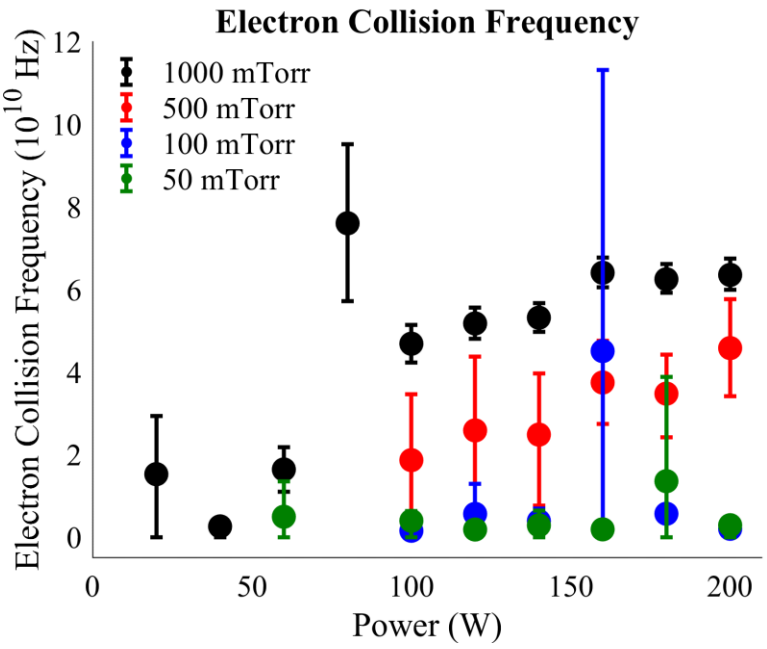

Figure 104 – Electron collision frequency

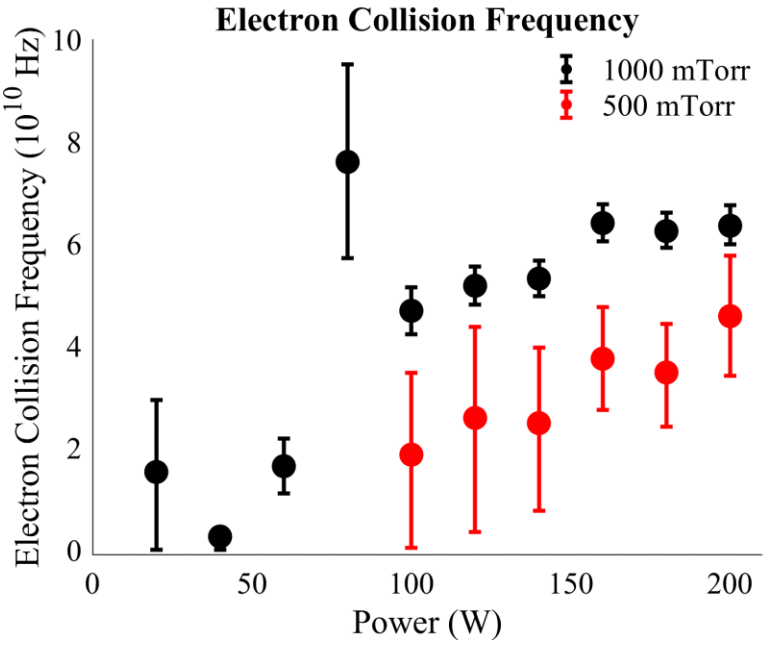

Figure 105 – Electron collision frequency (high-pressure conditions)

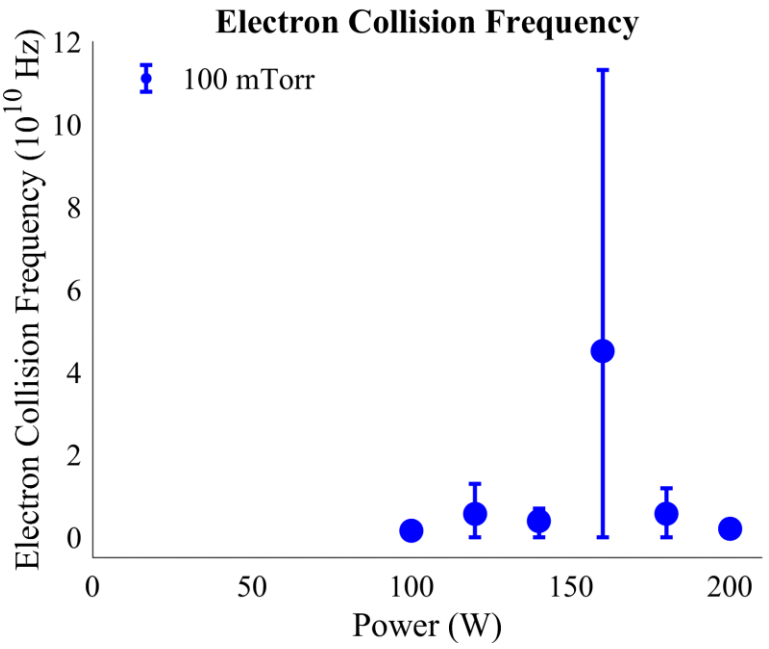

Figure 106 – Electron collision frequency (100 mTorr conditions)

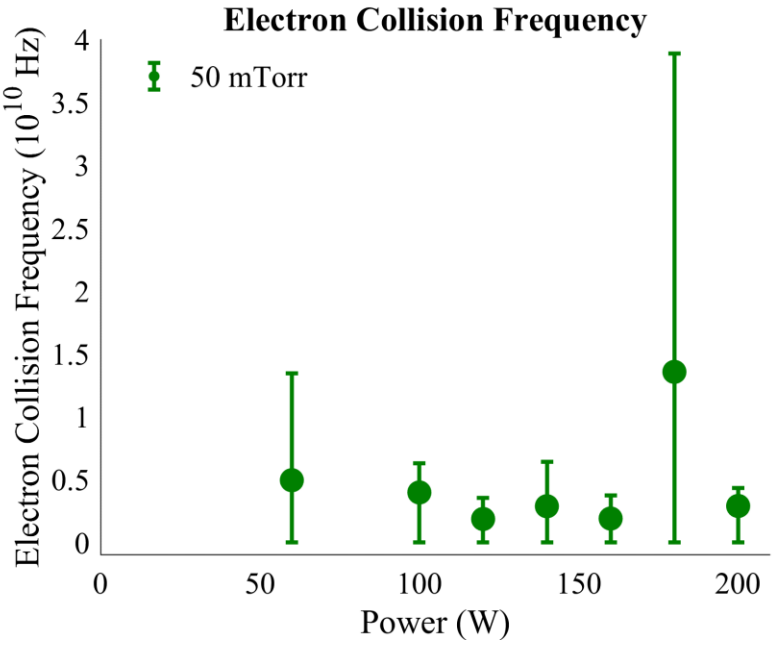

Figure 107 – Electron collision frequency (50 mTorr conditions)

Comparison of Figure 102 with Figure 35 shows that the normalized electron density values and trends are essentially identical for the standard and Bayesian analyses. The electron density computed for the 200 W, 1 Torr case, for example, differs by less than 0.03% between the two calculation methods.

The Bayesian results, however, reveal trends in the electron collision frequency. At 1 Torr, the electron collision frequency increases with power with decreasing rate as it approaches 6×10^{10} Hz at 200 W. Data points that deviate from this trend are accompanied by large uncertainties. Increasing electron collision frequency with increasing power is also apparent in the 500 mTorr data. The 100 mTorr and 50 mTorr conditions do not exhibit any discernable trends with power. However, for a given power, increasing the pressure tends to increase the electron collision frequency.

The absolute value of the total uncertainty decreases with decreasing electron density and collision frequency until the resolvability limits discussed in Section 5.2.1 are reached and the uncertainty does not change. However, the relative value of the uncertainty (with respect to the most probable value) increases with decreasing electron density and collision frequency and continues to increase beyond the resolvability limits. As shown in the plots above, the uncertainty near the resolvability limits changes abruptly with power and pressure. This indicates that the uncertainty at these values is highly sensitive to plasma conditions or differences in THz pulse properties that vary with each measurement.

6.2.1.2 Posterior PDFs

Figure 108, Figure 109, Figure 110, and Figure 111 show the posterior PDFs of the electron density, collision frequency, phase correction factor (φ_2), and magnitude correction factor (r), respectively, for the 200 W, 1 Torr condition. Figure 112 additionally

plots the joint PDF of the electron density and collision frequency. These plots are included here to show examples of the output data used to construct the figures in the previous section. It is important to note that Figure 112 does not suggest any correlation between the electron density and collision frequency, thereby supporting the form of the prior PDF discussed in Section 6.1.3.2.

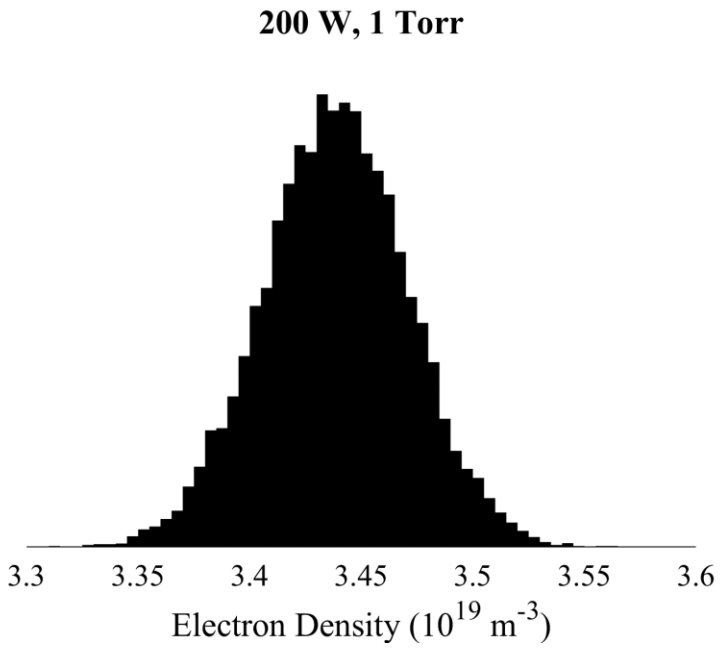

Figure 108 – Normalized electron density PDF (200 W, 1 Torr)

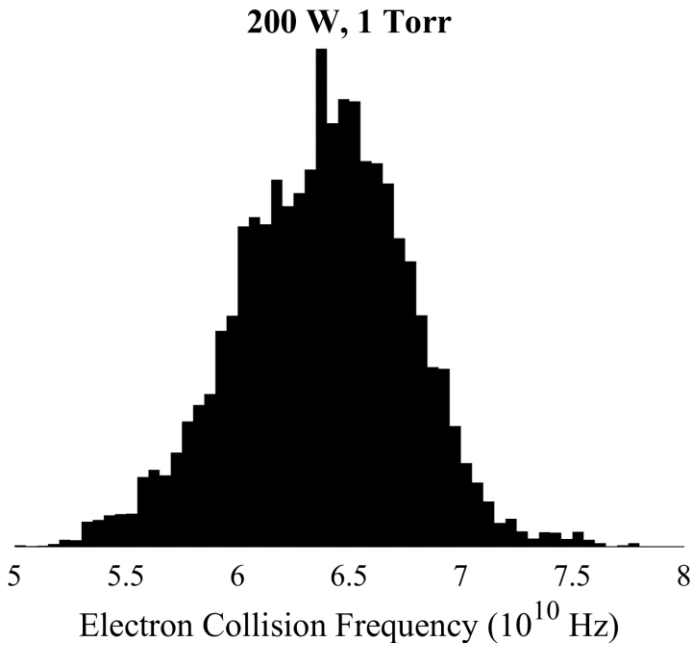

Figure 109 – Average electron collision frequency PDF (200 W, 1 Torr)

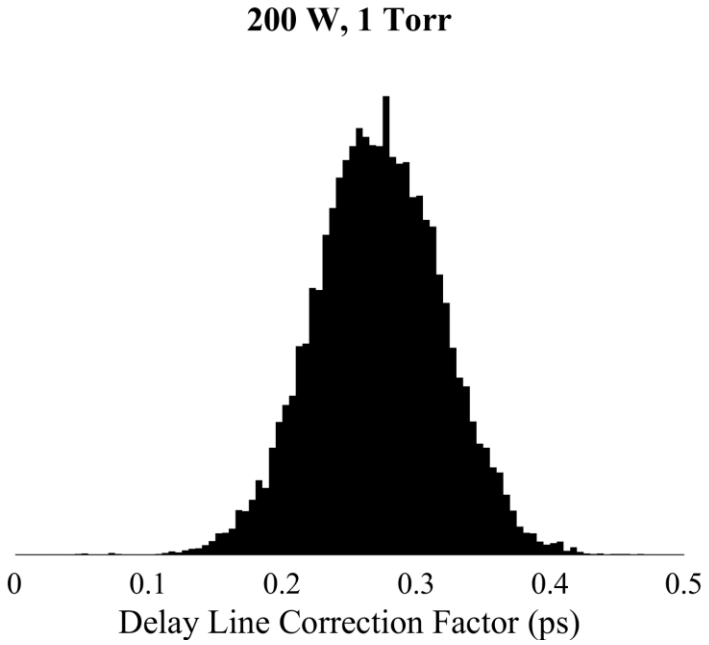

Figure 110 – Delay line correction factor PDF (200 W, 1 Torr)

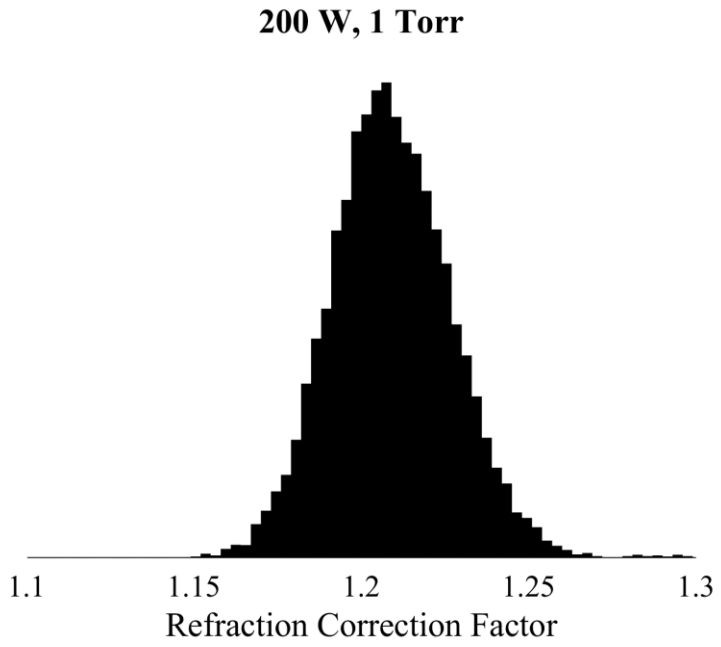

Figure 111 – Refraction correction factor PDF (200 W, 1 Torr)

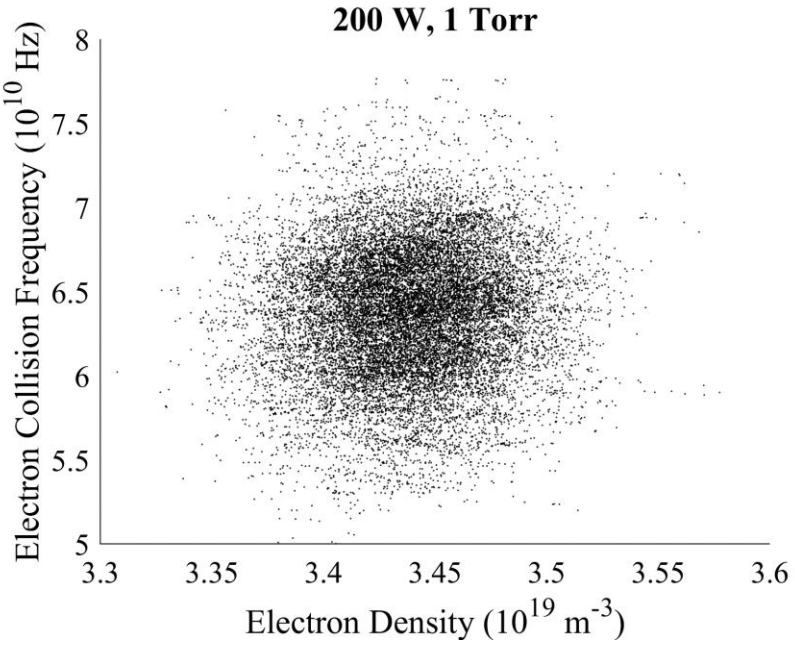

Figure 112 – Combined normalized electron density and average electron collision frequency PDF (200 W, 1 Torr)

6.2.2 Plasma Property Results (Average Density)

6.2.2.1 Electron Density and Collision Frequency

Figure 113 shows the average electron density for all plasma conditions, and Figure 114 shows the average electron density for the low-pressure conditions. Figure 115, Figure 116, Figure 117, and Figure 118 show the average electron collision frequency for all conditions, high-pressure conditions, 100 mTorr conditions, and 50 mTorr conditions, respectively. In all plots, error bars encompass a 2-sigma credibility interval (68.27…%). Some of the error bars in Figure 113 are smaller than the data points.

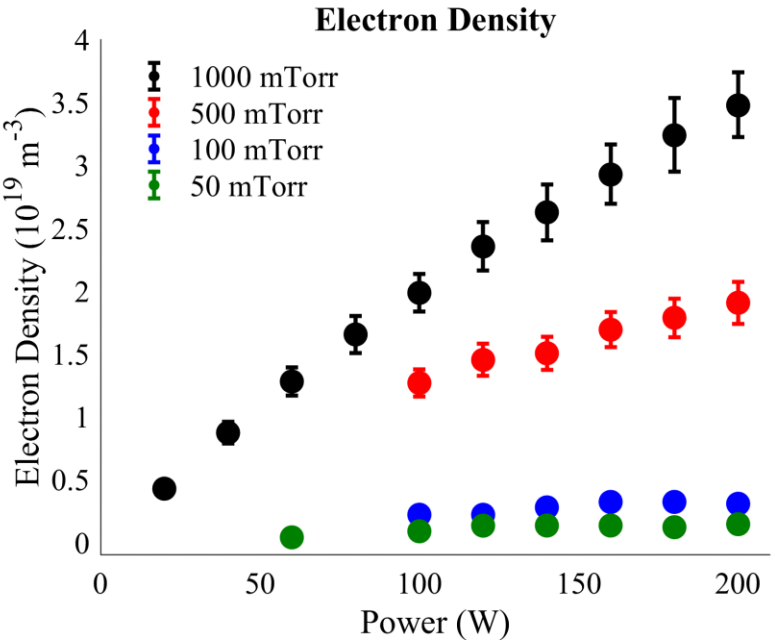

Figure 113 – Average electron density

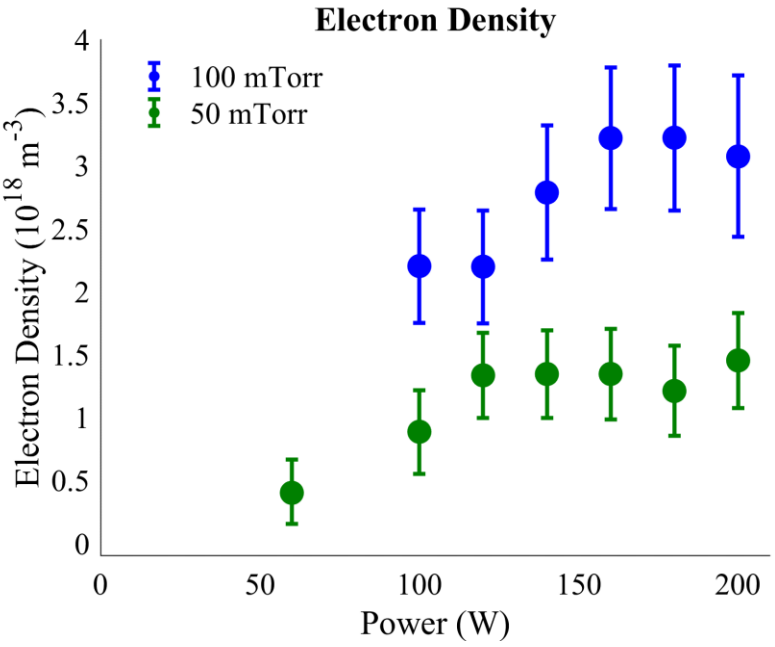

Figure 114 – Average electron density (low-pressure conditions)

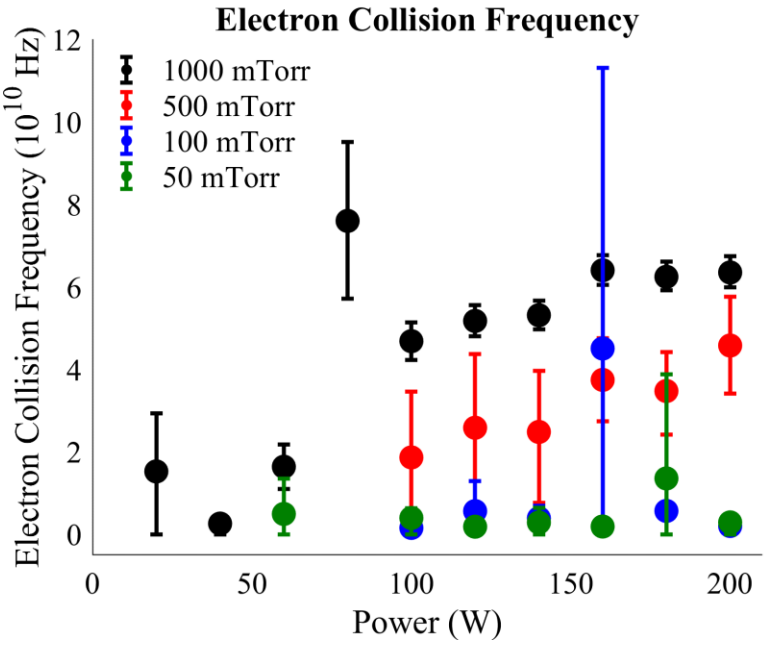

Figure 115 – Electron collision frequency

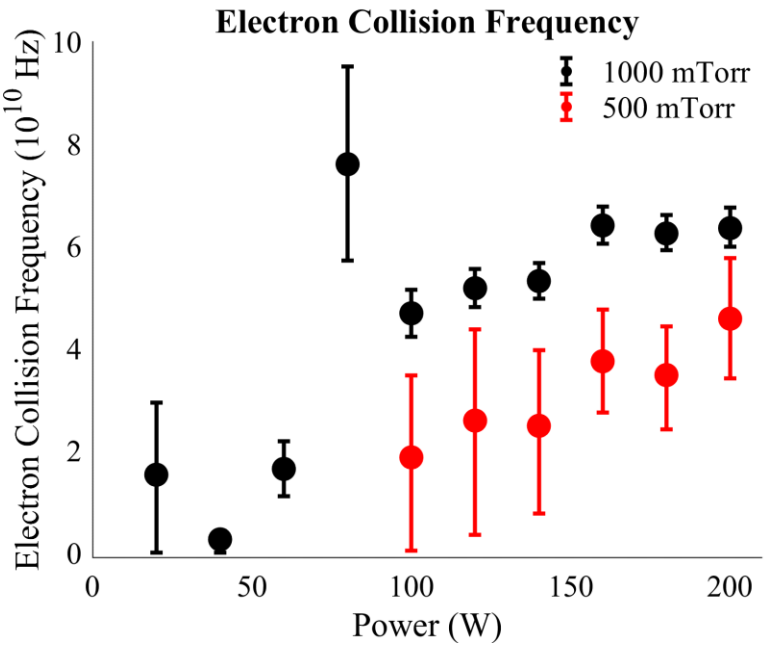

Figure 116 – Electron collision frequency (high-pressure conditions)

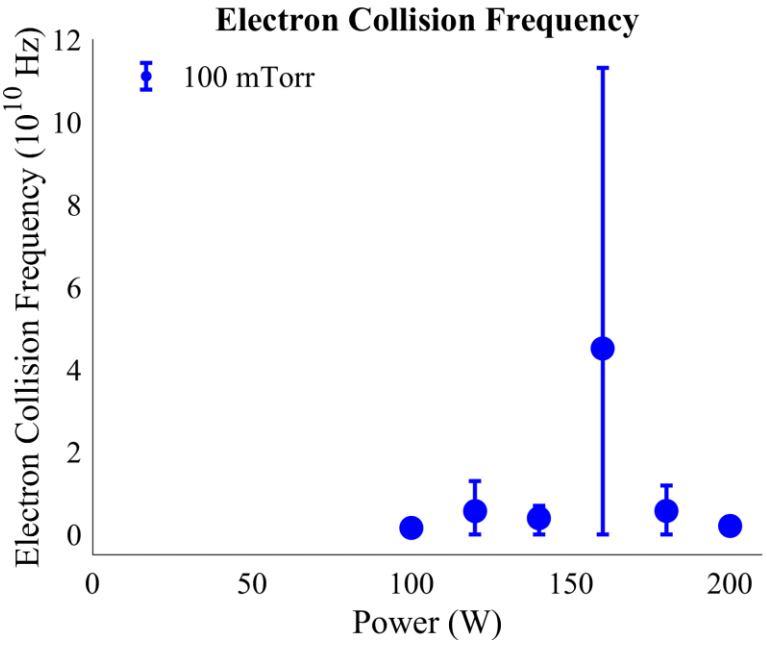

Figure 117 – Electron collision frequency (100 mTorr conditions)

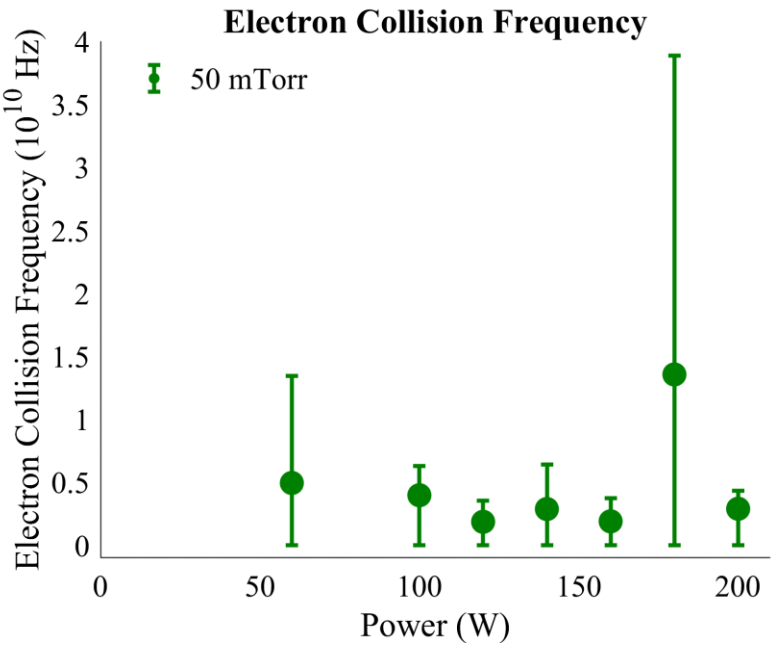

Figure 118 – Electron collision frequency (50 mTorr conditions)

The average electron density trends are similar to those of the normalized electron density. However, the implementation of a finite-width prior PDF for the plasma length increases the uncertainty of the data. This is apparent in Figure 113, where many error bars are large enough to be observed. The uncertainty bar width in the 200 W, 1 Torr case, for example, is approximately eight times greater for the average electron density than for the normalized electron density. Contrary to the electron density data, use of a finite-width prior PDF for the plasma length does not impact the electron collision frequency uncertainty. As discussed in Section 6.1.6, this outcome is expected.

6.2.2.2 Posterior PDFs

Figure 119, Figure 120, Figure 121, and Figure 122 show the posterior PDFs of the electron density, collision frequency, phase correction factor (φ_2), and magnitude

correction factor (r), respectively, for the 200 W, 1 Torr condition. Figure 123 additionally plots the joint PDF of the electron density and collision frequency. As expected, the general shapes and locations of the posterior PDFs are not impacted by the use of a finite-width plasma length prior PDF. However, the electron density and correction factor PDFs are wider than their counterparts in Section 6.2.1.2. The electron density PDF also appears to skew slightly to the left, indicating that the assumed uniform plasma length may be somewhat larger than the actual value. All the histograms have higher resolution than those in Section 6.2.1.2 because achievement of the termination criterion required generation of a longer Markov chain.

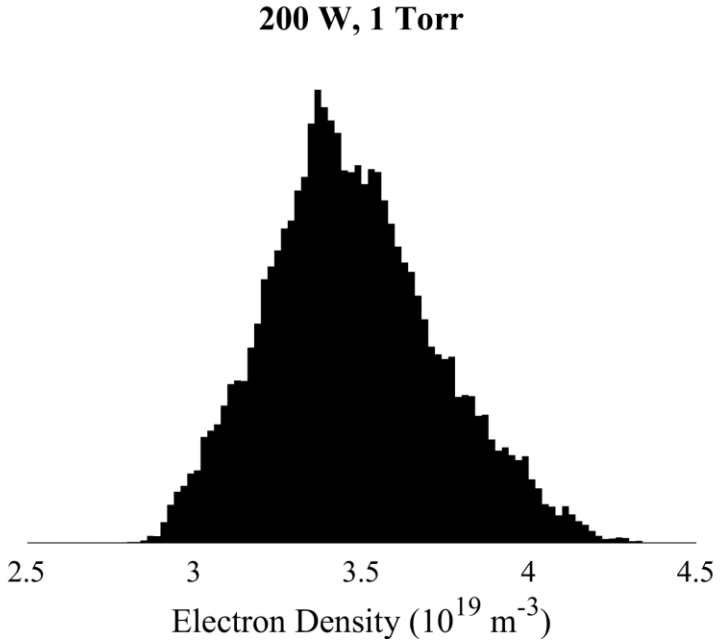

Figure 119 – Average electron density PDF (200 W, 1 Torr)

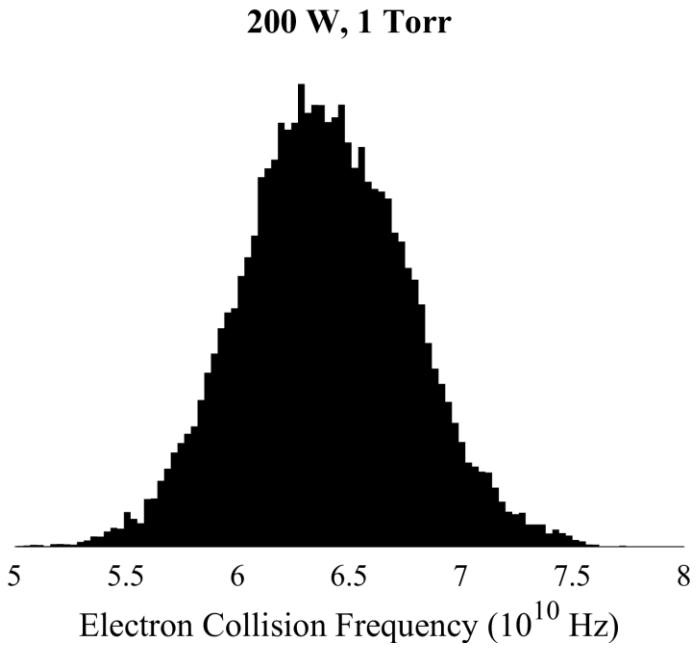

Figure 120 – Average electron collision frequency PDF (200 W, 1 Torr)

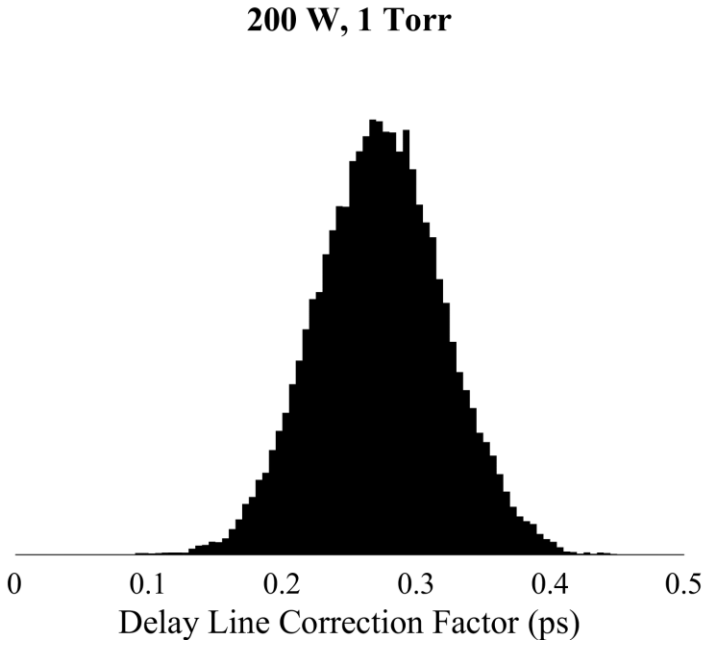

Figure 121 – Delay line correction factor PDF (200 W, 1 Torr)

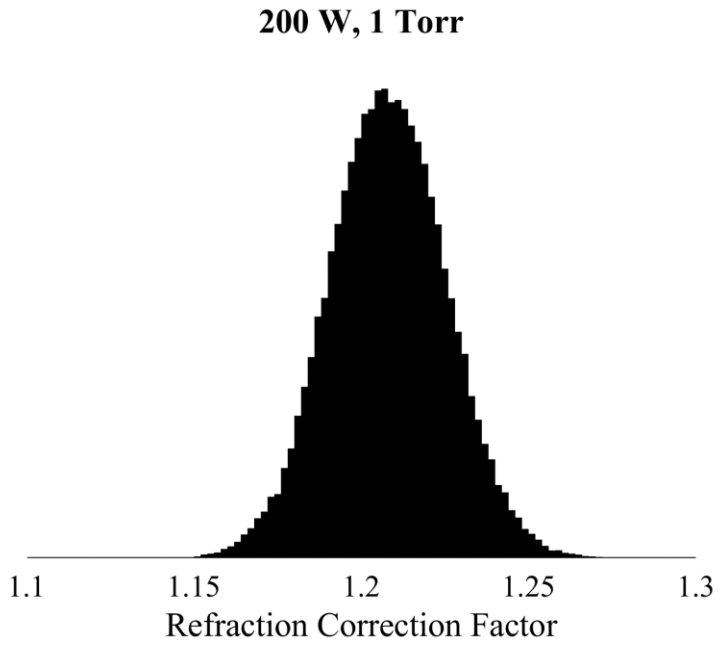

Figure 122 – Refraction correction factor PDF (200 W, 1 Torr)

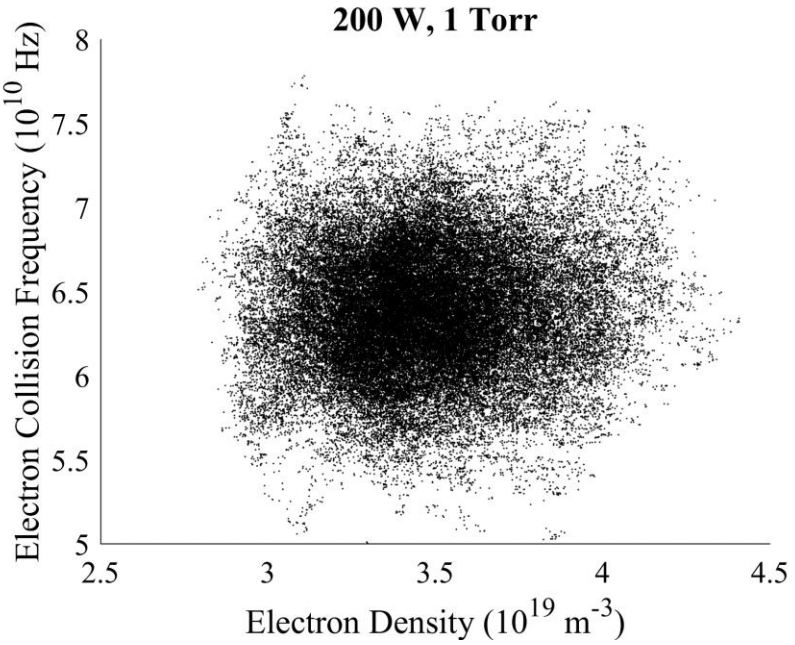

Figure 123 – Combined average electron density and average electron collision frequency PDF (200 W, 1 Torr)

6.3 Impact of THz Pulse Properties on Plasma Property Results

This section investigates the impact of THz pulse properties on the uncertainty of the output average electron density and collision frequency. The findings of this section carry implications regarding the uncertainty penalties incurred for altering pulse properties to save measurement time and equipment cost.

A single baseline measurement was taken with the RF ICP discharge operating at 200 W and 1 Torr. The baseline sample and reference pulses were then altered to generate the pulse variants discussed in each section. This method was used to eliminate possible day-to-day variation in RF ICP discharge or THz-TDS system operation. The plasma condition produces readily measurable electron density and collision frequency well within the measurement limits of the THz-TDS system. Changes in uncertainty caused by differences in pulse properties are, therefore, not primarily driven by changes in measurement capability.

In each case, the Bayesian inference scheme with the normal plasma length prior PDF was used to calculate parameter uncertainties. All error bars encompass a 2-sigma credibility interval (68.27…%). Section 6.3.1 shows the baseline reference and sample pulses, and Sections 6.3.1, 6.3.2, 6.3.4, and 6.3.5 demonstrate the impact of pulse duration, pulse resolution, number of samples recorded at each delay line position, and signal SNR on parameter uncertainty, respectively.

6.3.1 Baseline Pulses

As summarized in Table 8, the reference and sample baseline pulses have a temporal duration of 100 ps, temporal resolution of 50 fs, and are averaged across 1000 samples

recorded at each delay line position. Here, “temporal resolution” refers to both the step size of the delay line and the approximate FWHM of the THz pulse. Figure 124 shows the baseline reference pulse, and Figure 125 shows both the baseline reference and sample pulses. The secondary pulse near 60 ps is caused by internal FP reflections in the viewport windows. Because this FP-reflected pulse is present in both the sample and reference pulses, it does not need to be considered separately in the transfer function.

Table 8 – Baseline pulse parameters

Parameter	Value
Temporal Duration	100 ps
Temporal Resolution	50 fs
Number of Samples	1000

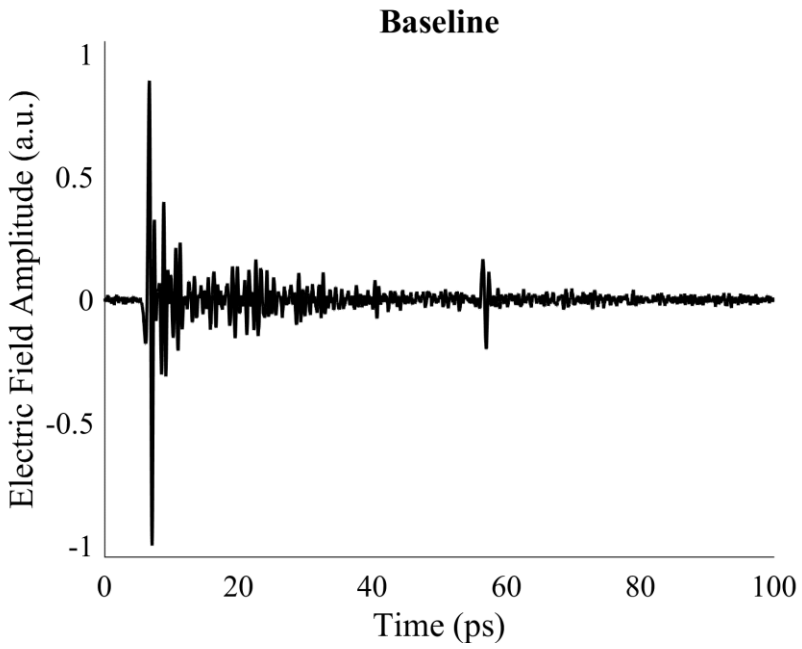

Figure 124 – Baseline reference pulse

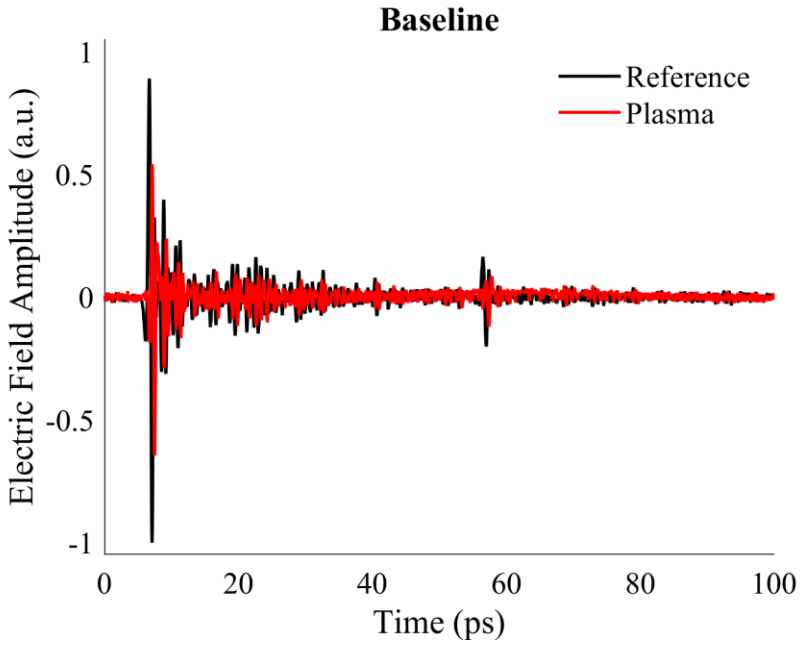

Figure 125 – Baseline reference and sample pulses (200 W, 1 Torr)

6.3.2 Pulse Duration

The baseline reference and sample pulses were trimmed to generate THz pulses with shorter durations. In all cases, except for the 7 ps pulses, the baseline pulse was trimmed only from the pulse end. The 7 ps pulses were created by trimming from both the beginning and end of the baseline pulses to avoid clipping the largest electric field values. Figure 126 shows the 10 ps reference pulse, and Figure 127 shows the 7 ps reference pulse. The penalty for trimming the beginning portion to generate the 7 ps pulse is that the 7 ps pulse tip has insufficient length to provide proper data leveling (discussed in Section 4.1.1.1). The pulse therefore appears tilted with respect to the plot axes.

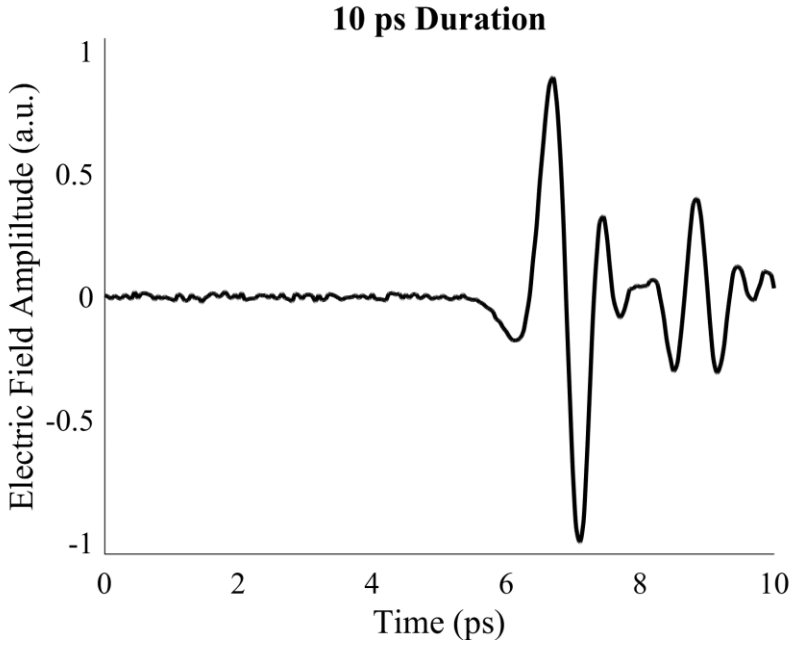

Figure 126 – 10 ps reference pulse

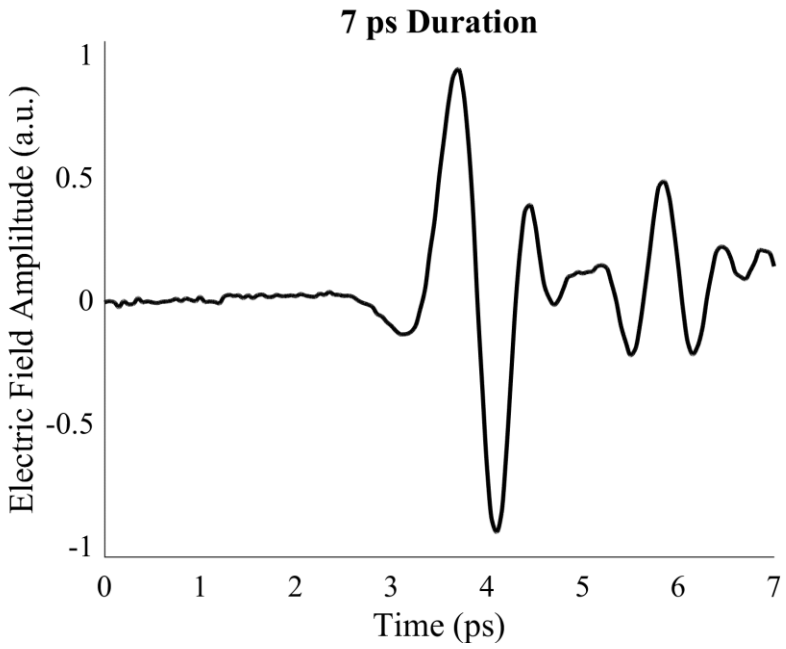

Figure 127 – 7 ps reference pulse

Figure 128 shows the calculated average electron density plotted as a function of pulse duration, and Figure 129 shows the calculated average electron collision frequency plotted as a function of pulse duration. Increasing pulse duration does not monotonically decrease the average electron density uncertainty. This is because multiple frequencies with resolvable phase for the electron density can be extracted from all pulse durations. The tilt in the 7 ps pulse does not contribute to enhanced electron density because the tilt has the same effect as the delay line registration error, which is corrected by the Bayesian inference scheme. Uncertainty in the plasma length, rather than uncertainty in phase measurement, dominates the electron density uncertainty.

The electron collision frequency uncertainty, however, more than quadruples when the pulse duration is decreased from 20 ps to 10 ps. According to the DFT given by Eqs. (37) and (38), decreasing the pulse duration decreases the number of resolvable

frequencies. The sharp increase in uncertainty with decreased pulse duration can therefore be attributed to the loss of THz frequencies with high SNR for these plasma conditions.

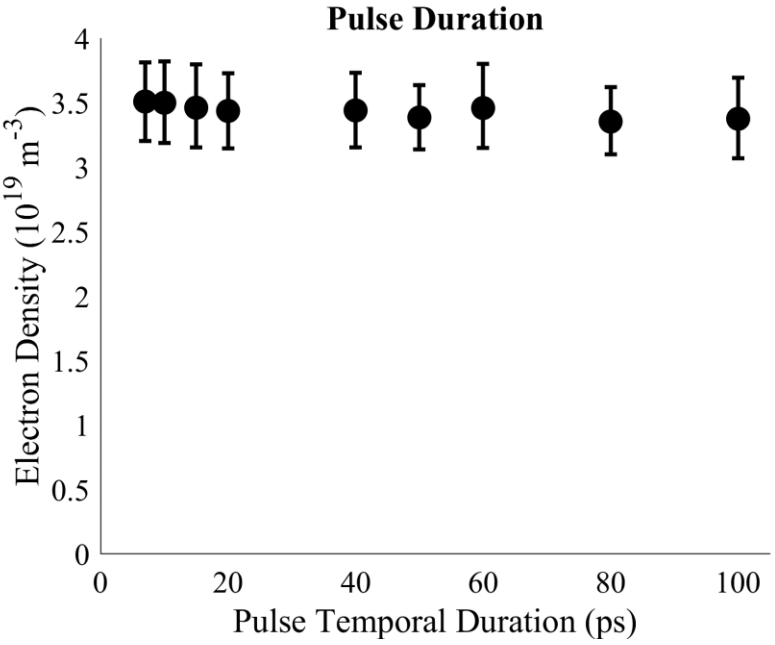

Figure 128 – Impact of pulse duration on calculated average electron density and uncertainty (200 W, 1 Torr)

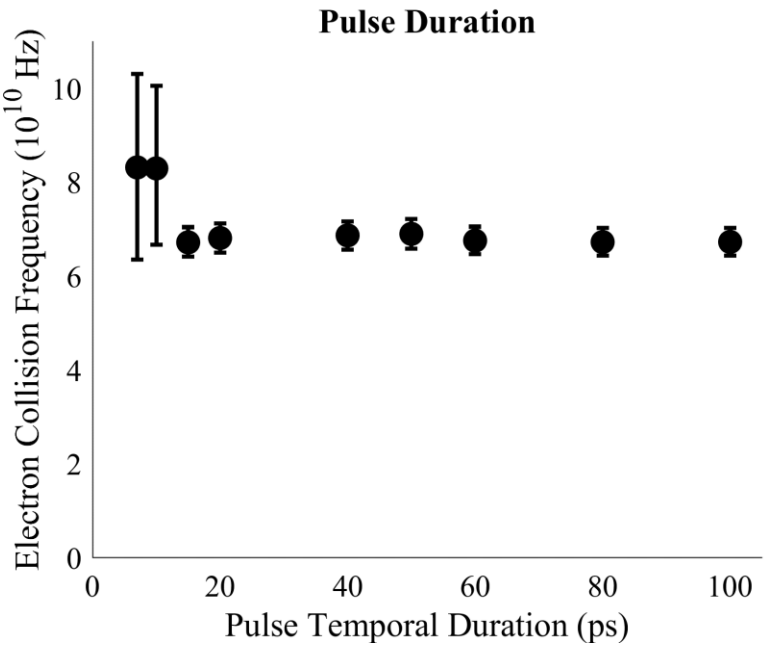

Figure 129 – Impact of pulse duration on calculated average electron collision frequency and uncertainty (200 W, 1 Torr)

6.3.3 Pulse Resolution

The baseline reference and sample pulses were re-sampled with lower temporal resolution to generate pulses for this section. Figure 130 shows the 250 fs resolution reference pulse.

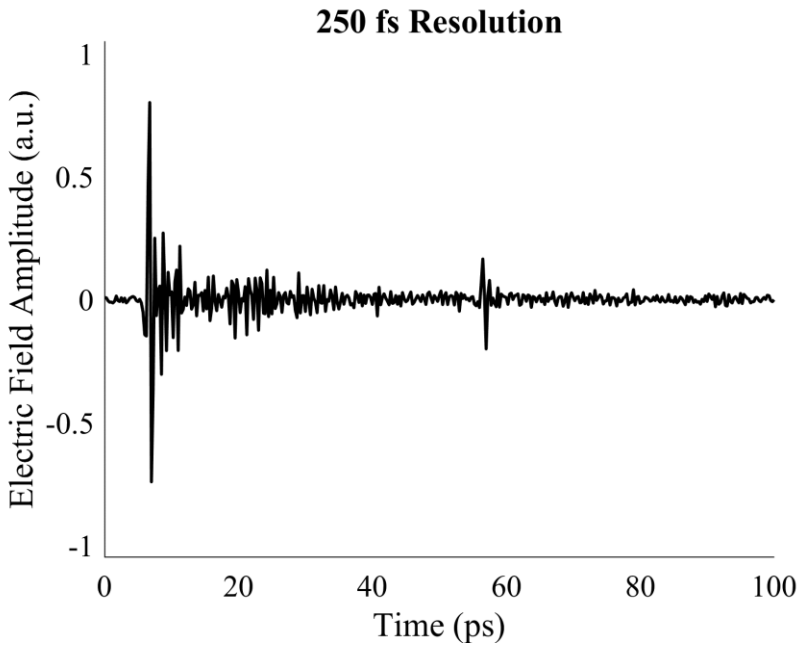

Figure 130 – 250 fs resolution pulse

Figure 131 and Figure 132 show the impact of the temporal pulse resolution on the calculated average electron density and collision frequency, respectively. The electron density calculation is relatively insensitive to the temporal resolution, whereas the electron collision frequency uncertainty approximately doubles when the temporal resolution increases from 100 to 150 fs. At these plasma conditions, the loss in phase resolution caused by the decrease in temporal resolution is insignificant compared to the uncertainty in the plasma length. This is because the loss in temporal resolution is not sufficient to increase the smallest resolvable electron density to the value of the measured electron density. The loss in temporal resolution from 100 to 150 fs directly results in loss of amplitude resolution and thereby causes the increase in collision frequency uncertainty.

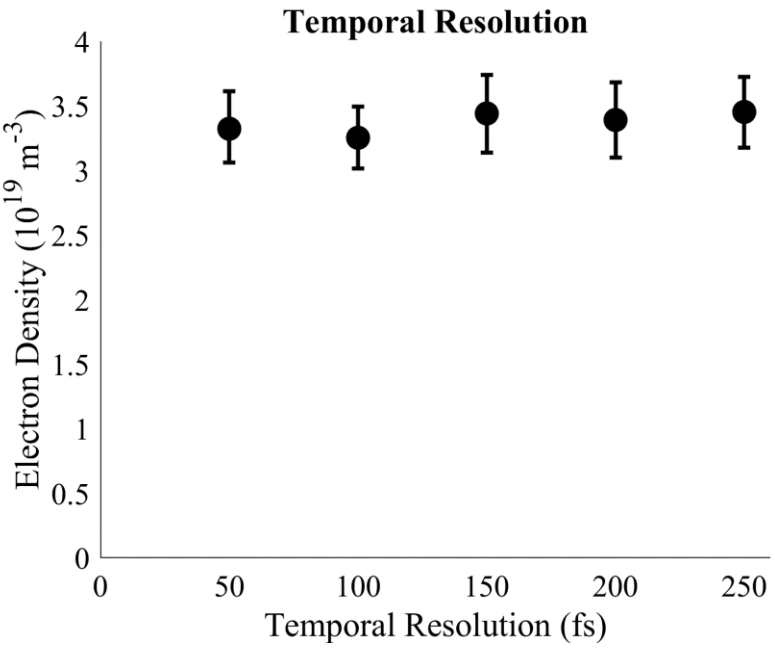

Figure 131 – Impact of pulse resolution on calculated average electron density and uncertainty (200 W, 1 Torr)

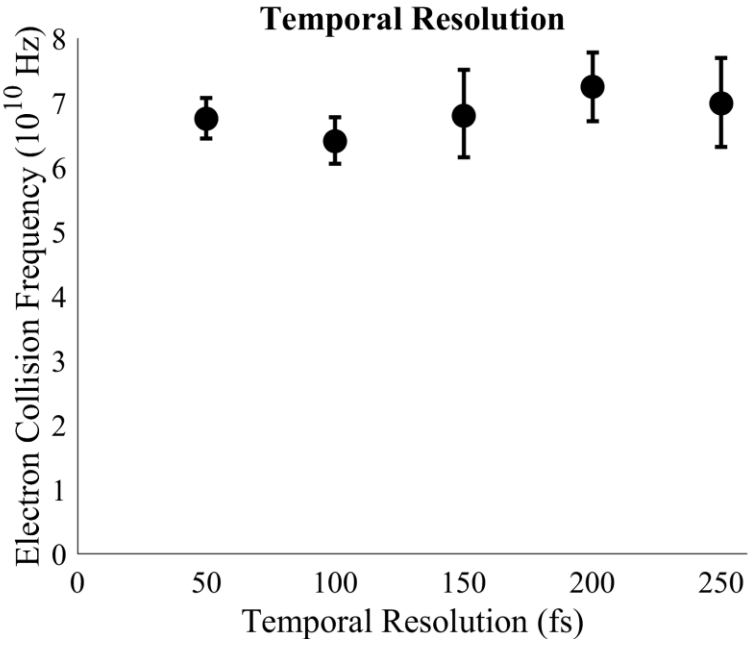

Figure 132 – Impact of pulse resolution on calculated average electron collision frequency and uncertainty (200 W, 1 Torr)

6.3.4 Number of Samples

The baseline reference and sample pulses were reconstructed with fewer samples at each delay line position. Figure 133 shows the pulse constructed from 10 samples at each delay line position. Differences between the 10 sample pulse and baseline (1000 sample pulse) are not discernible through comparison of Figure 124 and Figure 133.

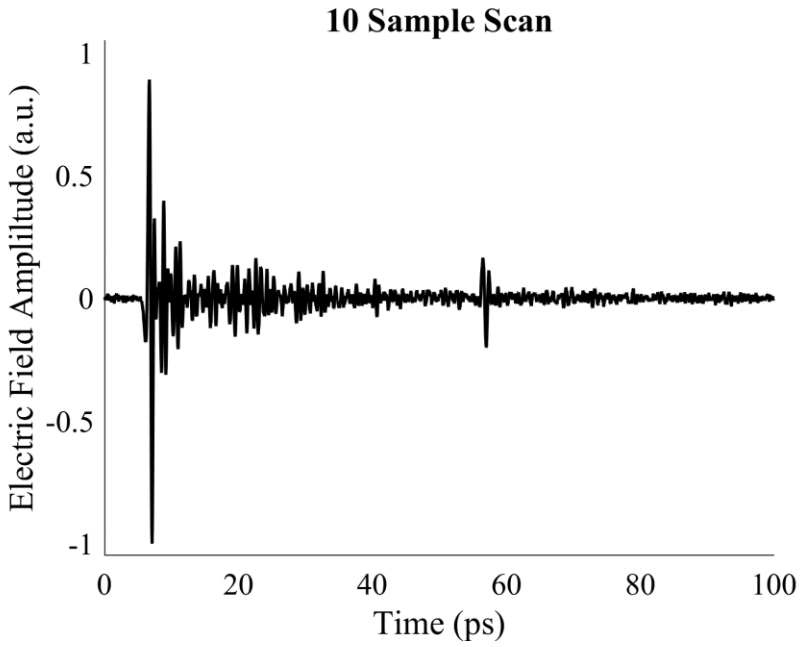

Figure 133 – 10 sample pulse

Figure 134 shows the calculated average electron density as a function of the number of samples, and Figure 135 shows the calculated average electron collision frequency as a function of the number of samples. In both cases, the results are insensitive to the number of samples. This result is somewhat unexpected, as decreasing the number of samples was originally expected to decrease the SNR. However, as shown in Figure 133, decreasing the number of samples does not significantly influence the SNR. The insensitivity of SNR and

subsequent insensitivity of uncertainty to the number of samples is driven by the lock-in detection method. The LIA operates as a filter and outputs a relatively smooth result, so sampling the output many times does not substantially increase the SNR.

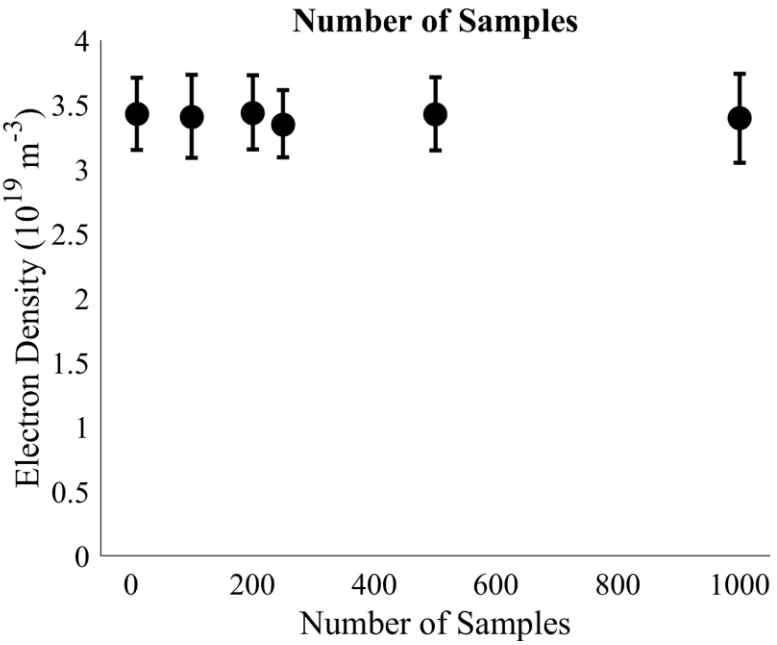

Figure 134 – Impact of number of sample averages on calculated average electron density and uncertainty (200 W, 1 Torr)

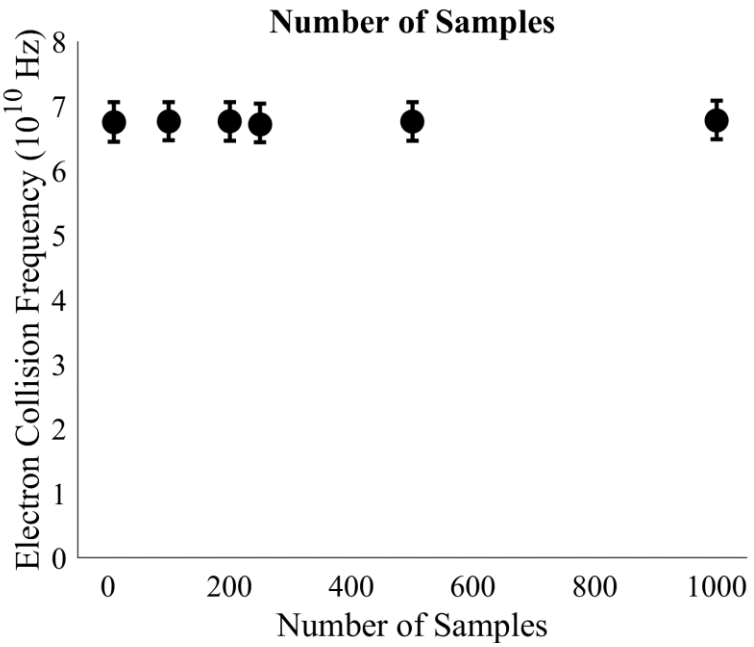

Figure 135 – Impact of number of sample averages on calculated average electron collision frequency and uncertainty (200 W, 1 Torr)

6.3.5 Signal SNR

Artificial normally distributed noise was added to the baseline sample and reference pulses at each index in the time domain. The noise level corresponds to the multiplicative factor of the standard deviation of the added noise. A level of 5, for example, denotes the addition of normally distributed noise with a standard deviation five times greater than the noise standard deviation of the original pulse. A level of 0 corresponds to no added noise. Figure 136 compares the reference pulses of each noise level, Figure 137 shows the original pulse spectrum, and Figure 138 shows the pulse spectrum for a noise level of 10.

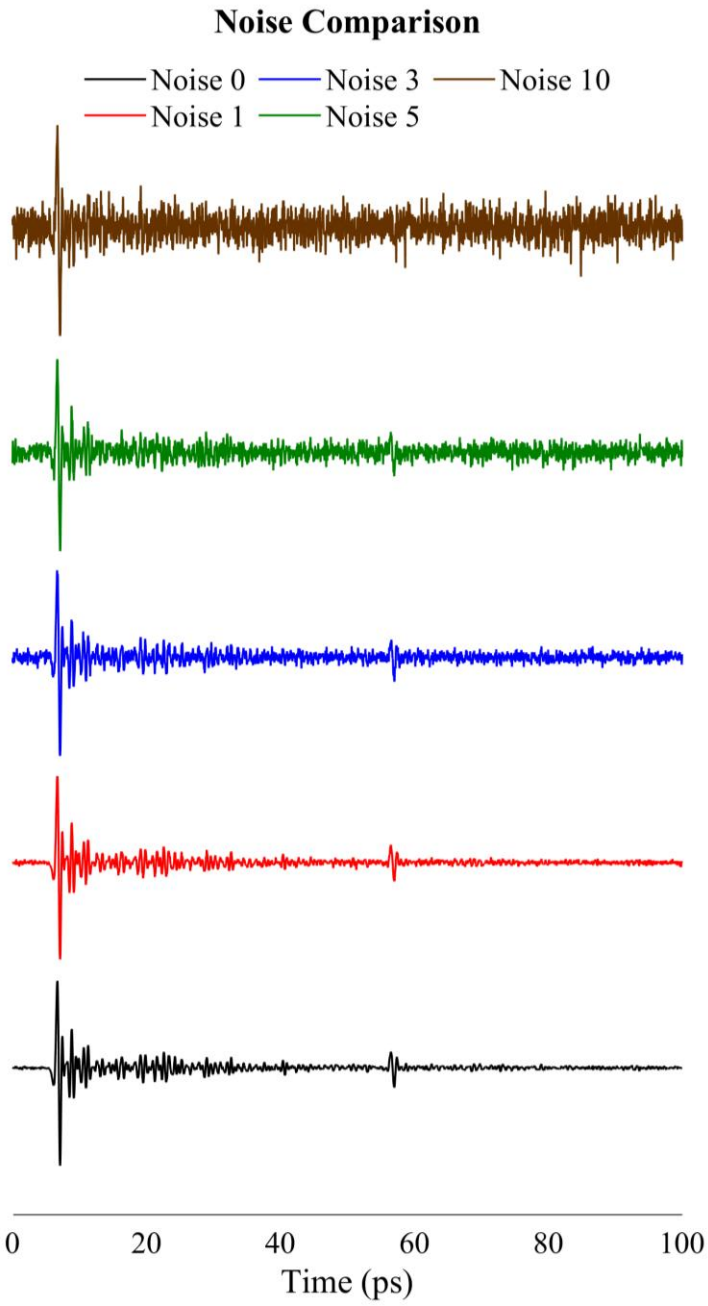

Figure 136 – Comparison of reference pulses with artificial noise

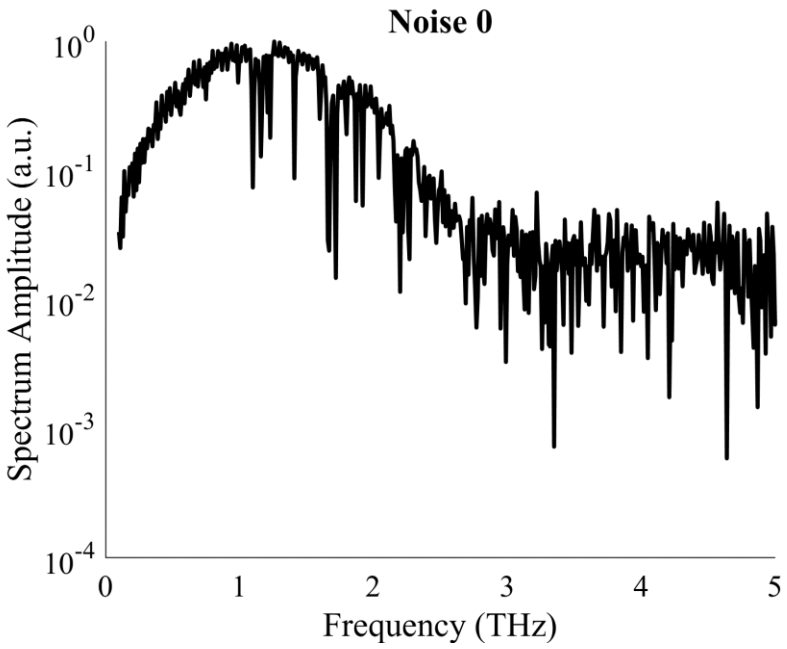

Figure 137 – Noise 0 reference spectrum

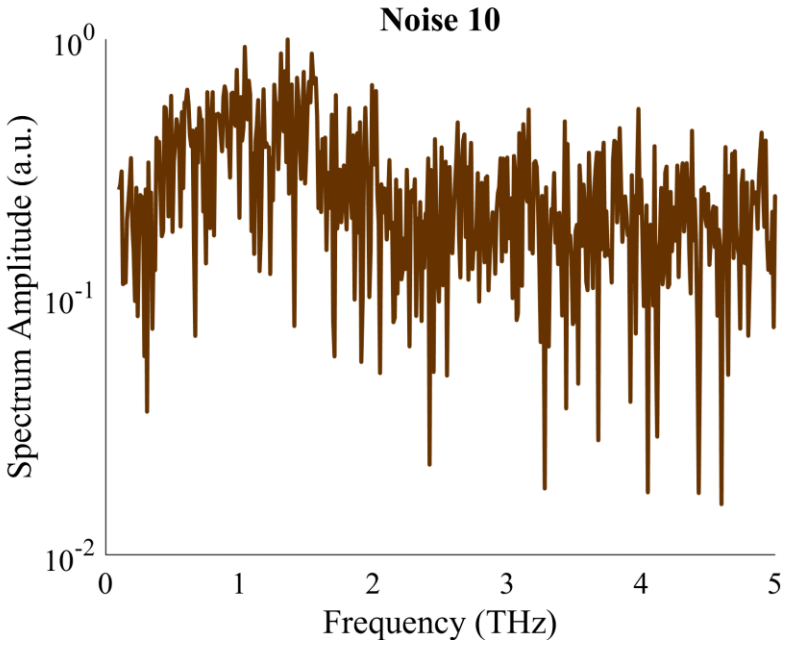

Figure 138 – Noise 10 reference spectrum

The average calculated electron density and collision frequency are shown as a function of the noise level in Figure 139 and Figure 140, respectively. Increased noise does not significantly impact the electron density uncertainty but does significantly increase the electron collision frequency uncertainty. This occurs because the signal amplitude noise has a much greater impact on the spectrum amplitude than the phase. The calculated electron collision frequency, in turn, depends strongly on the spectrum amplitude, whereas the calculated electron density is relatively insensitive to the spectrum amplitude. Instead, uncertainty in the plasma length drives the electron density uncertainty.

However, it should be noted that sufficient noise can interfere with phase-unwrapping or result in incorrect determination of the correction factors. In these cases, the output of the Bayesian inference scheme does not satisfactorily quantify the uncertainty.

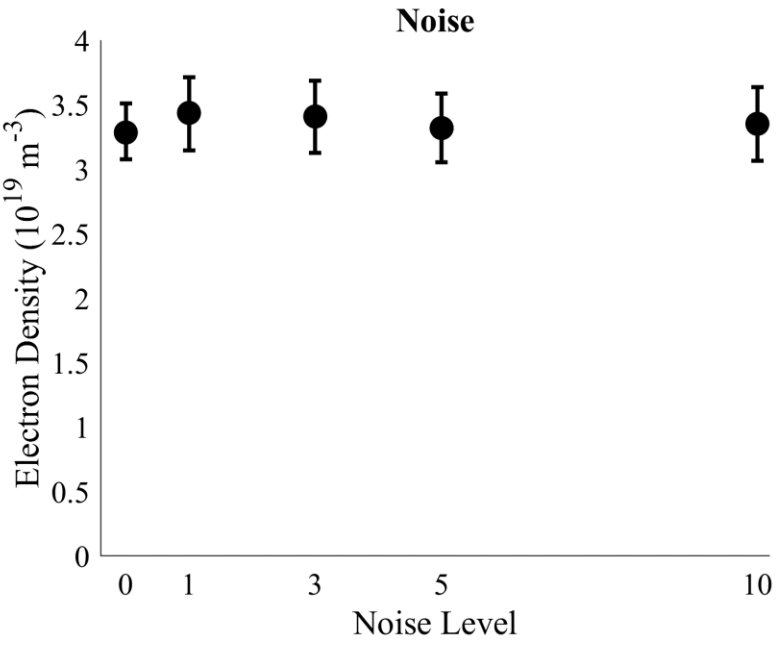

Figure 139 – Impact of pulse SNR on calculated average electron density and uncertainty (200 W, 1 Torr)

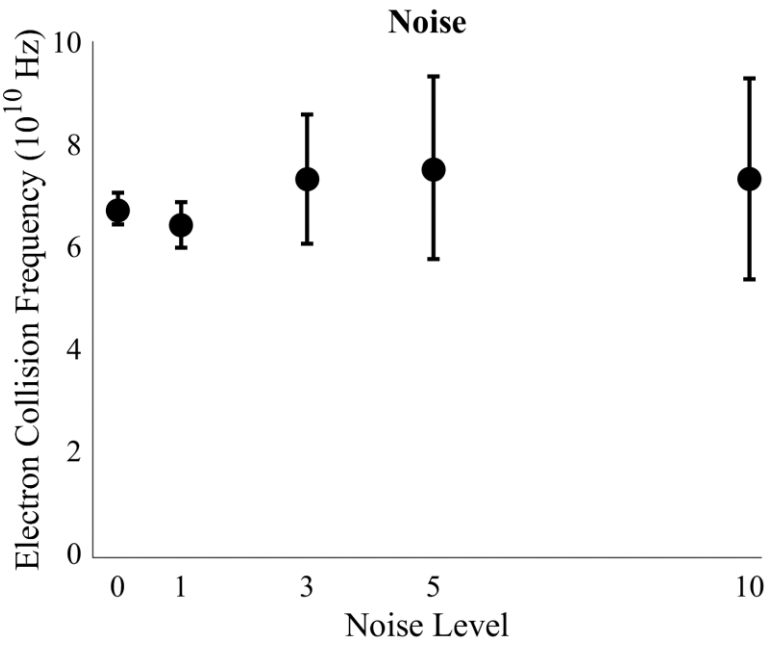

Figure 140 – Impact of pulse SNR on calculated average electron collision frequency and uncertainty (200 W, 1 Torr)

6.4 Summary

Section 6.1 details a novel Bayesian THz-TDS plasma diagnostic analysis framework, Section 6.2 presents plasma property results calculated with the analysis framework, and Section 6.3 studies the impact of THz pulse parameters on measurement uncertainty for a particular RF ICP plasma condition. The Bayesian framework, unlike the standard framework discussed in Chapter 4, is able to compute the electron collision frequency and provide uncertainties for both the electron density and collision frequency.

Uncertainties in the plasma length were found to be the largest contributor to uncertainty in the computed average electron density. For the plasma condition examined in Section 6.3, other factors have comparatively negligible impact on uncertainty. These factors are expected to become important if they interfere with the ability to perform phase

unwrapping or increase the minimum resolvable electron density to the order of the measured electron density. The uncertainty in the computed electron collision frequency was increased by any factor that amplified uncertainty in the transfer function magnitude. Signal SNR, in particular, was found to have a substantial impact on electron collision frequency uncertainty.

These findings indicate that there are measurement scenarios for which the total time required to make a measurement can be substantially reduced without significant penalty in the electron density uncertainty. The baseline pulse required a measurement time of approximately 20 min, but changing the pulse properties to a shorter duration, lower temporal resolution, and smaller number of samples could decrease the measurement time to under one minute without significantly impacting the electron density uncertainty.

CHAPTER 7. BOUNDED PLASMA MEASUREMENTS

This chapter presents the first-ever noninvasive measurements of plasma bounded and optically shielded by Hall thruster wall material. Section 7.1 details the experimental setup and develops the necessary theory, Section 7.2 presents measurements of wall material optical properties and discusses their implications, and Section 7.3 presents the bounded plasma measurement results.

7.1 Experimental Setup and Modified Analysis

This section details the bounded plasma experimental setup and presents the modified transfer function required for extracting plasma properties. Section 7.1.1 discusses the measurement configuration, Section 7.1.2 overviews the boundary materials, and Section 7.1.3 provides the equation required for plasma property extraction.

7.1.1 Measurement Configuration

Boundaries were placed inside the RF ICP discharge such that the plasma was in direct contact with the boundaries and the probing THz pulses transmitted through the boundaries. The boundaries were separated by 0.1 m to ensure plasma contact and were carefully aligned so that their surface normals were parallel with the axis of the discharge chamber.

Figure 141 shows a schematic of the measurement configuration. The plasma sheaths are not illustrated in Figure 141 because, at the plasma conditions presented here, the sheath thicknesses are expected to be on the order of 10^{-5} m [82]. The sheath thicknesses

are orders of magnitude smaller than the THz pulse wavelengths, so the sheaths are not expected to impact pulse propagation through the plasma.

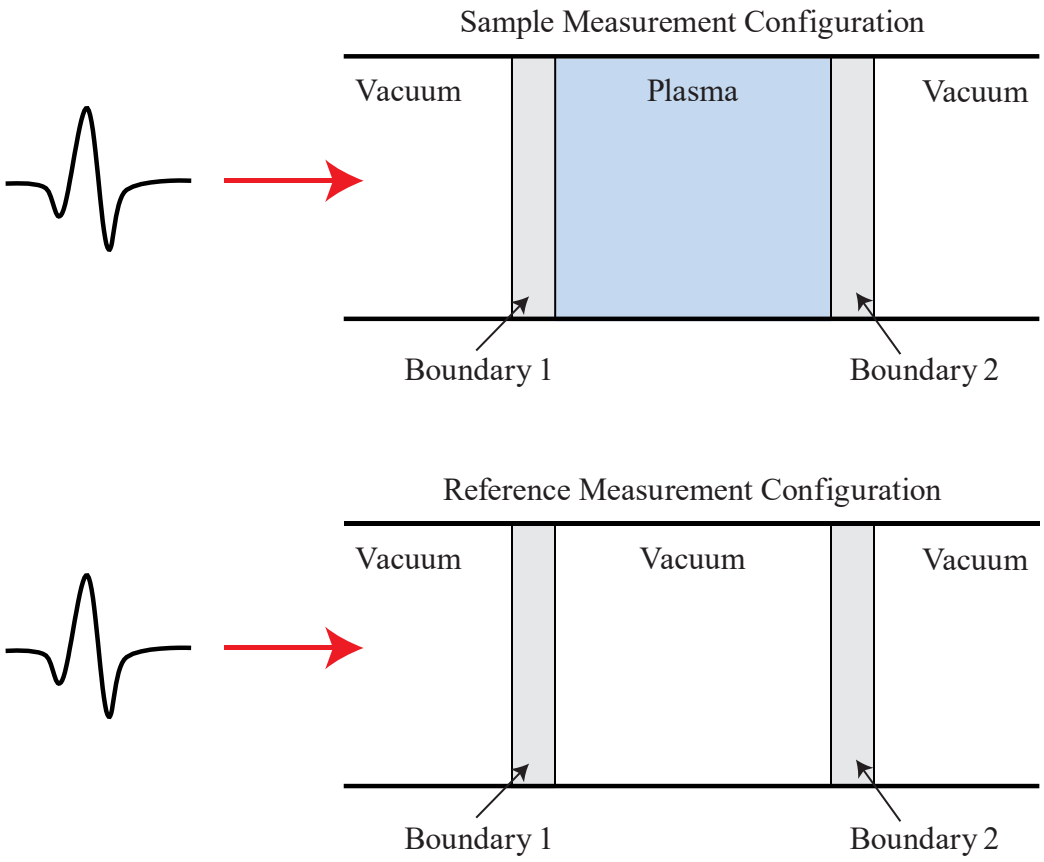

Figure 141 – Bounded plasma measurement configuration

Figure 142 shows an image of the plasma discharge operating at an input power of 200 W and argon pressure of 1 Torr with 0.3 in-thick grade M26 BN boundaries. The reduction in optical plasma emission brightness near the boundaries is caused by changes in the electron collision frequency near the boundary surface.

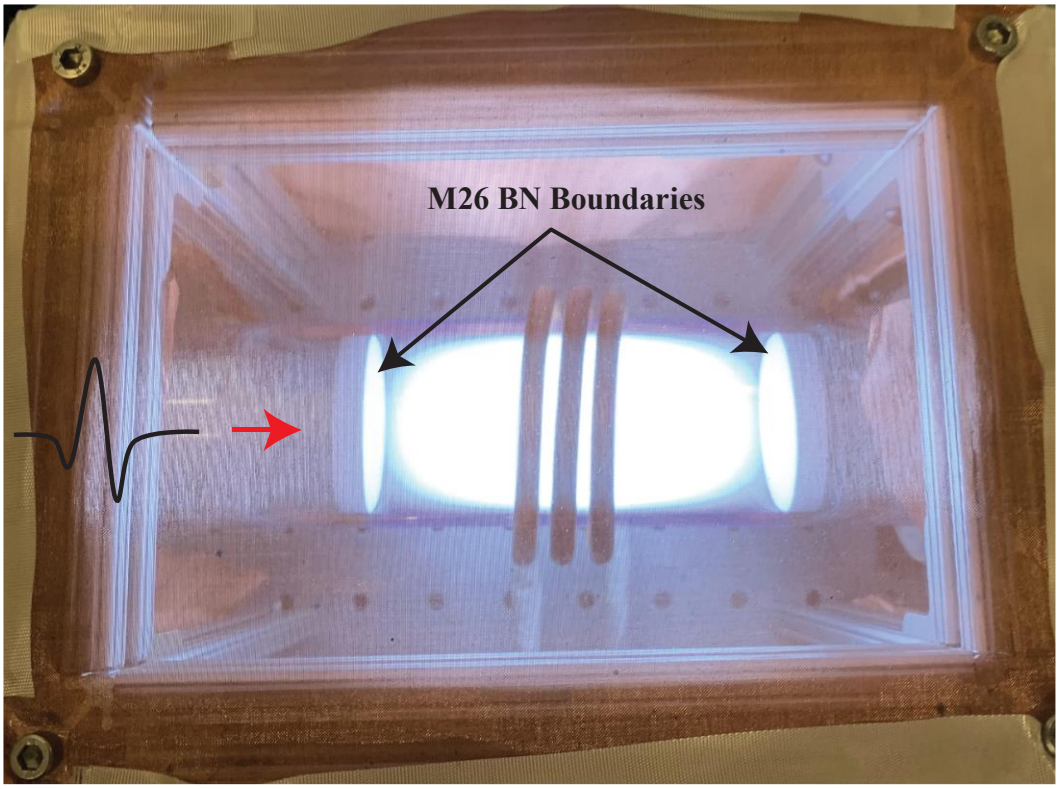

Scale: Distance between boundaries is 10 cm

Figure 142 – Plasma bounded by 0.3 in-thick M26 BN (200 W, 1 Torr)

7.1.2 Boundary Materials

Flight-grade Hall thruster walls are made from BN-SiO_2 composite [16]. BN-SiO_2 is manufactured by hot-pressing hexagonal close-packed (hcp) BN platelets in an amorphous SiO_2 binder. The composite is used as Hall thruster wall material because it exhibits low electrical conductivity at high temperatures, high mechanical strength, good thermal shock resistance, low outgassing rate, low secondary electron emission (SEE) rate, and low sputtering yield.

Three different grades of BN composite manufactured by Saint-Gobain Ceramic Materials were used as boundary materials in this dissertation: grades M26, M, and HP.

Grade M26 is 60% hcp BN and 40% SiO_2 by weight; grade M is 40% hcp BN and 60% SiO_2 by weight; and grade HP is > 95% hcp BN and < 5% $Ca_3B_2O_6$ binder by weight. Grades M26 and M are representative of flight-grade Hall thruster material. Grade HP is less expensive than grades M26 and M, so it is sometimes used in laboratory Hall thrusters.

Stock BN material purchased from Saint-Gobain was machined into disks with radius of 44 mm so that each disk approximately fills the inner diameter of the ICP discharge. The large disk radius prevents the escape of plasma around the disk edges and aids in the alignment of the disks within the discharge. The disks were machined into thicknesses of 0.3 in and 0.1 in. The 0.3 in thickness is representative of a standard Hall thruster wall thickness; the 0.1 in disks were used for supporting tests.

The hcp BN composites used in this study are orthotropic, so the material coordinate system can be decomposed into an optic axis and plane of isotropy. Radiation that propagates along the optic axis is guaranteed polarization components parallel to the plane of isotropy, so such radiation is insensitive to rotations of the material with respect to the radiation polarization. As shown in Figure 143, radiation that propagates in this manner is dubbed an “ordinary ray.”

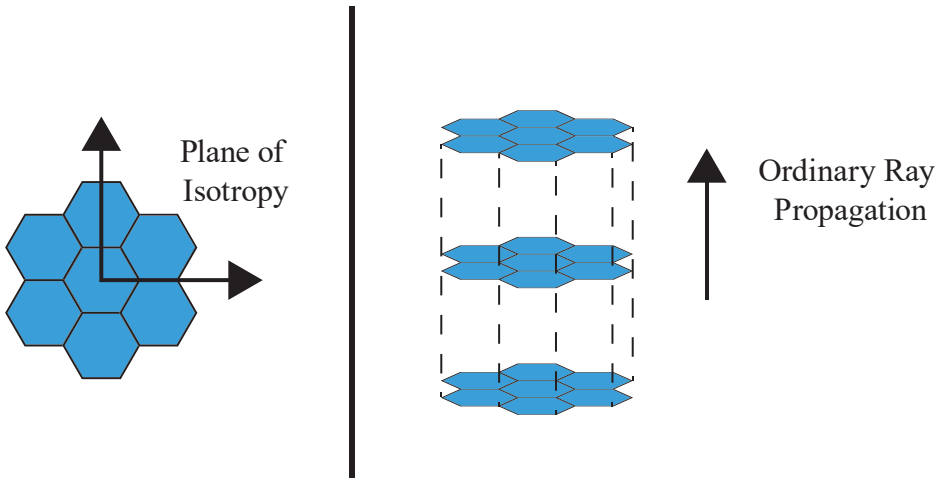

Figure 143 – Ordinary ray propagation in hcp BN microstructure

The orientation of the microstructure of a real Hall thruster wall is generally not reported and likely varies as a function of model and manufacturer. Because ordinary ray propagation simplifies the measurement setup by eliminating the dependence of radiation properties on material rotation, the BN composites were oriented such that the THz pulses propagated as ordinary rays. This was achieved by ensuring the hot-press direction was parallel to the disk surface normal.

7.1.3 Modified Transfer Function

The presence of non-vacuum sample boundaries alters the transfer function from the relation given by Eq. (9). Applying the general procedure used to derive Eq. (9) in Section 2.2.1 to the measurement configuration diagrammed in Figure 141, the reference and sample electric field spectra become

$$\hat{E}_{ref}(\omega) = \hat{E}_{gen}(\omega)G(\omega)D_{b_1v}(\omega)D_{vb_2}(\omega)\exp\left[i\frac{\omega}{c}\,L\right]$$

and

$$\hat{E}_{sam}(\omega) = \hat{E}_{gen}(\omega)G(\omega)D_{b_1p}(\omega)D_{pb_2}(\omega)FP(\omega)\exp\left[i\frac{\omega}{c}\int_0^L \tilde{n}_p(\omega,z)\mathrm{d}z\right], \tag{76}$$

where D_{b_1v} is the transmission coefficient from boundary 1 to vacuum, $D_{vb_2}(\omega)$ is the transmission coefficient from vacuum to boundary 2, $D_{b_1p}(\omega)$ is the transmission coefficient from boundary 1 to plasma, and $D_{pb_2}(\omega)$ is the transmission coefficient from plasma to boundary 2. Assuming the plasma is uniform, the transfer function is then given by

$$\frac{\hat{E}_{sam}(\omega)}{\hat{E}_{ref}(\omega)} = \frac{D_{b_1p}(\omega)D_{pb_2}(\omega)}{D_{b_1v}(\omega)D_{vb_2}(\omega)}FP(\omega)\exp\left[i\frac{\omega L}{c}\{\tilde{n}_p(\omega)-1\}\right]. \tag{77}$$

FP reflections inside the boundaries are shared by both the sample and reference propagation paths and are therefore not present in the transfer function. The FP term in Eq. (77) accounts for differences in FP reflections between the sample and reference configurations in the vacuum/plasma region between the boundaries. However, FP reflections in this region can be ignored if the first FP-reflected pulse arrives at the detector outside the measured incident pulse duration for both configurations. The time at which the first FP-reflected pulse will arrive in the incident THz pulse is equal to the time required for the reflected pulse to traverse twice the length of the vacuum/plasma region between

the boundaries [83]. Because the plasma refractive index is less than unity [10], the limiting time is that required for the THz pulse to traverse twice the length of the plasma:

$$t = \frac{2n_p(\omega)L}{c}. \tag{78}$$

Though smaller than unity, the plasma refractive index is typically very nearly equal to unity. For example, a uniform plasma length of 0.1 m, electron density of 4×10^{19} m^{-3}, and electron collision frequency of 7×10^{10} Hz yield a plasma refractive index equal to 0.998 at 1 THz. Figure 144 plots the time at which the first FP-reflected pulse arrives in the incident pulse as a function of plasma length for several representative plasma refractive index values.

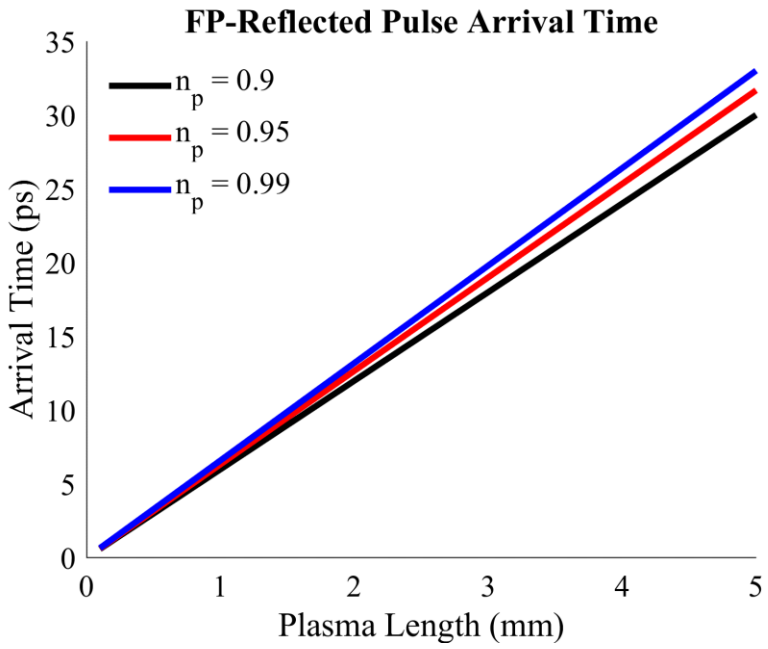

Figure 144 – Arrival time of first FP-reflected pulse in incident pulse

As discussed in Section 6.3.2, depending on the application, the incident pulse may be measured for durations (not including the tip) as short as 3-5 ps. FP reflections can therefore be ignored in plasmas with sub-mm length with appropriate temporal pulse windowing. The plasma length in the Hall thruster channel is typically on a mm-scale, and the plasma length inside the RF ICP discharge is 10 cm. In both environments, FP reflections may be discarded by appropriate temporal windowing of the incident THz pulse.

A transmission coefficient (D_{ab}) is related to its constituent complex refractive indices ($\tilde{n}_a$ and $\tilde{n}_b$) by

$$D_{ab} = \frac{2\tilde{n}_a(\omega)}{\tilde{n}_a(\omega) + \tilde{n}_b(\omega)}. \tag{79}$$

Inserting Eq. (79) into Eq. (77) and ignoring FP reflections, the transfer function becomes

$$\frac{\hat{E}_{sam}(\omega)}{\hat{E}_{ref}(\omega)} = \frac{\tilde{n}_p(\omega)\left[\tilde{n}_{b_1}(\omega)+1\right]\left[\tilde{n}_{b_2}(\omega)+1\right]}{\left[\tilde{n}_{b_1}(\omega)+\tilde{n}_p(\omega)\right]\left[\tilde{n}_{b_2}(\omega)+\tilde{n}_p(\omega)\right]} \exp\left[i\frac{\omega L}{c}\left\{\tilde{n}_p(\omega)-1\right\}\right], \quad (80)$$

where $\tilde{n}_{b_1}$ and $\tilde{n}_{b_2}$ denote the complex refractive indices of boundary 1 and boundary 2, respectively. These quantities must be measured independently and are given as a function of boundary material in Section 7.2.

The modified magnitude and phase needed for the Bayesian inference likelihood PDF discussed in Section 6.1.3.3 are given by

$$A_{mod}(\omega) = \left(\frac{1}{r}\right)\left|\frac{\hat{E}_{sam}(\omega)}{\hat{E}_{ref}(\omega)}\right|$$

and (81)

$$\Phi_{mod}(\omega) = \varphi_2\omega + \angle\frac{\hat{E}_{sam}(\omega)}{\hat{E}_{ref}(\omega)},$$

where the transfer function is given by Eq. (80) and $|\ \ |$ and $\angle$ denote the magnitude and phase, respectively. As the magnitude and phase of the transfer function given in Eq. (80) cannot be expressed analytically, they are computed numerically. The electron density and collision frequency are not explicitly shown in Eq. (80), but these values are related to the complex plasma refractive index by Eq. (21).

7.2 BN Optical Property Results

This section presents the real refractive indices and extinction coefficients that form the complex boundary refractive indices required for the bounded plasma measurements. Section 7.2.1 shows results from the boundary property measurement study and Section 7.2.2 discusses the implications of the results on bounded plasma measurements.

7.2.1 Refractive Indices and Extinction Coefficients

The complex refractive index of each boundary is required for the determination of plasma properties, according to the transfer function given by Eq. (80). The complex refractive index was measured for each boundary with the configuration shown in Figure 7. Figure 145, Figure 146, and Figure 147 show representative sample and reference pulses for the complex refractive index measurement made in 0.3 in-thick M26, M, and HP BN, respectively. Attenuation and delay of the pulse by the sample are readily apparent in each case. Overall attenuation is greatest in the M sample and least in the HP sample.

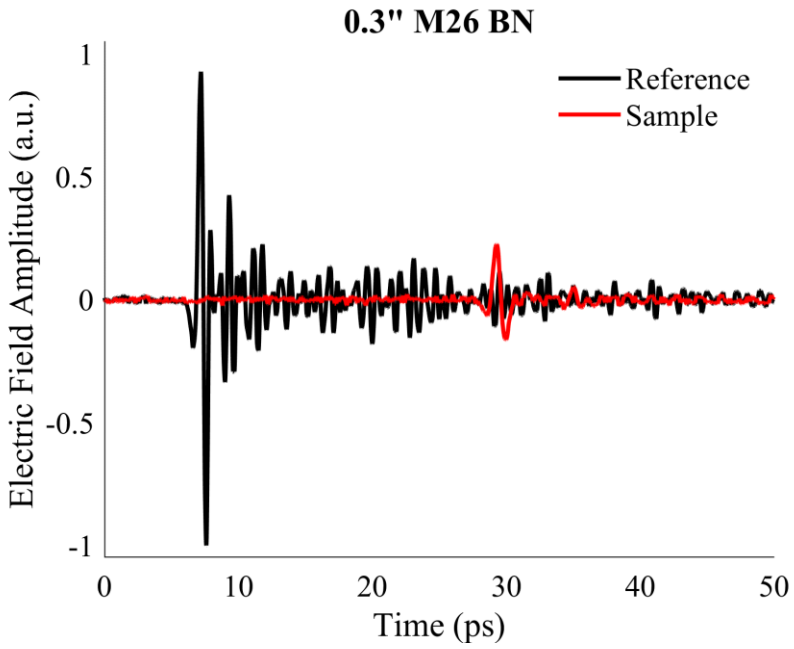

Figure 145 – Representative sample and reference pulses for 0.3 in-thick M26 BN boundary property measurement

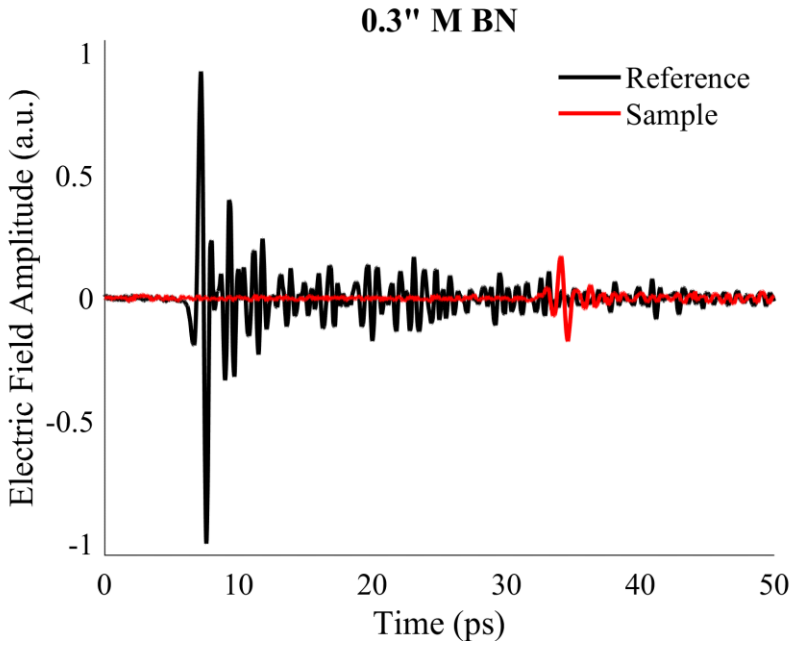

Figure 146 – Representative sample and reference pulses for 0.3 in-thick M BN boundary property measurement

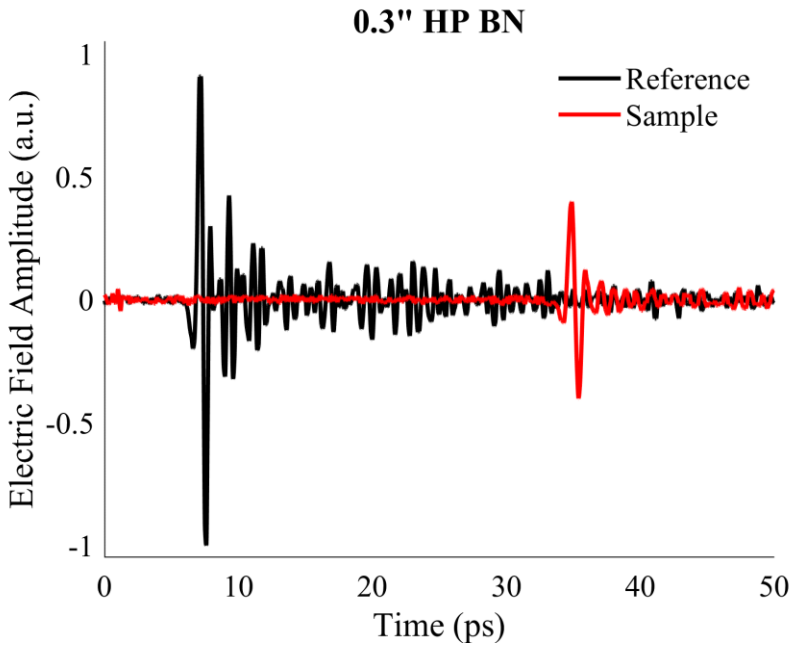

Figure 147 – Representative sample and reference pulses for 0.3 in-thick HP BN boundary property measurement

The complex refractive index is related to the real refractive index and extinction coefficient according to Eq. (4). Figure 148, Figure 149, and Figure 150 show the real refractive index and extinction coefficient calculated from the reference and sample pulses given above for the 0.3 in-thick M26, M, and HP BN samples, respectively. Values above 1.5 THz were not computed because SNR approaches unity in this range.

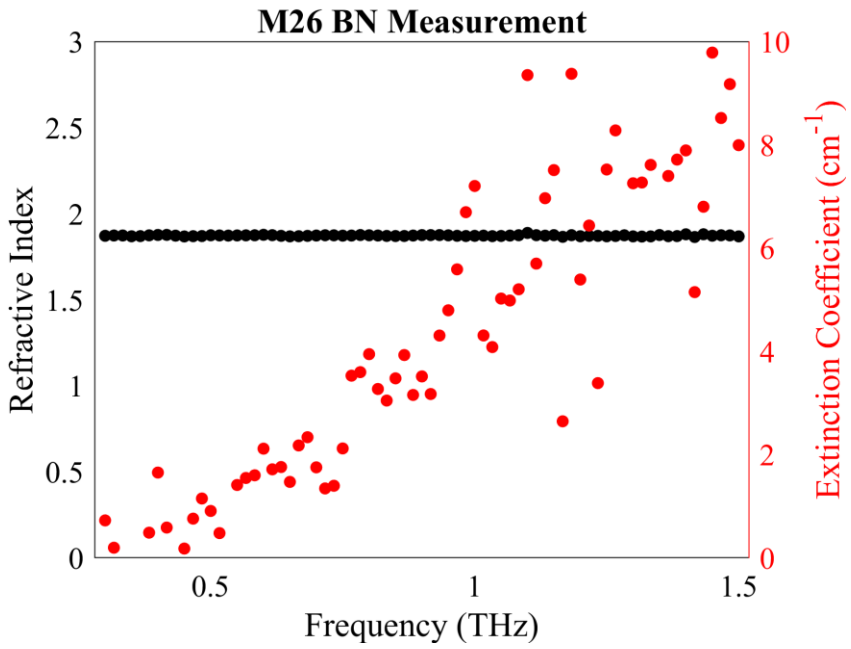

Figure 148 –M26 BN refractive index and extinction coefficient

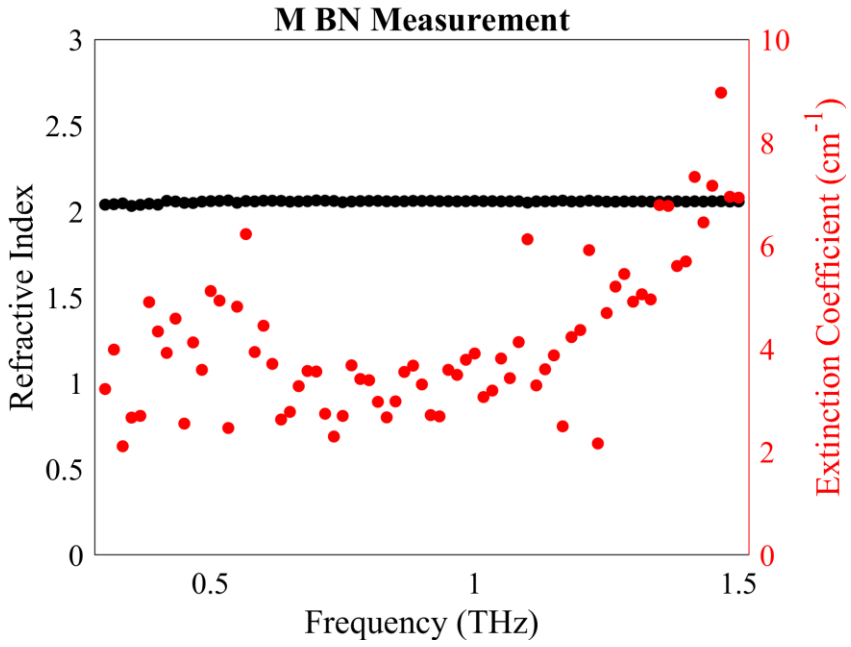

Figure 149 –M BN refractive index and extinction coefficient

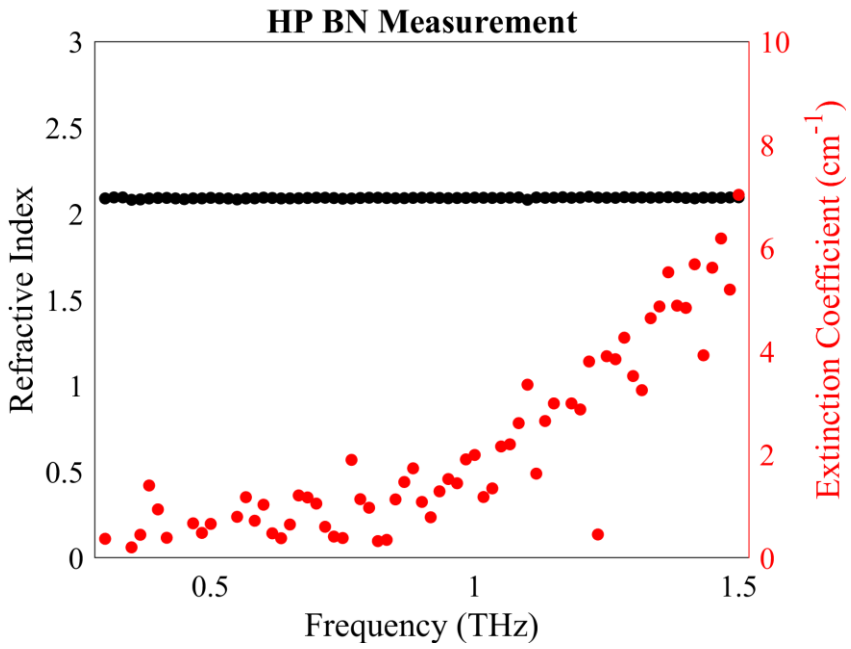

Figure 150 –HP BN refractive index and extinction coefficient

The refractive index of each BN grade, within the measurement range, does not vary by more than 0.01 as a function of THz frequency. The average refractive index is 1.87 for grade M26, 2.06 for grade M, and 2.09 for grade HP. The extinction coefficient, however, increases exponentially with THz frequency in all three grades. Grades M26 and HP feature similarly low extinction coefficient values on the order of 1 cm^{-1} at frequencies below 0.5 THz, but the extinction coefficient rises to approximately 4 cm^{-1} by 1 THz in grade M26 and only 2 cm^{-1} by 1 THz in grade HP. Grade M, on the other hand, does not have any extinction coefficients below 2 cm^{-1}. Consequently, as observed in the reference and sample pulse figures above, grade M causes the most THz pulse attenuation and grade HP induces the least THz pulse attenuation.

The optical property values presented above were measured in the absence of plasma heating. It is possible that, in the bounded plasma configuration, the plasma heats the

boundaries sufficiently to change the optical properties. According to Eq. (77), large changes in the optical properties would have minimal effect on the measured electron density but could significantly impact the measured electron collision frequency.

The impact of temperature on BN optical properties in the THz regime has not been published in the open literature, but work [84] has shown minimal temperature-driven property variation at other wavelengths. Furthermore, Naftaly et al. [36] found that THz BN optical properties are strongly related to porosity, and the BN data sheet provided by Saint-Gobain does not report variation in porosity (or most material properties) as a function of temperature for temperatures below 1000°C. The impact of temperature-induced changes to the optical properties due to plasma heating are therefore not expected to significantly impact the measured electron density and collision frequency.

7.2.2 Bounded Plasma Measurement Implications

The complex boundary refractive indices are required for extraction of the plasma properties, but they also provide insight into the measurement capability implications associated with bounded plasma measurements. The extinction coefficient is related to pulse attenuation according to Eq. (3) and can therefore be used to determine the expected remaining THz pulse signal amplitude after propagation through the boundary material. Using the extinction coefficient results presented in the previous section, Figure 151, Figure 152, and Figure 153 show the remaining signal amplitude as a function of boundary thickness for various THz frequencies for grades M26, M, and HP, respectively. The 0.5 and 1.5 THz curves are indistinguishable in Figure 152.

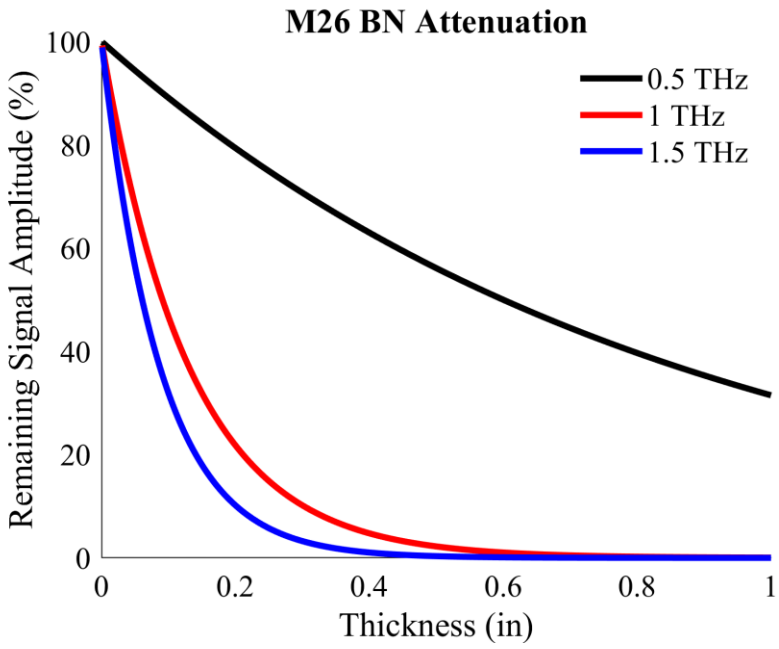

Figure 151 – M26 BN signal attenuation

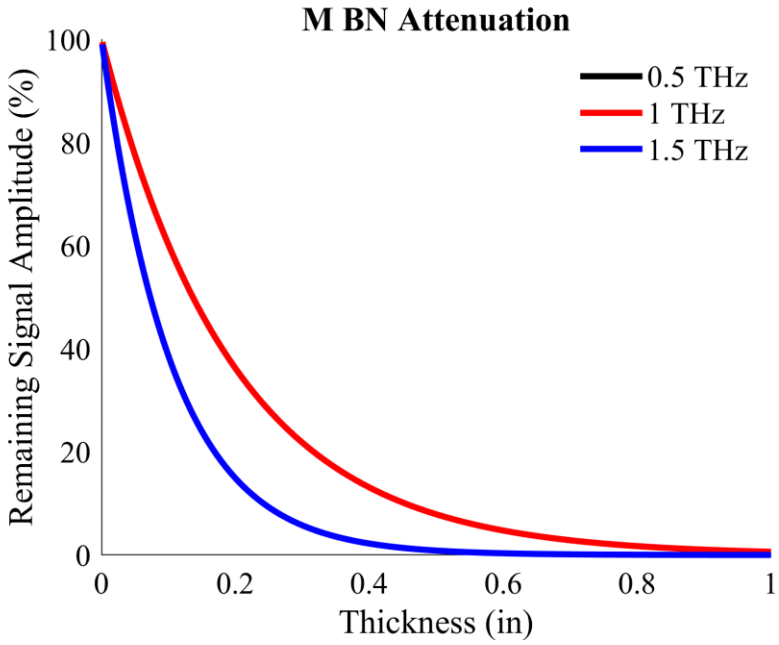

Figure 152 – M BN signal attenuation

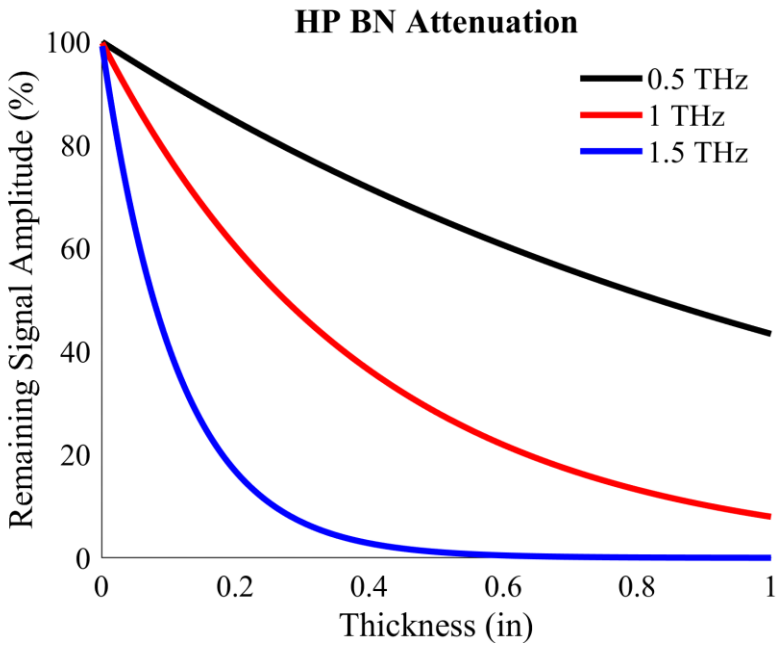

Figure 153 – HP BN signal attenuation

The thickness of each boundary in the bounded plasma measurements is 0.3 in, so the total propagation distance through the boundaries is 0.6 in. After propagation of 0.6 in, the expected remaining signal amplitude for grade M26 is approximately 50% at 0.5 THz and less than 2% at 1 and 1.5 THz. After propagation through grade M, the expected remaining signal amplitude is less than 5% at 0.5 and 1 THz and less than 1% at 1.5 THz. Propagation through grade HP, however, results in an expected remaining signal amplitude of greater than 60% at 0.5 THz, greater than 20% at 1 THz, and less than 5% at 1.5 THz.

As discussed in Sections 5.2.1 and 6.3.5, loss of SNR strongly impacts the uncertainty of the measured electron collision frequency but only weakly affects the uncertainty of the measured electron density, as long as the frequencies required to resolve the density can be distinguished above noise. The substantial loss of SNR caused by the M

and M26 BN boundaries is therefore expected to reduce the resolvability of the electron collision frequency but not greatly reduce the resolvability of the electron density.

7.3 Bounded Plasma Results

This section presents the average electron density and collision frequency measured for the bounded plasma configuration. The results in Section 7.3.1 were obtained with 0.3 in-thick boundaries of each grade of BN and a discharge operating pressure of 1 Torr. The results in Section 7.3.2 were obtained with 0.3 and 0.1 in-thick boundaries of M26 BN and discharge operating pressures of 1 and 5 Torr. In all cases, error bars encompass a 2-sigma credibility interval (68.27…%). Because the plasma length is limited by the presence of the boundaries, the plasma length can be measured more precisely as the distance between the boundaries. The plasma length prior PDF for all bounded plasma measurements therefore features a standard deviation of 0.003 m rather than 0.01 m.

7.3.1 M26, M, and HP BN Boundaries

Figure 154, Figure 155, and Figure 156 show sample and reference THz pulses for the bounded plasma configuration with 0.3 in-thick M26, M, and HP boundaries, respectively. In each figure, the discharge operating conditions are 100 W and 1 Torr. Due to the passage of the THz pulses through a total of 0.6 in of BN composite, the SNR is significantly reduced compared to the pulses shown elsewhere in the dissertation. However, the THz pulses are clearly detectable above the noise.

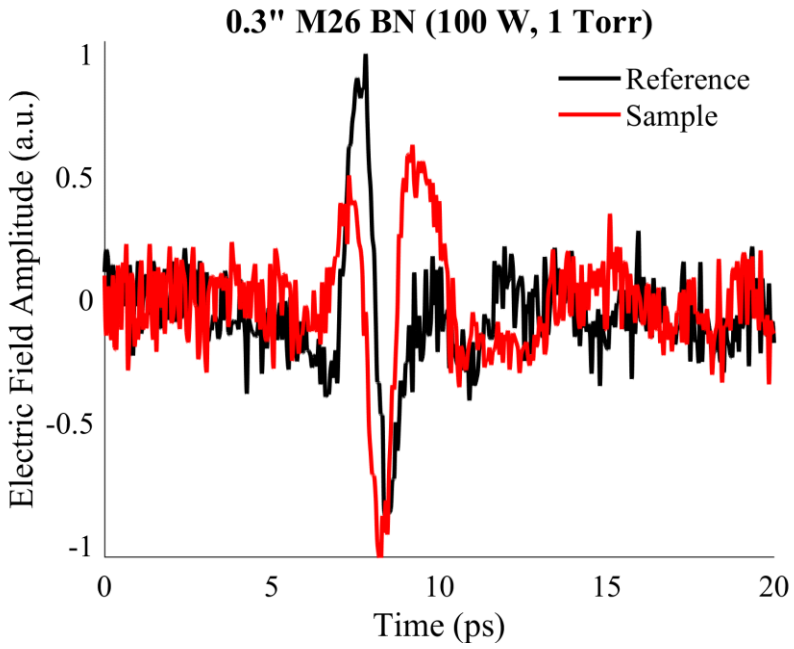

Figure 154 – Sample and reference pulses with 0.3 in-thick M26 BN boundaries (100 W, 1 Torr)

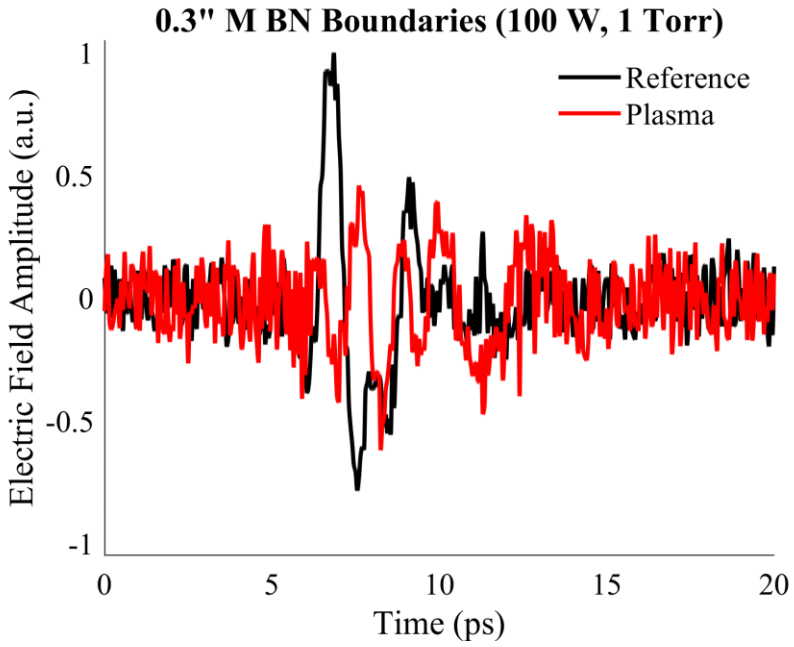

Figure 155 – Sample and reference pulses with 0.3 in-thick M BN boundaries (100 W, 1 Torr)

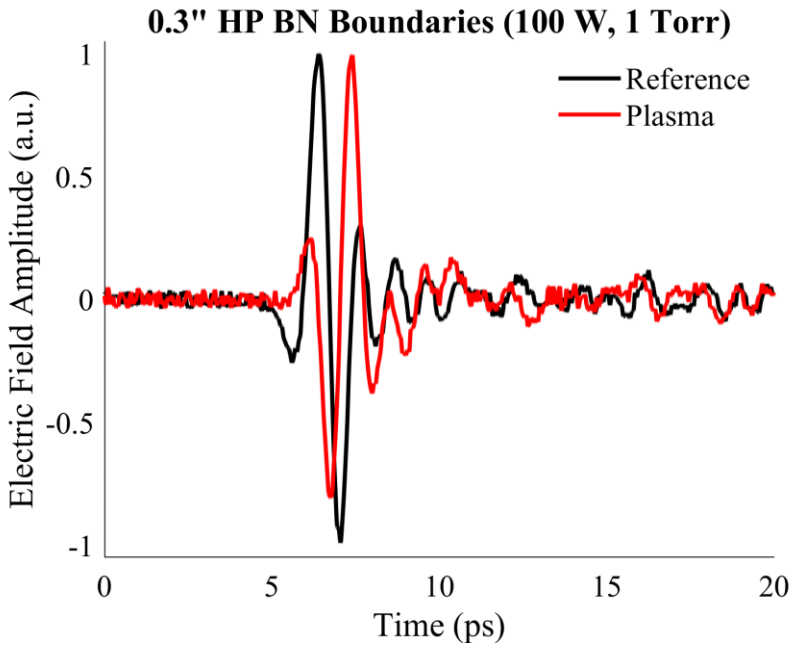

Figure 156 – Sample and reference pulses with 0.3 in-thick HP BN boundaries (100 W, 1 Torr)

Figure 160 shows the reference spectrum extracted from the grade M BN bounded configuration reference signal shown in Figure 155. As can be seen in Figure 160, the reference signal amplitude is approximately an order of magnitude greater than the noise for multiple frequencies ranging from 0.3 to 0.8 THz. Though the apparent time-domain SNR of the THz pulse is drastically reduced by transmission through the boundaries, sufficient signal is detectable at lower frequencies for computation of electron density.

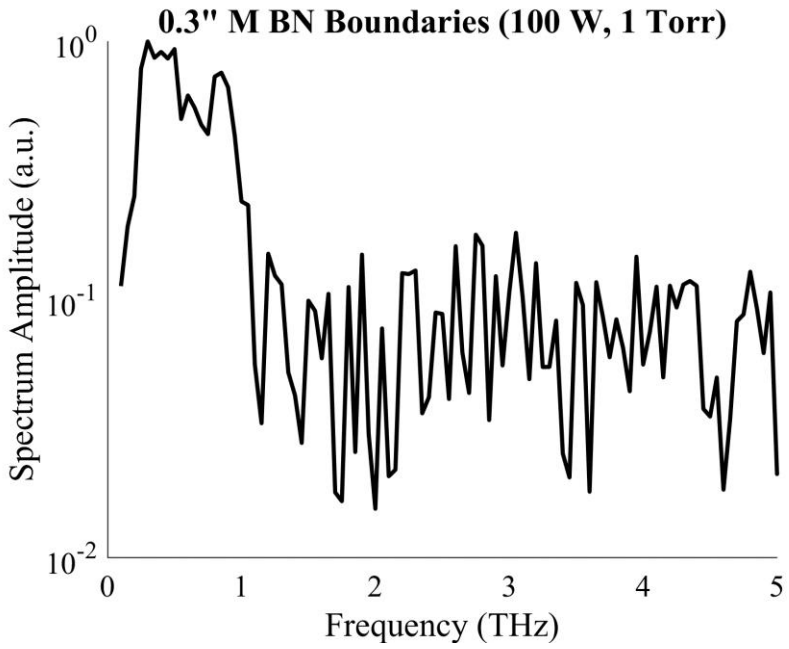

Figure 157 – Reference spectrum with 0.3 in-thick M BN boundaries (100 W, 1 Torr)

However, the low SNR and restricted range of detectable frequencies preclude determination of the magnitude correction factor and thereby prevent the Bayesian analysis scheme from achieving the termination criterion for the grade M BN bounded plasma measurement. The mean value of the marginalized PDF of the electron density conforms to the termination criterion discussed in Section 6.1.4, but the mean value of the marginalized PDF of the electron collision frequency does not.

Figure 158 and Figure 159 show the measured average electron density and collision frequency, respectively, for the bounded and unbounded plasma configurations. Electron collision frequency results are not presented for the plasma bounded by grade M BN.

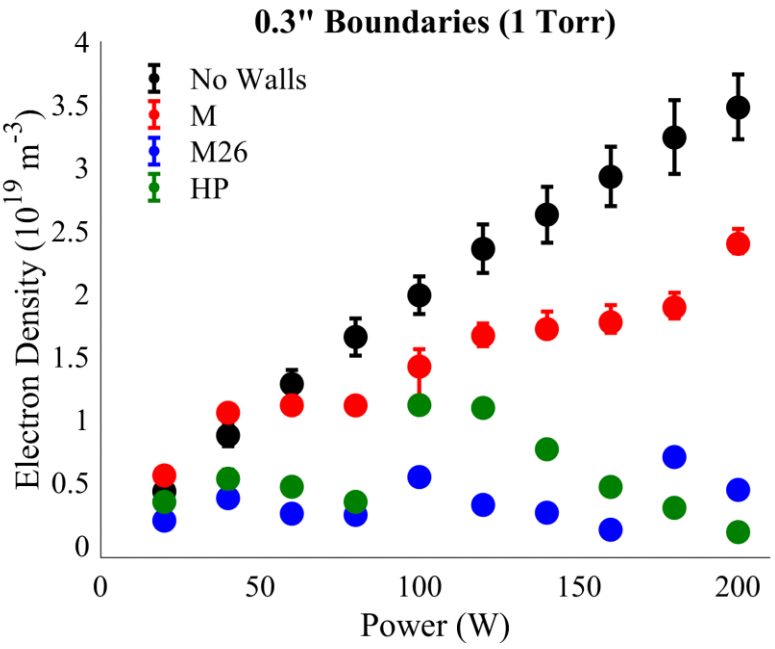

Figure 158 – Average electron density (1 Torr, 0.3 in-thick boundaries)

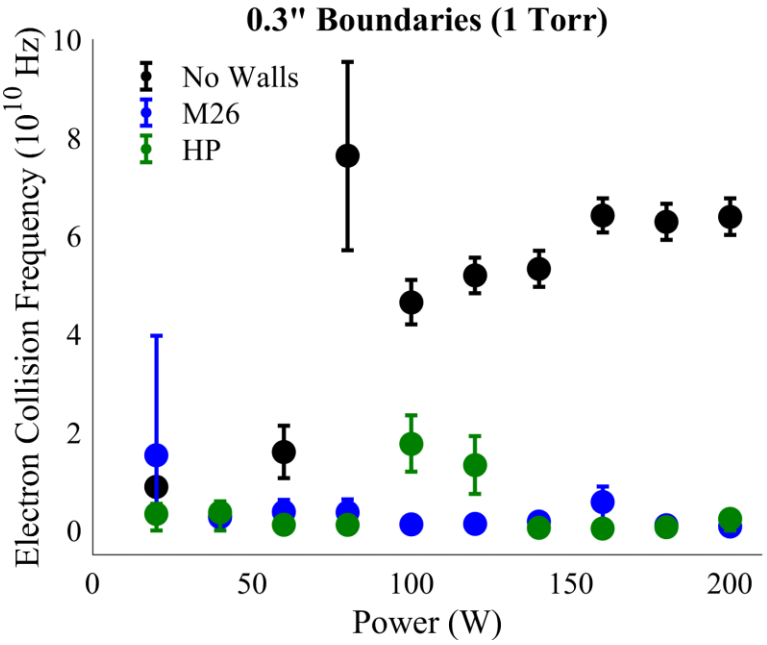

Figure 159 – Average electron collision frequency (1 Torr, 0.3 in-thick boundaries)

The electron density error bars encompass a smaller width for the bounded configuration cases than the unbounded configuration because, though the bounded configuration THz pulses feature much lower SNR, the reduction in length uncertainty results in an overall decrease in electron density measurement uncertainty. However, the reduction in length uncertainty does not impact the electron collision frequency uncertainty. In each case, the relative uncertainty for the bounded plasma configuration is larger than that for the unbounded configuration.

From 20 to 60 W, the M BN bounded configuration electron density approximately follows that of the unbounded configuration. However, starting at 80 W, though the M BN bounded configuration electron density continues to approximately follow a linearly increasing trend with power, the values diverge and become smaller than the unbounded densities. At each discharge power, the M BN bounded configuration electron density is larger than that of the M26 and HP BN bounded configurations.

The electron density trends for the M26 and HP BN bounded configurations are less consistent. The density rises from 20 to 40 W, decreases from 40 to 80 W, rises again to a maximum peak at 100 W, and decreases to 160 W. The HP BN bounded configuration density continues to decrease from 160 to 200 W, but the M26 BN bounded configuration density rises from 160 to 180 W and then decreases again to 200 W. The HP BN bounded configuration density is larger than the M26 BN bounded configuration density at all discharge powers, except for 180 and 200 W.

The large differences in peak electron density between the bounded configurations may be explained by differences in porosity between the BN grades. Due to the configuration of the RF ICP discharge, input argon must pass through the BN boundaries

before it is ionized. The neutral pressure inside the bounded region is therefore less than the reported neutral pressure measured outside the bounded region. Work has shown that the porosity of grades M, M26, and HP BN can vary by more than 100% on a lot-to-lot basis [85]. Based on the results found here, it likely that the grade M BN boundaries featured the largest porosity. This resulted in significantly larger neutral gas density in the region between the M BN boundaries than that inside the M26 and HP BN boundaries. As shown in the unbounded plasma measurements presented in Section 6.2.2.1, larger neutral gas densities tend to produce larger electron densities.

Other factors, such as secondary electron emission (SEE) and the interference of the boundaries with the coupling of power from the RF ICP discharge antenna to the plasma, may explain the changing trends observed in each bounded configuration [86-88]. As more energy is input into the plasma by the antenna, the electrons become more energized and strike the boundary walls with sufficient energy to produce secondary electrons with lower energy. The replacement of high-energy electrons with low-energy electrons at the boundaries becomes more pronounced at higher discharge powers and may lead to reduced ionization rate. The boundaries also interfere with the coupling of power into the plasma by acting as barriers through which the induced electric and magnetic fields must propagate. At higher powers, this interference may become severe enough to significantly reduce the ionization rate.

7.3.2 M26 BN Boundaries

This section compares the plasma property trends for three different M26 BN bounded plasma configurations: 1) 0.3 in-thick boundaries and operating pressure of 1 Torr, 2) 0.3 in-thick boundaries and operating pressure of 5 Torr, and 3) 0.1 in-thick

boundaries and operating pressure of 1 Torr. As all samples were machined from the same raw material, the purpose of this section is to provide a test of the explanations provided for the property trends observed in the previous section. Figure 160 and Figure 161 show the sample and reference pulses for configurations 2 and 3, respectively, for a discharge power of 100 W. Figure 162 and Figure 163 compare the average electron density and collision frequency, respectively, of the three configurations. At some discharge powers, low SNR prevented determination of the electron collision frequency.

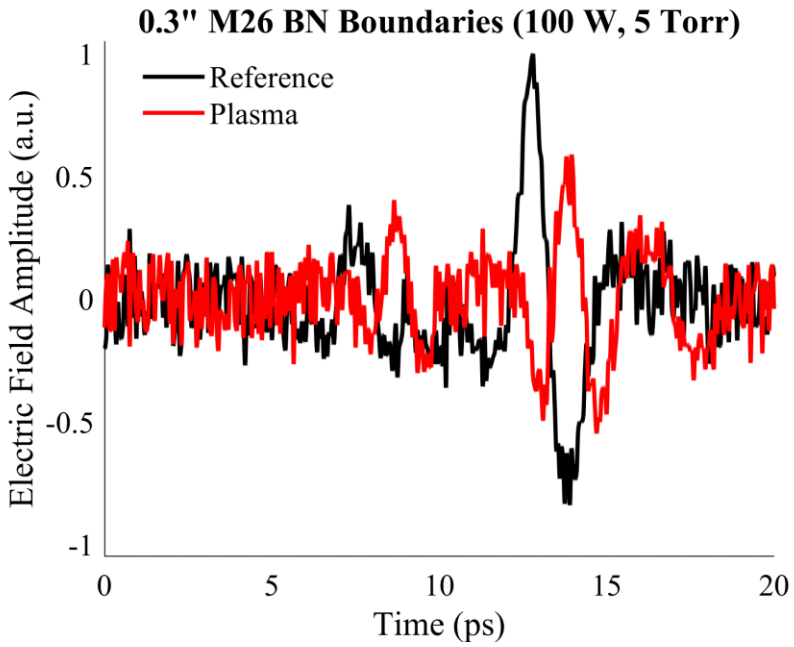

Figure 160 – Sample and reference pulses with 0.3 in-thick M26 BN boundaries (100 W, 5 Torr)

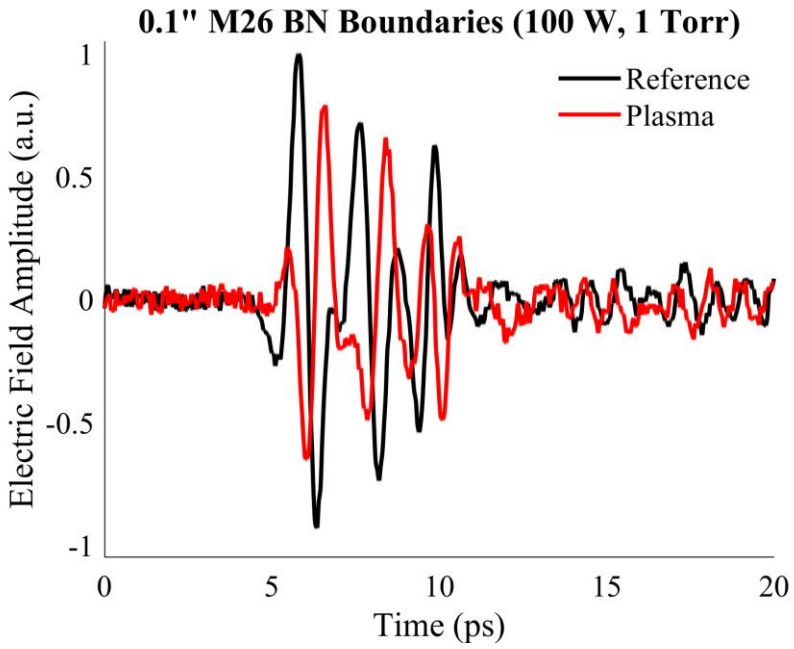

Figure 161 – Sample and reference pulses with 0.1 in-thick M26 BN boundaries (100 W, 1 Torr)

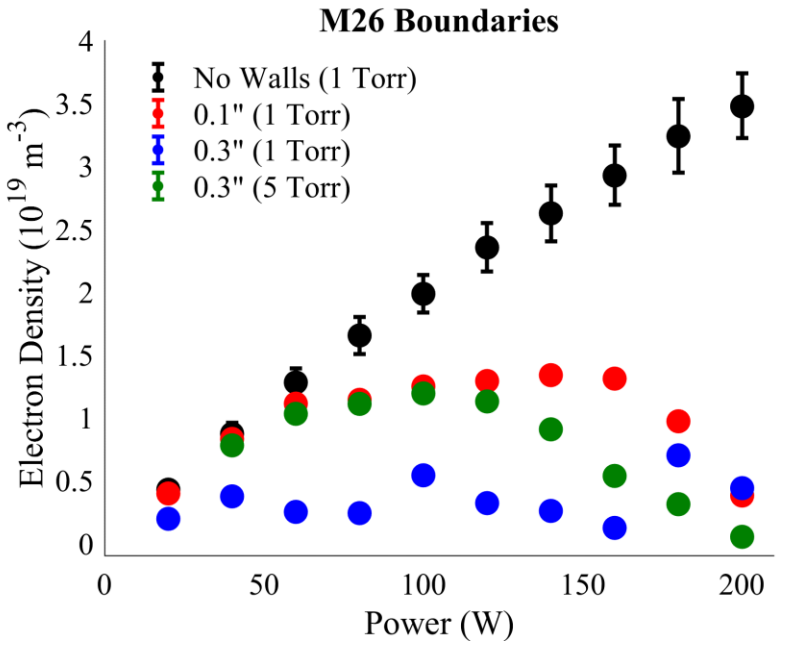

Figure 162 – Average electron density (M26 BN boundaries)

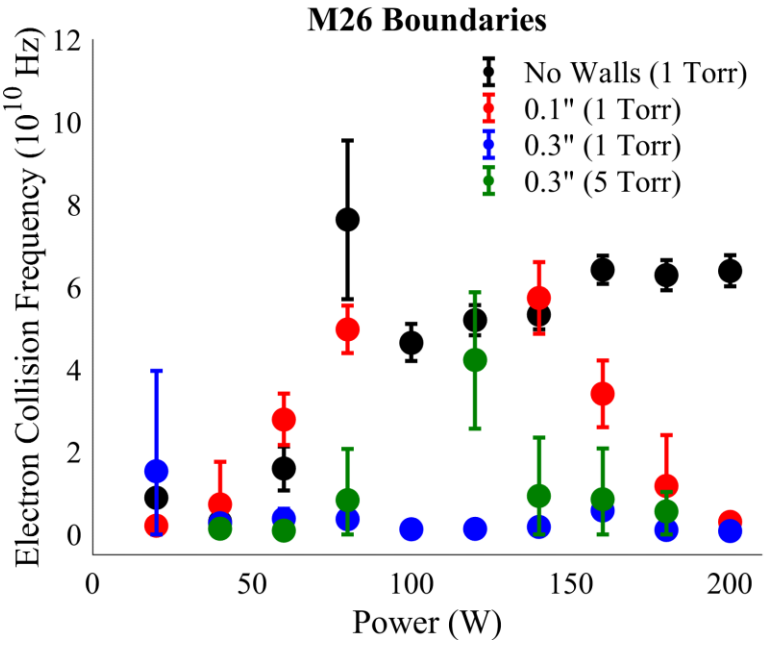

Figure 163 – Average electron collision frequency (M26 BN boundaries)

The electron density trends in Figure 162 appear to support the explanations given in the previous section. The 0.1 in-thick M26 BN boundaries allow more argon into the bounded region than do the 0.3 in-thick boundaries and thereby result in a larger electron density for the same reported pressure. Increasing the reported discharge pressure to 5 Torr with the 0.3 in-thick boundaries produces a similar effect; the larger overall discharge pressure results in a higher neutral pressure within the bounded region and thereby enables a higher electron density within the bounded plasma region.

The resultant larger electron densities for the higher bounded region neutral pressure configurations also result in more consistent trends with input power. After initially increasing with input power, the electron density plateaus for a range of input powers before beginning to decrease with input power. The reduced ionization efficiency caused

by the loss of high-energy electrons at the wall and reduced coupling of power to the plasma from interference by the boundaries are sufficient to slow and even reverse the increase of electron density with input power.

7.4 Summary

Section 7.1 augments the basic THz-TDS plasma theory to enable bounded plasma measurements. It was found that the ps-scale duration of the THz pulses enables application of the theory without complications from FP reflections in both the ICP discharge and Hall thruster channel. Section 7.2 provides the refractive index and absorption coefficient measured in relevant grades of BN used as Hall thruster channel material. Increases in SiO_2 composition were found to decrease the detected THz pulse SNR.

Section 7.3 presents the first-ever measurements of a plasma bounded and optically shielded by Hall thruster wall material. The results demonstrate that the large SNR losses caused by THz pulse propagation through wall material can preclude calculation of the electron collision frequency. The electron density, however, remains detectable even in the lowest SNR cases presented here. The results of Section 7.3, coupled with those of Section 5.3.2, provide strong evidence that THz-TDS is a viable candidate to make the first-ever noninvasive electron density measurement inside the Hall thruster channel. Its capability to make electron collision frequency measurements depends on specific BN composite thickness and grade, as well as the peak electron collision frequency value inside the channel and THz pulse SNR.

CHAPTER 8. CONCLUSIONS AND FUTURE WORK

8.1 Conclusions

The purpose of this work is to develop and evaluate THz-TDS for EP plasma diagnostics. To that end, this dissertation provides three major contributions: 1) Analysis of the THz-TDS domain of applicability; 2) Development of a novel Bayesian THz-TDS plasma diagnostic analysis framework and subsequent evaluation of THz-TDS uncertainty; and 3) Development and application of THz-TDS to noninvasively probe plasma bounded and optically shielded by Hall thruster wall material.

Study of the domain of applicability presented in Chapter 5 found that THz-TDS is capable of measuring a broad range of electron densities and collision frequencies and, under certain conditions, is impervious to thermal and magnetic field effects. The large domain of applicability makes THz-TDS a viable candidate for performing plasma diagnostics in many EP environments, including the Hall thruster channel, cathode plume, MPD thruster plume, and gridded ion thruster plume.

Chapter 6 introduces a novel Bayesian THz-TDS plasma diagnostic analysis framework that offers significant advantages over the standard analysis method. The Bayesian framework can compute electron density, electron collision frequency, and associated parameter uncertainties. Analysis with the framework found that, compared to electron collision frequency, electron density calculation uncertainties are largely insensitive to changes in pulse properties that do not inhibit basic data processing or cause the density resolvability limit to approach the measured electron density.

Chapter 7 develops the theory required to make bounded plasma measurements with THz-TDS and presents the first-ever noninvasive measurements of a plasma bounded and optically shielded by Hall thruster wall material. The wall material was found to drastically reduce the THz pulse SNR, but, though this reduction did inhibit calculation of electron collision frequency in some cases, the loss of SNR did not significantly impact electron density results. THz-TDS was therefore found to be a viable candidate for performing the first-ever noninvasive measurement of the Hall thruster discharge channel plasma.

8.2 Recommendations for Future Work

THz-TDS is in its infancy as a plasma diagnostic, and, though this dissertation makes important strides, many possibilities for future work remain. One of the most important areas of future work is the application of THz-TDS to an EP device operating in a standard EP test facility. Application of THz-TDS in this environment presents challenges, such as ambient vibrations and the necessity to couple either THz or laser radiation into a vacuum chamber. These challenges are likely best overcome through the use of a fiber-coupled THz-TDS system. Specifically, the development and application of a fiber-coupled THz-TDS system to measure Hall thruster channel plasma properties would represent a great contribution to the EP field.

Other major areas of future work could have wide-ranging applications across many areas of plasma physics. These entail the development and application of THz-TDS systems with increased spatial and temporal resolution. THz-TDS measures line-integrated electron density and line-averaged electron collision frequency, so three-dimensional spatial resolution may be achieved through the development of a THz-TDS tomography system.

As noted in Chapter 2, previous authors have used THz-TDS to measure "time-resolved" properties by simply implementing electronic gating techniques. Such measurements require assumption of repeatable plasma conditions and are more accurately described as phase-resolved. However, THz pulses have picosecond-scale temporal duration and could therefore presumably be used to achieve true picosecond-scale temporal resolution. More work is required in the areas of single-shot detection and fast scanning techniques, such as asynchronous optical sampling (ASOPS) and electronically-controlled optical sampling (ECOPS), to improve the true temporal resolution of THz-TDS. Systems with high true temporal resolution could capture plasma phenomena with presently infeasible detail.

APPENDIX A. THZ-TDS TROUBLESHOOTING

Even for researchers with optics experience, constructing and aligning an operational THz-TDS system is a nontrivial endeavor. The purpose of this appendix is to serve as a practical guide to help future researchers construct THz-TDS systems. This guide is limited THz-TDS configurations that emit THz radiation with a PCA and detect THz radiation electro-optically with a ZnTe crystal. Readers are encouraged to first read Chapter 3, as this guide assumes knowledge of the information covered in Chapter 3.

A.1 Overview

Problems in THz-TDS operation during the dissertation experimental setup phase were encountered due to failures to:

1. Maintain electrostatic-sensitive device (ESD) protocols with the PCA
2. Maintain proper temporal laser pulse width at the PCA and ZnTe
3. Ensure the probe and pump paths have identical length
4. Align the delay line and retroreflector
5. Ensure proper polarization of the THz and probe beams with respect to the ZnTe crystal
6. Focus and align the pump beam on the PCA gap
7. Align the THz beam along the probe beam path

If a THz-TDS system has been constructed but is not operational, the reader is recommended to ensure each of the above criteria have been met. Discussion of these criteria and advice for meeting these criteria are included below.

A.2 ESD Considerations

PCAs feature micron-scale electrode gaps patterned onto semiconducting material, so PCAs are ESDs that must be handled properly. Humans are capable of building kV-scale internal biases that are more than sufficient to damage PCAs. Whenever a PCA is handled, the user must maintain constant connection to electrical ground and ensure the workspace is also connected to electrical ground. Damage caused by failure to adhere to ESD protocols results in an electrical short across the PCA gap that renders the PCA inoperable. Electrical shorts can be detected through measurement of the PCA resistance (typically determined by measuring the current sourced by an applied voltage bias). Some manufacturers implement diodes into the PCA circuit to help protect against electrostatic discharge events, however, even in these cases, ESD protocols should always be practiced.

A.3 Pulse Duration

Emission and detection of THz radiation require ultrashort laser pulses (typically ~100 fs). Ultrashort laser pulses, however, suffer from GVD in a THz-TDS setup, so GVD compensation schemes may be required to ensure ultrashort laser pulses maintain their ultrashort nature after propagation to the PCA and ZnTe crystal. It is important that the temporal pulse width be measured directly upstream of both the PCA and ZnTe whenever any optic is added or removed from the system. More information on GVD compensation can be found in Chapter 3.

A.4 Path Lengths

The probe laser pulses must arrive at the ZnTe within the ps-scale time window of the THz pulses. It is therefore important that the probe path and pump path (including the THz beam path) be the same distance, to within about 30 mm. In practice, this is approximately achieved by measuring pump and probe paths with a tape measure and precisely achieved by scanning the delay line until the delay line position corresponding to the beginning of the THz pulse is located.

A.5 Delay Line Alignment

Misalignment of the delay line and/or retroreflector (or mirror setup) on the delay line may cause artificial biases in measured phase that, as discussed in Chapter 4, can lead to linear trends in measured plasma electron density with THz frequency. Delay line error can be minimized by iteratively adjusting the delay line, retroreflector, and input mirrors until translation of the delay line across its full range of motion generates miniscule changes in beam position far downstream of the delay line retroreflector output.

The delay line setup was aligned for this dissertation by checking the beam position through irises positioned 0.5-1.5 ft and 7-8 ft (depending on the delay line position) from the retroreflector output. Alignment was confirmed by measuring changes in the PCA photocurrent caused by translation of the delay line across the range required to resolve a 100 ps THz pulse (approximately 15 mm). Changes in the photocurrent were less than 0.1% across this range of motion. Considering the sensitivity of the photocurrent to micron-scale changes in focusing lens position, such a small change in photocurrent with delay line position was deemed acceptable.

A.6 Polarization and ZnTe Orientation

As detailed by Planken et al. [62], THz signal maxima exist for multiple configurations of the THz and probe beam polarizations and ZnTe crystal orientation. However, multiple minima with potentially undetectable signal strength also exist. It is therefore important to carefully control the polarizations of the THz and probe beams and the orientation of the ZnTe crystal. The THz pulse polarization is approximately determined by the orientation of the dipole gap. To first order, the polarization is in the direction along which the photocurrent travels across the gap. The probe beam polarization can easily be set by a half-wave plate and checked with a polarizing beam splitter temporarily placed upstream of the ZnTe crystal.

The configuration was optimized in the THz-TDS setup for this dissertation project by iteratively adjusting the probe polarization and ZnTe crystal orientation until the signal was maximized. As a starting point, the probe polarization was set to that of the expected THz pulse polarization and the ZnTe orientation was set so that both polarizations were approximately parallel to the $[1\bar{1}0]$ axis.

A.7 Pump Beam Alignment

The pump beam must be focused and aligned to the PCA gap to generate detectable THz radiation. Failure to focus to the gap can reduce the THz pulse SNR below detectability, and failure to align to the gap typically prevents emission of THz radiation altogether. As discussed in Chapter 3, proper focus and alignment were achieved with an aspheric lens situated in a custom mount that could position the lens with micron precision

both in the PCA plane and in the length separating the lens and PCA. The mount is shown in Figure 164.

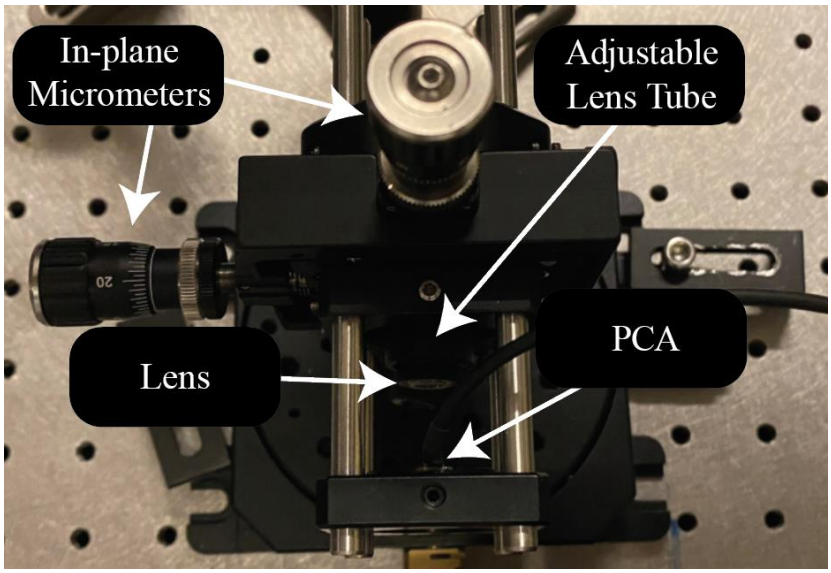

Figure 164 – PCA focusing mount

The position of the aspheric lens must be iteratively adjusted until the pump beam is properly focused and aligned onto the PCA gap. Focus and alignment are best verified through measurement of the microamp-scale photocurrent across the PCA gap. An initial position may be determined by visually centering the lens along the PCA gap axis and separating the lens and PCA by the reported lens focal length. For PCAs with small gaps (~5 microns) and minimum achievable Gaussian pump beam diameter on the order of the PCA gap, the lens position should be iterated until micron-scale deviations in PCA plane position result in substantial decreases in measured photocurrent (10-30% depending on the gap and minimum achievable beam sizes). Assuming the PCA gap is the smallest electrode separation on the PCA, the lens position is optimal when the photocurrent

sensitivity to positional changes is greatest. For many (but not all) PCAs, this is also the lens position for which the photocurrent is maximized.

It should be noted that, if the PCA gap is significantly larger than the minimum achievable beam diameter, the preceding alignment technique may not apply. In this case, THz beam quality is sensitive to the position of the focused beam within the PCA gap [41].

A.8 THz Beam Alignment

Alignment of the THz beam with the probe beam can be difficult, as there is typically no independent mechanism for detecting the position of the THz beam. The THz beam is highly divergent as it leaves the PCA and must therefore be coupled to air with a lens (typically silicon). Centering of the coupling lens to the PCA gap is vital to ensure the THz beam is properly focused, collimated, or semi-collimated. Some manufacturers sell PCAs with the coupling lens pre-aligned and thereby eliminate the need for the user to perform manual micron-scale alignment. The BATOP PCA used in this dissertation project was supplied with a pre-aligned coupling lens.

After coupling, the THz beam must be collimated, focused, and/or steered through the sample and then focused onto the ZnTe crystal. Lens and mirror positioning to achieve proper focus and collimation is generally achieved by initially carefully measuring beam propagation distances and then iteratively adjusting optical component positions to maximize THz signal strength.

Initial alignment was achieved in this dissertation project through alignment of the back-reflected probe beam. The ZnTe crystal was replaced with a mirror that was carefully aligned to ensure the back-reflected probe beam traveled back along the path from which it came. This was checked by comparing the positions of the incident back-reflected probe

beams on mirrors with an infrared viewer. Though the majority of the back-reflected probe beam traveled back through the hole in the parabolic mirror closest to the ZnTe in Figure 8, due to diffraction, some of the back-reflected beam was reflected to the parabolic mirror closest to the PCA. The parabolic mirror positions were adjusted until, with 90° beam turning angles, the back-reflected pulse was aligned to the center of the PCA parabolic mirror and was focused to the center of the coupling lens. Beam positions were checked with the infrared viewer.

APPENDIX B. THZ PCA FAILURE

The most significant experimental delays in this work were caused by prematurely failing THz PCAs. This appendix discusses THz PCA failure and is intended to serve as a practical reference for other researchers who encounter similar problems.

B.1 Overview

Initial efforts attempted to use the Menlo TERA8-1 wrapped dipole antenna, but multiple TERA8-1 antennae ceased to function after 24 hours of use – even though they were operated well within the manufacturers' optical power and voltage bias limits. Failure was characterized by rapid decrease in THz pulse SNR, antenna resistance, and photocurrent. Upon the onset of failure, the SNR of the pulse peak decreased from approximately 200:1 to 1:1 in two to three hours of continuous use. During failure, the antenna resistance and photocurrent decreased until the photocurrent was indistinguishable from the "dark" current (the current measured in the absence of the optical pump).

Menlo supplied multiple PCAs that remained operational for various periods of time, but no PCA survived long enough to complete the experiments required for this dissertation. PCAs that were operated with lower optical pump powers and voltage biases survived for longer periods of time but also exhibited lower SNR. Menlo was eventually dropped as a supplier after the company failed to resolve PCA life issues and additionally began supplying completely inoperable PCAs covered in thick film.

The next antenna model used was the BATOP PCA-60-05-10-800-h. However, the delivered PCA suffered severe performance loss within a few days of use. As with the Menlo TERA8-1, the BATOP PCA-60-05-10-800-h exhibited reduced SNR, resistance,

and photocurrent. BATOP performed an investigation, noted the same issues in their laboratory, and provided a replacement that maintained performance throughout the entire duration of the dissertation test campaign. However, it is important to note that the PCA was never operated at its maximum bias and input optical power limits. The PCA bias and input optical power limits provided by BATOP were 20 V and 10 mW, respectively, but the PCA was never operated above 15 V and 5 mW.

A bPCA-180-05-10-800-h bowtie antenna was also purchased from BATOP, but this antenna ceased to function after fewer than 24 hours of use. Lifetime issues with the PCA-60-05-10-800-h and bPCA-180-05-10-800-h identified by experimental efforts for this dissertation prompted BATOP to temporarily cease sales of many PCA models and launch an investigation into failure mechanisms. As of the time of this writing, the investigation is ongoing.

B.2 Failure Mechanism

Figure 165 compares the schematics of each PCA and shows the damage caused by use in the THz-TDS system. Optical damage to the LT-GaAs substrate is present in the Menlo PCA gap. The two BATOP PCAs exhibit optical damage in the substrate, as well as possible delamination and sputtering of the gold electrodes.

TERA8-1 bPCA-180-05-10-800-h PCA-60-05-10-800-h

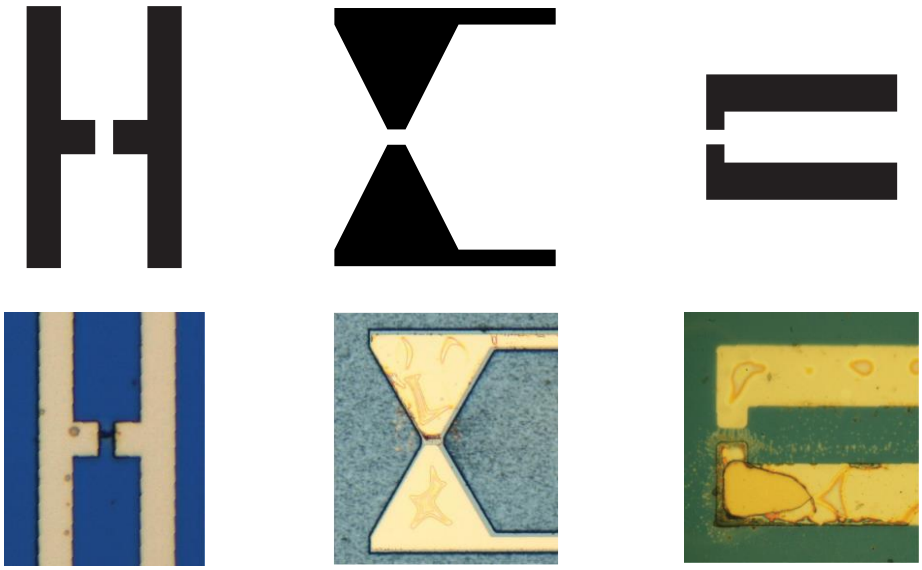

Scale: Antenna gap is 5 microns on each PCA

Figure 165 – PCA schematics and damage images

A possible source of the damage is the use of optical pump intensities that exceed the intensity threshold of the substrate. In addition to providing average power input limits, the manufacturers recommend not focusing the beam to Gaussian diameters smaller than the antenna gap. Analysis assuming Gaussian beam shape was implemented to design a beam positioning system with a focusing lens of sufficient focal length to ensure this criterion was met.

However, the manufacturers do not provide a minimum pump pulse duration limit. The pump pulse FWHM of the THz-TDS setup is approximately 50 fs, but most commercial antennae are qualified with input pulses with FWHM of approximately 100 fs. The use of a shorter pump pulse in this work may have increased the intensity above the substrate threshold and damaged the PCAs; however, because neither Menlo nor BATOP

is presently able to report intensity damage thresholds, this theory cannot be confirmed. More information on PCA damage mechanisms can be found in [89].

REFERENCES

[1] Jahn, R. G., *Physics of Electric Propulsion*, McGraw-Hill Book Company, New York, 1968.

[2] Goebel, D. M., and Katz, I., *Fundamentals of Electric Propulsion: Ion and Hall Thrusters*, John Wiley & Sons, Hoboken, New Jersey, 2008.

[3] Mazouffre, S., "Electric propulsion for satellites and spacecraft: established technologies and novel approaches," *Plasma Sources Science and Technology*, Vol. 25, No. 3, 2016, Paper 033002.

[4] Garner, C. E., Rayman, M. D., and Brophy, J. R., "In-Flight Operation of the Dawn Ion Propulsion System-Arrival at Ceres," *34th International Electric Propulsion Conference*, Electric Rocket Propulsion Society, IEPC, Kobe-Hyogo, Japan, 2015.

[5] Hofer, R., Lobbia, R., Chaplin, V., Ortega, A., Mikellides, I., Polk, J., Kamhawi, H., Frieman, J., Huang, W., Peterson, P., and Herman, D., "Completing the Development of the 12.5 kW Hall Effect Rocket with Magnetic Shielding (HERMeS)," *36th International Electric Propulsion Conference*, Electric Rocket Propulsion Society, IEPC Paper 2019-193, Vienna, Austria, 2019.

[6] Oh, D. Y., Collins, S., Drain, T., Hart, W., Imken, T., Larson, K., Marsh, D., Muthulingam, D., Snyder, J. S., Trofimov, D., Elkins-Tanton, L. T., Johnson, I., Lord, P., and Pirkl, Z., "Development of the Psyche Mission for NASA's Discovery Program," *36th International Electric Propulsion Conference*, Electric Rocket Propulsion Society, IEPC Paper 2019-192, Vienna, Austria, 2019.

[7] Steiger, C., Montagnon, E., Budnik, F., Manganelli, S., Altay, A., Striedter, F., Gray, H. L., Bolter, J., Wallace, N., and Sutherland, O., "BepiColombo – Solar Electric Propulsion System Operations for the Transit to Mercury," *36th International Electric Propulsion Conference*, Electric Rocket Propulsion Society, IEPC, Vienna, Austria, 2019.

[8] Lev, D., Myers, R. M., Lemmer, K. M., Kolbeck, J., Koizumi, H., and Polzin, K., "The technological and commercial expansion of electric propulsion," *Acta Astronautica*, Vol. 159, 2019, pp. 213-227.

[9] Thompson, A., "SpaceX Launches 60 Starlink Satellites, Nails Rocket Landing in Record-Breaking Flight", Space.com, January 7, 2020.
https://www.space.com/spacex-starlink-2-launch-success.html

[10] Chen, F. F., *Introduction to Plasma Physics and Controlled Fusion, 3rd ed.*, Springer International Publishing, Switzerland, 2016.

[11] Charles, C., "Plasmas for spacecraft propulsion," *Journal of Physics D: Applied Physics*, Vol. 42, No. 16, 2009, Paper 163001.

[12] Chabert, P., and Braithwaite, N., *Physics of Radio-Frequency Plasmas*, Cambridge University Press, New York, 2011.

[13] Chen, F. F., "Helicon discharges and sources: a review," *Plasma Sources Science and Technology*, Vol. 24, No. 1, 2015, Paper 014001.

[14] Lieberman, M. A., *Principles of plasma discharges and materials processing*, Hoboken, N.J. : Wiley-Interscience, Hoboken, N.J., 2005.

[15] Boeuf, J.-P., "Tutorial: Physics and modeling of Hall thrusters," *Journal of Applied Physics*, Vol. 121, No. 1, 2017, Paper 011101.

[16] Brown, N. P., and Walker, M. L. R., "Review of Plasma-Induced Hall Thruster Erosion," *Applied Sciences*, Vol. 10, No. 11, 2020, Paper 3775.

[17] Meezan, N. B., Hargus, W. A., Jr., and Cappelli, M. A., "Anomalous electron mobility in a coaxial Hall discharge plasma," *Physical Review E*, Vol. 63, No. 2, 2001, Paper 026410.

[18] Jorns, B., "Predictive, data-driven model for the anomalous electron collision frequency in a Hall effect thruster," *Plasma Sources Science and Technology*, Vol. 27, No. 10, 2018, Paper 104007.

[19] de Grys, K., Mathers, A., Welander, B., and Khayms, V., "Demonstration of 10,400 Hours of Operation on 4.5 kW Qualification Model Hall Thruster," *46th AIAA/ASME/SAE/ASEE Joint Propulsion Conference & Exhibit*, AIAA Paper 2010-6698, 2010.

[20] Laurent, B., Rossi, A., Öberg, M., Zurbach, S., Largeau, G., Lasgorceix, P., Estublier, D., and Boniface, C., "High Throughput 1.5 kW Hall Thruster for Satcoms," *36th International Electric Propulsion Conference*, Electric Rocket Propulsion Society, IEPC Paper 2019-274, Vienna, Austria, 2019.

[21] Levchenko, I., Xu, S., Mazouffre, S., Lev, D., Pedrini, D., Goebel, D., Garrigues, L., Taccogna, F., and Bazaka, K., "Perspectives, frontiers, and new horizons for plasma-based space electric propulsion," *Physics of Plasmas*, Vol. 27, No. 2, 2020, Paper 020601.

[22] Ahedo, E., and Merino, M., "On plasma detachment in propulsive magnetic nozzles," *Physics of Plasmas*, Vol. 18, No. 5, 2011, Paper 053504.

[23] Sarrailh, P., Belhaj, M., Inguimbert, V., and Boniface, C., "Synergic erosion of ceramic by electron and ion simultaneous irradiation of the Hall thruster channel walls," *35th International Electric Propulsion Conference*, Electric Rocket Propulsion Society, IEPC Paper 2017-314, Atlanta, GA, 2017.

[24] Deline, C. A., Bengtson, R. D., Breizman, B. N., Tushentsov, M. R., Jones, J. E., Chavers, D. G., Dobson, C. C., and Schuettpelz, B. M., "Plume detachment from a magnetic nozzle," *Physics of Plasmas*, Vol. 16, No. 3, 2009, Paper 033502.

[25] Olsen, C. S., Ballenger, M. G., Carter, M. D., Díaz, F. R. C., Giambusso, M., Glover, T. W., Ilin, A. V., Squire, J. P., Longmier, B. W., Bering, E. A., and Cloutier, P. A., "Investigation of Plasma Detachment From a Magnetic Nozzle in the Plume of the VX-200 Magnetoplasma Thruster," *IEEE Transactions on Plasma Science*, Vol. 43, No. 1, 2015, pp. 252-268.

[26] Lobbia, R. B., "A Time-resolved Investigation of the Hall Thruster Breathing Mode," Ph.D. Dissertation, Aerospace Engineering Dept., University of Michigan, Ann Arbor, MI, 2010.

[27] Lobbia, R. B., and Beal, B. E., "Recommended Practice for Use of Langmuir Probes in Electric Propulsion Testing," *Journal of Propulsion and Power*, Vol. 33, No. 3, 2017, pp. 566-581.

[28] Ellison, C. L., Raitses, Y., and Fisch, N. J., "Cross-field electron transport induced by a rotating spoke in a cylindrical Hall thruster," *Physics of Plasmas*, Vol. 19, No. 1, 2012, Paper 013503.

[29] Hutchinson, I. H., *Principles of Plasma Diagnostics*, Cambridge University Press, New York, 2002.

[30] Hargus, J. W. A., and Cappelli, M. A., "Laser-induced fluorescence measurements of velocity within a Hall discharge," *Applied Physics B*, Vol. 72, No. 8, 2001, pp. 961-969.

[31] Emile, C., and Sander, N., "Thomson scattering on non-equilibrium low density plasmas: principles, practice and challenges," *Plasma Physics and Controlled Fusion*, Vol. 57, No. 1, 2015, Paper 014026.

[32] Romadanov, I., Raitses, Y., Diallo, A., Hara, K., Kaganovich, I. D., and Smolyakov, A., "On limitations of laser-induced fluorescence diagnostics for xenon ion velocity distribution function measurements in Hall thrusters," *Physics of Plasmas*, Vol. 25, No. 3, 2018, Paper 033501.

[33] Washeleski, R. L., Meyer, E. J. I., and King, L. B., "Application of maximum likelihood methods to laser Thomson scattering measurements of low density plasmas," *Review of Scientific Instruments*, Vol. 84, No. 10, 2013, Paper 105101.

[34] Heald, M. A., and Wharton, C. B., *Plasma Diagnostics with Microwaves*, John Wiley & Sons Inc., New York, 1965.

[35] Kolner, B. H., Buckles, R. A., Conklin, P. M., and Scott, R. P., "Plasma Characterization With Terahertz Pulses," *IEEE Journal of Selected Topics in Quantum Electronics*, Vol. 14, No. 2, 2008, pp. 505-512.

[36] Naftaly, M., and Leist, J., "Investigation of optical and structural properties of ceramic boron nitride by terahertz time-domain spectroscopy," *Applied Optics*, Vol. 52, No. 4, 2013, pp. B20-B25.

[37] Lee, Y.-S., *Principles of Terahertz Science and Technology*, Springer, New York, 2009.

[38] Dexheimer, S. L., *Terahertz Spectroscopy: Principles and Applications*, CRC Press, Boca Raton, FL, 2008.

[39] Auston, D. H., Cheung, K. P., and Smith, P. R., "Picosecond photoconducting Hertzian dipoles," *Applied Physics Letters*, Vol. 45, No. 3, 1984, pp. 284-286.

[40] Neu, J., and Schmuttenmaer, C. A., "Tutorial: An introduction to terahertz time domain spectroscopy (THz-TDS)," *Journal of Applied Physics*, Vol. 124, No. 23, 2018, Paper 231101.

[41] Burford, N. M., and El-Shenawee, M. O., "Review of terahertz photoconductive antenna technology," *Optical Engineering*, Vol. 56, No. 1, 2017, Paper 010901.

[42] Wu, Q., and Zhang, X. C., "Free-space electro-optic sampling of terahertz beams," *Applied Physics Letters*, Vol. 67, No. 24, 1995, pp. 3523-3525.

[43] Jamison, S. P., Shen, J., Jones, D. R., Issac, R. C., Ersfeld, B., Clark, D., and Jaroszynski, D. A., "Plasma characterization with terahertz time–domain measurements," *Journal of Applied Physics*, Vol. 93, No. 7, 2003, pp. 4334-4336.

[44] Kolner, B. H., Conklin, P. M., Buckles, R. A., Fontaine, N. K., and Scott, R. P., "Time-resolved pulsed-plasma characterization using broadband terahertz pulses correlated with fluorescence imaging," *Applied Physics Letters*, Vol. 87, No. 15, 2005, Paper 151501.

[45] Ando, A., Kurose, T., Reymond, V., Kitano, K., Kitahara, H., Takano, K., Tani, M., Hangyo, M., and Hamaguchi, S., "Electron density measurement of inductively coupled plasmas by terahertz time-domain spectroscopy (THz-TDS)," *Journal of Applied Physics*, Vol. 110, No. 7, 2011, Paper 073303.

[46] Ebbinghaus, S., Schröck, K., Schauer, J. C., Bründermann, E., Heyden, M., Schwaab, G., Böke, M., Winter, J., Tani, M., and Havenith, M., "Terahertz time-domain spectroscopy as a new tool for the characterization of dust forming plasmas," *Plasma Sources Science and Technology*, Vol. 15, No. 1, 2006, pp. 72-77.

[47] Jang, D., Uhm, H. S., Jang, D., Hur, M. S., and Suk, H., "Electron density characterization of inductively-coupled argon plasmas by the terahertz time-domain spectroscopy," *Plasma Sources Science and Technology*, Vol. 25, No. 6, 2016, Paper 065008.

[48] Kang, K., Jang, D., and Suk, H., "Plasma density measurements using THz pulses from laser-plasmas," *Journal of Instrumentation*, Vol. 12, No. 11, 2017, Paper C11003.

[49] Meier, S. M., Tsankov, T. V., Luggenhölscher, D., and Czarnetzki, U., "Measurement of plasma densities by dual frequency multichannel boxcar THz time domain spectroscopy," *Journal of Physics D: Applied Physics*, Vol. 50, No. 24, 2017, Paper 245202.

[50] Meier, S. M., Hecimovic, A., Tsankov, T. V., Luggenhölscher, D., and Czarnetzki, U., "First measurements of the temporal evolution of the plasma density in HiPIMS discharges using THz time domain spectroscopy," *Plasma Sources Science and Technology*, Vol. 27, No. 3, 2018, Paper 035006.

[51] Curcio, A., and Petrarca, M., "Diagnosing plasmas with wideband terahertz pulses," *Optics Letters*, Vol. 44, No. 4, 2019, pp. 1011-1014.

[52] Zhao, Y., Wang, Y., Shi, J., Wu, D., Feng, C., Wu, G., Yuan, K., and Ding, H., "Comparison of Terahertz time domain spectroscopy and laser Thomson scattering for electron density measurements in inductively coupled plasma discharges," *Journal of Instrumentation*, Vol. 14, No. 12, 2019, pp. C12019-C12019.

[53] Chen, K., Xu, D., Li, J., Geng, X., Zhong, K., and Yao, J., "Application of terahertz time-domain spectroscopy in atmospheric pressure plasma jet diagnosis," *Results in Physics*, Vol. 16, 2020, Paper 102928.

[54] Hecht, E., *Optics, 5th ed.*, Pearson, Malaysia, 2017.

[55] Withayachumnankul, W., and Naftaly, M., "Fundamentals of Measurement in Terahertz Time-Domain Spectroscopy," *Journal of Infrared, Millimeter, and Terahertz Waves*, Vol. 35, No. 8, 2014, pp. 610-637.

[56] Duvillaret, L., Garet, F., and Coutaz, J., "A reliable method for extraction of material parameters in terahertz time-domain spectroscopy," *IEEE Journal of Selected Topics in Quantum Electronics*, Vol. 2, No. 3, 1996, pp. 739-746.

[57] Stix, T. H., *Waves in Plasmas*, American Institute of Physics, New York, 1992.

[58] Yuan, C., Zhou, Z., Xiang, X., Sun, H., Wang, H., Xing, M., and Luo, Z., "Propagation properties of broadband terahertz pulses through a bounded magnetized thermal plasma," *Nuclear Instruments and Methods in Physics Research Section B: Beam Interactions with Materials and Atoms*, Vol. 269, No. 1, 2011, pp. 23-29.

[59] Diels, J.-C., and Rudolph, W., *Ultrashort Laser Pulse Phenomena, 2nd Ed.*, Elsevier, Boston, MA, 2006.

[60] Jepsen, P. U., Jacobsen, R. H., and Keiding, S. R., "Generation and detection of terahertz pulses from biased semiconductor antennas," *Journal of the Optical Society of America B,* Vol. 13, No. 11, 1996, pp. 2424-2436.

[61] Van Rudd, J., and Mittleman, D. M., "Influence of substrate-lens design in terahertz time-domain spectroscopy," *Journal of the Optical Society of America B,* Vol. 19, No. 2, 2002, pp. 319-329.

[62] Planken, P. C. M., Nienhuys, H.-K., Bakker, H. J., and Wenckebach, T., "Measurement and calculation of the orientation dependence of terahertz pulse detection in ZnTe," *Journal of the Optical Society of America B,* Vol. 18, No. 3, 2001, pp. 313-317.

[63] Wu, Q., Litz, M., and Zhang, X. C., "Broadband detection capability of ZnTe electro-optic field detectors," *Applied Physics Letters*, Vol. 68, No. 21, 1996, pp. 2924-2926.

[64] Gallot, G., and Grischkowsky, D., "Electro-optic detection of terahertz radiation," *Journal of the Optical Society of America B,* Vol. 16, No. 8, 1999, pp. 1204-1212.

[65] MacDonald, N. A., Cappelli, M. A., and Hargus, W. A., "Time-synchronized continuous wave laser-induced fluorescence on an oscillatory xenon discharge," *Review of Scientific Instruments*, Vol. 83, No. 11, 2012, Paper 113506.

[66] Teo, S. M., Ofori-Okai, B. K., Werley, C. A., and Nelson, K. A., "Invited Article: Single-shot THz detection techniques optimized for multidimensional THz spectroscopy," *Review of Scientific Instruments*, Vol. 86, No. 5, 2015, Paper 051301.

[67] van Exter, M., Fattinger, C., and Grischkowsky, D., "Terahertz time-domain spectroscopy of water vapor," *Optics Letters*, Vol. 14, No. 20, 1989, pp. 1128-1130.

[68] Chen, F. F., Evans, J. D., and Zawalski, W., "Calibration of Langmuir probes against microwaves and plasma oscillation probes," *Plasma Sources Science and Technology*, Vol. 21, No. 5, 2012, Paper 055002.

[69] Williams, L. T., "Ion Acceleration Mechanisms of Helicon Thrusters," Ph.D. Dissertation, Aerospace Engineering Dept., Georgia Institute of Technology, Atlanta, GA, 2013.

[70] Grischkowsky, D., Keiding, S., van Exter, M., and Fattinger, C., "Far-infrared time-domain spectroscopy with terahertz beams of dielectrics and semiconductors," *Journal of the Optical Society of America B*, Vol. 7, No. 10, 1990, pp. 2006-2015.

[71] Briggs, W. L., and Henson, V. E., *The DFT: An Owner's Manual for the Discrete Fourier Transform*, Society for Industrial and Applied Mathematics, Philadelphia, 1995.

[72] Jepsen, P. U., "Phase Retrieval in Terahertz Time-Domain Measurements: a "how to" Tutorial," *Journal of Infrared, Millimeter, and Terahertz Waves*, Vol. 40, No. 4, 2019, pp. 395-411.

[73] Withayachumnankul, W., Fischer, B. M., Lin, H., and Abbott, D., "Uncertainty in terahertz time-domain spectroscopy measurement," *Journal of the Optical Society of America B*, Vol. 25, No. 6, 2008, pp. 1059-1072.

[74] Optoelectronics, B., "PCA - Photoconductive Antenna for Terahertz waves, 800 nm", September 8, 2020.
https://www.batop.de/products/terahertz/photoconductive-antenna/photoconductive-antenna-800nm.html

[75] Gamero-Castaño, M., and Katz, I., "Estimation of Hall Thruster Erosion Using HPHall," *29th International Electric Propulsion Conference*, Electric Rocket Propulsion Society, IEPC Paper 2005-303, Princeton, NJ, 2005.

[76] Goebel, D. M., Jameson, K. K., Watkins, R. M., Katz, I., and Mikellides, I. G., "Hollow cathode theory and experiment. I. Plasma characterization using fast miniature scanning probes," *Journal of Applied Physics*, Vol. 98, No. 11, 2005, Paper 113302.

[77] Mikellides, I. G., Katz, I., Goebel, D. M., and Jameson, K. K., "Evidence of nonclassical plasma transport in hollow cathodes for electric propulsion," *Journal of Applied Physics*, Vol. 101, No. 6, 2007, Paper 063301.

[78] Gardner, J. A., Kelly, A. J., and Nerheim, N. M., "Electron density and temperature measurements in the exhaust of an MPD source," *AIAA Journal*, Vol. 4, No. 2, 1966, pp. 291-295.

[79] de Boer, P. C. T., "Electric probe measurements in the plume of an ion thruster," *Journal of Propulsion and Power*, Vol. 12, No. 1, 1996, pp. 95-104.

[80] von Toussaint, U., "Bayesian inference in physics," *Reviews of Modern Physics*, Vol. 83, No. 3, 2011, pp. 943-999.

[81] Neal, R. M., "Slice sampling," *Annals of Statistics*, Vol. 31, No. 3, 2003, pp. 705-795.

[82] Langendorf, S., "Effects of Electron Emission on Plasma Sheaths," Ph.D. Dissertation, Aerospace Engineering Dept., Georgia Institute of Technology, Atlanta, GA, 2015.

[83] Withayachumnankul, W., Ferguson, B., Rainsford, T., Mickan, S., and Abbott, D., "Direct Fabry-Pérot Effect Removal," *Fluctuation and Noise Letters*, Vol. 06, No. 02, 2006, pp. L227-L239.

[84] Zunger, A., Katzir, A., and Halperin, A., "Optical properties of hexagonal boron nitride," *Physical Review B*, Vol. 13, No. 12, 1976, pp. 5560-5573.

[85] Mackey, J., Salem, J., Stanford, M., Kamhawi, H., McEnerney, B., and Hofer, R., "Lot-to-lot variability of BN grades for space electric propulsion applications," *44th International Conference and Expo on Advanced Ceramics and Composites*, American Ceramic Society, Daytona Beach, FL, 2020.

[86] Gascon, N., Dudeck, M., and Barral, S., "Wall material effects in stationary plasma thrusters. I. Parametric studies of an SPT-100," *Physics of Plasmas*, Vol. 10, No. 10, 2003, pp. 4123-4136.

[87] Stittsworth, J. A., and Wendt, A. E., "Reactor geometry and plasma uniformity in a planar inductively coupled radio frequency argon discharge," *Plasma Sources Science and Technology*, Vol. 5, No. 3, 1996, pp. 429-435.

[88] Wu, Y., and Lieberman, M. A., "The influence of antenna configuration and standing wave effects on density profile in a large-area inductive plasma source," *Plasma Sources Science and Technology*, Vol. 9, No. 2, 2000, pp. 210-218.

[89] Qadri, S. B., Wu, D. H., Graber, B. D., Mahadik, N. A., and Garzarella, A., "Failure mechanism of THz GaAs photoconductive antenna," *Applied Physics Letters*, Vol. 101, No. 1, 2012, Paper 011910.